FUNDAMENTAL STUDY OF THE DEVELOPMENT AND EVALUATION OF BIODEGRADABLE Mg-Y-Ca-Zr ALLOYS AS NOVEL IMPLANT MATERIALS

by

Da-Tren Chou

B.S.E. Biomedical Engineering, Case Western Reserve University, 2009

Submitted to the Graduate Faculty of

Swanson School of Engineering in partial fulfillment

of the requirements for the degree of

Doctor of Philosophy in Bioengineering

University of Pittsburgh

2015

UNIVERSITY OF PITTSBURGH

SWANSON SCHOOL OF ENGINEERING

This dissertation was presented

by

Da-Tren Chou

It was defended on

November 24, 2015

and approved by

Dissertation Director: Prashant N. Kumta, PhD, Edward R. Weidlein Chair Professor, Departments of Bioengineering, Mechanical Engineering and Materials Science, Chemical and Petroleum Engineering

Alejandro Almarza, PhD, Associate Professor, Oral Biology, Department of Bioengineering

Aaron Barchowsky, PhD, Professor, Department of Environmental and Occupational Health

Harvey Borovetz, PhD, Distinguished Professor, Department of Bioengineering, Robert L. Hardesty Professor, Department of Surgery, Professor, Department of Chemical and Petroleum Engineering

Howard Kuhn, PhD, Adjunct Professor, Department of Industrial Engineering

FUNDAMENTAL STUDY OF THE DEVELOPMENT AND EVALUATION OF BIODEGRADABLE Mg-Y-Ca-Zr ALLOYS AS NOVEL IMPLANT MATERIALS

Da-Tren Chou, Ph.D.

University of Pittsburgh, 2015

Degradable metals hold considerable promise as materials which exhibit higher mechanical properties than degradable polymers while corroding over time to alleviate complications such as stress-shielding and infection that is inherent to permanent, bioinert metallic biomaterials. Specifically, degradable magnesium (Mg) alloys have emerged as a promising alternative for orthopedic and craniofacial applications due to their positive bone remodeling behavior, good biocompatibility, and relatively high strength compared to polymers while exhibiting similar stiffness to natural bone. Increasing the strength to maintain device integrity during degradation while simultaneously controlling the rapid corrosion of Mg to reduce the risk of hydrogen gas accumulation and toxicity are ongoing paramount goals for optimizing Mg alloys for musculoskeletal applications. In order to address these goals, novel Mg-Y-Ca-Zr based alloys were developed with alloying elements judiciously selected to impart favorable properties. Processing techniques including solution heat treatment combined with hot extrusion were employed to further enhance the desired properties of the material namely, controlled corrosion, high strength and ductility, and minimal toxic response. Increasing the Y content contributed to improved corrosion resistance yielding corrosion rates similar to commercial Mg alloys. Hot extrusion was employed to reduce the grain size, thereby improving mechanical properties

through the Hall-Petch relation. Extrusion yielded extremely high strength relative to other Mg alloys, values approaching that of iron-based alloys, due to the presence of $Mg_{12}YZn$, a long period stacking order phase that served to impede dislocation propagation. Both as-cast and extruded Mg-Y-Ca-Zr alloys demonstrated excellent in vitro cytocompatibility eliciting high viability and proliferation of MC3T3 pre-osteoblast cells and human mesenchymal stem cells. Alloying elements Y and Zr were specifically shown to improve cell proliferation. Finally, implantation of Mg-Y-Ca-Zr based alloys into the mouse subcutaneous tissue and intramedullary cavities of fractured rat femurs resulted in a normal host response and fracture healing, without eliciting any local or systemic toxicity. Thus, the alloys investigated in this work demonstrated great potential for applications as orthopedic and craniofacial implant biomaterials, warranting additional pre-clinical safety and efficacy trials that will be conducted in the near future.

TABLE OF CONTENTS

ACKNOWLEDGEMENTS XXI

1.0 INTRODUCTION 1

1.1 CURRENT BIOMATERIALS FOR ORTHOPEDIC IMPLANTS 1

1.1.1 Inert metals 6

1.1.2 Inert and resorbable polymers 9

1.1.3 Ceramics 11

1.1.4 Resorbable metals 12

1.2 MAGNESIUM: A PROMISING BIOMATERIAL 16

1.2.1 Historical precedence of magnesium implants 16

1.2.2 Materials properties of magnesium 20

1.2.3 Corrosion mechanism of magnesium 22

1.2.4 Toxicity and biocompatibility of magnesium alloys 27

1.3 SPECIFIC AIMS 29

1.3.1 Specific Aim 1: Synthesize novel Mg-Y-Ca-Zr based alloys and perform materials characterization to assess the changes in microstructure after addition of alloying elements and post-processing treatments 30

1.3.2 Specific Aim 2: Characterize the effect of yttrium and zinc addition and post processing on the corrosion behavior and mechanical properties of Mg-Y-Ca-Zr alloys 31

1.3.3 Specific Aim 3: Evaluate the effect of Yttrium and Zinc addition, post processing, and alloying element salts, on cell viability and proliferation of pre-osteoblast and human mesenchymal stem cells. Further evaluate expression of

osteoblast differentiation markers and biocompatibility in murine subcutaneous tissue..... 31

1.3.4 Specific Aim 4: Assess the in vivo corrosion, bone formation, and host response of Mg-Y-Zn-Ca-Zr alloy in a rat femur osteotomy model 32

2.0 SPECIFIC AIM 1: SYNTHESIZE NOVEL MG-Y-CA-ZR BASED ALLOYS AND PERFORM MATERIALS CHARACTERIZATION TO ASSESS THE CHANGES IN MICROSTRUCTURE AFTER ADDITION OF ALLOYING ELEMENTS AND POST-PROCESSING TREATMENTS 34

2.1 INTRODUCTION 34

2.2 MATERIALS AND METHODS 37

2.2.1 Metallurgical processing of Mg-Y-Ca-Zr based alloys 37

2.2.2 Phase characterization of Mg-Y-Ca-Zr based alloys..... 39

2.2.3 Microstructure analysis of Mg-Y-Ca-Zr based alloys..... 39

2.3 RESULTS 40

2.3.1 Materials properties of as-cast and solution treated Mg-Y-0.6Ca-0.4Zr based alloys 40

2.3.2 Changes in phase and microstructure with extrusion and addition of Y and Zn to Mg-Y-1Zr-0.6Ca based alloys 45

2.4 DISCUSSION..... 50

3.0 SPECIFIC AIM 2: CHARACTERIZE THE EFFECTS OF YTTRIUM AND ZINC ADDITION AND POST PROCESSING ON CORROSION BEHAVIOR AND MECHANICAL PROPERTIES OF MAGNESIUM-YTTRIUM-CALCIUM-ZIRCONIUM ALLOYS 53

3.1 INTRODUCTION 53

3.2 MATERIALS AND METHODS 55

3.2.1 Corrosion testing of Mg-Y-Ca-Zr based alloys 55

3.2.2 Microhardness testing of Mg-Y-Ca-Zr based alloys..... 56

3.2.3 Mechanical testing of Mg-Y-Ca-Zr based alloys..... 57

3.2.4 Statistical analysis 57

3.3 RESULTS 58

3.3.1 Corrosion behavior of Mg-Y-Ca-Zr based alloys as a result of Y and Zn additions 58

3.3.2 Microhardness of Mg-Y-Ca-Zr based alloys as a result of Y and Zn additions 71

3.3.3 Mechanical properties of Mg-Y-Ca-Zr based alloys as a result of Y and Zn additions and extrusion 72

3.4 DISCUSSION 77

4.0 SPECIFIC AIM 3: EVALUATE THE EFFECT OF YTTRIUM AND ZINC ADDITION, POST PROCESSING, AND ALLOYING ELEMENT SALTS, ON CELL VIABILITY AND PROLIFERATION OF PRE-OSTEOBLAST AND HUMAN MESENCHYMAL STEM CELLS. FURTHER EVALUATE EXPRESSION OF OSTEOBLAST DIFFERENTIATON MARKERS AND BIOCOMPATIBILITY IN MURINE SUBCUTANEOUS TISSUE 85

4.1 INTRODUCTION 85

4.2 MATERIALS AND METHODS 88

4.2.1 Cell culture and maintenance 88

4.2.1.1 Mouse pre-osteoblast cell line (MC3T3-E1) 88

4.2.1.2 Human mesenchymal stem cells (hMSCs) 89

4.2.2 Direct LIVE/DEAD cell viability and adhesion test 89

4.2.3 F-actin and nuclei staining, SEM/EDX imaging of fixed cells 90

4.2.4 Alloy degradation product extract collection for indirect *in vitro* tests . 90

4.2.5 MTT cytotoxicity test 91

4.2.6 CyQUANT proliferation test 91

4.2.7 Alkaline phosphatase activity 92

4.2.8 Quantitative real-time polymerase chain reaction (qRT–PCR) 93

4.2.9 In vivo murine subcutaneous study 94

4.3 RESULTS 95

4.3.1 Cell viability and adhesion on surface of Mg-Y-Ca-Zr based alloys 95

4.3.2 Viability and proliferation of cells indirectly exposed to degradation products of Mg-Y-Ca-Zr based alloys 100

4.3.3 Proliferation of pre-osteoblasts and human mesenchymal stem cells indirectly exposed to degradation products of Mg-Y-Ca-Zr based alloys 104

4.3.4 Differentiation of human mesenchymal stem cells indirectly exposed to degradation products of Mg-Y-Ca-Zr based alloys 110

4.3.5 Proliferation of human mesenchymal stem cells exposed to salts of Mg, Y, Ca, Zr, Zn, and Al 113

4.3.6 Differentiation of human mesenchymal stem cells exposed to salts of Mg, Y, Ca, Zr, Zn, and Al 117

4.3.7 In vivo murine subcutaneous study 118

4.4 DISCUSSION 123

5.0 SPECIFIC AIM 4: ASSESS THE IN VIVO CORROSION, BONE FORMATION, AND HOST RESPONSE OF MAGNESIUM-YTTRIUM-ZINC-CALCIUM-ZIRCONIUM ALLOY IN A RAT FEMUR OSTEOTOMY MODEL 131

5.1 INTRODUCTION 131

5.2 MATERIALS AND METHODS 133

5.2.1 Preparation of Mg-Y-Zn-Ca-Zr implants 133

5.2.2 Animal model 134

5.2.3 X-ray imaging 136

5.2.4 Blood-cell count and serum biochemical measurements 136

5.2.5 Micro-computed tomography imaging 137

5.2.6 Histological preparation and analysis 138

5.2.7 Tissue digestion and elemental analysis 138

5.3 RESULTS 139

5.3.1 Fixation of femoral defect using Mg-Y-Zn-Ca-Zr alloy pin 139

5.3.2 Systemic toxicity to Mg-Y-Zn-Ca-Zr implants 141

5.3.3 Histological examination of liver and kidneys 146

5.3.4 *In vivo* corrosion of Mg-Y-Zn-Ca-Zr alloy pins and morphology of surrounding bone 149

5.3.5 Local tissue response to Mg-Y-Zn-Ca-Zr alloy pin 152

5.4 DISCUSSION 156

6.0 OVERALL CONCLUSIONS AND FUTURE WORK 162

APPENDIX A 167

APPENDIX B 203

APPENDIX C 206

BIBLIOGRAPHY 207

LIST OF TABLES

Table 1.1. Summary of biomaterials for orthopedic applications. Used with permission of [5].... 4

Table 1.2. Mechanical properties of metallic biomaterials compared to natural bone [5, 11-13].. 8

Table 1.3. Selected standard electrode potentials of metal in aqueous solution at 25 °C relative to the standard hydrogen electrode [57]..... 14

Table 2.1. Nominal composition of Mg alloys (wt.%) investigated in this work..... 37

Table 2.2. Temperatures used to preheat ingots for 30 minutes and during extrusion of solution treated alloys. ER = extrusion ratio. 38

Table 2.3. Chemical composition and impurities of Mg-based alloys (wt.%) as measured by ICP-OES. 40

Table 4.1. Summary of the pathophysiology and toxicology of Mg and alloying elements used in the alloys of this work [154, 180]. The toxicity levels for bone cells are according to the cytotoxicity test of the metal salts; (+) represents mild toxicity, (+-) symbolizes moderate toxicity, and (-) indicates severe toxicity. 87

Table 4.2. qRT-PCR primer sequences used for human mesenchymal stem cells..... 93

Table 5.1. Summary of number of rats in each groups at time points used in study. 136

Table 5.2. Average blood cell count of unoperated animals and animals implanted with WZ42 and Ti6Al4V alloy pins at 2, 8, and 14 weeks after implantation. 141

Table 5.3. Average values of serum metabolic parameters unoperated animals and animals implanted with WX42 and Ti6Al4V alloy pins at 2, 8, and 14 weeks after implantation. 143

Table 5.4. Average values of electrolyte parameters of unoperated animals and animals implanted with WX42 and Ti6Al4V alloy pins at 2, 8, and 14 weeks after implantation. 144

Table A.1 Chemical composition with standard deviation of the mixed Fe-30Mn (wt.%) powder used for 3D printing. 173

Table A.2. Mechanical properties of 3D printed Fe-30Mn compared to Fe-30Mn produced by sintering and rolling, pure Fe, and natural bone. 186

Table A.3. Electrochemical corrosion measurements conducted in Hanks‘ Balanced Salts solution at 37 °C of 3D printed Fe-30Mn and pure Fe: corrosion potential, corrosion current density, and corrosion current. * $p < 0.05$ between groups. 191

LIST OF FIGURES

Figure 1.1. Schematic diagram of the ideal change in strength over time of degrading orthopedic implants. Used with permission of [56]. 13

Figure 1.2. Publications from 2002 to 2014 on magnesium and stainless steel biomaterials (retrieved from the Web of Science using “magnesium” and “stainless steel” as a search query within the category “biomaterials”). 17

Figure 1.3. Pourbaix diagram of Mg in water at 25 °C showing corrosion, passivation, and immunity. The region of water stability lies between the dashed lines [106]. 23

Figure 1.4. Schematic depiction of the corroding surface of polycrystalline Mg alloys: (a) galvanic corrosion between Mg and grain boundaries; (b) partially protective film of $Mg(OH)_2$ covering the surface; (c) attack by chloride ions to transform $Mg(OH)_2$ into $Mg(Cl)_2$; (d) hydroxyapatite formation by consuming local Ca^{2+} and PO_4^{3-}; (e) particles removed from the bulk Mg entering the surrounding solution. Adapted from source, used with permission of [109]. 24

Figure 1.5. Flouroscopic images of cross-sections of a degradable polymer (a) and a magnesium rod (b) performed 10 mm below the trochanter major in a guinea pig femur. Both specimens were harvested 18 weeks postoperatively. In vivo staining of newly formed bone by calcein green. Scale bar=1.5mm; I=implant residual; P=periosteal bone formation; E=endosteal bone formation. Used with permission of [125]. 28

Figure 2.1. XRD patterns of as-cast pure Mg, WX11, and WX41. 41

Figure 2.2. Optical micrographs of Mg-Y-Ca-Zr alloys after polishing and etching: a) WX11 as-cast; b) WX11 T4 heat treated; c) WX41 as-cast; d) WX41 T4 heat treated; e) pure Mg as-cast; f) AZ31 as-drawn. 43

Figure 2.3. SEM images of Mg-Y-Ca-Zr alloys after polishing and etching: a) WX11 as-cast; b) WX11 T4 heat treated; c) WX41 as-cast; d) WX41 T4 heat treated with corresponding EDX of grain boundaries and precipitates as noted by arrows. Scale bar = 50 µm. 45

Figure 2.4. XRD patterns of extruded KX11, WK11, WK41, and WZ42..... 46

Figure 2.5. Optical micrographs showing the microstructure of Mg alloys extruded with extrusion ratio 10: a,f) KX11, b,g) WK11, c,h) WK41, d,i) WZ42 and extrusion ratio 30 –

e,j) WZ42, with sections take in the transverse direction (top, a-e) and longitudinal direction (bottom, f-j)..... 48

Figure 2.6. SEM images and EDX analysis at indicated locations of Mg alloys after polishing and etching: a) KX11; b) WK11; c) WK41; d) WZ42 after extrusion with extrusion ratio of 10. Sections were taken in the transverse plane to the direction of extrusion. Scale bar = 10 μm. 50

Figure 3.1. Corrosion properties of Mg-Y-Ca-Zr alloys, as-cast 99.99% pure Mg, and AZ31 in DMEM with 10% FBS: a) corrosion rate as measured using mass loss after 1, 2, and 3 weeks immersion (n = 3 per group per time point) and potentiodynamic corrosion (n = 1 per group). Significant difference ($p < 0.05$) between * and **; between † and ‡, between §. b) corrosion potential and breakdown potential (n = 1 per group); c) concentration of Mg released in corrosion media after 1, 2, and 3 weeks immersion (n = 3 per group per time point). Significant difference ($p < 0.05$) between * and **; † and ‡. 60

Figure 3.2. SEM images showing surface morphologies of a) WX11 as-cast; b) WX11 T4 heat treated; c) WX41 as-cast; d) WX41 T4 heat treated; e) pure Mg; f) AZ31 after potentiodynamic polarization in DMEM with 10% FBS at 37 °C and cleaning with CrO_3/$AgNO_3$ solution. Arrows denote corrosion at grain boundaries. 62

Figure 3.3. SEM images showing surface morphologies of a) WX11 as-cast; b) WX11 T4 heat treated; c) WX41 as-cast; d) WX41 T4 heat treated; e) pure Mg; f) AZ31 after 3 weeks static immersion in DMEM with 10% FBS at 37 °C. EDX was performed at various spots as denoted by arrows. 64

Figure 3.4. SEM images showing surface morphologies of a) WX11 as-cast; b) WX11 T4 heat treated; c) WX41 as-cast; d) WX41 T4 heat treated; e) pure Mg; f) AZ31 after 3 weeks static immersion in DMEM with 10% FBS at 37 °C and cleaning with CrO_3/$AgNO_3$ solution. 65

Figure 3.5. Average corrosion rates of extruded Mg-Y-Ca-Zr-based alloys compared to extruded pure Mg and AZ31 (in commercial and produced in-house forms). Groups labeled * were significantly different ($p < 0.05$) from one another at that time point and those labeled † were significantly different ($p < 0.05$) from all other groups at that time point. n = 3 for all groups at all time points. 67

Figure 3.6. SEM images at 50x and 250x magnification showing surface morphologies of extruded a) pure Mg, b) commercially obtained AZ31, alloys produced in-house extruded with extrusion ratio of 10: c) AZ31, d) KX11, e) WK11, f) WK41, and g) WZ42 after 1 week static immersion in HBSS at 37 °C and cleaning with CrO_3/$AgNO_3$ solution. 69

Figure 3.7. SEM images at 100x and 250x magnification showing cross sectional morphologies of extruded a) pure Mg, AZ31 obtained b) commercially and c) processed in-house, and d) KX11, e) WK11, f) WK41, and g) WZ42 alloys extruded with extrusion ratio 10 and h) WZ42 extruded with extrusion ratio of 30 after 5 weeks static immersion in HBSS at 37 °C and cleaning with CrO_3/$AgNO_3$ solution. Location of sample metal and mounting epoxy is indicated in a). 70

Figure 3.8. Vickers microhardness of extruded Mg alloys. Group labeled * was significantly different ($p < 0.05$) than all other groups, and groups labeled † were significantly different ($p < 0.05$) from all other groups but not from one another. ER = extrusion ratio. n = 5 for all groups at all time points. 71

Figure 3.9. Mechanical properties of Mg-Y-Ca-Zr alloys, pure Mg, and AZ31: a) ultimate compressive strength and ultimate compressive strain; Significant difference ($p < 0.05$) between * and all other groups; †, ‡ and other groups. b) compressive yield strength; Significant difference ($p < 0.05$) between * and all other groups; †, ‡ and other groups. c) ultimate tensile strength and ultimate tensile strain; Significant difference ($p < 0.05$) between *, § with all other groups; †, ‡ with other groups. d) tensile yield strength and Young's modulus; Significant difference ($p < 0.05$) between § with all other groups; †, ‡ with other groups. $n \leq 3$ for all groups at all time points. 73

Figure 3.10. Average ultimate tensile strength and strain of extruded Mg alloys. Measurements of ultimate tensile strains labeled * were significantly different ($p < 0.05$) from each other. Measurements of ultimate tensile stress labeled † were significantly different ($p < 0.05$) from all other groups but not from one another. Measurements of ultimate tensile stress labeled ‡ were significantly different from all other groups. ER = extrusion ratio. n = 5 for all groups at all time points. 75

Figure 3.11. Average tensile yield strength and Young's modulus of extruded Mg alloys. Measurements of yield strength labeled * were significantly different ($p < 0.05$) from all other groups; groups labeled † and ‡ were significantly different ($p < 0.05$) from all other groups but not from one another. ER = extrusion ratio. n = 5 for all groups at all time points. 76

Figure 3.12. The yield tensile strength and elongation of cast and wrought Mg alloys with alloys from this thesis included – WX11 and WX41 in as-cast form and KX11, WK11, WK41, and WZ42 extruded at a ratio of 10. Figure adopted from Zheng et al, used with permission of [154]. 84

Figure 4.1. Fluorescent images of live (green) and dead (red) MC3T3-E1 cells attached after 1 and 3 days culture on a & h) WX11 as-cast; b & i) WX11 T4 heat treated; c & j) WX41 as-cast; d & k) WX41 T4 heat treated; e & l) pure Mg; f & m) AZ31 as-drawn; g & n) tissue culture plastic. 96

Figure 4.2. Live (green) and dead (red) MC3T3 cells on the surface of polished and extruded Mg alloy surfaces after 1 (above) and 3 (below) days of culture. Scale bar = 200 µm. 97

Figure 4.3. Phalloidin staining for F-actin (red) and DAPI staining for cell nuclei (blue) of MC3T3 cells on the surface of polished extruded Mg alloy surfaces after 3 days of culture. Scale bar = 20 µm. 98

Figure 4.4. SEM images of MC3T3 cells attached to surface of extruded a) commercially obtained AZ31, b) pure Mg, c) KX11, d) WK11, e) WK41, and f) WZ42 after 3 days culture. 99

Figure 4.5. Average weight % of Ca and P on the surface of extruded Mg alloy samples after 3 days culture with MC3T3 cells, as determined by EDX. Groups marked with * were significantly different from one another. n = 4 for each group..... 100

Figure 4.6. Viability of MC3T3 cells cultured for a) 1 day and b) 3 days in extract media from as-cast and T4 heat treated WX11 and WX41 alloys and as-cast pure Mg. Significant difference ($p < 0.05$) between * and other groups or as connected. n = 5 per extract concentration per group per time point. 101

Figure 4.7. Viability of MC3T3 cells cultured for a) 1 day and b) 3 days in extract media containing degradation products from extruded alloys and commercial AZ31 and pure Mg. Groups labeled * significantly different ($p < 0.05$) from one another. Groups labeled with † significantly different ($p < 0.05$) with groups labeled with ‡. n = 4 per extract concentration per group per time point. 103

Figure 4.8. Proliferation of MC3T3 cells cultured for 3 days with extruded alloy extracts of AZ31, KX11, WK11, WK41, and WZ42 diluted to 25%, 10%, 1%, and 0.1%, compared to commercial pure Mg and AZ31 as a percentage of control cells cultured with regular extract media. Groups labeled * significantly different ($p < 0.05$) from other groups at same extract concentration. n = 4 per extract concentration per group per time point... 105

Figure 4.9. Florescence images of MC3T3 cells exposed to extruded alloy extracts diluted to 25%, 10%, 1%, and 0.1%, after 3 days culture with DNA bound to the CyQUANT dye. Scale bar (lower right, same for all images) = 200 µm..... 106

Figure 4.10. Proliferation of hMSCs cultured for a) 1 days, b) 3 days, and c) 5 days with extruded alloy extracts diluted to 50%, 25%, and 10% of AZ31, KX11, WK11, WK41, AND WZ42, compared to commercial pure Mg and AZ31 as a percentage of control cells cultured with regular extract media. Groups labeled * significantly different ($p < 0.05$) from one another. Groups labeled with † significantly different ($p < 0.05$) from all other groups at that time point. Groups labeled with ‡ significantly different from all other groups at that time point except WK41. n = 4 per extract concentration per group per time point. 108

Figure 4.11. Florescence images of hMSCs exposed to extruded alloy extracts diluted to 50%, 25%, and 10% after 5 days culture with DNA bound to the CyQUANT dye. Scale bar (lower right, same for all images) = 200 µm. 109

Figure 4.12. ALP quantification (normalized with DNA) using hMSCs in indirect method for extruded Mg alloys after a) 3 days, b) 7 days, and c) 14 days of culture with extracts diluted to 50%, 25%, and 10%. GM = growth media control; DM = differentiation media control. Groups labeled * significantly different ($p < 0.05$) from one another. Groups labeled with † significantly different ($p < 0.05$) from all other groups at that time point. n = 4 per extract concentration per group per time point..... 111

Figure 4.13. qRT-PCR gene expression data showing the expression of RUNX2, ALP, and OCN hMSCs cultured for a) 7 days, b) 14 days), and c) 21 days with 10% extracts diluted in differentiation media normalized with respect to cells cultured in growth media and

compared to differentiation media group where media did not contain extracts. n = 1 for all groups..... 113

Figure 4.14. Proliferation of hMSCs cultured for a) 1 days, b) 3 days, and c) 5 days with chloride salts of Mg (in concentrations of 50 mM, 20 mM, 10 mM, and 1 mM) and Y, Ca, Zr, Zn, and Al (in concentrations of 1 mM, 0.1 mM, 0.01 mM, and 0.001 mM) dissolved in growth media, as a percentage of control cells cultured with growth media and differentiation media. Groups labeled * were significantly different ($p < 0.05$) from control cells cultured in fresh growth media. n = 3 per extract concentration per group per time point. 115

Figure 4.15. Florescence images of hMSCs exposed to alloying element chloride salts of Mg (in concentrations of 50 mM, 20 mM, 10 mM, and 1 mM) and Y, Ca, Zr, Zn, and Al (in concentrations of 1 mM, 0.1 mM, 0.01 mM, and 0.001 mM) dissolved in growth media after 5 days culture with DNA bound to the CyQUANT dye. Scale bar (lower right, same for all images) = 200 µm..... 116

Figure 4.16. ALP quantification (normalized with DNA) using hMSCs in culture with chloride salts of Mg (in concentrations of 50 mM, 20 mM, 10 mM, and 1 mM) and Y, Ca, Zr, Zn, and Al (in concentrations of 1 mM, 0.1 mM, 0.01 mM, and 0.001 mM) dissolved in growth media for 14 days. Significant difference between groups labeled * and growth media control ALP activity. GM = growth media control; DM = differentiation media control. n = 3 per extract concentration per group per time point. 118

Figure 4.17. a-l) Histology images (H&E staining) of the skin above the implants of a, e, i) WX11 and b, f, j) WX41 as-cast alloys, c, g, k) pure Mg, and d, h, l) AZ31 after 7 days (a-d), 40 days (e-h), and 70 days (i-l) in the subcutis of nude mice. 120

Figure 4.18. Corrosion rate as calculated by mass loss of pellet samples before and after murine subcutaneous implantation at time points of 40 and 70 days. n = 1 for each group. 121

Figure 4.19. SEM images showing surface morphologies of a) WX11 as-cast; b) WX41 as-cast; c) pure Mg; d) AZ31 after 70 days implantation in murine subcutaneous tissue. EDX was performed at various spots as denoted by arrows. 122

Figure 4.20. SEM images showing surface morphologies of a) WX11 as-cast; b) WX41 as-cast; c) pure Mg; d) AZ31 after 70 days implantation in murine subcutaneous tissue and cleaning with CrO_3/$AgNO_3$ solution..... 123

Figure 5.1. Schematic (a) and photograph (b) of pins (lower) inserted into the femoral intramedullary cavity and wire cuffs (upper) wrapped around the mid-diaphyseal region. In a) the wire was machined straight then bent around the femur during surgery..... 134

Figure 5.2. Surgical procedure used to implant metallic samples: a) Photograph of pins inserted into the femoral intramedullary cavity (bottom) and wire cuffs wrapped around the mid-diaphyseal region (top). Pin model - a) Lines indicating where incision was made to expose the femur; b) Fracture being created in rat femur using circular saw; c) Pin inserted into marrow space of one side of fractured femur; d) Pin inserted into other side

of femur to bridge the fractured femur; e) Fracture closed with pin maintaining alignment and fixation; f) Surgical site fully closed and sutured. Cuff model - g) After incision to expose femur, the bone was left intact without osteotomy and a wire was wrapped around the midsection of the femur. 135

Figure 5.3. One week X-ray images of implanted WZ42 magnesium alloy (a) and Ti6Al4V (b) K-wires (designated by white arrow) in the right femur of rats; c) fracture misalignment (red arrow) and empty spaces near the WZ42 implants (yellow arrow, circled) were observed in some X-ray images. One week X-ray images of implanted WZ42 magnesium alloy (d) and Ti6Al4V (e) wire cuffs (designated by white arrow) in the right femur of rats. 140

Figure 5.4. Average Mg (a), Ca (b), and Zn (c) concentration in digested liver and kidney samples of rats implanted with femoral pins and cuffs of WZ42 and Ti6Al4V for 8 and 14 weeks compared to unoperated control rats. Significant difference * ($p < 0.05$) between Mg concentration in kidneys of rats implanted with WZ42 pins for 8 weeks and unoperated control rats and between † ($p<0.05$) between Zn concentrations in kidneys of rats implanted with WZ42 pins for 8 weeks and cuffs. $n \leq 3$ per extract concentration per group per time point. 145

Figure 5.5. Photomicrographs of H&E stained kidneys of rats with femurs fixed by pins of WZ42 (a, c) and Ti6Al4V (b, d) after 8 weeks (a, b) and 16 weeks (c, d). Stained images of kidneys from rats with implanted wire cuffs of WZ42 (e) and Ti6Al4V (f) wrapped around bone for 14 weeks. Photomicrograph g) from rat that was left unoperated. Scale bar = 50 µm. 147

Figure 5.6. Photomicrographs of H&E stained livers of rats with femurs fixed by pins of WZ42 (a, c) and Ti6Al4V (b, d) after 8 weeks (a, b) and 16 weeks (c, d). Stained images of livers from rats implanted with wire cuffs of WZ42 (e) and Ti6Al4V (f) wrapped around bone for 14 weeks. Photomicrograph g) from rat that was left unoperated. Scale bar = 50 µm. 148

Figure 5.7. To determine volume of the degrading WZ42 alloy, pins were distinguished from surrounding bone in micro-CT scans based on density thresholding with representative examples highlighted in green after implantation times of a) 2 weeks, b) 8 weeks, c) 14 weeks. Cuffs were fully degraded after 14 weeks (d) but new bone formation was seen in the region the wires occupied (arrows). 149

Figure 5.8. Corrosion rate and % volume remaining of WZ42 pins implanted in rat femurs for 2, 8, and 14 weeks. $n \geq 2$ for each group at each time point. * and † represent significant difference ($p < 0.05$) compared to measurements made at other time points. 151

Figure 5.9. Photomicrographs of Goldner's Trichrome stained sections (40x) of soft and hard tissue at the defect site fixed by pins of WZ42 magnesium alloy (a, c, e) and Ti6Al4V (b, d, f) after 2 weeks (a, b), 8 weeks (c, d), and 14 weeks (e, f) of implantation; g) representation of region of interest imaged along longitudinal plane at defect site.

Cytoplasm, fibrin, muscle, and osteoids are represented in red; collagen and bone are represented in green. The dashed line approximates the implant pin-bone interface. 153

Figure 5.10. Photomicrographs of the localization of ALP at 40x and 100x (inset) of tissue at the defect site fixed by pins of WZ42 magnesium alloy (a, c, e) and Ti6Al4V (b, d, f) after 2 weeks (a, b), 8 weeks (c, d), and 14 weeks (e, f) of implantation. Scale bar = 200 μm in 40x images, 100 μm in 100x. Pin located on left side of image in all. 154

Figure 5.11. Photomicrographs of Goldner's Trichrome stained sections (40x) of soft and hard tissue at the implant-bone interface where wire cuffs of WZ42 magnesium alloy (a) and Ti6Al4V (b) were wrapped around bone for 14 weeks of implantation. c) Representation of region of interest imaged along longitudinal plane at defect site. Cytoplasm, fibrin, muscle, and osteoids are represented in red; collagen and bone are represented in green. The dashed line approximates the location of the WZ42 wire. 155

Figure A.1. SEM of powder precursors used to fabricate Fe-30Mn 3DP parts: a) Fe -325 mesh powder; b) Mn -325 mesh powder; c) 70 wt.% Fe – 30 wt.% Mn mixed powder. 180

Figure A.2. XRD patterns of Fe-30Mn mixed powder and Fe-30Mn after 3DP, curing, and sintering. 181

Figure A.3. Photographs of example parts 3D printed from Fe-30Mn powder after sintering: part with square pore sizes of lengths a) 1 mm and b) 500 μm; miniature human femur c) before tumble finishing and d) after tumble finishing. 183

Figure A. 4. Microstructure of Fe-30Mn 3DP parts after sintering imaged using a) optical microscopy after polishing; b) SEM without polishing; c) SEM after polishing with EDX performed at regions indicated by arrows. 185

Figure A.5. Representative potentiodynamic polarization curves of 3D printed Fe-30Mn compared to pure Iron conducted in Hanks' Balanced Salts solution at 37 °C. 188

Figure A.6. Optical microscopy (a & b) and SEM images (c-f) showing surface morphologies of a, c, d) 3D printed Fe-30Mn with EDX analysis after potentiodynamic polarization tests and e) after cleaning in solution of HCl/Sb2O3/SnCl2; b & f) pure Iron after potentiodynamic polarization tests. 190

Figure A.7. Cytotoxicity of MC3T3 cells cultured for 1 and 3 days in extract media from 3D printed Fe-30Mn immersed in αMEM cell culture media supplemented with 10% FBS and 100 U/ml penicillin, and 100 μg/ml streptomycin. 192

Figure A.8. SEM image and EDX analysis of 3D printed Fe-30Mn sample after 3 days immersion in αMEM cell culture media supplemented with 10% FBS and 100 U/ml penicillin, and 100 μg/ml streptomycin. 193

Figure A.9. Fluorescent images from the live/dead assay of live (green) and dead (red) MC3T3 cells attached after 1 and 3 days culture on a & c) 3D printed Fe-30Mn; b & d) tissue culture plastic. 194

Figure A.10. SEM images of MC3T3 cells on the surface of 3DP Fe-30Mn after 1 and 3 days of culturing at a & c) 250x and b & d) 750x magnification. White arrow denotes cell-cell junction; black arrows denote cellular extensions to pore walls..... 195

Figure B.1. Backscattered electron microscopty of WK41 alloy with T4 solution treatment applied after casting at 400 °C for 10, 20, 40, and 70 h followed by water quenching.. 204

Figure B.2. Corrosion rate of WX41 alloy as-cast and T4 heat treated at 400 °C for various times and compared to commercial AZ31 and pure Mg after 10 days immersion in HBSS. .. 205

ACKNOWLEDGEMENTS

To my parents and sister:

Ti & Rosa, and Tze-Ann

Whose love and support for me have shaped me into the person I am today.

Firstly, I would like to state my most sincere appreciation for my dissertation adviser, Professor Prashant Kumta, PhD, for his outstanding and invaluable mentorship throughout my time spent here at the University of Pittsburgh. Without his trust and belief in me, reasoned guidance, and constant support of my goals, I would not have reached where I am today. I am grateful for Dr. Kumta's willingness to provide rational advice on any subject, within the realm of science and beyond that allowed me to grow and learn.

I would also like to thank the rest of my PhD thesis committee – Dr. Alejandro Almarza, Dr. Aaron Barchowsky, Dr. Harvey Borovetz, and Dr. Howard Kuhn, for their insight and advice ever since the start of my PhD. I learned a great deal with each collaboration and interaction we shared. I would like to specifically acknowledge Dr. Almarza for his assistance in utilization of his mechanical testing system.

I would like to extend my thanks to the Edward R. Weidlein Chair Professorship, the Center for Complex Engineered Multifunctional Materials, and NSF–CBET Grant # 0933153 for

partial support of this research. I am especially appreciative of the National Science Foundation Engineering Research Center for Revolutionizing Metallic Biomaterials (ERC-RMB) for providing funding for my research, and of everyone involved with the center. Special thanks go out to Dr. Jagannathan Sankar, Dr. Peter Seoane, Mr. Richard Hoff, Dr. William Wagner, and Dr. Zhigang Xu for the incredible opportunities for both research and professional development they provided through the ERC-RMB. I am also grateful to Andrew Holmes and the Swanson Center for Product Innovation for providing hours of training, expertise, and machine time to help in the manufacture of various specimens used in my work.

Of course, I could not have made it through my PhD without the help of all the Dr. Kumta lab members. I feel truly privileged to have worked with and learned from Boeun Lee, Dr. Abhijit Roy, Daeho Hong, Dr. Partha Saha, Dr. Moni Datta, Dr. Satish Singh, Jingyao Wu, and everyone else from the lab. Finally, I would like to voice my appreciation for the Department of Bioengineering and the numerous faculty and staff I've had the pleasure of interacting with here at the University of Pittsburgh for providing the amazing journey I have had the honor of experiencing – *Hail to Pitt!*

1.0 INTRODUCTION

1.1 CURRENT BIOMATERIALS FOR ORTHOPEDIC IMPLANTS

During the past hundred years, biomaterials and the medical devices that have been shaped from them have made monumental progress beyond the thousands of years of human history preceding the development of various biomaterials systems. Still, history is laden with examples of biomaterials that have laid the foundation for the tremendous progress the field has witnessed to reach the rich state it is in today. Even in Europe back in 200 A.D., wrought iron dental implants were used giving the appearance of viable osseointegration [1]. Sutures made from linen were used by early Egyptians, while catgut was used in the European Middle Ages [2]. The first successful contact lenses were used in the late 19^{th} century after being invented by Adolf Fick [3].

With the onset of World War II, as with many other technological advances, the knowledge base and development of biomaterials received a boost through the use of durable, inert materials by surgeons to replace injured or diseased tissue in the body. These materials often were made for other applications such as aerospace or automobiles, but were applied by enterprising physicians to address medical problems. The wartime theater where surgeons were forced to find solutions for an untold number of patients while often times facing very limited resources (along with a lack of governmental regulations and protections) pushed surgeons to

improvise and ultimately forge a new era of biomaterials which included polymers such as polyurethanes, Teflon, and nylon, and metals such as titanium and stainless steel.

From this foundation, the field of biomaterials has emerged, with the term defined as follows:

"A biomaterial is a nonviable material used in a medical device, intended to interact with biological systems" [4].

When interacting with biological systems, the biomaterial must be biocompatible, that is it must perform with an appropriate host response in a specific application [4]. Thus, when designing and testing biomaterials, a specific device or application must be considered where the criteria of appropriate host response can be defined and tailoring of the biomaterial can take place in order to satisfy those requirements. The work described in this thesis aims to develop a set of biomaterials which satisfy requirements for orthopedic applications.

Orthopedic implants serve the treatment of bone and joint problems which cause pain and distress for millions of people globally. Such ailments are also growing at a rapid pace, accounting for half of all chronic diseases in people over the age of 50 in the developed world, with the number of people affected by bone related diseases expected to double during the time span of 2007 to 2020 [5]. These conditions take a costly toll on the human body and therefore often require surgical intervention for the treatment of cases including bone fractures, joint deterioration, low back pain, osteoporosis, and scoliosis. An enormous $35.5 billion global market [6] is driven to treat these various conditions using orthopedic devices designed to perform desired biological functions by substituting, repairing, or providing additional stability for different tissues in the musculoskeletal system, i.e. bone, cartilage, ligaments, and tendons.

Load-bearing biomaterials, specifically to address orthopedic ailments, must meet a number of unique requirements that are dependent on the specific device and application. The ability to withstand cyclic load-bearing is a general necessity for orthopedic biomaterials, thus mechanical properties such as high strength, ductility, and hardness are often tested for these materials. Other appropriate properties of formability, biocompatibility, and corrosion resistance in the complex, harsh conditions in the human body must be considered as well, all which led to metals becoming the initial gold standard for a number of biomaterial applications. Ceramics and polymers are also used, which have facilitated growth in the field of biodegradable implants in orthopedic surgical procedures. A summary of biomaterials and their respective orthopedic applications is listed in Table 1.1. The field has matured to an extent that all of the materials can be further classified as either bio-inert or bio-active, depending on their interactions with surrounding tissue and the healing process, as well as biocompatible. A description into each class of materials is provided below.

Table 1.1. Summary of biomaterials for orthopedic applications. Used with permission of [5].

Materials	Orthopedic applications
Metals	
stainless steel (316, 316L)	fracture plates, screws, hip nails
Co–Cr–Mo alloys	prostheses stems, load-bearing components in total joint replacement
HA-coated Ti alloys	hip and knee prostheses, screws and pins for bone fixation
Ti6Al4V	prostheses stems
TNZT alloys (Ti–Nb–Zr–Ta)	under investigation
NiTi	internal fixator for long bone shafts, spinal correctors, vertebral spacer anchoring of prostheses and staples
Ni-free shape memory alloys	under investigation
Ceramics	
high alumina ceramics	orthopedic load-bearing applications
ISO alumina standard 6474	dental implants
PSZ	alveolar ridge augmentations, otolaryngological coatings for tissue ingrowth, maxillofacial reconstruction
Calcium phosphate cements	
R cement	cleft palate, apical barrier
H cement	periodontal pockets, filling periapical
Biopex	alveolar bone augmentation, bony defects
BoneSource	periodontal osseous defects, repair of large periodefects
Calcibon	periapical surgery
Cementek	
fracture grout	
KyphOs	
mimix	
Norian SRS	
rebone	
a-BSM/biobon/embark	
Bioglasses	
45S5 BG	
45S5.4F BG	maxillofacial reconstruction
45B15S5 BG	middle-ear reconstruction, dental implants
52S4.6 BG	percutaneous access devices, junction of spinal vertebrae
S45P7	
55S4.3 BG	
Glass–ceramics	
KGC ceravital	
KGS ceravital	
KGy213 ceravital	dental implants
	maxillofacial reconstruction

Table 1.1 (continued)

A/W GC	vertebral prosthesis devices
MB GC	iliac crest prostheses
Bioverit	
Polymers	
polymethacrylic acid (PMMA)	acrylic bone cements
	anchoring of hip prostheses
	vertebroplasties and kyphoplasties
polyethylene (PE)	liner of acetabular cups in hip arthroplasties, tibial insert and patellar components in total knee, arthroplasties
polydimethylsulphoxide (PDMS)	replacement for small joints in hand and foot
polypropylene (PP)	bone fixation devices
polysulphone (PS)	bone fixation devices, total joint arthroplasties
polycarbonate (PC)	bioabsorbable fixation devices and bone regeneration
	drug delivery
polyglycolic acid (PGA)	bioabsorbable fixation devices and bone regeneration, drug delivery
polylactic acid (PLA)	bioabsorbable fixation devices and bone regeneration, drug delivery
polycaprolactone (PCL)	bioabsorbable devices for bone regeneration
polydioxanone (PDS)	bioabsorbable fixation devices, bone regeneration

1.1.1 Inert metals

As discussed earlier, throughout most of the 20th century, pioneering surgeons designed implants using materials with established success in industrial applications. Metallic biomaterials were first selected based on their requirement to be as inert as possible in order to minimize corrosion and the release of ions and wear particles upon implantation into the human body. Stainless steel and cobalt-chromium-based alloys were first used for orthopedic applications. The high Cr concentration in stainless steel provided the important benefit of a strongly adherent, self-healing oxide layer of Cr_2O_3 which imparted corrosion resistance. Additions of alloying elements such as Ni and Mo further improved the strength and corrosion resistance. The most frequently used grade of stainless steel, 316L, contains a controlled low amount of carbon to further resist corrosion. Stainless steel is most commonly used in trauma devices such as fracture places and screws and has additional advantages of low cost, high availability, and easy processing.

Cobalt-chromium-based and titanium-based alloys began replacing stainless steel in applications such as orthopedic joint prostheses due to their better mechanical and corrosion properties, improving on the relatively poor wear resistance of austenitic stainless steel where wear debris particles were generated from the metal-on-metal friction. For these purposes, Co-Cr is especially appropriate because of its excellent corrosion and wear resistance and superior fatigue strength. To illustrate these properties, wrought CoNiCrMo alloy has been used in high load-bearing joints such as ankle implants.

Titanium (Ti) and its alloys carry the advantage of being lightweight, with a density of 4.5 g/cm^3 compared to 7.9 g/cm^3 for 316 stainless steel and 8.3 g/cm^3 for cast Co-Cr-Mo alloys

[7]. Ti implants also became recognized for their osseointegration property where bone formed a direct structural and functional connection with the surface of titanium [8]. This phenomenon was especially important for dental and orthopedic applications in order to reduce the risk for implant loosening and ultimately failure. Again, the formation of a protective oxide layer, in this case $TiO_{2,}$ on the implant surface provides the mechanism for corrosion resistance. Commercially pure Ti (CP Ti) and Ti6Al4V are the most commonly materials in this class for fabrication of various medical implants. CP Ti finds the most use in dental implants while Ti6Al4V is used predominantly in orthopedic applications. Whereas Ti alloys possess high strength-to-weight ratio, excellent mechanical properties, and corrosion resistance, they are difficult to process. In addition, concerns with vanadium (V) have been raised as a cytotoxic element, thus leading to development of V-free alloys as an example of alloys being designed with specific application as biomaterials being the final goal [9].

Titanium when alloyed together with nickel forms NiTi alloys which have a “shape memory effect” where the material may recover its shape upon heating after having been plastically deformed. Here, the transition from a low temperature microstructure to a high temperature microstructure provides this effect. The unique shape memory property can be harnessed to allow NiTi to be well suited for applications such as dental restoration wiring, osteotomy staples, and fracture repair [10]. Similar to potential risks of V in Ti6Al4V, concerns over the toxicity of Ni have also been raised, limiting its adoption in Europe and the U.S. A list of mechanical properties of the various metals used for orthopedic applications is shown in Table 1.2.

Table 1.2. Mechanical properties of metallic biomaterials compared to natural bone [5, 11-13].

Material	Elements (weight %)	Elastic modulus (GPa)	Yield strength (MPa)	Ultimate strength (MPa)
Natural bone		14.1-17.3	104–121	151
stainless steel 316L	balance Fe 17–20 Cr 12–14 Ni 2–3 Mo max 0.03 C	205–210	170–750	465–950
CoCrMo F75	balance Co 27–30 Cr 5–7 Mo max 2.5 Ni	220–230	275–1585	600–1785
MP35N	balance Co 33–37 Ni 19–21 Cr 9–10.5 Mo		414–1999	931–2068
Ti grade 4	balance Ti max 0.4 O	105	692	785
Ti4Al6V	balance Ti 5.5–6.5 Al 3.5–4.5 V	110	850–900	960–970
Ti6Al7Nb	balance Ti 6Al 7Nb	105	921	1024
Ti35Nb5Ta7Zr (TNZT)	balance Ti 35 Nb 5Ta 7Zr	55	530	590
NiTi	55.9–56.1 Ni balance Ti	20–70 (martensite) 70–110 (austenite)	50–300 (martensite) 100–800 (austenite)	755–960
TiNb	balance Ti 25–40 Nb	60–85	—	—
Mg sheet	99.98 Mg	45	90	160
Fe	99.8 Fe	200	150	210
Fe-30Mn sheet	balance Fe 30 Mn		239	518

In addition to risks involving alloying elements in metallic biomaterials, all of these systems discussed thus far possess elastic moduli significantly greater than natural bone. Because of this mismatch in modulus, when in contact with bone these metallic devices will take on the bulk of the load resulting in a lack of mechanical stimulus on the adjacent bone. This effect, called stress-shielding, may induce bone resorption, weakening and loosening of the implant, decreased implant stability, and eventually potential failure [14]. Despite efforts to minimize corrosion, metallic implants have been found to release ions and particles which have elicited toxic effects on surrounding tissues and organs, while also leading to implant loosening [15-18]. Other concerns include hypersensitivity [19], growth restriction in pediatric patients [20], implant migration, and imaging interferences [21]. Due to these complications as well as the risks of infection, an estimated 10% of patients undergo a secondary operation for the removal of inert metallic implants [22], exposing them to additional complications, pain, and lengthening the recovery process.

1.1.2 Inert and resorbable polymers

Initially, polymers used in orthopedic biomaterials included silicone rubber, polyethylene (PE), acrylic resins, polyurethanes, polypropylene (PP), and polymethylmethacrylate (PMMA). In the 1960s, pioneering surgeon, Sir John Charnley, borrowed from dentistry in adopting PMMA for anchoring prostheses to surrounding bone in cemented arthroplasties [23]. PMMA remains the most common choice for bone cements for orthopedic surgeons, which can be molded into shape and cured *in vivo* while having necessary mechanical properties. Ultrahigh-molecular-weight polyethylene (UHMWPE) was also used by Charnley as a liner for of acetabular cups in total hip arthroplasties where the properties of low coefficient of friction and low wear rate were desirable.

Silicone elastomers have been employed since the 1960s as well for arthroplasties of the finger, wrist, and elbow with reports of good stability and low rate of complications [24-26]. A recurring theme for these first-generation polymer biomaterials is the encapsulation of the implant by a layer of fibrous tissue which may prevent direct bone-to-biomaterial interfacing and compromise implant stability. Other complications manifested years after implantation, leading to severe lytic reactions and chronic inflammatory responses from micro-fragments [27].

The second generation of polymeric biomaterials saw a paradigm shift to polymers which exhibited a gradual chemical breakdown and resorption for the basic purpose of not necessitating a second surgical event for removal. This class included both synthetic and natural polymers such as polyglycolic acid (PGA), polylactic acid (PLA), poly(ε-caprolactone) (PCL), chitosan, and hyaluronic acid. Degradation of resorbable polymers is mainly through hydrolysis of the polymer chain backbone, with additional enzymatic degradation [28, 29]. Polymeric biodegradable sutures made from PGA and PLA were first approved in the 1960s [30]. Since then, many orthopedic applications have benefited from these materials including bone substitution, repair of bone fractures, cartilage, meniscus, and intervertebral discs, taking the form of screws, plates, suture anchors, tacks, rods, and pins [31]. Because they are less stiff and dense than traditional metallic implants, polymeric implants offer additional advantages in that they reduce the stress shielding effect, while circumventing artefacts in diagnostic imaging that are presented by metals.

Unfortunately, resorbable polymer devices are currently limited to certain applications. PLA and PGA are presently used for bone fixation, however are still inferior in mechanical properties to their metallic counterparts, thus are only used for less demanding indications [32]. Because of this lack in strength and rigidity, larger and bulkier designs must be used for polymer

osteosynthesis devices compared to metals. Since 1989, a number of complications have arisen from degradable orthopedic biomaterials including swelling, sterile sinus formation, synovial inflammation, bone resorption, foreign body reactions, and osteoarthritis [33-38]. Foreign body giant cell reactions (FBGCR) may arise due to micro-particles and hydrophobic characteristics of the PLA and PGA [39]. The highly-crystalline fragments and particles may take over 10 years to fully degrade and result in chronic inflammatory responses [40, 41] and tumorigenesis [42]. Other implications from the degradation process of PLA and PGA are a drop in pH and change in osmolarity which further cause toxic responses [43-46].

1.1.3 Ceramics

First generation ceramic biomaterials encompassed alumina, zirconia, and porous ceramics. Early applications of bioceramics were to replace traditional metallic femoral heads of hip prostheses with high-density and high-purity alumina [47]. Ceramics were later used to line acetabular cups due to their excellent wear rates, corrosion resistance, and biocompatibility, improving upon previous polyethylene cups [48]. Porous ceramics were introduced to allow for bone ingrowth to provide better stabilization for implants. Ceramics, mainly bioglasses (BGs), glass-ceramics, and calcium phosphates (CaP) have been utilized mainly as bone substitutes and bone void fillers since the 1970s [49]. Due to poor mechanical properties such as low tensile strength and fracture toughness, BGs are not appropriate for load-bearing applications [5]. The similarities between CaP based materials with natural bone, i.e. the mineralized component hydroxyapatite, $Ca_{10}(PO_4)_6(OH)_2$, along with β-tricalcuim phosphate (β-TCP), has led to wide adoption as a bioactive ceramic with osteoconductive properties [50]. Degradation of CaPs varies, with HA being relatively inert, while other CaPs such as TCP having higher solubility [51,

52]. However, CaP blocks are brittle thus prone to fatigue fractures, therefore restricting their use for complex weight bearing locations [53]. The generally slowly resorbing nature of bulk ceramics has also led to problems very similar to the inert metallic as well as polymeric systems, such as hindering the replacement by natural bone [54].

1.1.4 Resorbable metals

To avoid the negative consequences presented by inert metals, ceramics, and polymers, resorbable metals have been gaining considerable traction in the research world and just recently in clinical use for orthopedic applications. For resorbable metals to be successful as orthopedic applications, they must fulfill the following criteria [49, 55]:

1) The material must be biocompatible and its degradation by-products must be non-cytotoxic.
2) The material must be biodegradable and should degrade at the same rate as the healing rate of the surrounding tissue.
3) The mechanical properties of the material and device must be appropriate to regenerate bone tissue while bearing load at the site of implantation. The material must also maintain its structural integrity during the early stages of new bone formation.

In terms of satisfying these criteria, biodegradable metals use their corrosion properties as an advantage, flying in stark contrast to the convention of developing metals which are designed to be as inert as possible. This degradation must occur in a controlled manner so that while the implant is degrading and its strength diminishes, load is gradually transferred to the healing bone

tissue until it completely disappears once the tissue has fully healed. This profile of gradual degradation and reduction in mechanical support from a high initial point is shown in Figure 1.1.

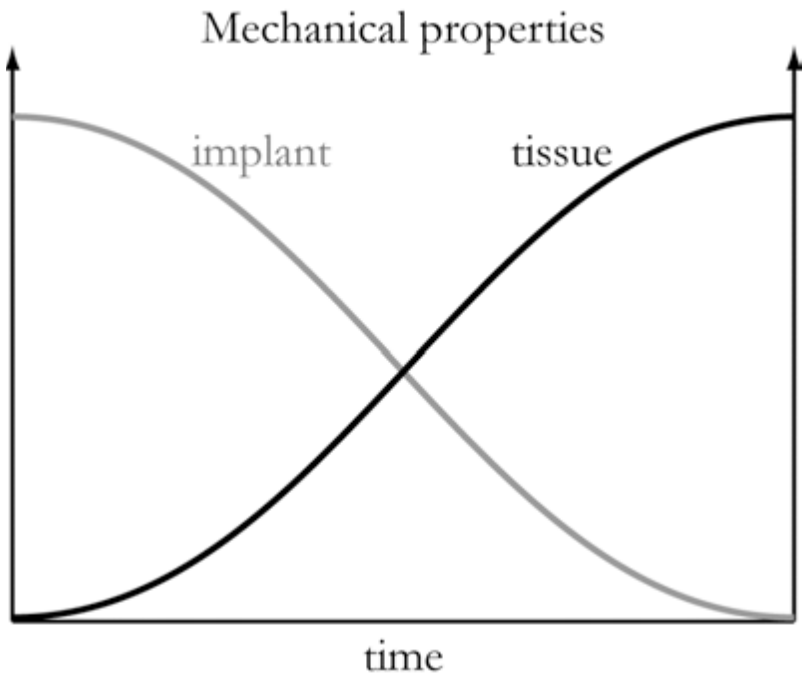

Figure 1.1. Schematic diagram of the ideal change in strength over time of degrading orthopedic implants. Used with permission of [56].

Compared to polymers, biodegradable metals also offer superior mechanical properties, crucial for orthopedic applications. Their degradation response however, unlike polymers, occurs via the electrochemical reaction upon introducing the metal to an aqueous environment wherein metals give away electrons and form positive ions during the anodic dissolution of the metal and a reduction (cathodic) reaction takes place, leading to the formation of a corrosion product:

$M \rightarrow M^{n+} + ne^-$ (anodic reaction) (1)

$2H_2O + 2e^- \rightarrow H_2 + 2OH^-$ (cathodic reaction) (2)

$2H_2O + O_2 + 4e^- \rightarrow 4OH^-$ (cathodic reaction) (3)

$$M^{n+} + nOH^- \rightarrow M(OH)_n \text{ (product formation)} \quad (4)$$

Where M is a metal with valence number of *n*.

Table 1.3 shows standard electrode potentials of the anodic reaction of most metals at room temperature, providing a comparison of their relative ease to lose electrons to form ions in an aqueous solution. The more negative the standard electrode potential, the more readily the metals lose electrons and form ions, and hence are more susceptible to corrosion.

Table 1.3. Selected standard electrode potentials of metal in aqueous solution at 25 °C relative to the standard hydrogen electrode [57].

Half-reaction	*E°(V)*
$Ni^{2+}(aq) + 2\ e^- \rightarrow Ni(s)$	-0.25
$Co^{2+}(aq) + 2\ e^- \rightarrow Co(s)$	-0.28
$Cd^{2+}(aq) + 2\ e^- \rightarrow Cd(s)$	-0.403
$Cr^{3+}(aq) + e^- \rightarrow Cr^{2+}(aq)$	-0.41
$Fe^{2+}(aq) + 2\ e^- \rightarrow Fe(s)$	-0.44
$Ga^{3+}(aq) + 3\ e^- \rightarrow Ga(s)$	-0.53
$Cr^{3+}(aq) + 3\ e^- \rightarrow Cr(s)$	-0.74
$Zn^{2+}(aq) + 2\ e^- \rightarrow Zn(s)$	-0.763
$Cr^{2+}(aq) + 2\ e^- \rightarrow Cr(s)$	-0.91
$Mn^{2+}(aq) + 2\ e^- \rightarrow Mn(s)$	-1.18
$V^{2+}(aq) + 2\ e^- \rightarrow V(s)$	-1.18
$Zr^{4+}(aq) + 4\ e^- \rightarrow Zr(s)$	-1.53
$Al^{3+}(aq) + 3\ e^- \rightarrow Al(s)$	-1.66
$Mg^{2+}(aq) + 2\ e^- \rightarrow Mg(s)$	-2.37
$Na^{+}(aq) + e^- \rightarrow Na(s)$	-2.714
$Ca^{2+}(aq) + 2\ e^- \rightarrow Ca(s)$	-2.87
$Sr^{2+}(aq) + 2\ e^- \rightarrow Sr(s)$	-2.89
$Ba^{2+}(aq) + 2\ e^- \rightarrow Ba(s)$	-2.9

$Rb^+(aq) + e^- \rightarrow Rb(s)$	-2.925
$K^+(aq) + e^- \rightarrow K(s)$	-2.925
$Li^+(aq) + e^- \rightarrow Li(s)$	-3.045

Among these metals, there are three predominant classes of resorbable metals which occupy the space: iron-based alloys, zinc-based alloys, and magnesium-based alloys.

Iron-based biodegradable metals of the three have the highest strength, up to 1550 MPa for Fe-10Mn-1Pd (wt. %) [58]. *In vivo* studies using both pure Fe [59, 60] and Fe-10Mn-1Pd and Fe-21Mn-0.7C-1Pd (wt. %) [61] demonstrated that Fe-based alloys corrode very slowly inside the body and therefore their suitability for bulk temporary implants has been called into question. Whereas the *in vitro* degradation rate of Fe-10Mn-1Pd and Fe-21Mn-0.7C-1Pd exceeded that of pure Fe, the *in vivo* degradation rate as measured after implantation in a rat transcortical femur model showed no significant difference between the groups [61].

Due to the observations of slow *in vivo* degradation, physical metallurgical principles and techniques have been attempted in accelerate corrosion. Alloying Fe with elements such as Mn, Pd, W, Sn, B, C, S, and Si [13, 58, 62-69] along with microstructural modification using electroformed iron have been pursued to accelerate corrosion [70, 71]. The more refined microstructure and microstructural defects of electroformed iron resulted in more areas for corrosion attack [71]. Mn has been widely explored as an alloying element for Fe which lowers the standard electrode potential of Fe and exhibits anti-ferromagnetic behavior over 29 wt. % to avoid limitations in imaging [72, 73]. With the low degradation rate of iron biomaterials, high biocompatibility has been observed with no significant inflammatory response or systemic toxicity [60, 74].

Zn based alloys have only recently emerged as a candidate biodegradable metal during the 21st century, with Vojtěch et al. reporting the use of Zn-1Mg and Zn-3Mg (wt. %) as a material for bone fixation [75]. The addition of 1 wt. % Mg improved mechanical properties while greater Mg content resulted in a detrimental effect on the mechanical properties, verified by Wang et al. who alloyed Zn with up to 45 wt. % Mg [76]. Zn based biomaterials have also exhibited degradation rates slower than Mg-based systems and faster than Fe-based systems, with an *in vivo* degradation rate in rat arteries of 0.22 mm/year [77]. However, Zn materials are limited by their relatively low strength and plasticity compared to other metals [75] though Zn based bulk metallic glass (BMG) $Ca_{32}Zn_{38}Mg_{12}Yb_{18}$ showed significantly higher strength and good cytocompatibility with MG63 osteoblast cells [78]. Nonetheless, both Fe and Zn based degradable biomaterials are in a nascent phase with only preliminary animal studies having taken place, and efficacy studies with prototype devices still very much needed before clinical trials and ultimate human use. On the other hand, Mg based alloys have made far more progress, which will be discussed in the following section.

1.2 MAGNESIUM: A PROMISING BIOMATERIAL

1.2.1 Historical precedence of magnesium implants

The potential benefits of magnesium as a degradable biomaterial has resulted in a rapid rise over recent years in research interest, as manifested by an exponential increase over the past ten years in publications, now dwarfing those of traditional metallic biomaterials such as stainless steel as seen in Figure 1.2.

Figure 1.2. Publications from 2002 to 2014 on magnesium and stainless steel biomaterials (retrieved from the Web of Science using “magnesium” and “stainless steel” as a search query within the category “biomaterials”).

Despite its seemingly meteoric rise, magnesium had actually been used as a biomaterial in numerous instances over the past 200 years. Elemental magnesium was discovered by the English chemist Sir Humphry Davy in 1808 who isolated magnesium by decomposing wet magnesium sulphate by electrolysis using a voltaic cell and a mercury cathode. Early uses for magnesium were mainly limited to the pyrotechnical industry including powder and wires [79]. These wires were used by physician Edward C. Huse in 1878 as ligatures to stop bleeding of the radial artery and in an varicocele operation [80]. Dr. Huse enthusiastically noted Mg’s ability to be absorbed in this first recorded use of it as a biomaterial, also promoting that it could be used “everywhere under all conceivable circumstances and contingencies”, “will never break”, “can never provoke irritation”, and finally “will always act, *tuto cito et jucunde*”, Latin for safely,

quickly, and pleasantly [80]. From this initial glowing endorsement, Austrian physician Erwin Payr went on to pioneer the field of biodegradable magnesium implants. While Payr found available Mg wire too brittle to be relied upon as a suture material [81], he discovered a variety of other medical applications for the degradable metal. From 1892-1905, Payr discussed the use of pure Mg in devices including tubular connectors for blood vessel, intestine, and nerve anastomosis, plates, arrows, sheets, and rods [81-87].

In 1932, Dr. Lambotte reported the implantation of a Mg plate fixed with six steel screws to stabilize a 17 year old adolescent's fractured tibia [88]. Substantial gas cavities, local swelling, and pain unfortunately resulted, due to a mismatch in the electrode potentials of Mg and steel leading to galvanic corrosion and the accelerated attack of the anode Mg in the galvanic couple. After realizing his mistake, Lambotte conducted trials with only Mg device in rabbits and dogs where he observed full resorption of Mg within seven to ten months without signs of any postoperative pain or distress [88]. These encouraging results led Lambotte and his colleague, Jean Verbrugge, to treat four children with supracondylar humerus fractures using Mg nails [89-91]. All healed naturally without suppuration or granulation tissue formation, with the only complication manifesting in the formation of gas pockets, which disappeared after a few weeks and did not cause a major concern. Verbrugge also implanted Mg plate and screws for a transdiaphyseal humerus fracture of an 8 year old child, for which the plate had nearly completely degraded with formation of gas pockets by three weeks' time although the bone fracture had undergone healing.

None of the patients Verbrugge implanted with Mg osteosynthesis devices showed signs of infection or adverse reactions to the degrading Mg, which did not appear to cause any difference in the periosteal reaction compared to traditional inert implants [90, 91]. Following

the footsteps of Dr. Verbrugge, Dr. Earl McBride procured magnesium alloys from his contemporary in Antwerp and investigated Mg screws, nails, pegs, plates, circular bands, and medullary pegs for fracture fixation [92, 93]. McBride found that magnesium adequately maintained fixation of bone fragments for union to occur while having a shorter, more favorable absorption time than other contemporary degradable materials such as beef bone or cow horn. He also importantly observed the stimulation of periosteal proliferation and encouraged its use in limited orthopedic applications. In 1948, Troitskii and Tsitrin documented success in using Mg-Cd plates and screws for osteosynthesis [94]. Again, full degradation and stimulation of callus bone formation were observed, resulting in reported faster recovery for patients.

Despite this non-trivial body of work of implantable Mg devices, especially in orthopedic applications, Mg has only recently been approved by regulatory bodies for clinical use. The MAGNEZIX® compression screw for small bone fractures obtained CE marking of Medical Devices for medical applications within Europe in 2013 after a randomized, controlled clinical study was conducted using the Mg alloy screw in hallux valgus surgery [95]. More recently, in 2015, U&I Corporation received the South Korean Ministry of Food And Drug Safety approval for the K-MET, another positive approval showing applicability of Mg for osteosynthesis. This recent momentum for the adoption of Mg implants shows the impetus to optimize Mg alloys to fulfill the potential that so many throughout history believed in. Thorough testing of Mg alloy properties must take place to achieve optimal characteristics to meet the needs of orthopedic biomaterials and remedy the problems other orthopedic biomaterials currently face.

1.2.2 Materials properties of magnesium

Critical to orthopedic implants is their mechanical and other material properties which dictate their success in sustaining the stresses of load-bearing applications. Mg has a number of advantageous properties many of which are comparable to natural bone [96]. It is very lightweight, with a density of 1.74 g/cm^3, similar to that of cortical bone (1.8 – 2.1 g/cm^3), and much less than stainless steel, titanium alloys, and Co-Cr alloys. The elastic modulus of magnesium alloys of 41-45 GPa [96] is much closer to natural bone compared to other commonly used metallic implants as seen in Table 1.2, thus reducing the risk of stress shielding. The high specific toughness, rigidity, good machinability, and ability of Mg to be cast also make it an attractive material for medical applications.

However, compared to other permanent metals, absolute strength and plastic deformability is limited due to Mg's hexagonal close-packed structure (HCP), which shows a principle slip plane on the (0001) basal plane along the $< 11\bar{2}0 >$ direction [97]. With only two independent slip systems, the Taylor criterion which states that five independent slip systems must be available for homogenous plastic flow to occur [98] is not met. Furthermore, the critical resolved shear stress (CRSS) for the basal slip system of Mg is much lower than for non-basal slip systems of other metals [99]. In order to activate the additional slip systems (pyramidal and prismatic), the temperature must be increased to increase ductility (as shown in Figure 1.4b) and to conduct forming techniques. Another consequence of the low number of slip systems is preferential orientation of the crystals during forming, generating a textured material [100]. Thus, during extrusion for example, the basal planes are mainly oriented in the same direction as extrusion, resulting in anisotropic properties.

To overcome these issues and to effectively improve mechanical properties, grain refinement methods are applied. An increase in ductility occurs upon reduction in grain size at a transition grain size with a “low-to-high-ductility” transition as temperature increases at different grain sizes [101].

This phenomenon occurs due to cross slip from basal to non-basal planes having the ability to occur, with dislocations on basal and non-basal planes present within fine grains as opposed to at the grain boundaries as well as grain boundary sliding [102, 103]. With micron size grains, compatibility stresses are restricted near grain boundaries and have much higher influence on fine-grained materials.

Grain refinement also has a profound effect on material strength through the Hall-Petch relation where grain boundaries act as pinning points to impede the propagation of dislocations [104, 105]. This effect of grain boundary strengthening limits dislocation accumulation, where dislocations generate repulsive stress fields to allow dislocation sources in adjacent grains to be activated and continue deformation. By diminishing dislocation accumulation, higher force must be applied to activate dislocations thereby elevating the metal’s strength. The Hall-Petch relation is expressed by the following equation:

$$\sigma_{\mathrm{Y}} = \sigma_0 + k_{\mathrm{Y}} \cdot d^{-\frac{1}{2}}$$

Where σ_{Y} is the yield stress, σ_0 is the friction stress when dislocations move on the slip plane, d is the average grain size, and k_{Y} is the stress concentration factor.

Microstructure modification by work hardening, where the density of grain boundaries is increased by forming techniques, such as extrusion and rolling is also used to increase the strength. Dislocations interact through their repulsive and attractive stress fields leading to entanglement, again impeding dislocation propagation as seen in grain boundary strengthening.

Introducing alloying elements can also improve strength via solid solution strengthening, whereby dislocation movement is impeded by lattice distortions caused by solute elements where the stress fields around the solutes interfere with those of the dislocations. When alloying elements are above their solubility limit in Mg, secondary phase precipitates are formed, which may lead to precipitation hardening whereby these particles create stress fields which again interact with dislocations, increasing yield strength. A related method to improve strength is age hardening, a heat treatment used to increase yield strength. First, the alloy is heated to dissolve solute atoms after which rapid cooling across the solvus line of the solute element is performed to generate a supersaturated solid solution that remains stable due to the quenching, preventing diffusion. Aging is then conducted where the supersaturated solid is heated below the solvus temperature to produce finely dispersed precipitates which restrict dislocation movement during deformation leading to strength enhancement.

1.2.3 Corrosion mechanism of magnesium

Magnesium and its alloys are known to have a low corrosion resistance in aqueous environments relative to other metals as described in section 1.1.4. This property, while severely detrimental to structural applications, is central to its use as a biodegradable implant material. The corrosion behavior of Mg in water at room temperature is plotted in the Pourbaix diagram shown in Figure 1.3, showing that Mg undergoes corrosion at physiological pH of 7.4.

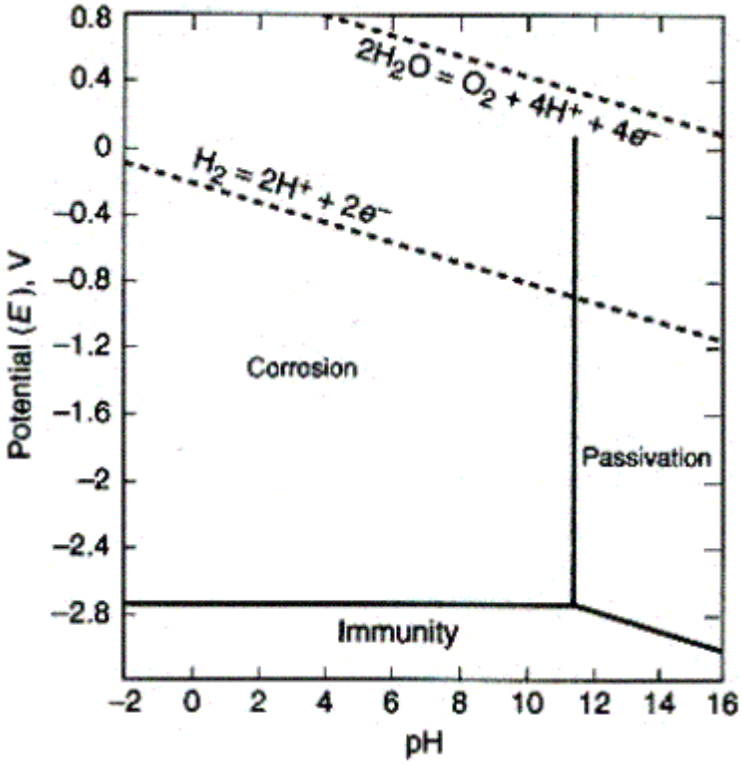

Figure 1.3. Pourbaix diagram of Mg in water at 25 °C showing corrosion, passivation, and immunity. The region of water stability lies between the dashed lines [106].

Mg corrodes in aqueous solutions according to the following overall reaction leading to the formation of hydrogen gas and magnesium hydroxide:

$$Mg_{(s)} + 2H_2O_{(aq)} \leftrightarrow H_{2\,(gas)} + Mg(OH)_{2\,(s)}$$

This overall reaction includes the following partial reactions:

$$Mg_{(s)} \leftrightarrow Mg^{2+}_{(aq)} + 2e^- \text{ (anodic reaction)}$$

$$2H_2O_{(aq)} + 2e^- \leftrightarrow H_{2\,(gas)} + 2OH^-_{(aq)} \text{ (cathodic reaction)}$$

$$Mg^{2+}_{(aq)} + 2OH^-_{(aq)} \leftrightarrow Mg(OH)_{2\,(s)} \text{ (product formation)}$$

The magnesium hydroxide forms a quasi-passive layer accumulating on the surface of the degrading magnesium, providing some protection. Chloride ions in solution at concentrations above 30 mmol/l may result in the breakdown of the magnesium hydroxide layer, converting it to

soluble magnesium chloride salt [107]. Inside the human body, fluids contain chloride concentration of about 150 mmol/l which may cause severe pitting corrosion on Mg alloys and the release of hydrogen gas that may accumulate into harmful pockets. Undissolved $Mg(OH)_2$ on the surface of degrading Mg may also provide favorable sites for hydroxyapatite (HA) nucleation by consuming calcium and phosphate ions from the surrounding fluid [108]. This overall corrosion behavior of polycrystalline Mg alloys in biological solutions is illustrated in Figure 1.4.

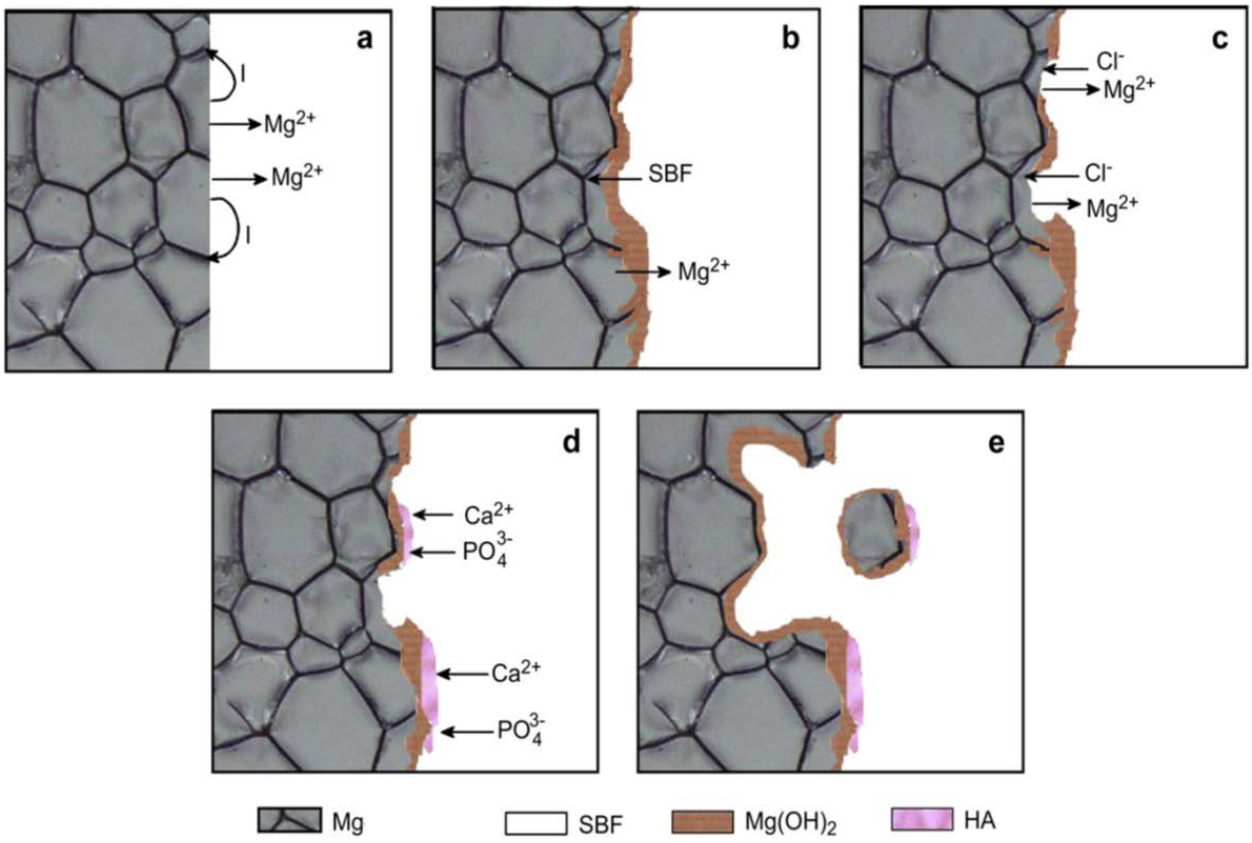

Figure 1.4. Schematic depiction of the corroding surface of polycrystalline Mg alloys: (a) galvanic corrosion between Mg and grain boundaries; (b) partially protective film of $Mg(OH)_2$ covering the surface; (c) attack by chloride ions to transform $Mg(OH)_2$ into $Mg(Cl)_2$; (d) hydroxyapatite formation by consuming local Ca^{2+} and PO_4^{3-}; (e) particles removed from the bulk Mg entering the surrounding solution. Adapted from source, used with permission of [109].

Magnesium corrosion may take place by galvanic corrosion observed when severe corrosion occurs in the Mg matrix close to cathodic areas. Whereas external galvanic corrosion could occur if Mg were in contact with a nobler metal, as was the case in Lambotte's Mg plate coupled with steel screws, this issue is easily mitigated by eliminating contact with other metals and the risk of internal galvanic corrosion is far more prevalent. Internal galvanic corrosion occurs with the presence of cathodic secondary phases or impurities in the Mg matrix. Most alloying elements are therefore selected with a lower potential difference with regards to their secondary phases and Mg, resulting in less severe corrosion. Characteristic impurities, such as Fe, Cu, Ni, and Be, have low solubility in Mg and low hydrogen overvoltage resulting in significant micro-galvanic corrosion. To limit the amount of impurities, careful selection of high purity alloying elements and master alloys along with controlled processing methods is hence very much required. Beyond 35-50 ppm for Fe, 100-300 ppm for Cu, 20-50 ppm for Ni, and 4 ppm for Be, substantial galvanic corrosion will occur which will threaten the mechanical integrity of a Mg implant device [110].

As discussed in the previous section, processing techniques and alloying elements play critical roles in affecting a Mg alloy's grain size and grain size distribution. Grain boundary distribution not only affects mechanical properties but also may serve as a site for corrosive attack due to their high internal energy and segregation of alloying elements to represent cathodic regions to the anodic Mg matrix in the interior of the grains. Although logic would dictate that coarse grains would be preferable to reduce areas where corrosion may set in, contradictory reports of minimized segregations in small grained Mg alloys leading to a more uniform corrosion behavior with smaller pits [111] have been discussed. Other explanations of

fine-grained alloys possessing greater corrosion resistance include grain boundaries acting as corrosion barriers with their reduced propensity for corrosion due to similar work potentials as the matrix phase [112, 113]. The method of imparting grain refinement has influence as well, with dislocations reported to locally decrease the equilibrium potential and increasing dissolution [114] while extrusion compared to equal channel angular pressing (ECAP) resulting in superior corrosion resistance due to larger grain area and interphase boundaries [115].

Application of these specific corrosion behaviors must also be considered for orthopedic implants where the Mg device is placed under conditions of excessive stress. During these scenarios, stress corrosion cracking (SCC) can occur even at stresses below yield strength, leading to premature brittle cracks initiated at locations with sharp contours such as corrosion pits and pre-existing macro/microscopic flaws. With propagation of these cracks the risk of sudden implant failure becomes a major concern for orthopedic implants, especially for devices such as screws, plates, and pointed pins which possess sharp contours. Mg alloys have been reported to be susceptible to SCC in chloride solutions [116], and even in “inert” metals such as stainless steels and titanium [117, 118]. SCC fracture propagation may either occur at the anodic matrix close to the grain boundary through electrochemical corrosion (intergranular failure) or by preferential attack near cathodic precipitates and stress concentrations or at areas of $Mg(OH)_2$ protective film rupture due to stress (transgranular failure) [119]. Hydrogen embrittlement (HE) may also cause SCC, where hydrogen diffusion to tip of cracks and magnesium hydride formation may lead to brittle facture or decohesion [120].

Magnesium alloys must overcome the risk of rapid corrosion which may lead to implant instability and premature failure within 3-4 months, when it must remain mechanically stable as an orthopedic biomaterial to allow for fracture healing, callus formation, new bone formation,

and finally functional bone tissue healing to sufficiently restore strength at the injury site [121]. Thus addressing the rapid corrosion of Mg is vital due to its direct impact on the mechanical properties and biocompatibility.

1.2.4 Toxicity and biocompatibility of magnesium alloys

Magnesium is the fourth most abundant cation in the human body, with about 21-28 g stored in the body and approximately half of it stored in bone tissue [122]. The normal blood serum level and extracellular fluid level of Mg is around 0.7-1.06 mmol/L [110], and people normally consume about 300 mg of Mg per day. Mg is also essential to human metabolism, is a cofactor for many enzymes, and stabilizes the structures of DNA and RNA. The $Mg(OH)_2$ corrosion product is also non-toxic and along with excess Mg, are harmlessly excreted through urine [122], to such an extent that the most common cause of hypermagnesemia being renal failure [123]. Hydrogen gas released from the degrading Mg diffuses over time through the skin or can be removed by aspiration but nonetheless do not appear to cause any harm in earlier clinical studies [88, 89].

Especially advantageous for orthopedic applications, Mg has been shown to have a positive influence on bone growth [124-126], with *in vivo* studies showing higher bone mass found around Mg bone implants compared to controls of polymeric (Figure 1.5) or titanium implants [125, 127].

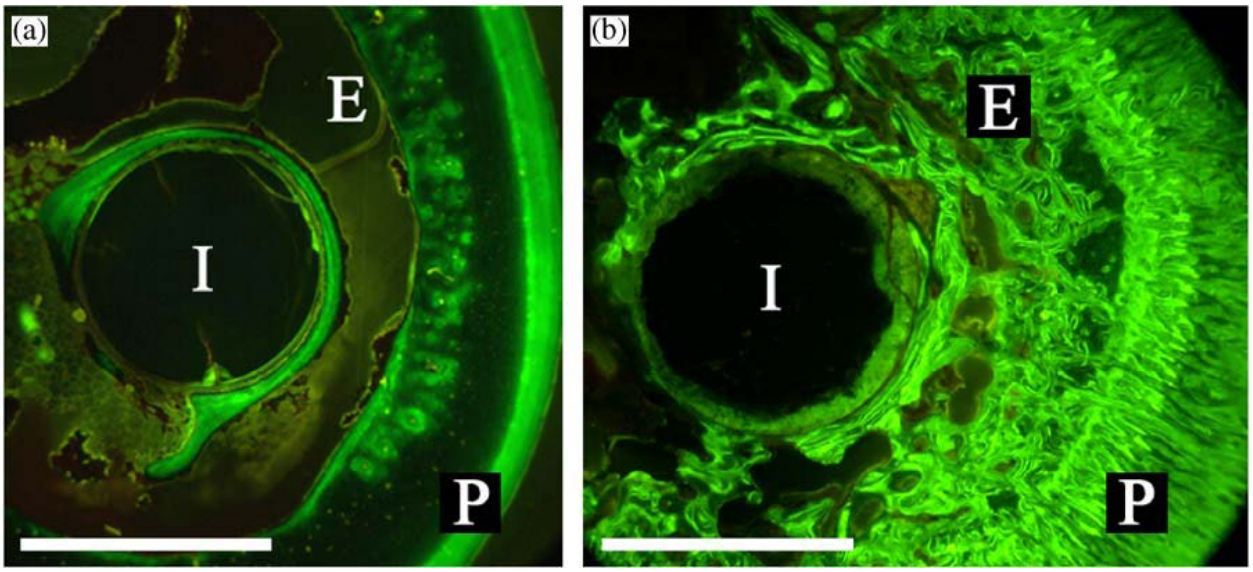

Figure 1.5. Flouroscopic images of cross-sections of a degradable polymer (a) and a magnesium rod (b) performed 10 mm below the trochanter major in a guinea pig femur. Both specimens were harvested 18 weeks postoperatively. In vivo staining of newly formed bone by calcein green. Scale bar=1.5mm; I=implant residual; P=periosteal bone formation; E=endosteal bone formation. Used with permission of [125].

The rich historical precedence of Mg in orthopedic implants discussed earlier along with the advantages in terms of the physical, chemical and biological properties make Mg alloys suitable for load bearing orthopedic and craniofacial applications. This work seeks to optimize a system of alloys featuring elements such as Y, Ca, Zn, and Zr primarily for orthopedic applications while also evaluating their effect on bone healing as well as *in vitro* and *in vivo* cell and tissue response. Accordingly, four specific aims have been crafted as discussed henceforth.

1.3 SPECIFIC AIMS

Biodegradable materials for orthopedic and craniofacial applications have been primarily developed to avoid complications associated with the use of inert metals. However, the onset or mere risk of complications often necessitates the removal of metallic implants following healing. Biodegradable magnesium (Mg) has demonstrated promise due to its similar mechanical properties to natural bone. Magnesium degrades to form a soluble corrosion product harmlessly excreted through urine as discussed above, though rapid corrosion of Mg alloys that may reduce implant stability and result in potentially toxic hydrogen gas formation which may accumulate around the implant. The goal of this proposed work is thus to develop alloys which address the rapid corrosion of Mg by synthesizing novel polycrystalline Mg alloys containing yttrium (Y), zirconium (Zr), and other alloying elements selected due to their known biocompatibility as well as their ability to induce corrosion resistance to the Mg alloys and improve the mechanical properties, particularly mechanical strengths, and utilizing appropriate post-processing techniques (i.e. heat treatment and extrusion). These techniques are primarily employed to improve the corrosion resistance and mechanical properties compared to pure Mg to arrive at the optimized alloy systems for orthopedic and craniofacial implant applications.

The specific hypothesis to be tested by the specific aims below is that Mg-Y-Ca-Zr based alloys with controlled amounts of Y, addition of Zn to introduce a long-period stacking order secondary phase, and significant grain refinement using extrusion will:

1) Improve the mechanical properties of the alloys,
2) Increase corrosion resistance,
3) Maintain cell function without eliciting toxicity, and
4) Demonstrate *in vivo* biocompatibility and allow for bone fracture healing.

Alloying elements were accordingly added as indicated because magnesium corrosion and mechanical properties are strongly affected by the presence of these elements even when present in the metal as a solid solution [128]. Further, Y and Ca contribute to grain boundary strengthening of magnesium alloys [129] and improve the corrosion resistance [109, 130, 131]. Zr also serves as an effective grain refining agent [132], imparting grain boundary strengthening [110] and corrosion resistance [133]. Post-processing techniques were used to modify the microstructure as this is well known to improve the mechanical response and corrosion behavior. *In vitro* corrosion and mechanical properties and the effect of the alloys and their degradation products on pre-osteoblast cells and human mesenchymal stem cells were used to evaluate the effect of alloying elements and post-processing. The most viable alloy candidate for orthopedic and craniofacial applications was then selected based on high strength, corrosion resistance, and low cytotoxicity, combined with promotion of osteoblast differentiation. This alloy was further investigated for *in vivo* biocompatibility and effect on bone healing by implantation into the intramedullary cavity of a rat femur after a full osteotomy.

A summary of the specific aims of this thesis to achieve the work described above are given below:

1.3.1 Specific Aim 1: Synthesize novel Mg-Y-Ca-Zr based alloys and perform materials characterization to assess the changes in microstructure after addition of alloying elements and post-processing treatments

In this specific aim, novel Mg-Y-Ca-Zr-based alloys were synthesized using melting and casting followed by heat treatment and extrusion. Rationale for the addition of the various alloying elements is described, as well the effects of the addition of these elements on modifying the

microstructure by virtue of materials characterization, including microstructure analysis and phase characterization are analyzed and discussed.

1.3.2 Specific Aim 2: Characterize the effect of yttrium and zinc addition and post processing on the corrosion behavior and mechanical properties of Mg-Y-Ca-Zr alloys

Grain refinement and the presence of secondary phases and elements diffused into the Mg alloys are known to significantly affect the corrosion behavior and mechanical properties of the alloy. Having analyzed the microstructure and phases present in the alloys in Specific Aim 1, the goal is to evaluate the corrosion behavior of the alloys using potentiodynamic polarization measurements and mass loss in a simulated physiological solution. A second goal is to perform mechanical testing in tension and compression. The results of these tests were then used to understand microstructural/composition-functional relationship of the Mg-Y-Ca-Zr system of alloys.

1.3.3 Specific Aim 3: Evaluate the effect of Yttrium and Zinc addition, post processing, and alloying element salts, on cell viability and proliferation of pre-osteoblast and human mesenchymal stem cells. Further evaluate expression of osteoblast differentiation markers and biocompatibility in murine subcutaneous tissue

This portion of the study included the evaluation of the effect of the degrading magnesium alloys on pre-osteoblast and human mesenchymal stem cell viability, proliferation, and differentiation. This study is conducted by exposing cells to media containing degradation products, adding alloying element salts to cell culture media, seeding cells directly on the surface of the alloys.

The effect of Mg alloys on osteogenic differentiation has also been investigated by measuring alkaline phosphatase activity, and gene expression of osteogenic markers of cells seeded on the alloys. Finally, a preliminary *in vivo* study was conducted by implanting the alloys into mouse subcutaneous tissue and analyzing the local host response. Corrosion behavior was also evaluated by mass loss *in vivo*.

1.3.4 Specific Aim 4: Assess the in vivo corrosion, bone formation, and host response of Mg-Y-Zn-Ca-Zr alloy in a rat femur osteotomy model

With the ultimate goal of fabricating orthopedic medical devices from the alloys described in this thesis, observing the biological responses following implantation of the material in a bone healing animal model is a required step to determine the safety of the Mg alloy. Following the preliminary study of as-cast Mg-Y-Ca-Zr alloys that were implanted into the subcutaneous tissue of nude mice, this aim focuses on assessing the behavior of the degradation behavior of the Mg-Y-Zn-Ca-Zr alloy in a bone model *in vivo*. Two devices were accordingly manufactured and implanted into Sprague-Dawley rats as described below:

1) Sharpened pins were implanted into the medullary cavity of rat femurs accessed by a full osteotomy
2) Wires were wrapped around the midsection of rat femurs

Degradation behavior was determined quantitatively using micro-CT analysis of the implants and degradation product volume before and after implantation. The host response of the degrading alloy and its corrosion products on bone formation around the implant was then investigated following histological analysis of the implant region. Finally, local and systemic toxicity was also evaluated using histology and elemental analysis of the kidney and liver,

combined with a detailed blood profile to assess the pathological response after 2, 8, and 14 weeks of implantation.

2.0 SPECIFIC AIM 1: SYNTHESIZE NOVEL MG-Y-CA-ZR BASED ALLOYS AND PERFORM MATERIALS CHARACTERIZATION TO ASSESS THE CHANGES IN MICROSTRUCTURE AFTER ADDITION OF ALLOYING ELEMENTS AND POST-PROCESSING TREATMENTS

2.1 INTRODUCTION

Accelerated corrosion of Mg alloys as indicated in section 1.2 has limited its adoption as a biomaterial due to the accumulation of hydrogen gas pockets around the implant as well as insufficient mechanical performance and implant stability throughout the degradation and tissue healing process [134, 135]. In order to improve corrosion resistance and increase mechanical properties of pure Mg, the addition of suitable alloying elements Y, Ca, Zr, and Zn were introduced as outlined as a rationale for this aim.

In alloying Mg, there are only limited choices biocompatible alloying elements that can be selected among Al, Mn, Zn, Ca, Li, Zr, Y, and rare earth (RE) elements that are used to generate Mg implant materials, generally influencing the mechanical and material properties of Mg alloys [110]. Mg-Y-Ca-Zr alloys have been successfully fabricated as ignition-proof alloys due to their ability to improve oxidation resistance [136, 137]. The introduction of Y can be justified by its ability to contribute to grain boundary strengthening of the magnesium alloys [129] and also improving the corrosion resistance at wt. % higher than 3% when alloyed with

Mg [130, 138]. Ca, as well as Y help to form a stable and chemically less reactive hydroxide layer to impart greater corrosion resistance as shown by density functional theory calculations [139]. Ca is also a major component of mineralized natural bone [140] and is the most abundant mineral in the human body that is known to improve the corrosion resistance and mechanical properties of Mg alloys when added up to 1 wt. % [109, 131]. Zr on the other hand, serves as an effective grain refining agent [132, 141-143] by imparting grain boundary strengthening [110] and corrosion resistance [133]. Zr also is a powerful iron removal agent, typically helping to reduce the content of iron to under 20 ppm in Zr-containing magnesium alloys, thus decreasing the risk for corrosion from iron impurities [100]. Further, adding Ca to Zr-containing alloys promotes solute undercooling, in turn, facilitating more suitable sizes for Zr nuclei to become effective nucleation sites to further reduce grain size [132, 136, 141-143]. Zn is also one of the most abundant essential elements in the human body, and can improve the corrosion resistance and mechanical properties of Mg alloys as well as the castability in larger amounts (greater than 2 wt. %). The combination of Y and Zn in Mg alloys also has been shown to result in the formation of a specific structure, long period stacking order (LPSO) structure, which consists of periodic stacks of close-packed planes along the atomic c-axis, resulting in high strength and ductility.

The original Mg-Y-Ca-Zr alloy system used in the preliminary studies was modified and enhanced to create the second group of alloys discussed in this thesis. First, the Zr content was increased from 0.4 wt. % to 1 wt. % due to indications from ICP-OES measurements that the amount of Zr going into the solution was much lower than expected in the Mg-alloy cast ingots. This reduction in the amount of Zr is commonly observed due to settling of Zr particles into a Zr rich layer at the bottom of the crucible, with only Zr remaining in the molten Mg solution having

an effect in the grain refining process [79]. Hence Zr is added above the final desired weight percentage to compensate for losses during melting, contamination, pickup of iron, precipitation, etc. to maintain adequate levels without further processing [79]. In order to further determine the effects of Y addition on the Mg alloy, an alloy without Y (Mg-1Zr-0.6Ca) was also synthesized to compare to the alloys containing Y.

Alloys containing Y and Zr have achieved clinical success having been used in drug eluting stents in patients with de-novo coronary lesions [144] and screws in hallux valgus surgery (which received CE marking of Medical Devices for medical applications within Europe) [95]. Both devices demonstrated good safety profiles and performance as alternative to resorbable polymeric and metallic materials.

In addition to selection of alloying elements, processing methods also highly influence the microstructure and hence properties of the alloys. In this study, T4 solution treatment at 525 °C for 8 hours was attempted to reduce the volume fraction of secondary phases by providing the driving force for favoring diffusion into the α-Mg matrix. Hot extrusion was also conducted as a means to impart grain refinement, which is in actuality a more effective approach for producing homogenous and fine grains than other methods for producing wrought Mg such as rolling and forging [145].

The nominal compositions of the various alloys and processing methods used for generating the alloys considered in this specific aim are listed in Table 2.1. The alloy abbreviations used to designate the alloys discussed in this thesis shown in Table 2.1 were determined using ASTM B 275 standard on codification, where no more than two letters representing alloying elements of the two greatest amounts are to be listed [146]. W represents yttrium, X represents calcium, K represents Zr, and Z represents Zn. The codification WX11 and

WX41 alloys in the as-cast and T4 heat treated form was changed to WK11 and WK41 after addition of 1.0 wt. % Zr made it the second greatest alloying element present, thus replacing the X for calcium with a K for zirconium.

Table 2.1. Nominal composition of Mg alloys (wt.%) investigated in this work.

Alloy	Chemical compositions (wt.%)					
	Y	Ca	Zr	Zn	Mg	Condition tested
WX11	1.0	0.6	0.4	0.0	Balance	As-cast and T4
WX41	4.0	0.6	0.4	0.0	Balance	As-cast and T4
KX11	0.0	0.6	1.0	0.0	Balance	Extruded
WK11	1.0	0.6	1.0	0.0	Balance	Extruded
WK41	4.0	0.6	1.0	0.0	Balance	Extruded
WZ42	4.0	0.6	1.0	2.0	Balance	Extruded

2.2 MATERIALS AND METHODS

2.2.1 Metallurgical processing of Mg-Y-Ca-Zr based alloys

Elemental ingots of Mg (US Magnesium Inc., Salt Lake City, UT, 99.97%), Ca (Alfa-Aesar, Ward Hill, MA, 99.5%), and Zn (Alfa-Aesar, 99.99%) were weighed according to the nominal composition and melted in a mild steel crucible using an electrical resistance furnace (Wenesco Inc., Chicago, IL) with the addition of a Mg-30Y wt. % master alloy melted from pure Mg and Y (Alfa-Aesar, 99.9%) prepared inside a graphite crucible melted using an induction furnace (MTI Corporation, Richmond, CA) purged with ultrahigh-purity (UHP) Ar and vacuumed to avoid oxidation of the pure elements. The master alloys and pure elements were cleaned thoroughly to remove residue and oxide scale and melted in a mild steel crucible using the Wenesco electrical

resistance furnace under the protection of Ar + 0.5% SF_6 cover gas. The melting and pouring temperature was 750 °C, and once the temperature was reached, equivalent amount of zirconium was added using Zirmax (Mg-33.3% Zr) master alloy (Magnesium Elektron Ltd., Manchester, UK). After the Mg-Zr master alloy was added, the melt was stirred for 10 s at an interval of 1 min and 5 min to dissolve and disperse the zirconium particles uniformly into the melt. The melt was held for an additional 30 min and poured into a cylindrical mild steel mold preheated to 500 °C with dimensions of 44.5 mm diameter × 82.5 mm length. The holding and stirring times to release Zr particles from the Zirmax master alloy was essential to achieve higher solubility of Zr in the melt and optimal grain refinement [147]. To compare as-cast samples to solution treated samples, a heat treatment of (T4) at 525 °C for 6 h was performed on the alloy ingots inside a tubular furnace covered under continuous UHP Ar flow and quenched in room temperature water.

Extruded alloys were prepared from as-cast alloys by first applying solution treatment at 400 °C for 20 hours and quenching in room temperature water to increase the alloys' ductility and homogenize the secondary phases while not causing grain growth, as shown in Appendix B. After reducing the ingot diameter to 37.8 mm using a lathe, the alloys were hot extruded with an extrusion ratio of 10 and 30 at the following temperatures:

Table 2.2. Temperatures used to preheat ingots for 30 minutes and during extrusion of solution treated alloys. ER = extrusion ratio.

Alloy	Extrusion temperature	
	ER 10	ER 30
KX11	350 °C	
WK11	350 °C	
WK41	400 °C	
WZ42	425 °C	450 °C

The alloys were compared to as-cast Mg (US Magnesium Inc.), as-drawn 99.9% pure Mg (Goodfellow Corp., Coraopolis, PA), and as-drawn AZ31 (Goodfellow Corp.) in reported tests. Inductively coupled plasma optical emission spectroscopy (ICP-OES, iCAP duo 6500 Thermo Fisher, Waltham, MA), was used to experimentally confirm the alloy compositions and presence of impurities by dissolving alloy samples in 15% nitric acid, diluting in water 5x, and measuring concentration of the alloying elements and impurity elements of the solution containing the dissolved alloys.

2.2.2 Phase characterization of Mg-Y-Ca-Zr based alloys

In order to determine the phase formation, X-ray diffraction (XRD) was conducted using Philips X'Pert PRO diffractometer employing CuK_{α} (λ=1.54056 Å) radiation with a Si-detector (X'celerator). The X-ray generator operated at 45 kV and 40 mA at a 2θ range of 10-80°. Peak identification was determined using the X'Pert High Score Plus software.

2.2.3 Microstructure analysis of Mg-Y-Ca-Zr based alloys

Samples of the Mg alloys were mounted in epoxy, mechanically polished (Tegramin-20, Struers, Ballerup, Denmark) with 1200 grit SiC paper down to 0.05 µm with an alumina slurry, and chemically etched in a solution of 5 mL acetic acid, 6 g picric acid, 10 mL water, and 100 mL ethanol. The microstructure was observed using optical microscopy (Axiovert 40 MAT, Carl Zeiss, Jena, Germany) and scanning electron microscopy (SEM, JEOL JSM-6610, JEOL Ltd.,

Tokyo, Japan) with energy dispersive X-ray (EDX, EDAX Genesis, Mahwah, NJ) to conduct elemental analysis. Average grain size was measured according to ASTM E112 [148] following the Abrams three-circle procedure with ~70 grains considered for each calculation.

2.3 RESULTS

2.3.1 Materials properties of as-cast and solution treated Mg-Y-0.6Ca-0.4Zr based alloys

Inductively coupled plasma optical emission spectroscopy (ICP-OES) measurements (Table 2.3) showed some reduction in alloying elements from their as-weighed nominal compositions likely due to the re-melting process. A reduction in Zr was primarily due to settling of large zirconium particles and clusters in the liquid melt [149] and was counteracted by adding more Zr when melting, increasing from the content in the preliminary study of 0.4 wt. % (for WX11 and WX41 alloys) to 1.0 wt. % (for KX11, WK11, WK41, and WZ42 alloys). Low impurity levels were observed, as necessary to avoid substantial galvanic corrosion.

Table 2.3. Chemical composition and impurities of Mg-based alloys (wt.%) as measured by ICP-OES.

Alloy	Chemical compositions (wt.%)										
	Y	Ca	Zr	Zn	Al	Cu	Fe	Mn	Ni	Si	Mg
WX11	0.66 ± 0.03	0.52 ± .01	0.13 ± 0.004	--	--	0.016	0.003	0.008	0.008	0.006	Balance
WX41	3.18 ± 0.10	0.63 ± 0.41	0.074 ± 0.013	--	--	0.015	0.009	0.005	0.003	0.007	Balance
KX11	0.0033	0.52 ± 0.002	0.62 ± 0.005	<0.0001	0.0003	0.0005	0.0008	0.003	<0.0001	<0.0001	Balance
WK11	0.98 ± 0.003	0.51 ± 0.002	0.63 ± 0.003	<0.0001	0.0003	0.008	0.001	0.003	<0.0001	<0.0001	Balance
WK41	3.37 ± 0.18	0.40 ± 0.065	0.51 ± 0.009	<0.0001	<0.0001	0.004	0.003	0.003	<0.0001	<0.0001	Balance
WZ42	3.98 ± 0.033	0.54 ± 0.005	0.61 ± 0.008	2.00 ± 0.015	<0.0001	0.002	0.001	0.003	<0.0001	<0.0001	Balance

The presence of different phases in the Mg alloys was characterized by X-ray diffraction (XRD) as shown in Figure 2.1. The XRD patterns show that all the alloys were composed of hcp α-Mg, without detecting the presence of any unalloyed Y, Ca, Zr, or intermetallic phases. However, there was a distinct preferential orientation of the Mg (101) plane in all of the synthesized as-cast and solution treated alloys compared to as-cast pure Mg which shows the typical Mg (002) plane to be the most intense peak likely due to the presence of Zr acting as nucleating sites for grain refinement leading to possible preferential orientation.

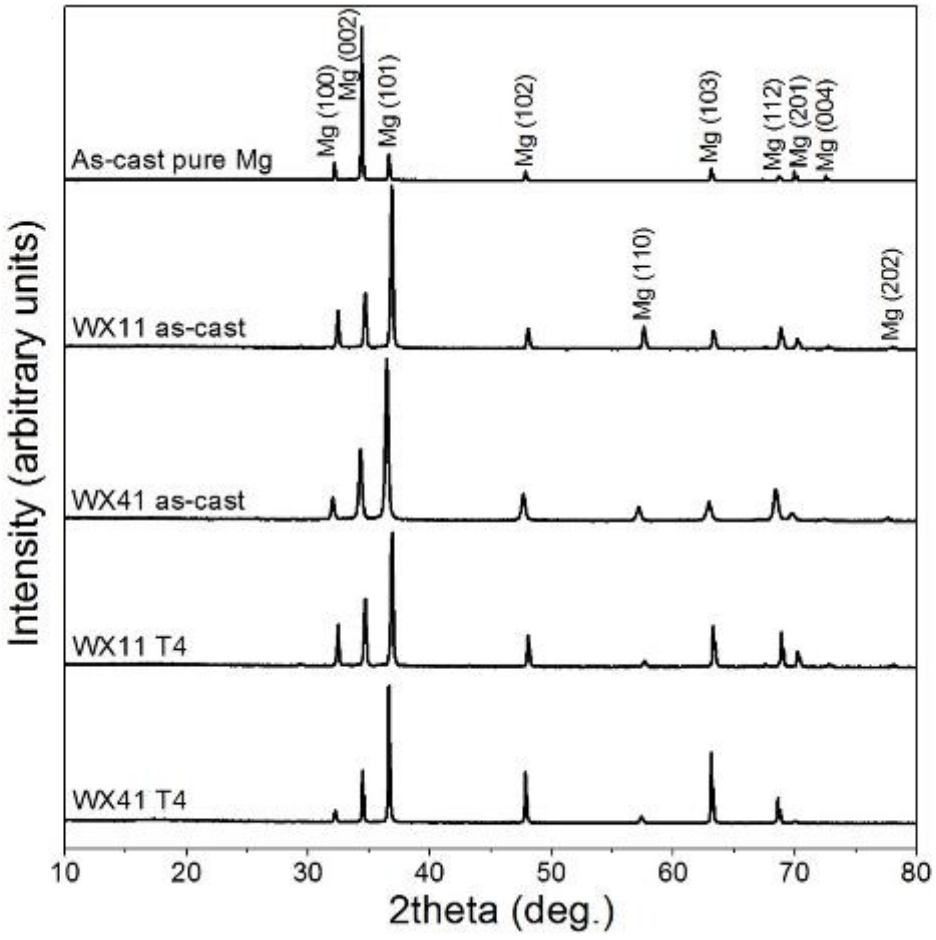

Figure 2.1. XRD patterns of as-cast pure Mg, WX11, and WX41.

Figure 2.2 shows optical microscopy images of the microstructure of as-cast and solution treated WX11 and WX41 alloys containing grains of α-Mg with secondary phases (dark regions) located at the grain boundaries and precipitates within the matrix.

The average grain size of the alloys was: WX11 as-cast - 79 µm, WX11 T4 treated – 98 µm, WX41 as-cast – 98 µm, and WX41 T4 – 200 µm, dominated by the presence of uniform equiaxed α-Mg grains throughout the microstructure. As expected, the solution treatment led to an increase in the grain size. However, addition of alloying elements greatly reduced the grain size compared to high-purity Mg as shown in Figure 2.2e, which noticeably lacked the presence of dark secondary phases. As-drawn AZ31, having undergone grain refinement due to the commercial drawing process, exhibited much finer grain size (Figure 2.2f) compared to the Mg-Y-Ca-Zr alloys WX11 and WX41 and pure Mg which received no bulk forming processes.

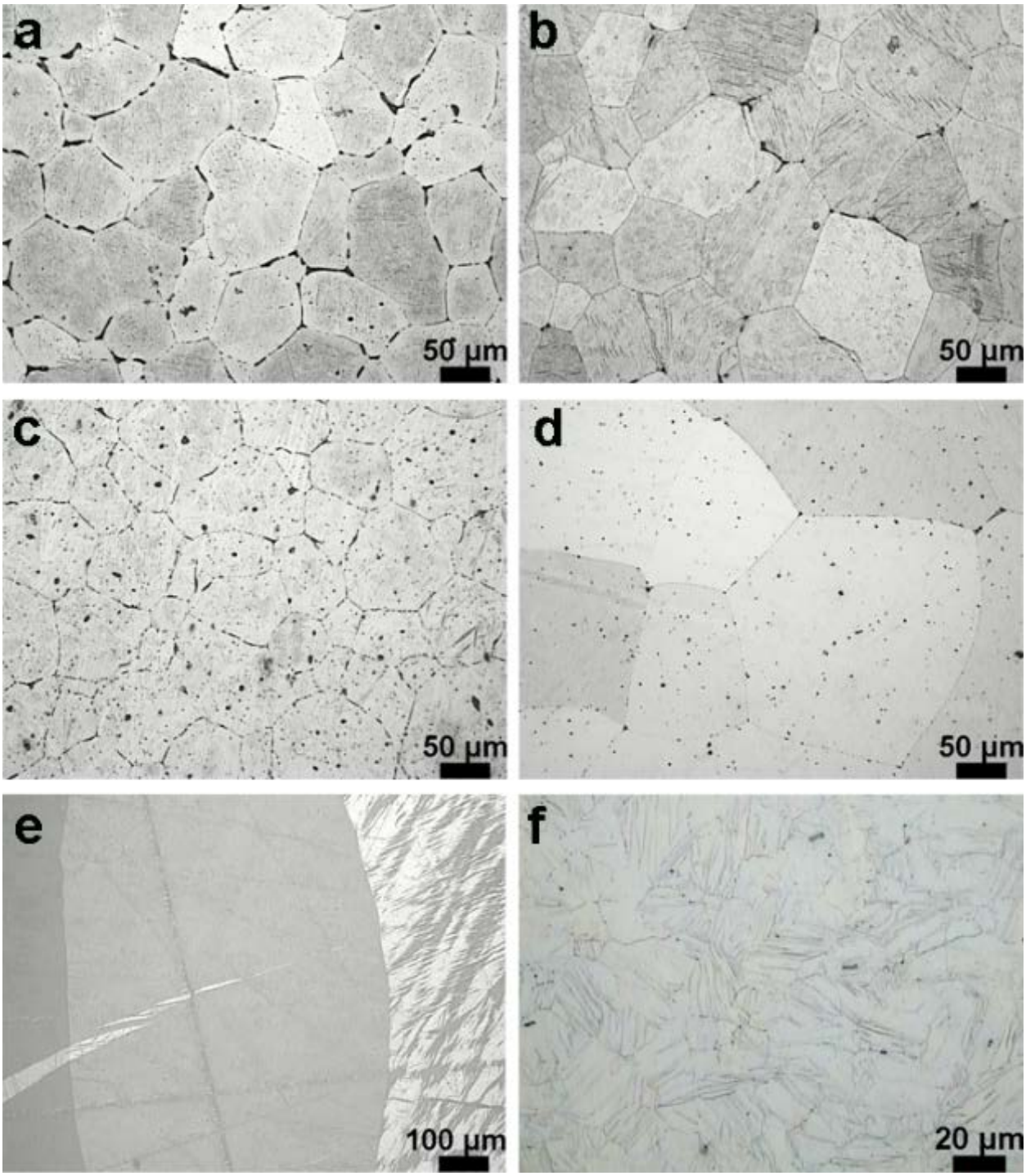

Figure 2.2. Optical micrographs of Mg-Y-Ca-Zr alloys after polishing and etching: a) WX11 as-cast; b) WX11 T4 heat treated; c) WX41 as-cast; d) WX41 T4 heat treated; e) pure Mg as-cast; f) AZ31 as-drawn.

SEM and EDX (Figure 2.3) confirmed the optical microscopy images in that the WX11 and WX41 as-cast alloys contained grain boundaries and precipitates of higher amounts of Y and Ca (Figure 2.3a and c), indicating the presence of secondary phases of composition, with lower amounts of Y, Ca, and Zr at the grain boundaries but consisting mostly of Y in precipitates, due to precipitate segregation during solidification, a common phenomenon with casting. T4 solution treatment successfully dissolved these secondary phases into the bulk α-Mg, leading to partial homogenization of the as-cast alloy. The Y-rich intermetallic particles were observed to contain about 75% wt. % Y to form αY, which were still present after T4 solution treatment (Figure 2.3b and d). A higher volume fraction of second phase particles was observed in the WX41 alloys due to its higher Y content compared to WX11. The increase in grain size after T4 solution treatment was likely due to energy driving coalescence of smaller grains along the triple point grain boundary regions and formation of supersaturated α-Mg solid solution after the precipitates dissolved into the matrix as to be expected following heat treatment.

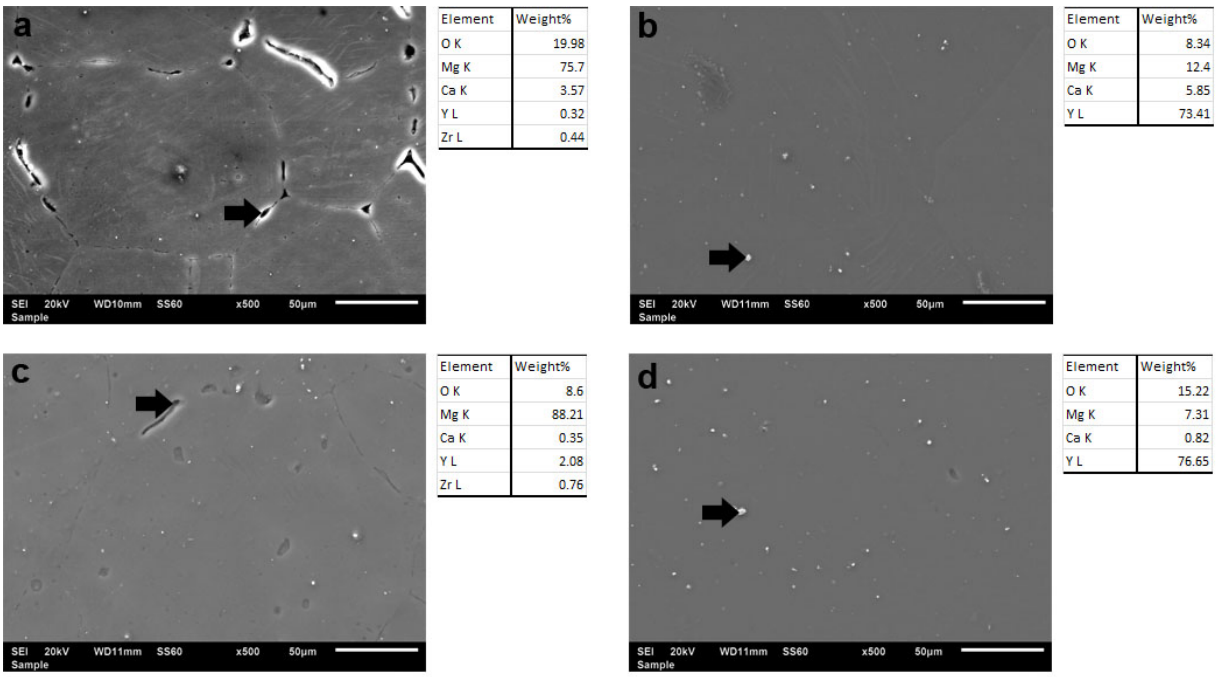

Figure 2.3. SEM images of Mg-Y-Ca-Zr alloys after polishing and etching: a) WX11 as-cast; b) WX11 T4 heat treated; c) WX41 as-cast; d) WX41 T4 heat treated with corresponding EDX of grain boundaries and precipitates as noted by arrows. Scale bar = 50 µm.

2.3.2 Changes in phase and microstructure with extrusion and addition of Y and Zn to Mg-Y-1Zr-0.6Ca based alloys

The modified Mg-Y-Ca-Zr alloy system contained 1.0 wt. % Zr. An alloy without Y (Mg-1Zr-0.6Ca) and an alloy containing Zn (Mg-4Y-2Zn-1Zr-0.6Ca) were also synthesized to compare the materials and *in vitro* characteristics to the Mg-Y-Zr-Ca alloys. These alloys were extruded at an extrusion ratio of 10 (initial cross sectional area divided by final cross sectional area) at temperatures shown in Table 2.2 and subject to further analysis.

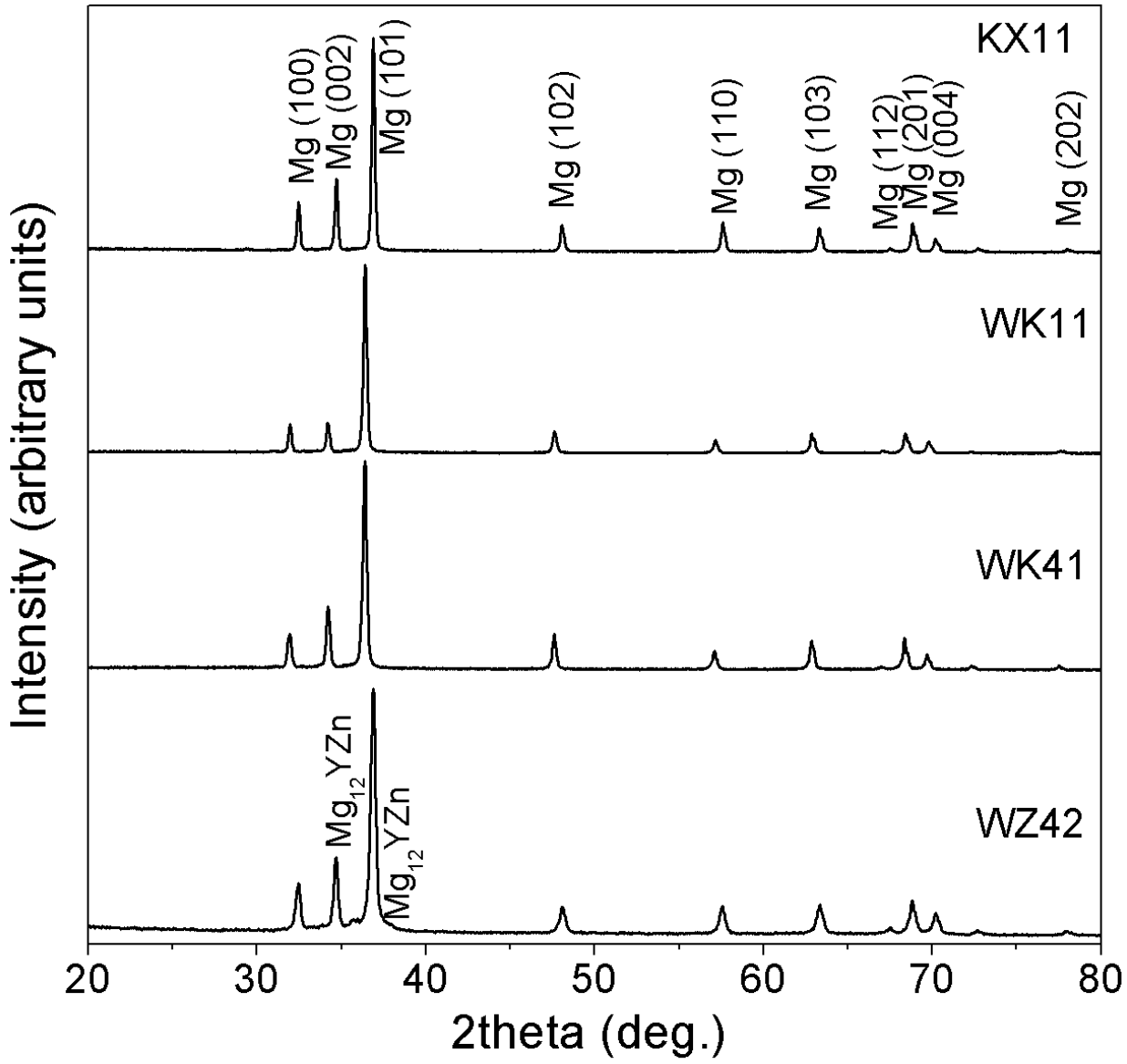

Figure 2.4. XRD patterns of extruded KX11, WK11, WK41, and WZ42.

XRD (Figure 2.4) of the Mg alloys shows that after extrusion for KX11, WK11, and WK41, the alloys consisted still mainly of single phase Mg. The addition of Y led to a shift in all the peak positions, particularly of the (101) oriented peak at ~37^{o} 2 □ value due t expansion caused by the introduction of Y into the Mg hcp lattice. Similar preferred orientation is seen here unaffected by the increase in Zr content. As expected, the WZ42 alloy, which contained Y and Zn, contained the presence of the LPSO phase $Mg_{12}YZn$.

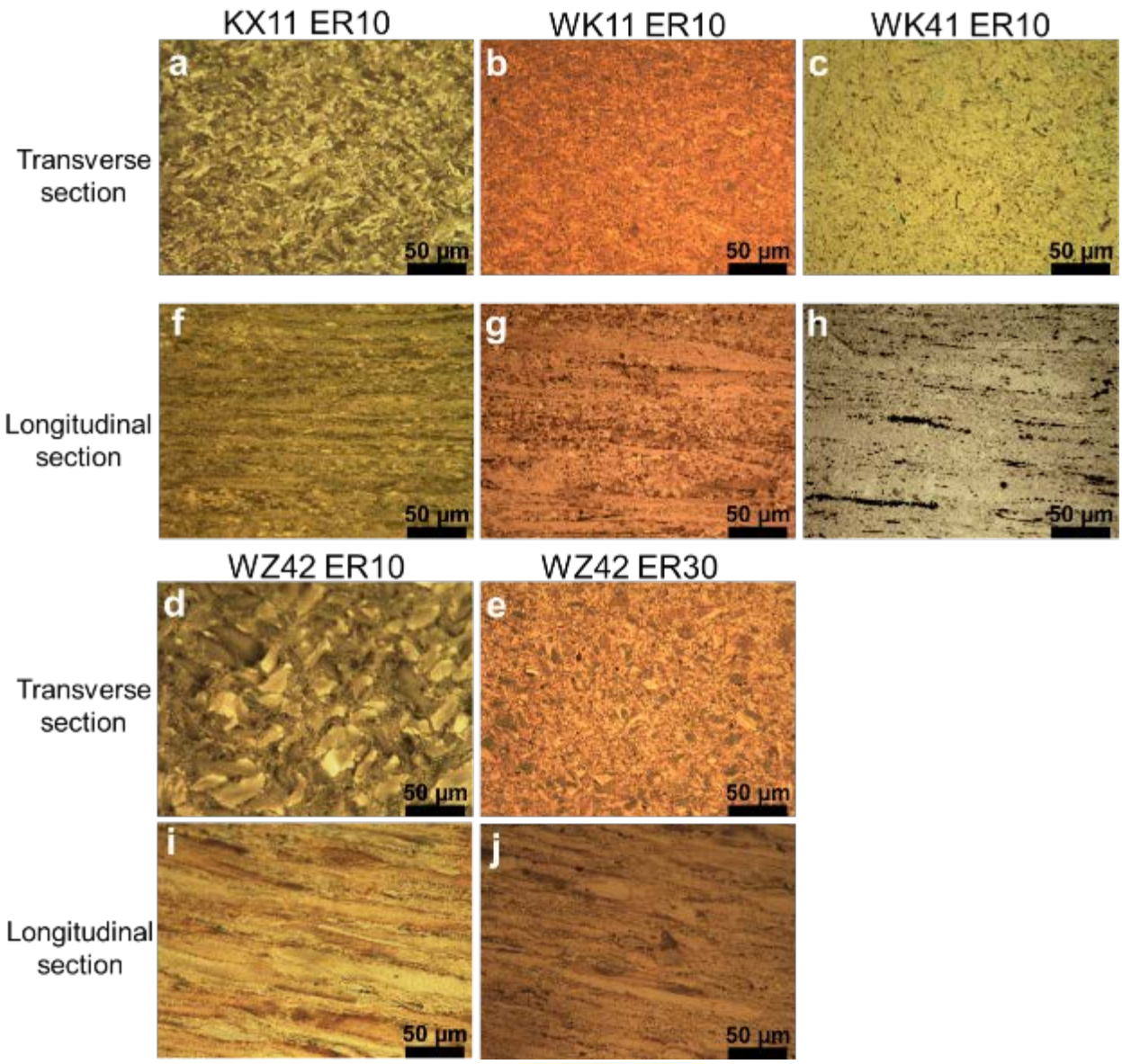

Figure 2.5. Optical micrographs showing the microstructure of Mg alloys extruded with extrusion ratio 10: a,f) KX11, b,g) WK11, c,h) WK41, d,i) WZ42 and extrusion ratio 30 – e,j) WZ42, with sections take in the transverse direction (top, a-e) and longitudinal direction (bottom, f-j).

After extrusion, the Mg alloys underwent significant grain refinement as shown in the optical microscopy images of microstructure (Figure 2.5). Compared to the as-cast and T4 treated alloy microstructure shown in Figure 2.2, after hot extrusion, the grain size was reduced to well under 50 μm. The WZ42 alloy contained grains both small and large, and when extruded at an extrusion ratio of 30 compared to 10, resulted in more of the large grains of ~20 – 40 μm being disrupted into more refined grains of < 15 μm in the transverse direction.

Further inspection of the microstructure was conducted using SEM and EDX (Figure 2.6). Bright regions in the back-scattered SEM images revealed intermetallic phases consisting of Mg, Ca, Y, and Zr, as well as impurity elements of Al, however since an extremely low concentration of Al was measured in the alloys using ICP-OES in Table 2.3, the Al detected by EDX may have come from the alumina slurry used during polishing. Non-equilibrium phases containing alloying elements were present in KX11 and WK11 (Figure 2.6a, b). WK41 (Figure 2.6c) contained the phase Mg_2Y as it contained more Y, ~4 wt. %, compared to WK11 which only contains ~1 wt. % Y. In the WZ42 alloy, a unique LPSO phase consisting of Mg, Zn, and Y roughly corresponding to $Mg_{12}YZn$ with Mg atomic percent 12 times that of Y was confirmed by SEM and EDX analysis shown in Figure 2.6d. The amount of bright regions of precipitates in the alloys increased with the higher amount of alloying elements added to the Mg solution, in the order of KX11 < WK11 < WK41 < WZ42. The size of the secondary phases, with the exception of the LPSO phase in the WZ42 alloy, appeared to be generally smaller, < 2 μm, and more dispersed in the extruded alloys seen in Figure 2.6 compared to the as-cast and T4 heat treated alloys of Figure 2.3.

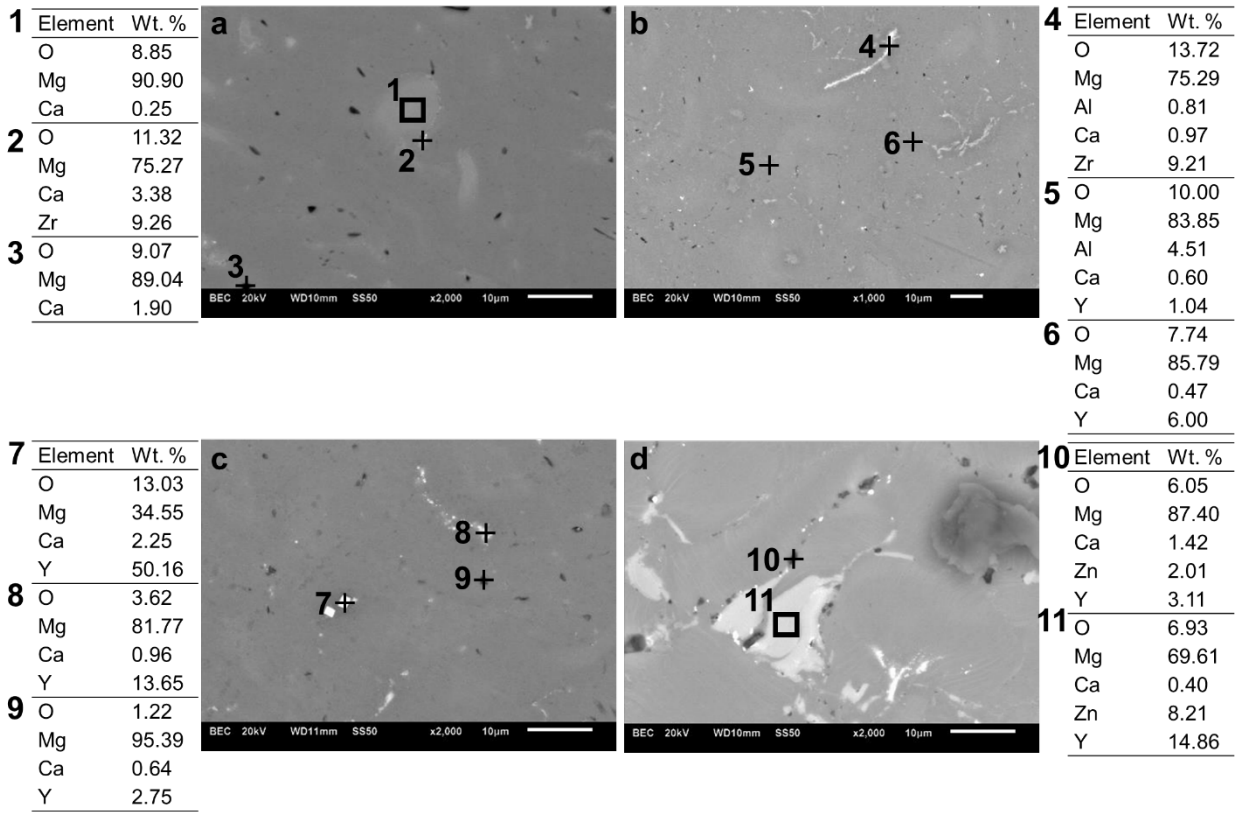

Figure 2.6. SEM images and EDX analysis at indicated locations of Mg alloys after polishing and etching: a) KX11; b) WK11; c) WK41; d) WZ42 after extrusion with extrusion ratio of 10. Sections were taken in the transverse plane to the direction of extrusion. Scale bar = 10 µm.

2.4 DISCUSSION

Alloying elements strongly affect the microstructure and mechanical properties of magnesium alloys. Higher Y content has been reported to result in grain coarsening [150], which was observed to a small degree in Figure 2.2 when comparing the WX11 to the WX41 alloys. The measured Zr content as seen in Table 2.3 was also reduced in the WX41 alloy, which may also

have contributed to the higher grain size compared to WX11. Y-rich intermetallic particles with Y wt. % of ~75% were observed in the Mg-Y-Zr-Ca alloys as has been observed in Mg-Y binary alloys [130], though implementation of T4 solution treatment resulted in dissolution of second phase precipitates from the grain boundaries as well as grain coarsening.

The alloy compositions studied were modified and expanded after the initial studies using as-cast Mg-Y based alloys. First, to further explore the effect of Y and Zn addition, a composition without Y was added to compare with the Y-containing alloys, and added Zn to explore the effects of the LPSO phase of $Mg_{12}YZn$ intermetallic. Due to a loss of Zr during melting which was observed in the as-cast alloys, which saw a diminished Zr content from the nominal concentration of 0.40% reduced to 0.13% and 0.074% wt. % as measured by ICP-OES for the WX11 and WX41 alloys, respectively, the amount of Zr added to the initial melts was increased. The loss of Zr occurred because once saturation with Zr has been achieved, Zr is continually lost from the Mg solution as it reacts with iron from the crucible and other contaminants, also forming hydrides with hydrogen [79]. Thus, it is crucial to add an excess of active Zr to the melt to compensate for the losses occurring [79]. Another change that was implemented was reducing the temperature for heat treatment. As seen in Figure 2.2b and 2.2d, significant grain growth was observed after conducting heat treatment on the WX11 and WX11 alloys at 525 °C, reducing the positive effects of grain refinement imparted by the Zr addition. The temperature of solution treatment was reduced to 400 °C while extending the time from 8 hours to 20 hours, still resulting in diffusion of precipitates while lowering corrosion rate and avoiding significant grain growth, as shown in Appendix B, Figure B.1 and Figure B.2.

This modified alloy system was then hot extruded which drastically changed the alloy microstructure. While the X-ray diffraction patterns still showed single-phase Mg for all alloys

except WZ42 which contained LPSO $Mg_{12}YZn$, the grain size dramatically decreased after extrusion. Extrusion process for Mg alloys is a thermo-mechanical process influenced by the working temperature and extrusion ratio. Increasing extrusion temperature increases grain size due to dynamic recrystallization where nucleation and growth of new grains occur during deformation [151]. However, the effect of extrusion ratio on grain size has been met with contradictory results, with some studies reporting a grain size decrease with increasing extrusion ratio [145, 152] whereas other reported the contrary [153]. Here, a breakdown was observed of the large LPSO phase grains, while overall the grains seen in the longitudinal section did not appear to drastically change. The occurrence of this fiber-shaped LPSO phase elongated along the direction of extrusion has been observed in other Mg-Zn-Y containing alloys [153], where a higher extrusion ratio generated more heat during extrusion bringing about dynamic recrystallization, seen to a greater effect in the extrusion ratio 30 WZ42 alloy. This effect may be due to conflicting influences of a higher temperature used for extrusion performed at extrusion ratio 30 (450 °C) as opposed to 425 °C when the alloy was extruded at an extrusion ratio of 10, acting to recrystallize and grow grains while the higher deformation served to reduce grain size. All the alloys appeared to undergo partial dynamic recrystallization with a combination of fine equiaxed grains and long elongated grains retained from the original solution treated microstructure.

3.0 SPECIFIC AIM 2: CHARACTERIZE THE EFFECTS OF YTTRIUM AND ZINC ADDITION AND POST PROCESSING ON CORROSION BEHAVIOR AND MECHANICAL PROPERTIES OF MAGNESIUM-YTTRIUM-CALCIUM-ZIRCONIUM ALLOYS

3.1 INTRODUCTION

Critical in gaining a deep understanding of the Mg-Y-Ca-Zr based alloys of this work was to draw relationships between the microstructure and composition with the functional properties of corrosion behavior and mechanical properties. For orthopedic biomaterials, both characteristics are essential in determining the efficacy of a device.

The first major challenge in developing a biodegradable osteosyntheses response was to achieve mechanical properties that are in the likely same range as those characteristic of permanent metallic implants [32]. Biodegradable materials must maintain stability in complex *in vivo* environments, bearing a combination of various mechanical loads including tension, compression, and fluid shear stress [154]. Whereas degradable polymers have improved since the 1980s due to progress in knowledge and production methods, their mechanical properties still do not approach those of permanent metals. Thus, devices made from biodegradable polymers are designed to compensate the lack of strength and rigidity though the use of larger, bulkier designs. Naturally, the location of the skeletal injury often dictates the mechanical requirements of the

implant and material [155]. As the material degrades, the decrease in strength should be steady, predictable, and repeatable, resulting in gradual transfer of load to the surrounding and newly formed bone whose growth may be encouraged by the increased loading [156].

The property of degradation of implanted materials for orthopedic devices is also of interest to eliminate the need for device removal in a second surgery while providing room for growth of native tissue. No implant residues should remain, while the degradation products can be metabolized by the human body at an appropriate rate to maintain load for the given application.

As discussed earlier, alloying elements were added to contribute to improvement of the mechanical properties and corrosion resistance. A common effect of their incorporation was to impart solid solution strengthening, precipitation strengthening, and grain boundary strengthening. The post-processing technique of heat treatment to diffuse the secondary phases limits the extent of microgalvanic corrosion wherein the anodic α-Mg matrix has a lower corrosion potential than any secondary phases, corroding preferentially as a galvanic couple [157]. Grain refinement achieved through hot extrusion also was expected to improve the mechanical strength by grain boundary strengthening. This aim sought to assess the effects of these alloy additions, namely progressively increasing Y content and Zn incorporation, as well as the effect of heat treatment and extrusion on the mechanical properties and degradation of the resultant Mg alloy systems in order to determine optimal processing conditions for achieving high strength and corrosion resistant alloys.

3.2 MATERIALS AND METHODS

3.2.1 Corrosion testing of Mg-Y-Ca-Zr based alloys

The potentiodynamic polarization technique was used to test corrosion of the WX11 and WX41 as-cast and T4 treated alloys. Samples were connected to a copper wire using silver epoxy and mounted in epoxy resin. The mounted samples of dimensions 10 mm × 10 mm × 1 mm were mechanically polished, sonicated in isopropyl alcohol, and dried in air. The potentiodynamic corrosion study was carried out with an electrochemical workstation (CH-604A, CH Instruments, Inc., Austin, TX) at a scanning rate of 1 mV/s and potential window of 500 mV above and below the open circuit potential. A three electrode cell was employed with platinum as the counter electrode, Ag/AgCl as the reference electrode, and the sample as the working electrode. The test was performed in Dulbecco's Modified Eagle Medium (DMEM, with 4.5 g/l glucose, L-glutamine, and sodium pyruvate, Cellgro, Manassas, VA) supplemented with 10% fetal bovine serum (FBS), 100 U/ml penicillin, and 100 μg/ml streptomycin at pH 7.2 ± 0.2 and held at 37.4 °C. Before each measurement, the sample was immersed in the corrosion media to provide stability. The cathodic and anodic portions of the generated Tafel plots were fit linearly to allow calculation of corrosion potential, E_{corr}, and corrosion current density, i_{corr}.

Corrosion of the Mg alloys was also measured using mass loss in a corrosion solution. Polished samples of the as-cast and T4 treated WX11 and WX41 were immersed in DMEM with with 10% fetal bovine serum (FBS), 100 U/ml penicillin, and 100 μg/ml streptomycin at 37 °C, while the extruded KX11, WK11, WK41, and WZ42 alloys were immersed in HBSS at 37 °C. Samples removed after up to 5 weeks of immersion were dried at room temperature and their surfaces and surface cross sections analyzed using SEM and EDX to analyze the surface layer

composition and morphology. The sample masses were measured after immersion in a solution containing 200 g/L of chromic acid and 10 g/L of $AgNO_3$ for 1 minute to remove the corrosion products. The corrosion rate was calculated according to ASTM G31-72 [158] using the following equation:

$$C = (K \times W)/(A \times T \times D)$$

Where C is the corrosion rate (mm $year^{-1}$, mmpy), the constant K is 8.76 x 10^4, W is the mass loss (g), A is the sample area exposed to solution (cm^2), T is the time of exposure (h), and D is the density of the material (g cm^{-3}).

3.2.2 Microhardness testing of Mg-Y-Ca-Zr based alloys

Vickers microhardness was measured by applying a load of 100 g for 10 s to samples polished and etched for microstructure, and measuring the indentation created by the square pyramidal diamond indenter using optical microscopy. The Vickers Pyramid number (HV) was determined by F/A, where F is the force applied to the diamond indenter in kilograms-force and A is the surface area of the resulting indentation in square millimeters. A was determined by the formula:

$$A = \frac{d^2}{2\sin(\frac{136°}{2})}$$

where d is the average length of the diagonal left by the indenter in millimeters. The HV number was then calculated by:

$$HV = \frac{F}{A} = \frac{2\sin(\frac{136°}{2})F}{d^2}$$

where F is in kgf.

3.2.3 Mechanical testing of Mg-Y-Ca-Zr based alloys

For mechanical testing, samples were machined along the long axis of the Mg alloy ingots and extruded rods in dimensions in accordance with ASTM-E8-04 [159] for tensile testing and ASTM-E9-09 [160] for compressive testing. Tensile bar samples with a gauge area of 3 × 3 mm and length of 12 mm were machined for tensile samples. Compressive cylindrical samples were machined of 10 mm diameter × 20 mm length. Compressive and tensile testing for as-cast and T4 solution treated alloys WX11 and WX41 were conducted by OrthoKinetic Testing Technologies, LLC (Southport, NC) at room temperature using an MTS11 – 50 kN electro-mechanical load frame (MTS, Eden Prairie, MN) with laser extensometer. For extruded alloys KX11, WK11, WK41, and WZ42, tensile tests were performed using an Instron 5566 mechanical testing system (Instron, Norwood, MA) with static axial clip-on extensometer. Tensile tests were conducted at room temperature at a crosshead speed of 1.3 mm/min, while compression tests were carried out at a speed of 2 mm/min. Engineering yield strength, ultimate strength, Young's modulus (E), percent elongation were determined from the stress-strain curves. Ultimate strengths of the alloys were determined as the maximum tensile stress from the stress-strain curves. Yield strengths were determined as the stress at the yield point during the tensile tests.

3.2.4 Statistical analysis

Statistical analysis was conducted using SPSS Statistics 17.0 (SPSS Inc., Chicago, IL). Differences between groups were analyzed using one-way ANOVA with post-hoc testing using Tukey's test when group sizes were equal or Gabriel's pairwise test when group sizes were

unequal. $P < 0.05$ was accepted as a statistically significant difference between means and is denoted in figures. Error bars within figures represent standard deviation.

3.3 RESULTS

3.3.1 Corrosion behavior of Mg-Y-Ca-Zr based alloys as a result of Y and Zn additions

The corrosion rates of the as-cast and T4 Mg-Y-Ca-Zr alloys (WX11 and WX41) compared to pure as-cast Mg and as-drawn AZ31 were calculated based on mass loss after immersion as well as by potentiodynamic polarization measurements, and are shown along with corrosion potential and concentration of Mg ions released into the immersion solution in Figure 3.1. The corrosion potential (Figure 3.1b) of the WX41 alloys was higher than the WX11 alloys and the control materials, pure Mg and AZ31, respectively. T4 solution treated alloys conducted on the as-cast WX11 and WX41 alloys at 525 °C also demonstrated a higher corrosion potential and breakdown potential compared to their as-cast counterparts. Potentiodynamic corrosion rates of the WX41 alloys were lower than the WX11 alloys and were similar to that of commercial AZ31. Solution treatment increased potentiodynamic corrosion rate of the WX11 alloy, though did not affect WX41.

Figure 3.1a shows that alloy corrosion rate calculated from the mass loss immersion test appeared to start stabilizing after 2 weeks of immersion. After 2 weeks of immersion, the corrosion rate of WX41 as-cast was significantly lower than those of the WX11 alloys. The 2 week corrosion rates of the WX41 alloys were also not significantly different than high-purity Mg. After 3 weeks of immersion, once again the WX41 as-cast alloys demonstrated a lower

corrosion rate compared to WX11, and similar to high purity Mg. T4 solution treatment did not appear to have a major effect on immersion corrosion rate. The corrosion media used for the mass loss corrosion experiments was used to determine concentration of Mg released into solution after 1, 2, and 3 weeks (Figure 3.1c). The WX41 alloys again showed higher corrosion resistance compared to WX11, releasing lower concentration of Mg at each time point, comparable to as-cast pure Mg and commercially obtained AZ31. Heat treatment did not seem to affect Mg ion released.

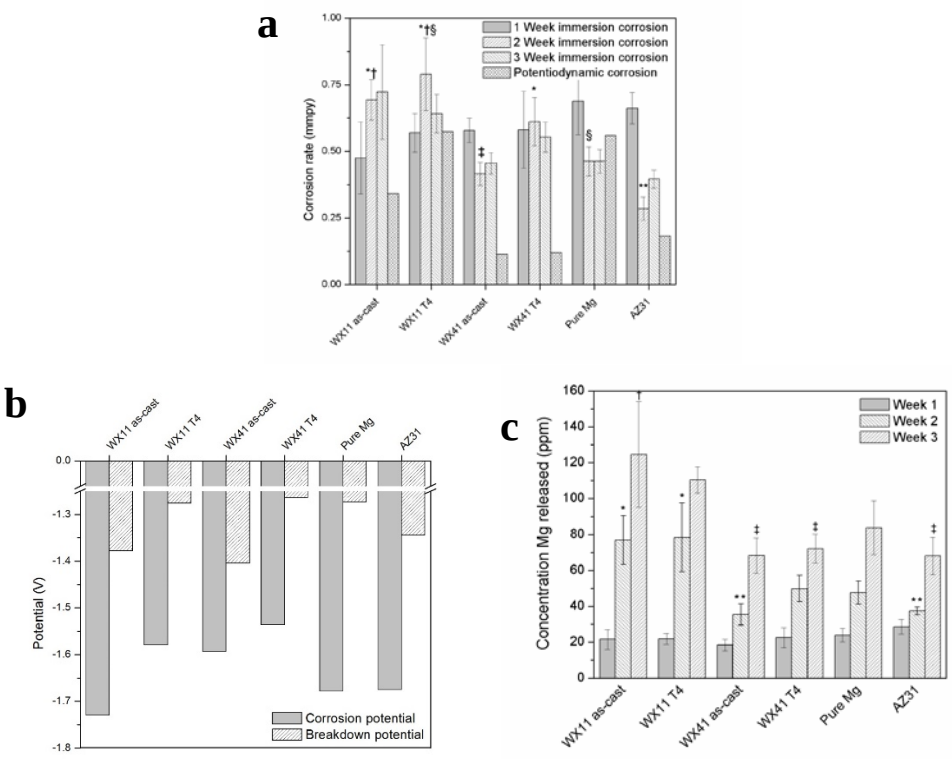

Figure 3.1. Corrosion properties of Mg-Y-Ca-Zr alloys, as-cast 99.99% pure Mg, and AZ31 in DMEM with 10% FBS: a) corrosion rate as measured using mass loss after 1, 2, and 3 weeks immersion (n = 3 per group per time point) and potentiodynamic corrosion (n = 1 per group). Significant difference ($p < 0.05$) between * and **; between † and ‡, between §. b) corrosion potential and breakdown potential (n = 1 per group); c) concentration of Mg released in corrosion media after 1, 2, and 3 weeks immersion (n = 3 per group per time point). Significant difference ($p < 0.05$) between * and **; † and ‡.

Figure 3.2 shows SEM micrographs of the Mg-Y-Ca-Zr alloys after potentiodynamic polarization test cleaned with $CrO_3/AgNO_3$ solution to remove the corrosion products. All the samples demonstrated localized pitting corrosion, a commonly seen phenomena in Mg alloys [128] including Y-containing alloys [161], while the as-cast alloys (Figure 3.2a and c) also show

corrosion occurring at corrosion-prone grain boundary regions (arrows) due to higher secondary phase localization.

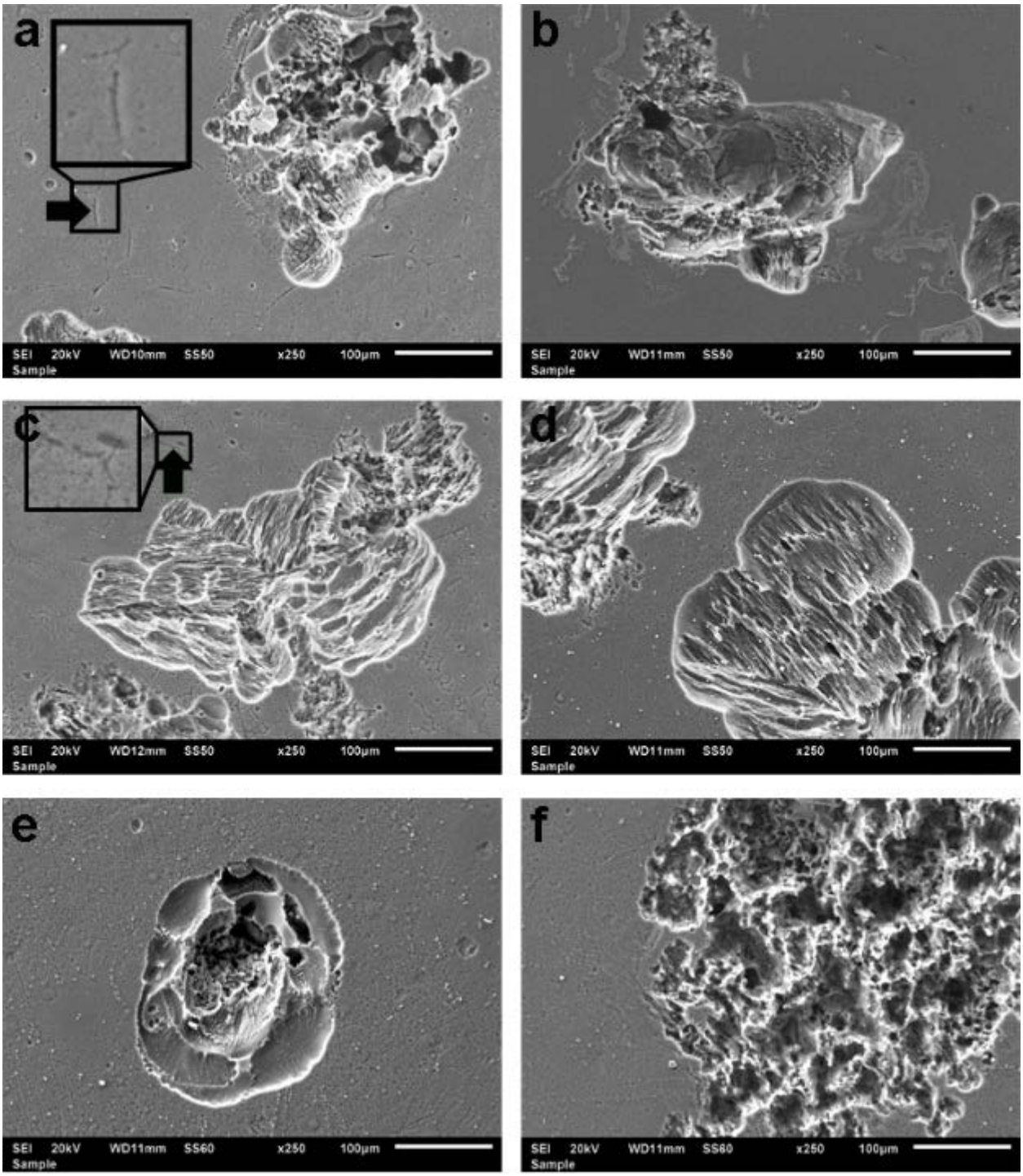

Figure 3.2. SEM images showing surface morphologies of a) WX11 as-cast; b) WX11 T4 heat treated; c) WX41 as-cast; d) WX41 T4 heat treated; e) pure Mg; f) AZ31 after potentiodynamic polarization in DMEM with 10% FBS at 37 °C and cleaning with CrO_3/$AgNO_3$ solution. Arrows denote corrosion at grain boundaries.

Micrographs of dried samples after 3 weeks immersion were captured using SEM to further assess corrosion (Figure 3.3). Localized corrosion was observed with deposits of corrosion product rich in C and O on the corroded surface (EDX shown in Figure 3.3a and b). The region immediately surrounding these corrosion deposits was generally rich in Mg (Figure 3.3a and e). Finally, most of the surface of the samples was covered in a layer rich in O, Ca, P, and Mg. Ca and P that are essential components in bone, and have been reported as forming a layer of amorphous calcium phosphate layer on rare earth containing alloys after degradation *in vivo* [125, 162]. After removal of corrosion products, SEM shown in Figure 3.4 revealed that the 3 week immersion corrosion samples exhibited linked up corrosion cavities on all materials.

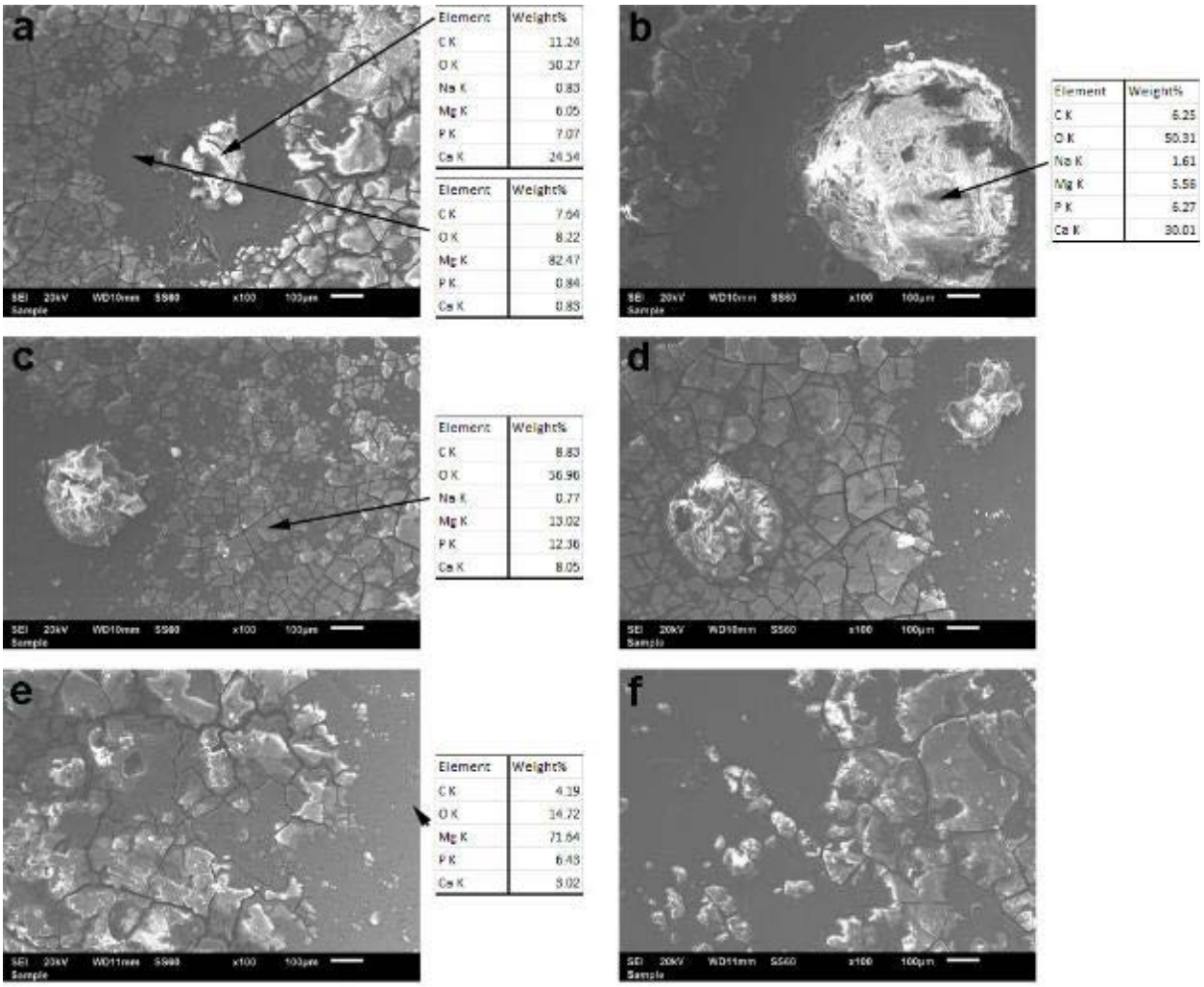

Figure 3.3. SEM images showing surface morphologies of a) WX11 as-cast; b) WX11 T4 heat treated; c) WX41 as-cast; d) WX41 T4 heat treated; e) pure Mg; f) AZ31 after 3 weeks static immersion in DMEM with 10% FBS at 37 °C. EDX was performed at various spots as denoted by arrows.

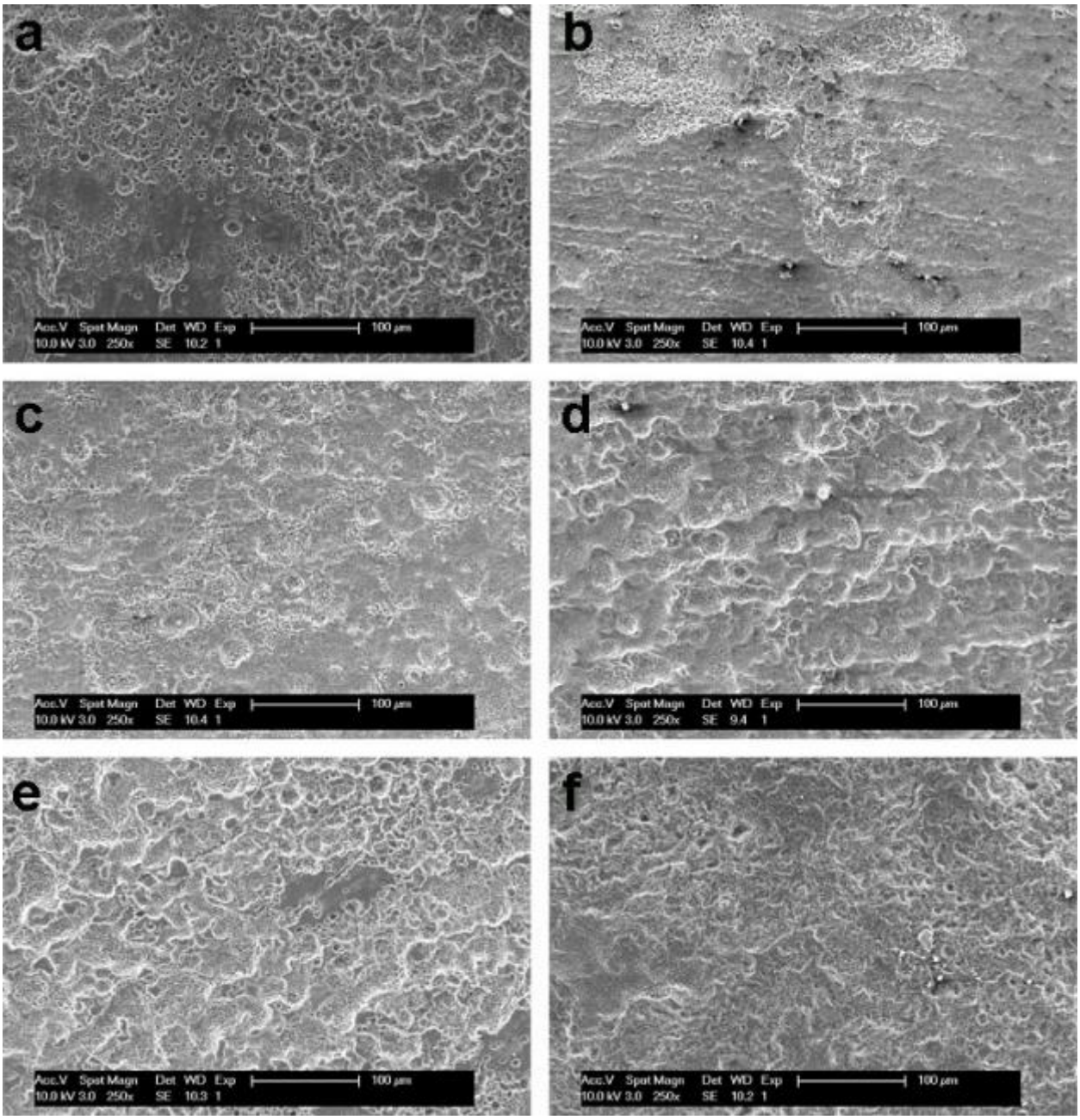

Figure 3.4. SEM images showing surface morphologies of a) WX11 as-cast; b) WX11 T4 heat treated; c) WX41 as-cast; d) WX41 T4 heat treated; e) pure Mg; f) AZ31 after 3 weeks static immersion in DMEM with 10% FBS at 37 °C and cleaning with CrO_3/$AgNO_3$ solution.

Extruded alloys also underwent corrosion testing after being immersed in solution for 1, 3, and 5 weeks at 37 °C, with average values plotted in Figure 3.5. Compared to the commercial material controls, the alloys demonstrated a significantly lower corrosion rate than pure Mg but generally higher than AZ31 but comparable or lower than in-house generated AZ31, despite most alloy corrosion rates not being significantly different from AZ31 after 1 week degradation. AZ31 alloy produced using the same conditions as the other novel alloys (AZ31 in-house) and also extruded at a ratio of 10 corroded more rapidly than the commercially obtained AZ31, with corrosion rates similar to or higher than the Mg-Y-Ca-Zr based alloys. Finally, a comparison between WZ42 extruded at an extrusion ratio of 30 resulted in higher corrosion rates than when the same composition alloy was extruded at a lower ratio of 10, with this result potentially compounded by the additional 25 °C required for an extrusion ratio of 30 allowing further precipitation of intermetallics. Generally a trend was observed where the corrosion rate was reduced by increasing the Y content. Alloying WK41 with Zn (WZ42) did not significantly affect the corrosion rate. No discernable correlations were observed between corrosion rates and time of immersion.

Comparing the immersion corrosion rates of the extruded alloys to the as-cast and solution treated (Figure 3.1), both groups of alloys degraded faster relative to extruded commercial AZ31. Furthermore, for both as-cast/solution treated and extruded alloys, an increasing content of Y reduced the corrosion rate, an important aspect of introducing and increasing the amounts of Y.

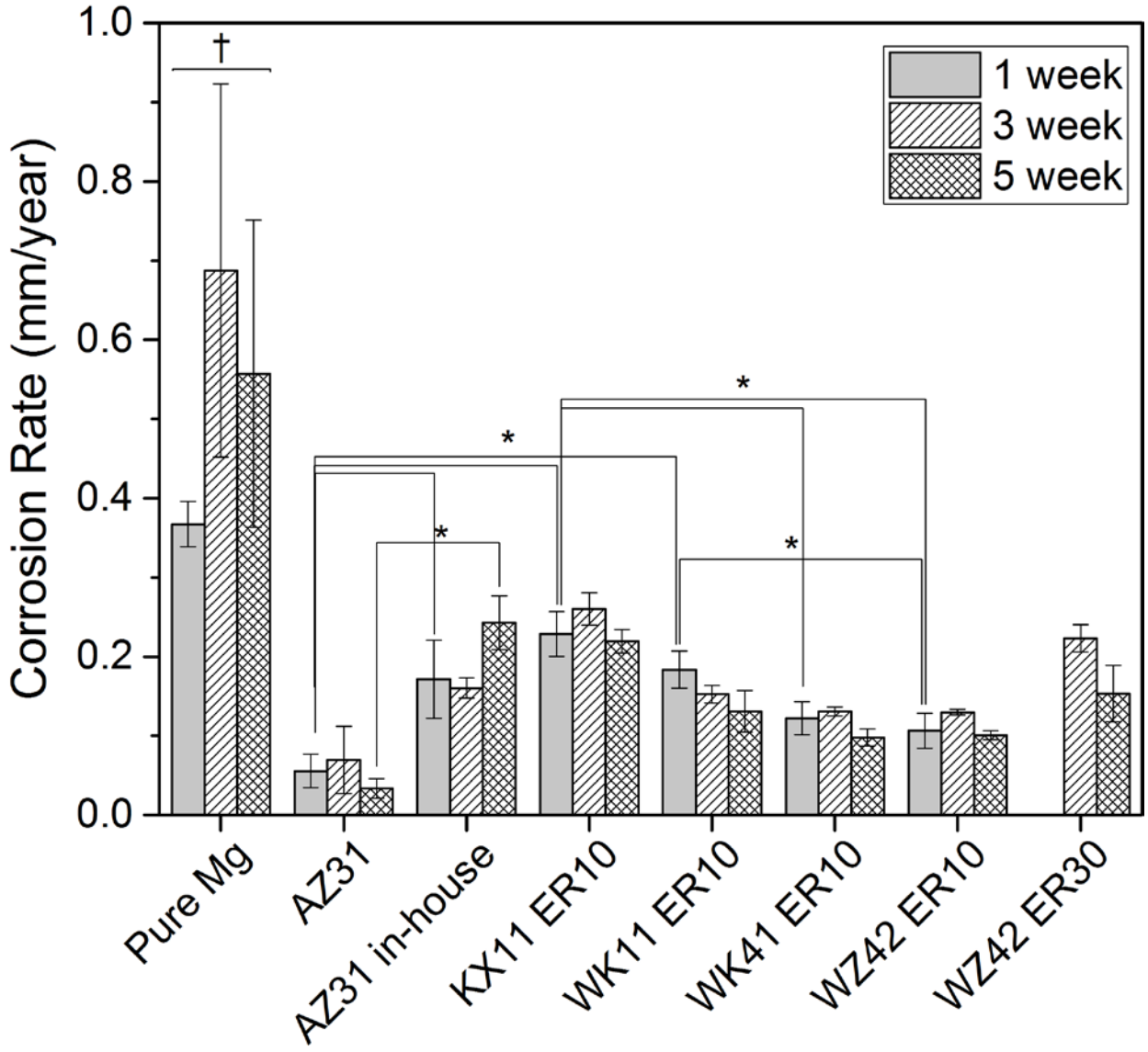

Figure 3.5. Average corrosion rates of extruded Mg-Y-Ca-Zr-based alloys compared to extruded pure Mg and AZ31 (in commercial and produced in-house forms). Groups labeled * were significantly different ($p < 0.05$) from one another at that time point and those labeled † were significantly different ($p < 0.05$) from all other groups at that time point. $n = 3$ for all groups at all time points.

Following removal of degradation products to measure mass loss, samples immersed for 1 week were imaged for their surface morphology (Figure 3.6), and cross section imaged after 5 weeks immersion (Figure 3.7) using SEM. The surfaces of all the Mg alloys revealed filiform corrosion with the presence of pits. Still, the surface after 1 week remained largely uniform having undergone little corrosion. Pure Mg however did suffer from more severe pitting corrosion, with pits in the discontinuous surface seen in Figure 3.7a. Fairly uniform surfaces of the alloys developed were seen in the cross sectional images after 5 weeks, with regions that appeared flat with scattered pits, most prevalent in WK11, pure Mg, and AZ31 cast in-house. While the depth of corrosion in WZ42 with ER 10 appeared greater than ER 30, the latter form of the alloy's surface appeared to be more discontinuous with cracks visible on the surface layer. The more rapid corrosion of AZ31 cast in-house compared to commercial AZ31 was visible in the deep pits seen in Figure 3.7c.

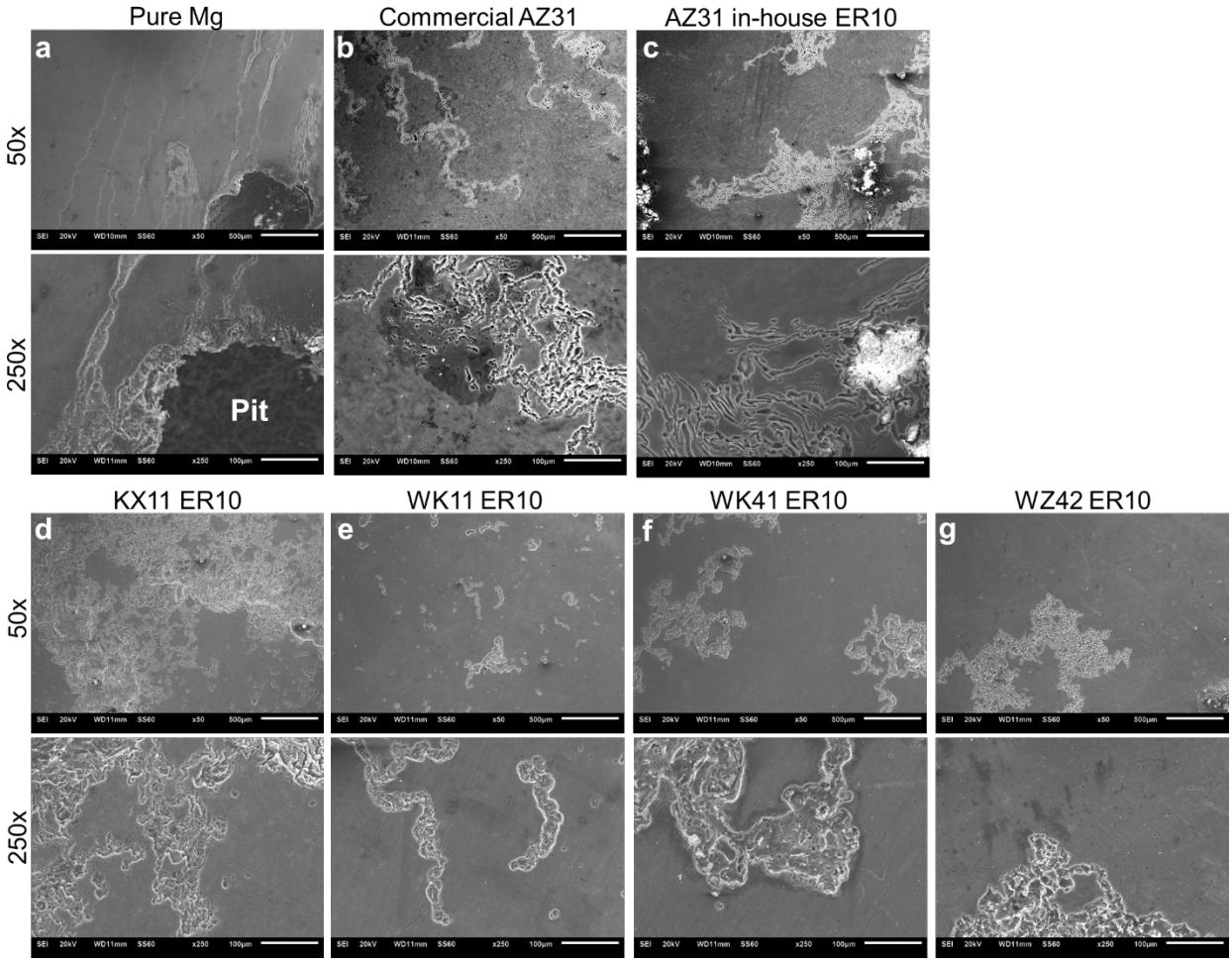

Figure 3.6. SEM images at 50x and 250x magnification showing surface morphologies of extruded a) pure Mg, b) commercially obtained AZ31, alloys produced in-house extruded with extrusion ratio of 10: c) AZ31, d) KX11, e) WK11, f) WK41, and g) WZ42 after 1 week static immersion in HBSS at 37 °C and cleaning with CrO_3/$AgNO_3$ solution.

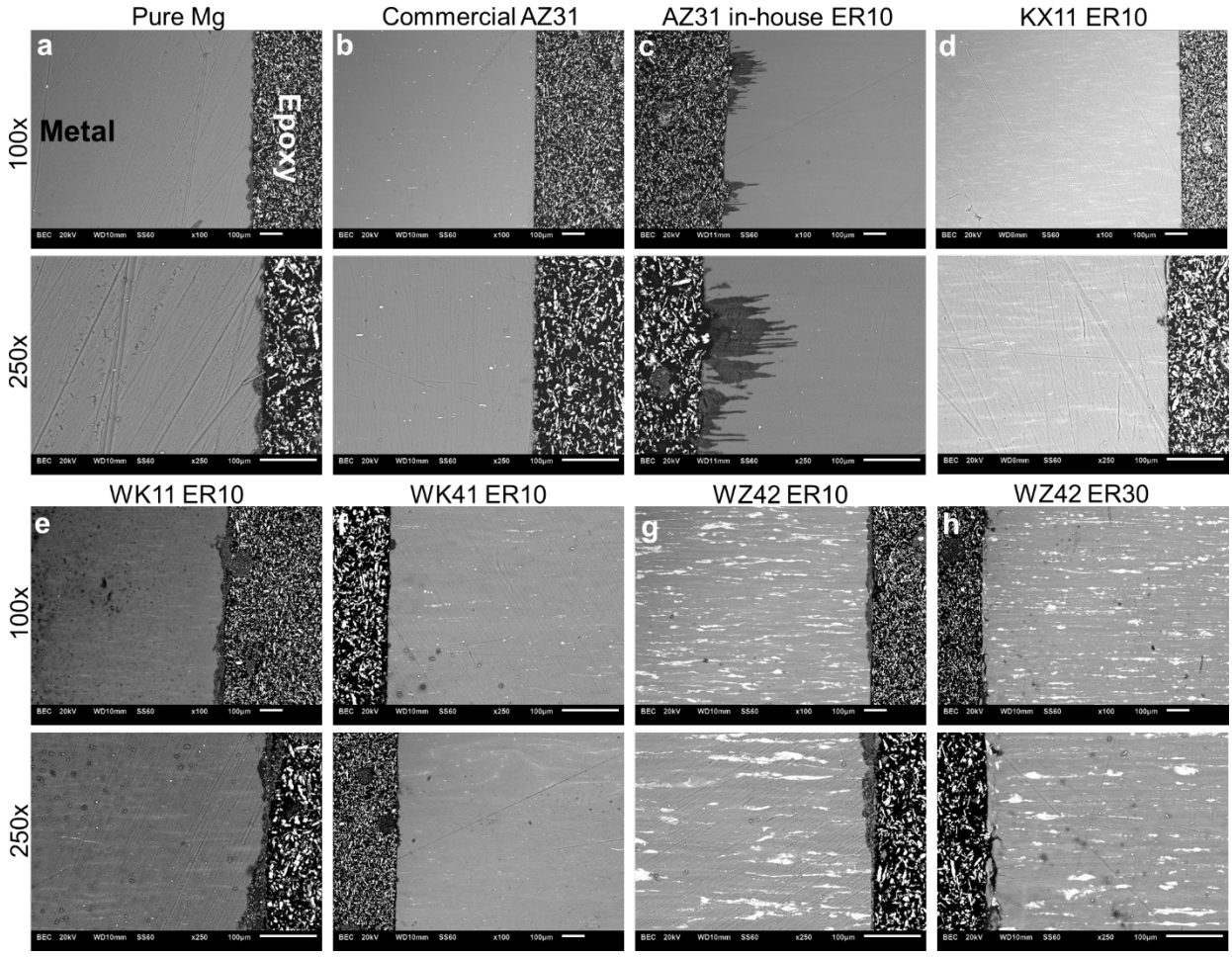

Figure 3.7. SEM images at 100x and 250x magnification showing cross sectional morphologies of extruded a) pure Mg, AZ31 obtained b) commercially and c) processed in-house, and d) KX11, e) WK11, f) WK41, and g) WZ42 alloys extruded with extrusion ratio 10 and h) WZ42 extruded with extrusion ratio of 30 after 5 weeks static immersion in HBSS at 37 °C and cleaning with CrO_3/$AgNO_3$ solution. Location of sample metal and mounting epoxy is indicated in a).

3.3.2 Microhardness of Mg-Y-Ca-Zr based alloys as a result of Y and Zn additions

Microhardness results shown in Figure 3.8 demonstrated significantly increased values over pure Mg upon the addition of alloying elements. Furthermore, a significant increase in microhardness was observed with the addition of Zn to the Y containing alloys. No change was observed in the microhardness of the WZ42 alloy extruded at a ratio of 10 compared to 30.

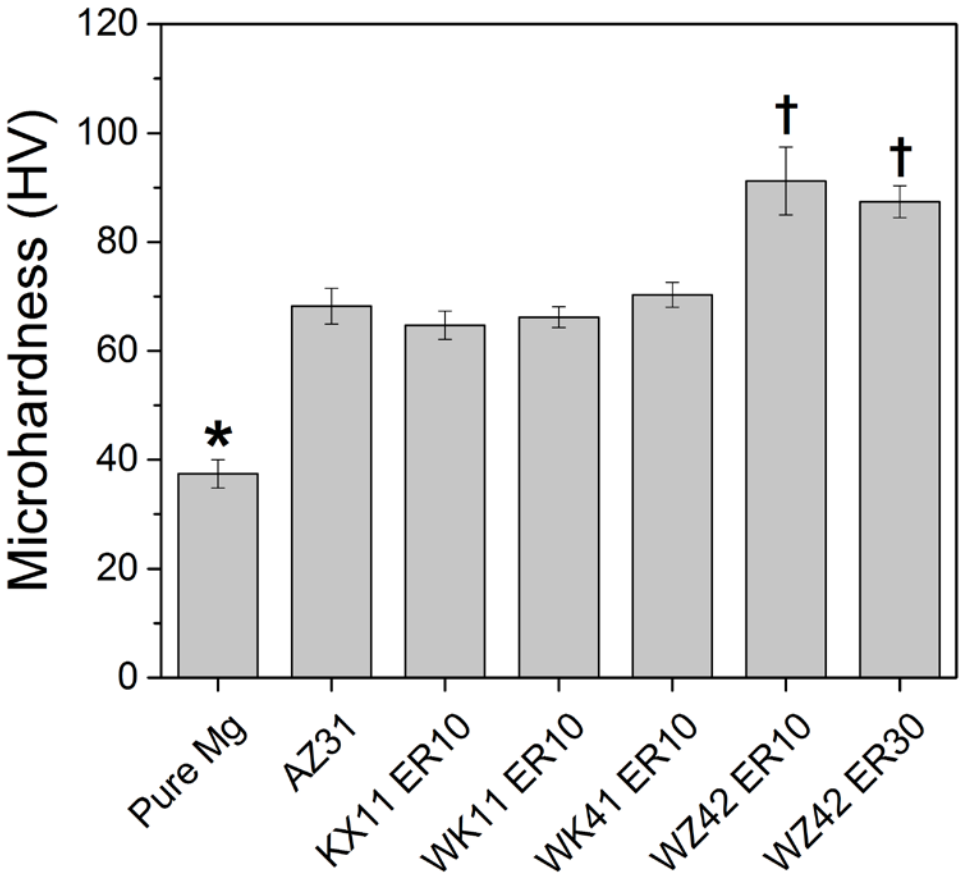

Figure 3.8. Vickers microhardness of extruded Mg alloys. Group labeled * was significantly different ($p < 0.05$) than all other groups, and groups labeled † were significantly different ($p < 0.05$) from all other groups but not from one another. ER = extrusion ratio. n = 5 for all groups at all time points.

3.3.3 Mechanical properties of Mg-Y-Ca-Zr based alloys as a result of Y and Zn additions and extrusion

Compression and tensile mechanical properties of the as-cast and heat treated alloys are presented in Figure 3.9. Ultimate compressive strain (Figure 3.9a) of as-cast WX11 and WX41 alloys were significantly larger than that of as-cast pure Mg and as-drawn AZ31. Ultimate compressive strength (Figure 3.9a) for the as-cast experimental alloys was also greater than for as-cast pure Mg, while AZ31 exhibited significantly greater ultimate compressive strength over all of the other materials tested due to the significant work hardening and grain refinement imparted on it by the drawing process. T4 solution treatment applied to the as-cast alloys at 525 °C resulted in a significant reduction in compressive strength and strain, while an increase in compressive yield strength (Figure 3.9b) was observed with an increased Y content. As-cast WX41 demonstrated significantly higher ultimate tensile strength (Figure 3.9c) than as-cast WX11. Similar to compression test results, applying the T4 solution applied at 525 °C to the as-cast Mg-Y-Ca-Zr alloys resulted in a reduction in the ultimate tensile strength and tensile yield strength compared to the as-cast alloys, while no significant effect on tensile strain could be observed after heat treatment. AZ31 displayed much higher tensile strength and strain over the other tested materials. Tensile properties of the Mg-Y-Ca-Zr alloys were either greatly improved or observed to be comparable to those of pure Mg. Values of Young's modulus (Figure 3.9d) for the tested alloys varied between 34-60 GPa, similar to the measured value for AZ31 (42 GPa), with high variance within the groups observed.

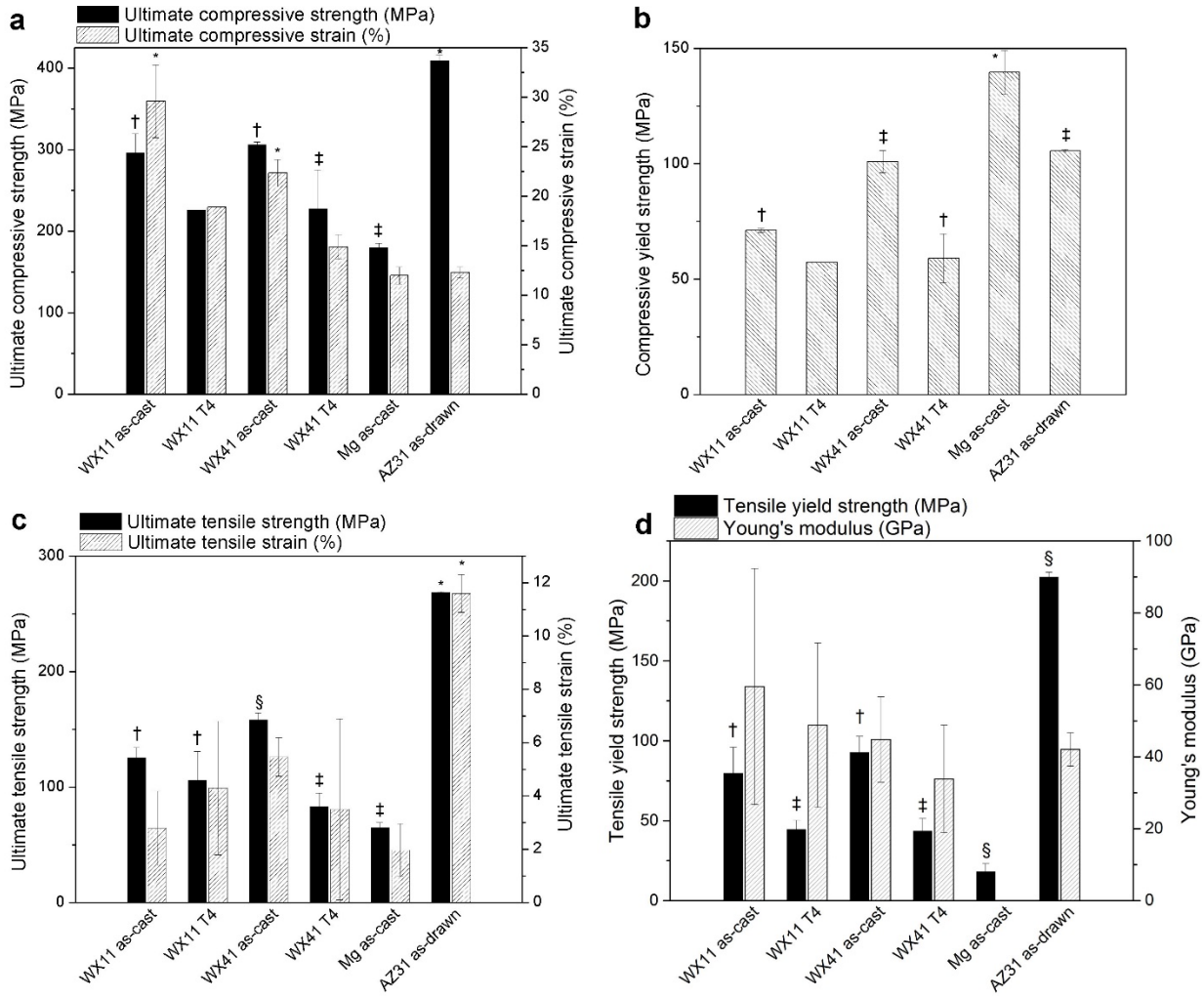

Figure 3.9. Mechanical properties of Mg-Y-Ca-Zr alloys, pure Mg, and AZ31: a) ultimate compressive strength and ultimate compressive strain; Significant difference ($p < 0.05$) between * and all other groups; †, ‡ and other groups. b) compressive yield strength; Significant difference ($p < 0.05$) between * and all other groups; †, ‡ and other groups. c) ultimate tensile strength and ultimate tensile strain; Significant difference ($p < 0.05$) between *, § with all other groups; †, ‡ with other groups. d) tensile yield strength and Young's modulus; Significant difference ($p < 0.05$) between § with all other groups; †, ‡ with other groups. $n \leq 3$ for all groups at all time points.

Tensile mechanical properties of the extruded alloys are reported in Figure 3.10 and Figure 3.11. Ultimate tensile strength (Figure 3.10) for all the extruded Mg alloys developed in this work were significantly higher than the commercial controls – extruded pure Mg and AZ31. While the ultimate tensile strength remained similar for KX11, WK11, and WK41, it was drastically improved upon adding Zn to the composition in the form of WZ42, for which strength was significantly higher when extruded at ER 10 versus 30. The ultimate tensile strain of all measured extruded materials were all similar except for KX11, which had a significantly higher elongation than all other groups save AZ31.

Yield strength (Figure 3.11) of the extruded alloy KX11, WK11, WK41, and WZ42 were higher than commercial pure Mg and commercially obtained extruded AZ31, with WK41 having the lowest yield strength among those alloys in its system, whereas again the WZ42 alloys possessed significantly higher strength. The Young's modulus of all the tested alloys were not significantly different from each other, ranging from 40-60 GPa.

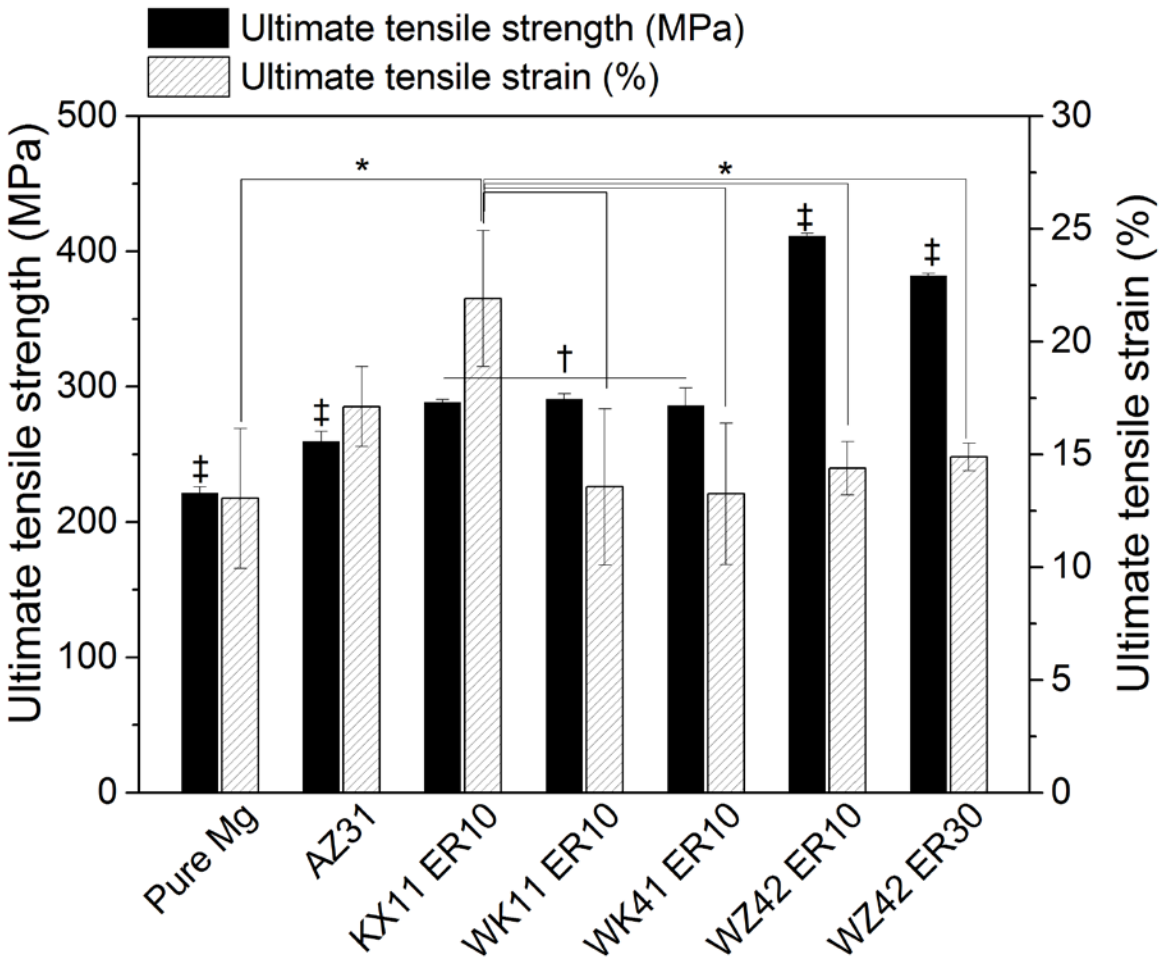

Figure 3.10. Average ultimate tensile strength and strain of extruded Mg alloys. Measurements of ultimate tensile strains labeled * were significantly different ($p < 0.05$) from each other. Measurements of ultimate tensile stress labeled † were significantly different ($p < 0.05$) from all other groups but not from one another. Measurements of ultimate tensile stress labeled ‡ were significantly different from all other groups. ER = extrusion ratio. n = 5 for all groups at all time points.

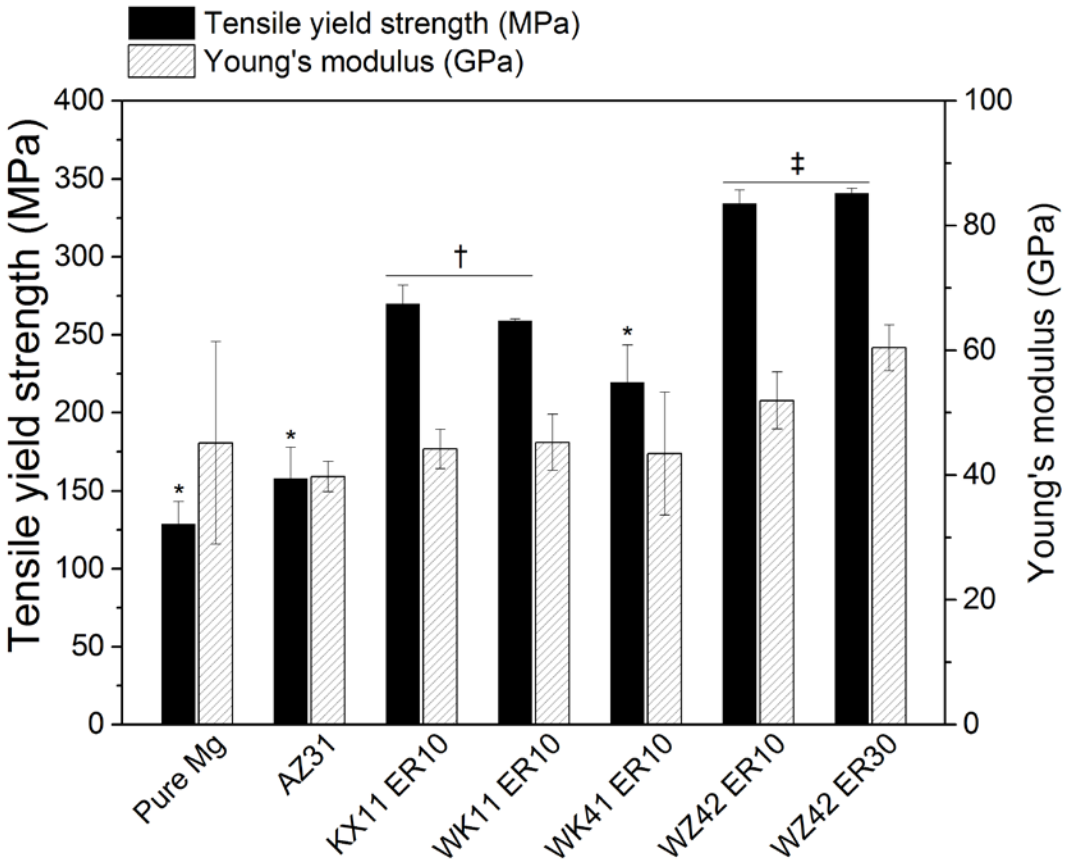

Figure 3.11. Average tensile yield strength and Young's modulus of extruded Mg alloys. Measurements of yield strength labeled * were significantly different ($p < 0.05$) from all other groups; groups labeled † and ‡ were significantly different ($p < 0.05$) from all other groups but not from one another. ER = extrusion ratio. n = 5 for all groups at all time points.

3.4 DISCUSSION

In this specific aim, the three main variables of: 1) alloy composition (increasing amount of Y and addition of Zn), 2) extruded versus non-extruded, and 3) as-cast versus T4 solution treated were explored for their effects on corrosion behavior and mechanical properties.

Corrosion resistance has been a major point of interest in magnesium alloy research due to severe pitting corrosion observed in Mg alloys when exposed to physiological chloride environment beyond 150 mmol/L [163] as well as at sites of low hydrogen overpotential [128]. Microstructure and grain size play crucial roles in controlling corrosion, with reports of an increase in grain size resulting in a change in corrosion resistance. Comparing the immersion corrosion rates of the extruded alloys (Figure 3.5) to the as-cast and solution treated alloys (Figure 3.1a), both groups of alloys degraded faster relative to extruded commercial AZ31. Corrosion rates of the extruded alloys did not improve significantly over the as-cast and T4 treated alloys studied here, and may be due to a number of causes. On one hand, Aung and Zhou [112] demonstrated that increasing grain size through heat treatments at various temperatures of AZ31B-H24 resulted in an increase in corrosion rate as explained by the grain boundaries acting as a physical corrosion barrier. Fine grained alloy microstructures processed by friction stir processing of Mg-Y-RE [164] and equal channel angular pressing (ECAP) of AZ31 [165] also displayed better corrosion behavior as a result of the finer grained alloys. Small grain size was suggested to lead to greater corrosion resistance by the presence of a more compact layer of phosphorous containing compounds and magnesium hydroxide when the alloy is exposed to physiological medium serving to protect against the action of chloride ions resulting in higher charge transfer resistance [165, 166] as well as more uniform corrosion with smaller pits because of the fine grain size [111]. On the other hand however, conflicting studies have shown that

reduction in grain size leads to a decrease in corrosion resistance, through addition of a grain-refining agent [167] or ECAP [168] as a result of corrosion initiation and propagation at grain boundaries, with corrosion filaments following grain boundary paths, acting as sites of micro-galvanic corrosion. It is expected that the lack of noticeable change in corrosion from change in grain size as stemming from a combination of these conflicting effects on corrosion by microstructural variations.

Another method of controlling corrosion rate was by applying a T4 solution treatment to reduce the volume fraction of secondary phases by diffusion into the α-Mg matrix, thus limiting the extent of microgalvanic corrosion where the anodic α-Mg matrix has a lower corrosion potential than any secondary phase, corroding preferentially as a galvanic couple [157]. This was observed in comparing the corrosion surface of as-cast to solution heat treated alloys in Figure 3.1, where the as-cast alloys with higher secondary phase concentration at the grain boundaries encountered visible corrosion at these grain boundaries, which was not seen in the solution treated alloys.

Differing the Y content in Mg-alloys may affect the corrosion behavior as reported by Liu and colleagues [130]. By increasing Y content, the volume fraction of Y-containing intermetallics increases, thereby enhancing the microgalvanic corrosion. On the other hand, Liu et al. [130] determined that increasing Y above 3% may also result in a more protective passivation layer of Y_2O_3 and decreased cathodic current, which was also determined theoretically [139].

This stronger passivation of alloys containing greater Y content was shown in the higher corrosion potentials (Figure 3.1b) of as-cast and T4 treated WX41 compared to the as-cast and T4 treated versions of WX11. T4 solution treatment was also observed to shift the corrosion

potential of the Mg-Y-Ca-Zr alloys to more noble potentials due to the reduction of intermetallic particles along the grain boundaries into the solid solution, possibly allowing for the protective oxide layer to cover a larger region of the alloy surface, as suggested by Neil et al. [167] after heat treating Mg-Zn-RE-Zr alloys. After solution treatment, more positive breakdown potentials of the Mg-Y-Ca-Zr alloys were also observed, indicating a higher resistance to the breakdown of the passive film and onset of pitting corrosion [167]. The potentiodynamic corrosion rates (Figure 3.1a) as calculated using corrosion current density of the Mg-Y-Ca-Zr alloys decreased with an increase in Y content, which occurs through suppression of the cathodic reaction in the corrosion process [168]. Immersion corrosion (Figure 3.1a) and Mg concentration measurements (Figure 3.1c) confirmed this reduction in corrosion rate from WX11 to WX41 alloys. In the extruded alloys, an increase in Y content similarly led to a reduction in corrosion rate as seen in the results of Figure 3.5. KX11, the alloy processed without Y exhibited the highest corrosion rate while also displaying a surface most affected by corrosion compared to the alloys containing Y which displayed a more uniform surface (Figure 3.6). Filiform corrosion has been observed in Mg-Y containing alloys [169] which occurs due to the non-uniform hydroxide film on the surface allowing for locations of active corrosion to remain which can propagate. This active corrosion site produces high concentrations of local Mg^{2+} which attracts chloride ion, allowing the filiform corrosion to be maintained in random directions. This corrosion mechanism was confined to the surface due to the formation of $Mg(OH)_2$ and other passivating products such as Y_2O_3 which prevents the corrosion from propagating into the interior of the Mg sample as seen in the cross sectional images of the experimental alloys in Figure 3.7d-h.

Solution treatment of the as-cast alloys WX11 and WX41 caused a large increase in the potentiodynamic corrosion rate of WX11, while only a slight increase in corrosion rate was

observed for WX41. However, these trends were not reflected in the immersion corrosion and Mg concentration measurements, where T4 treatment did not result in a marked change or decrease in the corrosion rate. This may have been due to a combination of T4 treatment dissolving the intermetallic phases, reducing microgalvanic galvanic corrosion, while also increasing grain size, which may retard passivation kinetics [164]. The linked up corrosion cavities seen on the surface of the alloys are commonly observed on corroded Mg alloys [170].

Corrosion rate calculated from potentiodynamic polarization curves were lower than those calculated from mass loss during immersion possibly because the corrosion mechanism of Mg involves a fraction of the uni-positive Mg ion reacting as an intermediate step, reacting chemically as well as partially electrochemically, causing electrochemical measurements to underestimate the corrosion rate compared to weight loss or hydrogen evolution methods [130, 170, 171]. Corrosion products developed over a 3 week immersion period in DMEM with 10% FBS (Figure 3.3) revealed large amounts of Ca and P in deposits (EDX in Figure 3.3a & b), consistent with observations of aggregations of calcium-containing corrosion products [121]. The presence of Ca and P containing cations may result in passivation and pit formation (as seen in Figure 3.2) because of the precipitation of phosphate and carbonate salts [172, 173].

Interestingly, a stark contrast was observed between the commercially obtained AZ31 and AZ31 as-cast, heat treated, and extruded in-house at an extrusion ratio of 10. Likely the differences in production process where industrial scale methods of generating bulk quantities in more controlled environments resulted in a more homogenous AZ31 with fewer impurities compared to the lab-scale operation which was used to produce AZ31 in-house [174]. These impurities, defects, and inclusions likely led to the more rapid corrosion of our AZ31.

Experimental error propagation resulting in variation in immersion corrosion rates within groups may have arisen due to variabilities in weight measurement from the scale, variations in the surface area from machining error, and slight differences in immersion time, in addition to variation between sample homogeneity and surface finish through machining and polishing.

Mechanical properties of Mg alloys are known to be sensitive to changes in microstructure according to the Hall-Petch relation where finer grains results in higher grain boundary strengthening [49, 50]. In this work, grain size increased after performing T4 solution treatment on as-cast alloys, but decreased after performing hot extrusion. Appropriately, the as-cast Mg-Y-Ca-Zr alloys maintained higher strength in compression and tension and higher compressive strain compared to the alloys after grain coarsening occurred from solution treatment. The higher presence of secondary phases in the as-cast Mg-Y-Ca-Zr alloys may have contributed to precipitation strengthening by acting as impediments for dislocation movement during plastic deformation. This phenomenon as well as solid solution strengthening has been utilized in RE containing alloys [32], and may explain the marginally higher tensile strengths for as-cast alloys containing higher Y content. As-drawn AZ31 solidifies with a fine grain size to meet mechanical property requirements for industrial applications [51], while the as-cast high purity Mg devoid of any alloying elements exhibited comparatively low mechanical properties, suffering from a lack of solid solution strengthening or precipitation strengthening. The extruded pure Mg also demonstrated significantly lower strength compared to all alloys tested. After extrusion, significant grain refinement occurred causing a significant increase in strength, with ultimate tensile strength of the as-cast and T4 treated alloys before extrusion not exceeding 175 MPa increasing to over 286 MPa for alloys following hot extrusion. Unlike the increase in strength seen after increasing the Y content in as-cast WX41 versus WX11 (Figure 3.9), an

increase in Y did not result in an increase in strength in the extruded alloys. Despite the higher percentage of alloying elements and precipitates, extruded WK41 which contained 4 wt. % Y did not show higher strength than KX11 and WK11 which contained 0 and 1 wt. %, respectively. This is likely due to the higher temperature to preheat the alloy slug held during extrusion required to soften the ingot to allow to pass through the die for WK41 which causes the alloy to undergo a higher extent of dynamic recrystallization and grain growth, hence reducing strength. With the introduction of Zn and thereby the LPSO phase in the WZ42 alloy, high microhardness and strength with moderate elongation were observed, with the Hall-Petch relationship and alignment of the LPSO phase along the direction of extrusion acting as hardening phases via a short-fiber strengthening mechanism like a composite material [175]. WZ42 extruded at a ratio of 30 may have seen its slight reduction in ultimate tensile strength due to higher deformation and temperature increase during hot extrusion leading to further dynamic recrystallization. Finally, a significantly higher elongation in the KX11 alloy lacking Y has been confirmed experimentally where higher Y content led to weakened ductility [154] as greater Y content in the solid solution and precipitates deteriorate the alloy ductility [110].

The Young's modulus of the tested alloys all were in a similar range being more appropriate for orthopedic applications than stainless steel or titanium as they were closer to the modulus of natural bone (6-24 GPa) [15]. This may reduce the risk of stress shielding compared to the traditionally used permanent metals.

Experimental error resulting in variation in mechanical testing results within groups may have occurred due to slight variability in sample dimensions from machining error, variances in data collection of the force and strain measured by the mechanical testing unit, and deviations in

sample alignment when positioning samples, in addition to differences in sample to sample homogeneity.

Compared to other alloys reported in literature, the high strength of the WZ42 alloy compared especially favorably. In a comprehensive representation of degradable metals (Figure 3.12), WZ42 exhibits a yield tensile strength approaching that of wrought Fe, above any other Mg alloy reported thus far, with a moderate elongation of ~15%. Due to the high strength and reasonable ductility, this alloy was selected as the most optimum candidate for *in vivo* rat animal testing described in detail in Specific Aim 4. The other extruded alloys, KX11, WK11, WK41, also demonstrated high strength comparatively with moderate elongation. The as-cast WX11 and WX41 alloys demonstrated similar mechanical properties to the other cast Mg alloys included in the figure.

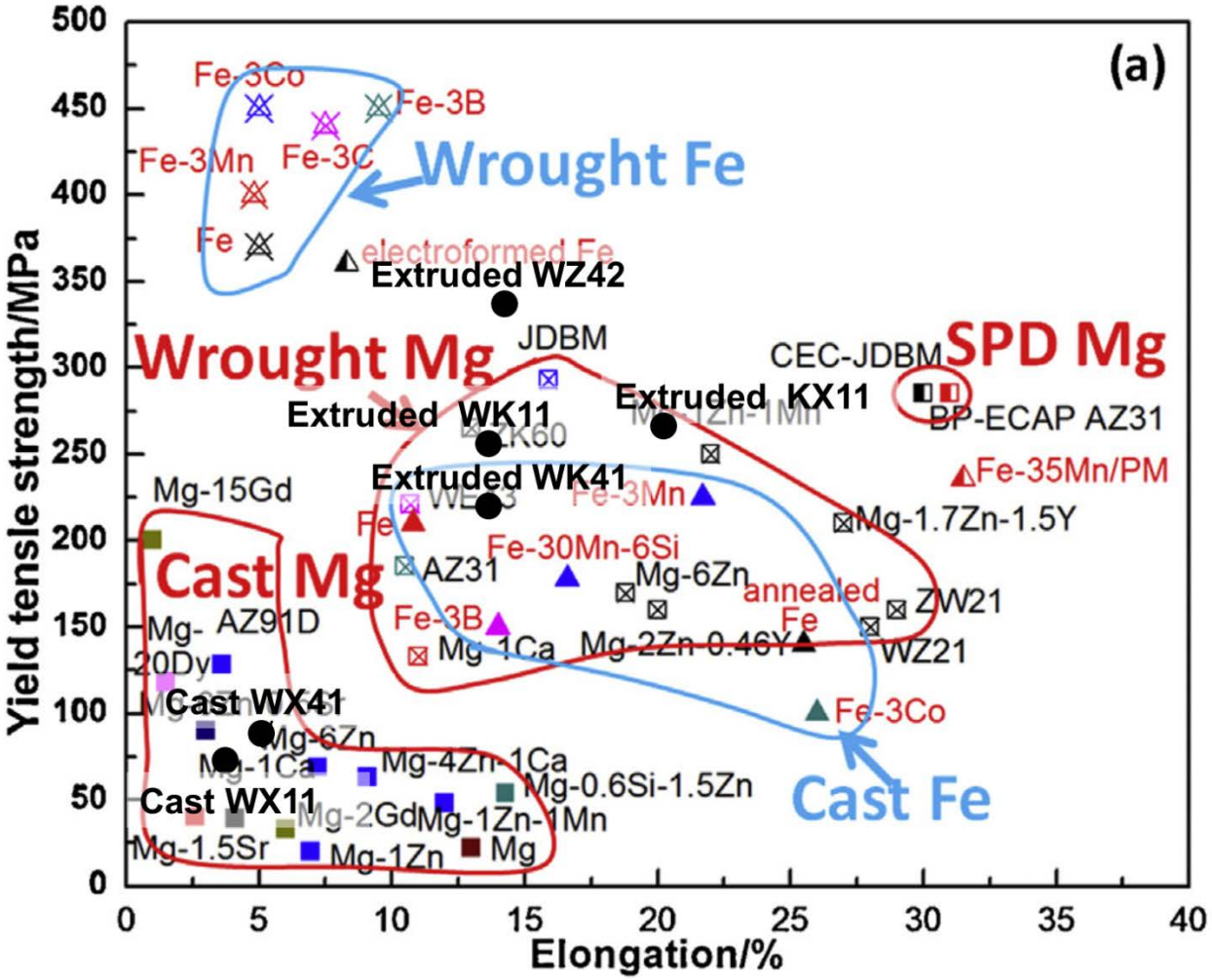

Figure 3.12. The yield tensile strength and elongation of cast and wrought Mg alloys with alloys from this thesis included – WX11 and WX41 in as-cast form and KX11, WK11, WK41, and WZ42 extruded at a ratio of 10. Figure adopted from Zheng et al, used with permission of [154].

4.0 SPECIFIC AIM 3: EVALUATE THE EFFECT OF YTTRIUM AND ZINC ADDITION, POST PROCESSING, AND ALLOYING ELEMENT SALTS, ON CELL VIABILITY AND PROLIFERATION OF PRE-OSTEOBLAST AND HUMAN MESENCHYMAL STEM CELLS. FURTHER EVALUATE EXPRESSION OF OSTEOBLAST DIFFERENTIATON MARKERS AND BIOCOMPATIBILITY IN MURINE SUBCUTANEOUS TISSUE

4.1 INTRODUCTION

It is of paramount importance to completely validate and demonstrate the biosafety of the degradation products of degradable magnesium for it to be adopted as an acceptable biomaterial for implantable devices. As discussed earlier, the degradation of Mg alloys gives rise to metal cations, oxides, hydroxides, phosphates, and carbonates, while also changing local pH and generating hydrogen gas which leads to gas pocket formation when implanted into animals. Below a threshold concentration, these degradation products are considered tolerable by the human body and do not result in any catastrophic outcomes leading to loss of patient life [110, 176]. The effects of the degradation products on local cells and tissue and their ability to be cleared by the body depends largely on their solubility in aqueous solutions. The most common and by far, the most stable byproduct of Mg alloy degradation is $Mg(OH)_2$ which has a moderate solubility (K_{sp}) of 8.9×10^{-12} with the next product that is formed by conversion of the hydroxide

to a salt being $MgCl_2$ which in contrast, is extremely soluble. The toxicity of the other alloying elements and their salts also must be considered to gain a full understanding of the potential toxicity of Mg alloys. Not only is it important to understand the toxicity and cellular responses to degradation products of the Mg alloys, but it is also extremely important to consider the direct interaction between the implant surface and local cells to ensure that the cells may attach and proliferate on the Mg implant surface.

For bone applications, implant materials should allow for growth of surrounding bone tissue and thereby reduce the incidence of implant loosening [177, 178]. From this standpoint, Mg has shown advantages of stimulating bone formation around and in contact with Mg implants [125-127, 179] to allow for better implant stability, integration with surrounding bone, and replacement of the biomaterial by native tissue. To compare between different materials and their characteristics before proceeding with costly and time-consuming animal tests and to reduce the ethical burden of these trials, *in vitro* tests are used to preselect the appropriate implant material candidates.

In addition to testing the alloys themselves, it was also sought to assess the individual contributions of each alloying element to the effects on cell response. Table 4.1 lists the toxicity and tolerance information on Mg and the alloying elements used in this study. In this aim it was decided to expand on these tests of the alloying element salts while also adding alloy extracts to pre-osteoblast and human mesenchymal stem cells to evaluate their viability, proliferation, and differentiation into the osteoblast lineage. In addition, a preliminary murine subcutaneous implant model was used to compare WX11 and WX41 as-cast samples for local toxicity and corrosion as an *in vivo* biocompatibility pilot study.

Table 4.1. Summary of the pathophysiology and toxicology of Mg and alloying elements used in the alloys of this work [154, 180]. The toxicity levels for bone cells are according to the cytotoxicity test of the metal salts; (+) represents mild toxicity, (+-) symbolizes moderate toxicity, and (-) indicates severe toxicity.

Element	Human amount	Blood serum level	Pathophysiology	Toxicology	Daily allowance	Toxicity to bone cells
Mg	25 g	0.73-1.06 mM	Activator of many enzymes; co-regulator of protein synthesis and muscle contraction; stabilizer of DNA and RNA	Excessive Mg leads to nausea	0.7 g	+
Ca	1100 g	0.919-0.993 mM	More than 99% has a structure function in the skeleton; the solution Ca has a signal function, including muscle contraction, blood clotting, cell function, etc.	Inhibit the intestinal absorption of other essential minerals	0.8 g	+
Zn	2 g	12.4-17.4 µM	Trace element; appears in all enzyme classes; most Zn appears in muscle	Neurotoxic and hinder bone development at higher concentration	15 mg	-
Zr	<250 mg	0.011 mg/dm^{-3}	Probably excreted in feces; low systemic toxicity to animals	High concentration in liver and gall bladder	3.5 mg 53 µg	+
Y	0.5 mg	0.1 mg/l	Substituted for Ca^{2+} and matters when the metal ion at the active site; compound of drugs for treatment of cancer	Concentrated in liver, kidney, spleen, lungs, high affinity for bone in areas of high osteoblastic activity [181]	4.4 µg	+-

4.2 MATERIALS AND METHODS

4.2.1 Cell culture and maintenance

MC3T3 pre-osteoblast cell line and human mesenchymal stem cells (hMSCs) were used to test the cytocompatibility of the alloys studied. These two cell lines were used to test the effects of the alloys on both osteoblast pre-cursor cells, hMSCs, and further differentiated mesenchymal cells, pre-osteoblasts, before full osteoblastic maturity. Their culture conditions are described below.

4.2.1.1 Mouse pre-osteoblast cell line (MC3T3-E1)

The murine pre-osteoblastic cell line (MC3T3-E1, American Type Culture Collection, Rockville, MD) were cultured in growth media consisting of modified Eagle's medium alpha (αMEM, Life Technologies, Carlsbad, CA), 10% fetal bovine serum (FBS), 100 U/ml penicillin, and 100 μg/ml streptomycin at 37 °C in an environment of 95% relative humidity with 5% CO_2. Cells after passage four were used in all experiments at a seeding density of 50,000 cells mL^{-1}. For osteogenic differentiation studies, MC3T3-E1 growth media was used supplemented with 100 nM dexamethasone, 50 μM ascorbic acid, and 10 mM β-glycerophosphate, also known as differentiation inducing media.

4.2.1.2 Human mesenchymal stem cells (hMSCs)

hMSCs obtained from normal human bone marrow (Lonza, Allendale, NJ) were cultured in growth media of αMEM with 20% FBS, 100 U/ml penicillin, and 100 μg/ml streptomycin at 37 °C in an environment of 95% relative humidity with 5% CO_2. Cells after passage three were used. In osteogenic differentiation studies, growth media was supplemented with 100 nM dexamethasone, 50 μM ascorbic acid, and 10 mM β-glycerophosphate as differentiation inducing media.

4.2.2 Direct LIVE/DEAD cell viability and adhesion test

MC3T3-E1 cells were cultured directly on the Mg alloys, as-cast and extruded pure magnesium, and extruded AZ31. 1 mm thick samples were polished up to 1200 grit, ultrasonically cleaned in isopropyl alcohol, air dried, and UV sterilized for 1 h. The alloy samples were incubated in cell culture media for 10 min after which cells were seeded on the samples at a density of 4×10^4 cells/mL. Cell viability was evaluated at 1 and 3 days using the LIVE/DEAD Viability/Cytotoxicity Kit (Invitrogen Corporation, Karlsruhe, Germany) following the manufacturer protocol. This kit determines cell viability by differentiating between live and dead cells with fluorescence microscopy of two different wavelengths. Briefly, the Mg-Y-Ca-Zr samples with attached MC3T3-E1 cells were washed with PBS and stained for 30 min at room temperature with 2 μmol/L ethidium homodimer^{-1} and 4 μmol/L calcein AM in PBS. After incubation in the LIVE/DEAD solution for 30 min in room temperature, live cells and dead cells images were captured using fluorescence microscopy.

4.2.3 F-actin and nuclei staining, SEM/EDX imaging of fixed cells

MC3T3 cells seeded on alloys cultured for 72 hours were fixed with 4% paraformaldehyde, permeabilized with 0.1% Tween 20 solution. F-actin staining was performed using tetramethyl rhodamine isothiocyanate-conjugated phalloidin and nuclei staining was performed using DAPI. Fluorescence images were visualized with a fluorescence microscope. Following fluorescence imaging, samples were dehydrated in a gradient ethanol/PBS mixture (30%, 50%, 70%, 90%, 95%, 100%) for about 10 minutes each and dried. Sample surfaces with attached cells were then observed by SEM and surface elemental composition was measured using EDX.

4.2.4 Alloy degradation product extract collection for indirect *in vitro* tests

Mg alloy samples, as-cast and extruded pure magnesium, and extruded AZ31 were polished up to 1200 grit, ultrasonically cleaned in isopropyl alcohol, air dried, and sterilized by ultraviolet radiation for 1 h. The specimens were incubated in MC3T3 growth media, hMSC growth or differentiation media at 37 °C in a humidified atmosphere with 5% CO_2 for 72 h. The sample weight to extraction medium ratio for as-cast and T4 treated WX11 and WX41 was 0.2 g/mL in accordance with the EN ISO standard 10933:12 [41], while for studies involving extruded KX11, WK11, WK41, and WZ42 the ratio used was ~0.8 cm^2/ml media to provide further dilution as recommended by Fischer et al [182]. This starting extraction ratio was designated as 100% extract, with less concentrated extracts prepared by diluting the 100% extract to concentrations of 50%, 25%, and 10% or 25%, 10%, 1%, and 0.1% to explore a broader range of concentration. Extracts were sterile filtered through 0.2 μm syringe filters before being added to cells in the MTT, CyQUANT, alkaline phosphatase assays below.

4.2.5 MTT cytotoxicity test

MC3T3 cells were seeded in 96-well cell culture plates at 6 x 10^3 cells/200 µl medium in each well and incubated for 24 h. Culture medium without extract served as the negative control and 10% DMSO culture medium as the positive control. After the 24 hour incubation, medium was replaced with 200 µl of extraction medium with varying concentrations and incubated for 1 and 3 days. The cytotoxicity of the corrosion extracts were tested using the MTT assay. Media and extracts were replaced with fresh cell culture medium to prevent interference of the magnesium in the extract with the tetrazolium salt [42]. The MTT assay was performed according to the Vybrant MTT Cell Proliferation Kit (Invitrogen Corp.) by first adding 10 µl of 12mM 3-(4,5-Dimethylthiazol-2-yl)-2,5-diphenyltetrazolium bromide (MTT) dissolved in phosphate buffer solution (PBS) to each well. The samples were incubated with MTT for 4 h, after which 100 µl formazan solubilization SDS-HCl solution was added to each well and incubated for up to 12 h. The absorbance of the samples was measured using the Synergy 2 Multi-Mode Microplate Reader (BioTek Instruments, Winooski, VT) at a wavelength of 570 nm. The absorbance of the samples with mean positive control subtracted was divided by the absorbance of the mean positive control subtracted from the mean negative control to determine percent viability of cells compared to the controls, where cells cultured with fresh media constituted 100% cell viability.

4.2.6 CyQUANT proliferation test

MC3T3 and hMSC cells were seeded in 96-well cell culture plates at 6 x 10^3 cells/200 µl medium in each well and incubated for 24 h. Culture medium without extract served as the negative control and 10% DMSO culture medium as the positive control. After the 24 hour

incubation, medium was replaced with 200 µl of extraction medium with varying concentrations and incubated for 1, 3, and 5 days. The effects on cell proliferation from the corrosion extracts were tested using the CyQUANT assay, where the CyQUANT dye binding solution binds to cellular DNA, which is highly regulated and closely proportional to cell number. The media was removed and cells rinsed with Dulbecco's Phosphate-Buffered Saline (DPBS). After removing the DPBS, 50 µL of the CyQUANT dye binding solution was added to each well which was then covered and incubated at 37 °C for 30 minutes, the fluorescence intensity of each sample well was measured using the microplate reader with excitation at 485 nm and emission detection at 530 nm. The fluorescence intensity of the samples was divided by the intensity of the mean negative controls (cells cultured in fresh media) to determine percent viability of cells compared to the control, with cells cultured with fresh media constituting 100% normal proliferation. After measurement the cells were also imaged using fluorescence microscopy with excitation wavelength of excitation ~494 nm amd emission ~517 nm

4.2.7 Alkaline phosphatase activity

Alkaline phosphatase plays an important role in the mineralization process by hydrolyzing organic phosphate substrates to release free inorganic phosphate, a mineralization promoter, and decreasing the concentration of extracellular pyrophosphate, an inhibitor of mineral formation [183]. ALP activity was quantified using the p-nitrophenol phosphate (pNPP) technique. After 3, 7, and 14 days of culture of hMSCs with the different extract media collected in growth media, the cells were rinsed with DPBS and lysed for 20 min using cell lysate (Sigma-Aldrich). ALP activity was measured using pNpp as the substrate according to the manufacturer’s protocol. The substrate solution was incubated with cell lysis supernatant for 1 h at 37 °C without exposure to

light, followed by termination of the reaction by adding 0.5 M NaOH. pNpp produced was measured at 410 nm using the microplate reader and normalized to the total DNA content as measured using the Quant-iT DNA assay (Thermo Fisher). ALP activity was compared to hMSCs cultured in growth media and differentiation media.

4.2.8 Quantitative real-time polymerase chain reaction (qRT–PCR)

After culturing in osteogenic media, RNA extraction was performed using the NucleoSpin RNA II kit (Macherey Nagel, Bethlehem, Pa) according to the manufacturer's protocol. The RNA concentration and purity were determined by measuring the absorbance at 260 and 280 nm using a microplate reader. Reverse transcription was then performed using the ImProm II Promega reverse transcription kit (Promega, Madison, WI) according to the manufacturer's protocol. Primers for human glyceraldehyde 3-phosphate dehydrogenase (GAPDH), runt-related transcription factor 2 (RUNX2), alkaline phosphatase (ALP), and osteocalcin (OCN) were used in the qRT-PCR experiments (Table 4.2). RUNX2 is the first transcription factor required for inducing mesenchymal cells into immature osteoblasts, where its expression is upregulated [184]. ALP is an important enzyme maximally expressed during the matrix maturation phase of osteoblast differentiation as it provides high concentrations of phosphate at the site of mineral deposition [185]. OCN is a bone-specific protein synthesized by osteoblasts that indicates osteogenic maturation, implicating bone mineralization and calcium ion homeostasis [186].

Table 4.2. qRT-PCR primer sequences used for human mesenchymal stem cells.

	Forward primer (5′–3′)	Reverse primer (5′–3′)
GAPDH	TTGTCCTGCGACTTCAACA	GTGGTCCAGGGTTTCTTACTCC

	Forward primer (5′–3′)	Reverse primer (5′–3′)
RUNX2	AACCCACGAATGCACTATCCA	CGGACATACCGAGGGACATG
ALP	GACCCTTGACCCCCACAA	GCTCGTACTGCATGTCCCCT
Osteocalcin	CCGGAGCAGTGTGAGCTTATA	GATGCGTTTGTAGGCGGTC

4.2.9 In vivo murine subcutaneous study

All experimental procedures for the murine subcutaneous study were approved by the Animal Care and Use Committee (IACUC) at the University of Cincinnati. Healthy nude mice were housed under controlled conditions and maintained with a standard pellet diet and water. Mice were anesthetized using isoflurane through a nosecone. A skin incision was made to create a subcutaneous pocket on the back of the mouse. Pure Mg, AZ31, and WX11 and WX41 as-cast alloys of dimensions 5 mm diameter × 1.4 mm thickness were inserted into the pocket and the incisions were closed by surgical staples. After 7, 40 and 70 days, the mice were sacrificed in a CO_2 chamber followed by the cervical dislocation. The Mg/Mg alloy implants with surrounding tissue were recovered, carefully separated from the tissue, cleaned, air-dried, and the final mass was measured to determine change in mass due to corrosion to calculate corrosion rate according to the mass loss equation in section 3.2.1. Tissue surrounding the implant was fixed in 10% formalin in PBS, paraffin-embedded, and sectioned (4 μm/section) for hematoxylin-eosin (H&E) staining. 70 day explanted samples were also imaged using SEM and analyzed using EDX before and after removal of corrosion products.

4.3 RESULTS

4.3.1 Cell viability and adhesion on surface of Mg-Y-Ca-Zr based alloys

Figure 4.1 shows pre-osteoblast MC3T3-E1 cells cultured directly on the WX11 and WX41 alloys for 1 and 3 days, and then stained with calcein-AM (green fluorescence in live cells) and ethidium homodimer-1 (red fluorescence in dead cells). After 1 and 3 days of culture, both WX11 and WX41 as-cast and T4 heat treated alloys (Figure 4.1a-d, h-k) demonstrated comparable live cell density compared to pure Mg (Figure 4.1e & l) and AZ31 (Figure 4.1f & m). Relatively few apoptotic cells compared to live cells were observed on each material, indicating generally good cell viability. Tissue culture plastic displayed higher cell viability compared to the Mg-based materials. No significant differences in cell morphology were observed among the different groups. Cell density was still high among the Mg-Y-Ca-Zr alloys after 3 days culture compared to 1 day, indicating the cells were not significantly affected by prolonged direct exposure times to the corroded environment.

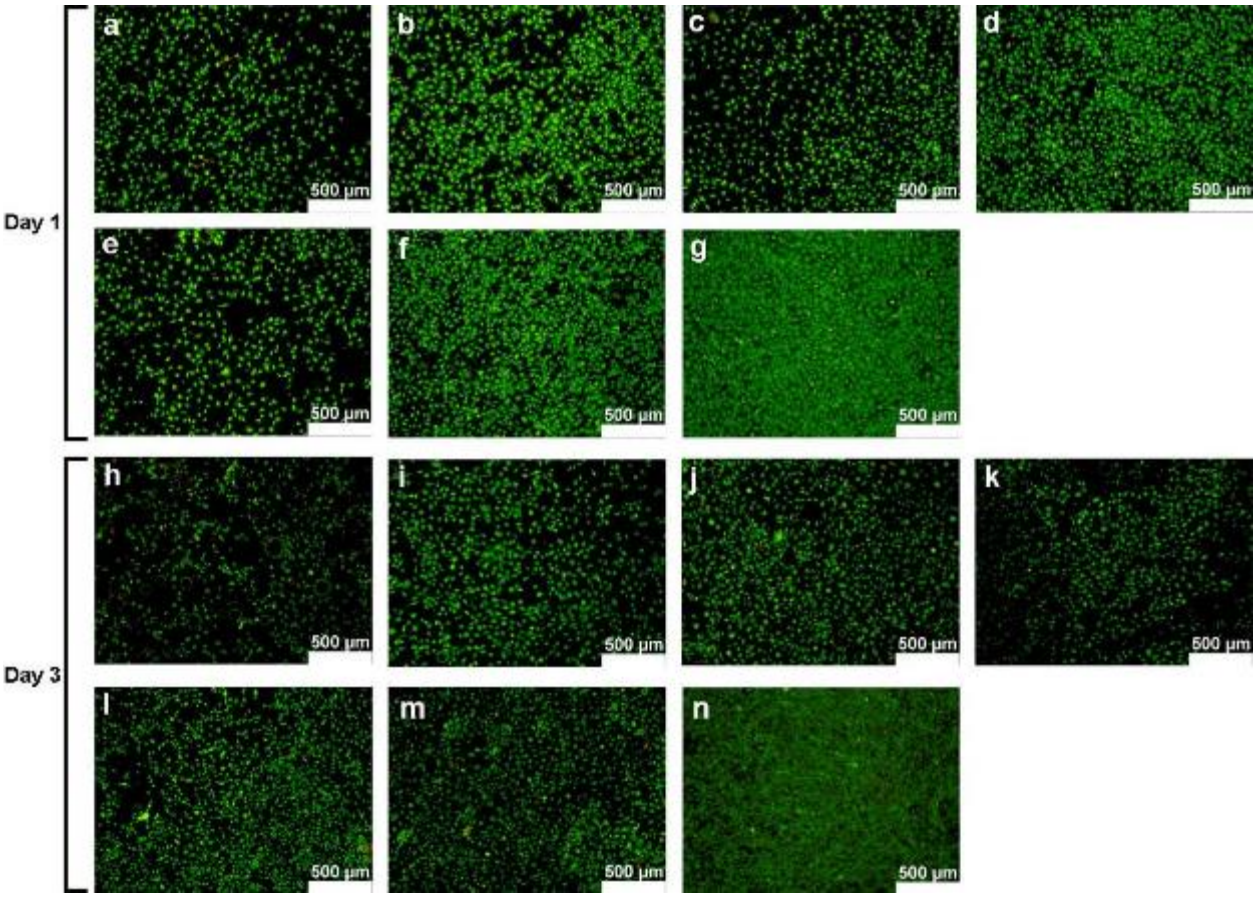

Figure 4.1. Fluorescent images of live (green) and dead (red) MC3T3-E1 cells attached after 1 and 3 days culture on a & h) WX11 as-cast; b & i) WX11 T4 heat treated; c & j) WX41 as-cast; d & k) WX41 T4 heat treated; e & l) pure Mg; f & m) AZ31 as-drawn; g & n) tissue culture plastic.

The direct live/dead assay for extruded alloys (Figure 4.2) displayed high cell density of attached live MC3T3 cells on the extruded alloys after 1 and 3 days of culture. Relatively few apoptotic cells compared to live cells and normal cell morphology was observed on each alloy, indicating high cell viability. After 1 day, cell density on the WZ42 alloy appeared similar to that of tissue culture plastic, and higher than the other alloys. After 3 days culture, live cell

attachment on the WK41 and WZ42 alloys was very high and similar to that on tissue culture plastic. Comparing the cell density on the alloys from 1 to 3 days, the increasing number indicated healthy cell proliferation. Cell morphology shown in the f-actin and nuclei staining of Figure 4.3 shows healthy, spread cell morphology with filaments plainly observed demonstrating good cell adhesion.

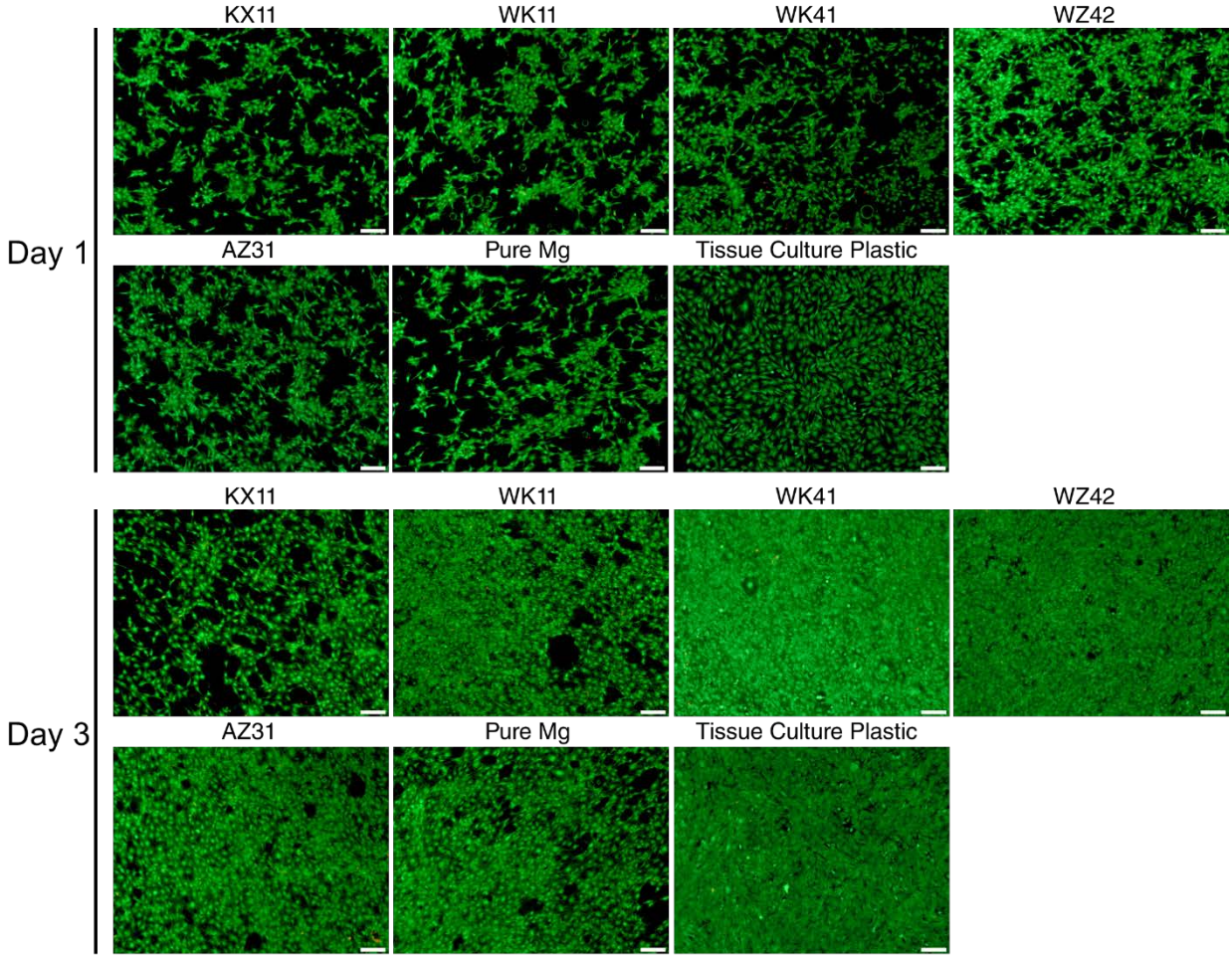

Figure 4.2. Live (green) and dead (red) MC3T3 cells on the surface of polished and extruded Mg alloy surfaces after 1 (above) and 3 (below) days of culture. Scale bar = 200 μm.

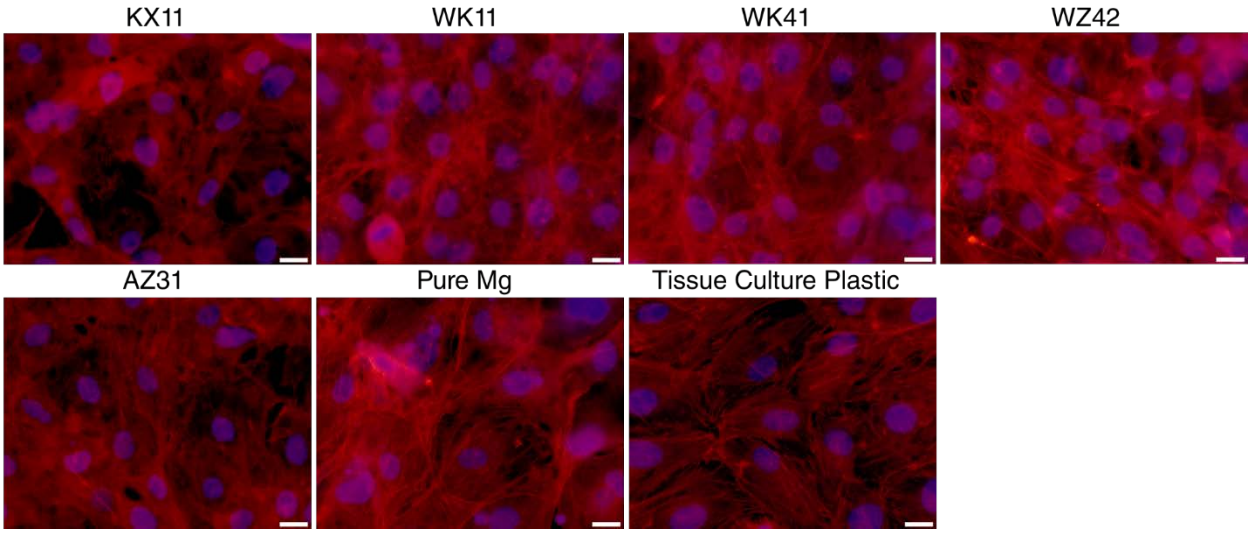

Figure 4.3. Phalloidin staining for F-actin (red) and DAPI staining for cell nuclei (blue) of MC3T3 cells on the surface of polished extruded Mg alloy surfaces after 3 days of culture. Scale bar = 20 μm.

The alloy samples with MC3T3 cells attached to the surface were then imaged using SEM (Figure 4.4). High cell attachment, especially seen in samples WK41 and WZ42 alloys was confirmed, as well as the relatively lower cell number attached to the KX11 alloy. Deposits of corrosion product were also observed on the surface of the corroded Mg alloys, as seen in the brighter areas in the SEM images.

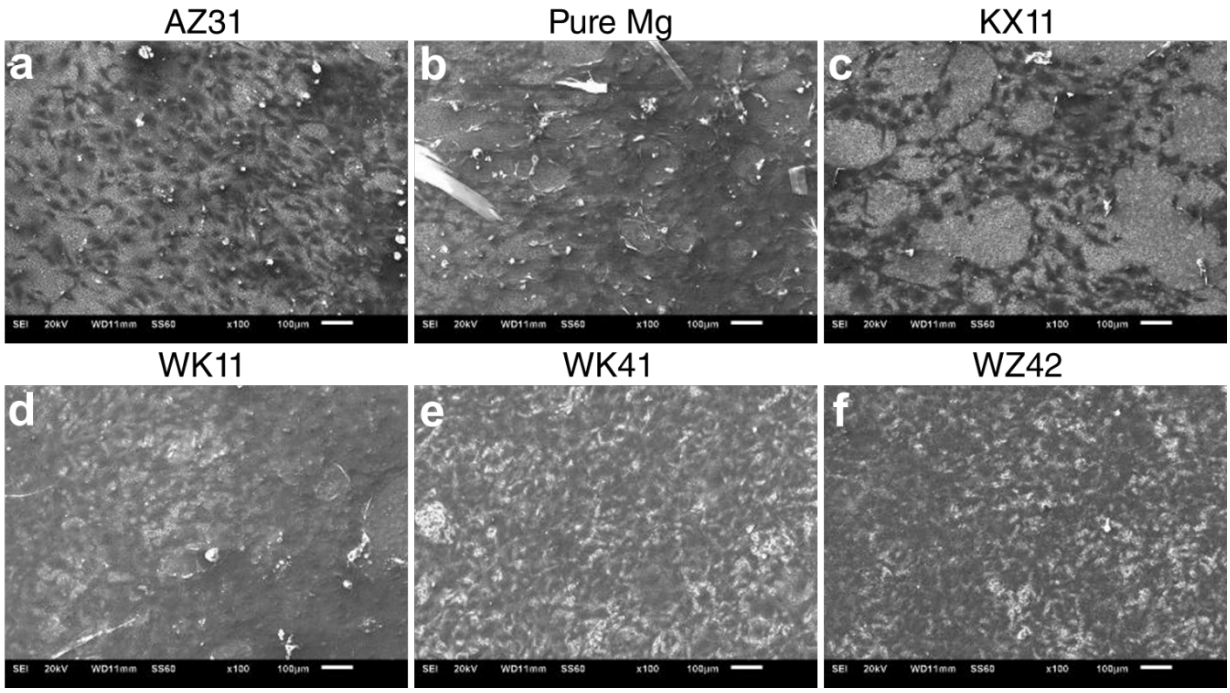

Figure 4.4. SEM images of MC3T3 cells attached to surface of extruded a) commercially obtained AZ31, b) pure Mg, c) KX11, d) WK11, e) WK41, and f) WZ42 after 3 days culture.

Full frame EDX analysis was also performed on various regions throughout the samples during imaging with SEM. Calcium and phosphorous weight percentages were graphed in Figure 4.5 which shows maximal Ca and P content present in the WZ42 alloy, while the surface of the KX11 alloy having the lowest concentration present. Percentage P present in the substrate surface rose with the addition of Y in the alloys.

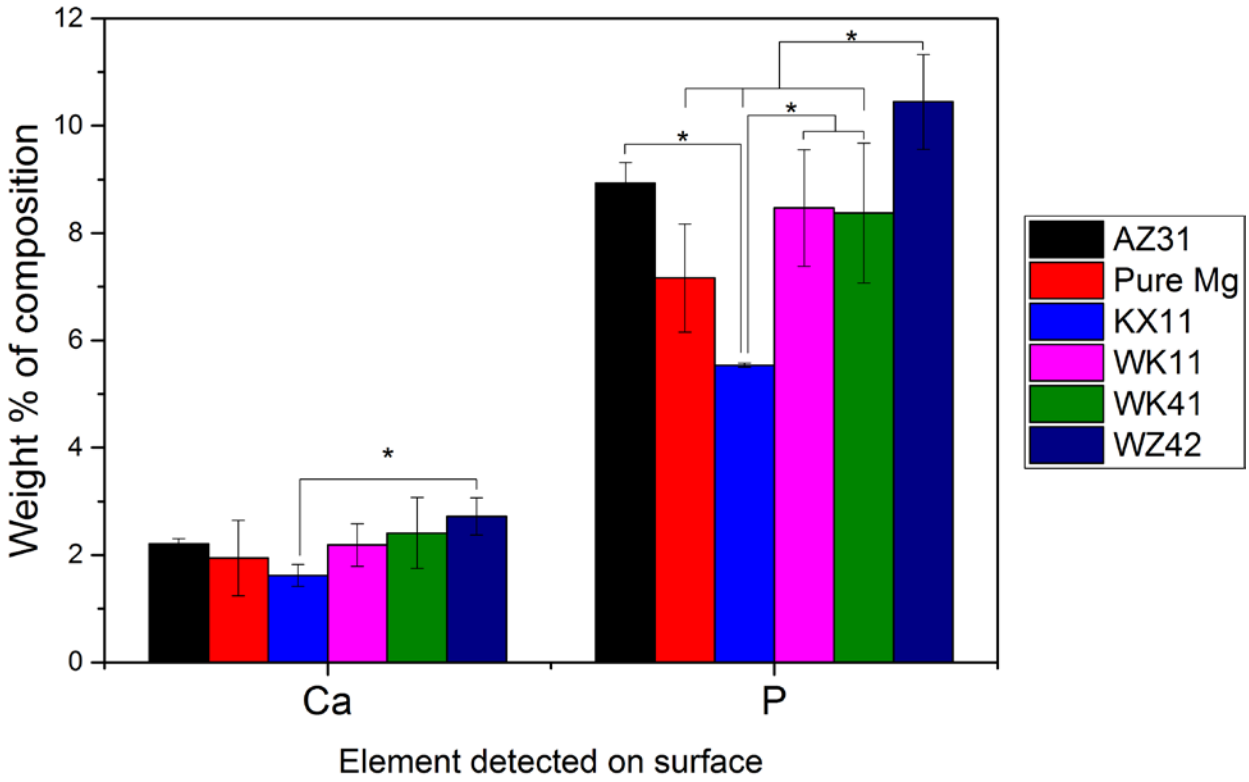

Figure 4.5. Average weight % of Ca and P on the surface of extruded Mg alloy samples after 3 days culture with MC3T3 cells, as determined by EDX. Groups marked with * were significantly different from one another. n = 4 for each group.

4.3.2 Viability and proliferation of cells indirectly exposed to degradation products of Mg-Y-Ca-Zr based alloys

Figure 4.6 shows the indirect cytotoxicity results of WX11 samples performed using MC3T3-E1 cells and the MTT assay. For both culture periods, cell viability was expectedly most reduced with 100% extract concentration, and increased as the extract percentage decreased. After 1 day of culture with extracts (Figure 4.6a), no cytotoxicity was observed for 25% and 10% extract concentrations as no reduction in cell viability was observed. After 3 days of culture (Figure

4.6b), the cell viability was reduced to above 70% at 25% and 10% extract concentrations. This is consistent with findings that show high extract concentrations are cytotoxic and lead to osmotic shock, suggesting that a 10-fold extract dilution be used as an indicator for acceptable cytocompatibility response for as-cast magnesium materials [182]. WX11 as-cast also displayed significantly higher cell viability at 50% extract concentration compared to WX11 T4, WX41 as-cast, WX41 T4, and pure Mg after 1 day and 3 days in extract media. After 1 day of culture with extract, however, WX11 and WX41 as-cast and T4 treated alloys showed significantly higher cell viability compared to pure Mg at 25% extract concentration, though no difference between them could be observed after 3 days of culture.

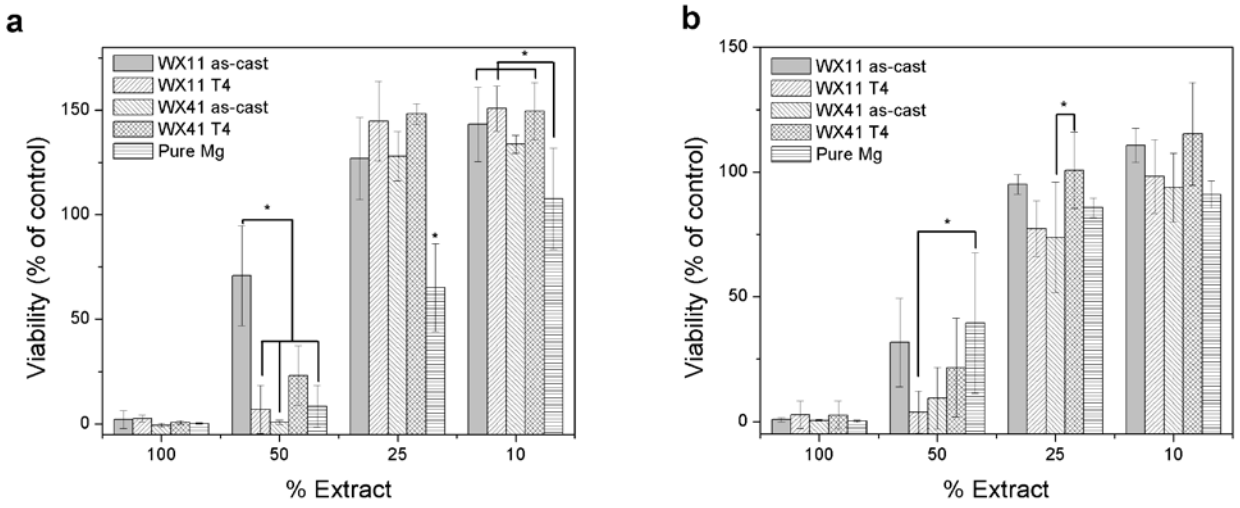

Figure 4.6. Viability of MC3T3 cells cultured for a) 1 day and b) 3 days in extract media from as-cast and T4 heat treated WX11 and WX41 alloys and as-cast pure Mg. Significant difference ($p < 0.05$) between * and other groups or as connected. n = 5 per extract concentration per group per time point.

The MTT assay conducted with MC3T3 cells with extract from extruded alloys (Figure 4.7) displayed low toxicity of the alloy extract, with at least 70% cell viability observed for all extract dilutions. Reduction of cell viability by more than 30% is considered a cytotoxic effect according to EN ISO 10993:5, thus the alloys may be considered non-cytotoxic. Comparing the alloys, WK11 and WK41 were observed to cause slightly reduced viability after 3 days culture at 100% extract concentration, though viability was restored after 3 days of culture.

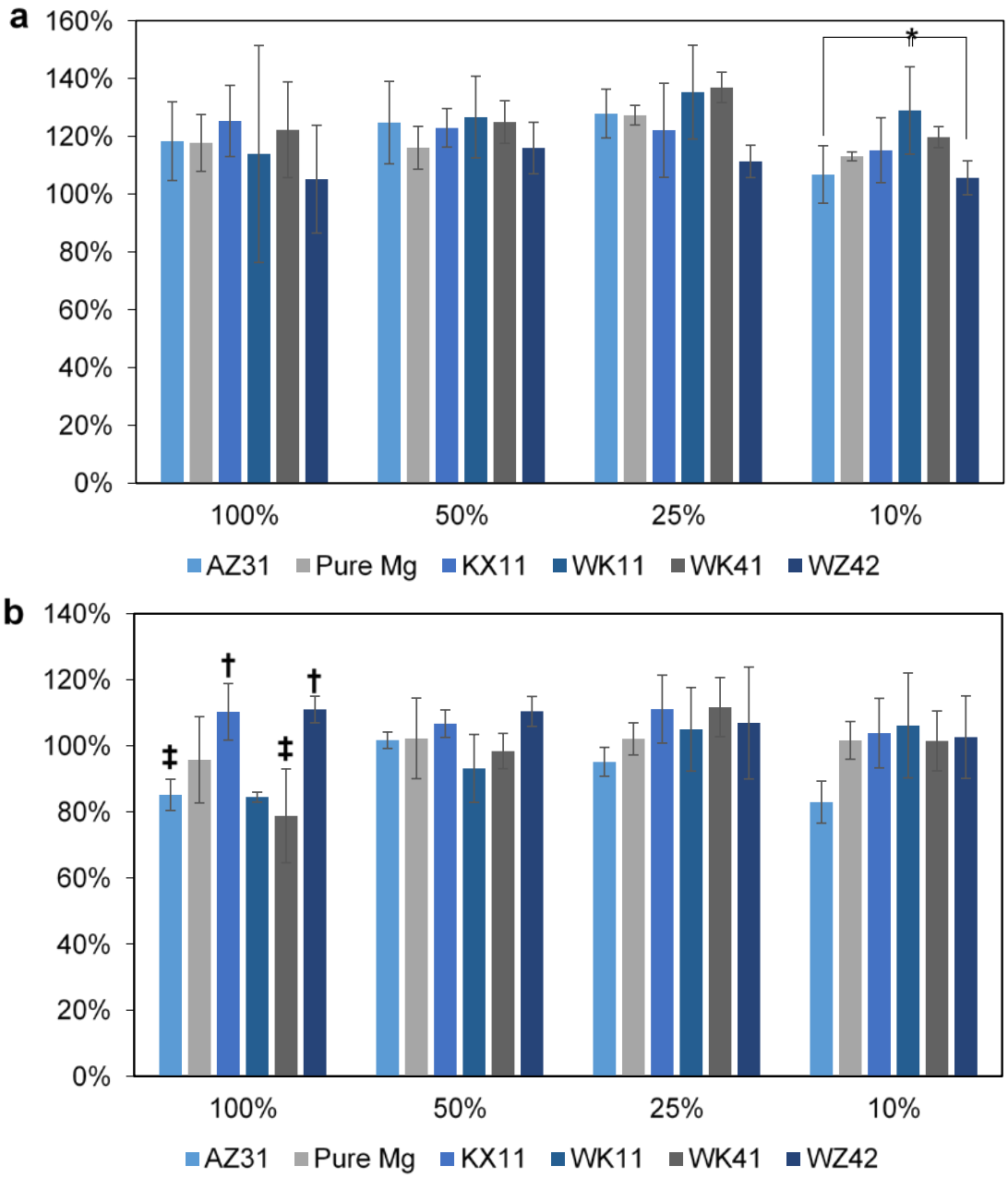

Figure 4.7. Viability of MC3T3 cells cultured for a) 1 day and b) 3 days in extract media containing degradation products from extruded alloys and commercial AZ31 and pure Mg. Groups labeled * significantly different ($p < 0.05$) from one another. Groups labeled with † significantly different ($p < 0.05$) with groups labeled with ‡. n = 4 per extract concentration per group per time point.

4.3.3 Proliferation of pre-osteoblasts and human mesenchymal stem cells indirectly exposed to degradation products of Mg-Y-Ca-Zr based alloys

Proliferation of MC3T3 cells was assessed using the CyQUANT assay which utilizes the PicoGreen fluorochrome to bind to dsDNA to indicate relative levels of proliferation. After 3 days culture of MC3T3 cells with extruded alloy extracts (Figure 4.8), proliferation was again most reduced with 100% extract concentration, and increased as the extract percentage decreased. With 100% extract concentration, WZ42 yielded significantly higher proliferation compared to the other groups. All the alloys displayed similar proliferation at all other concentrations. However, the extract collected from extruded AZ31 obtained commercially resulted in reduced proliferation compared to other groups when diluted to 1% and 0.1 % while the AZ31 made in-house and extruded to the 10:1 ratio indicated much higher proliferation than commercial AZ31 and similar to the other Mg alloys. Fluorescent images showing cells incorporating the DNA-binding dye are shown in Figure 4.9, confirming the stable proliferation of cells exposed to alloy extract, with generally higher cell density with decreasing extract concentration.

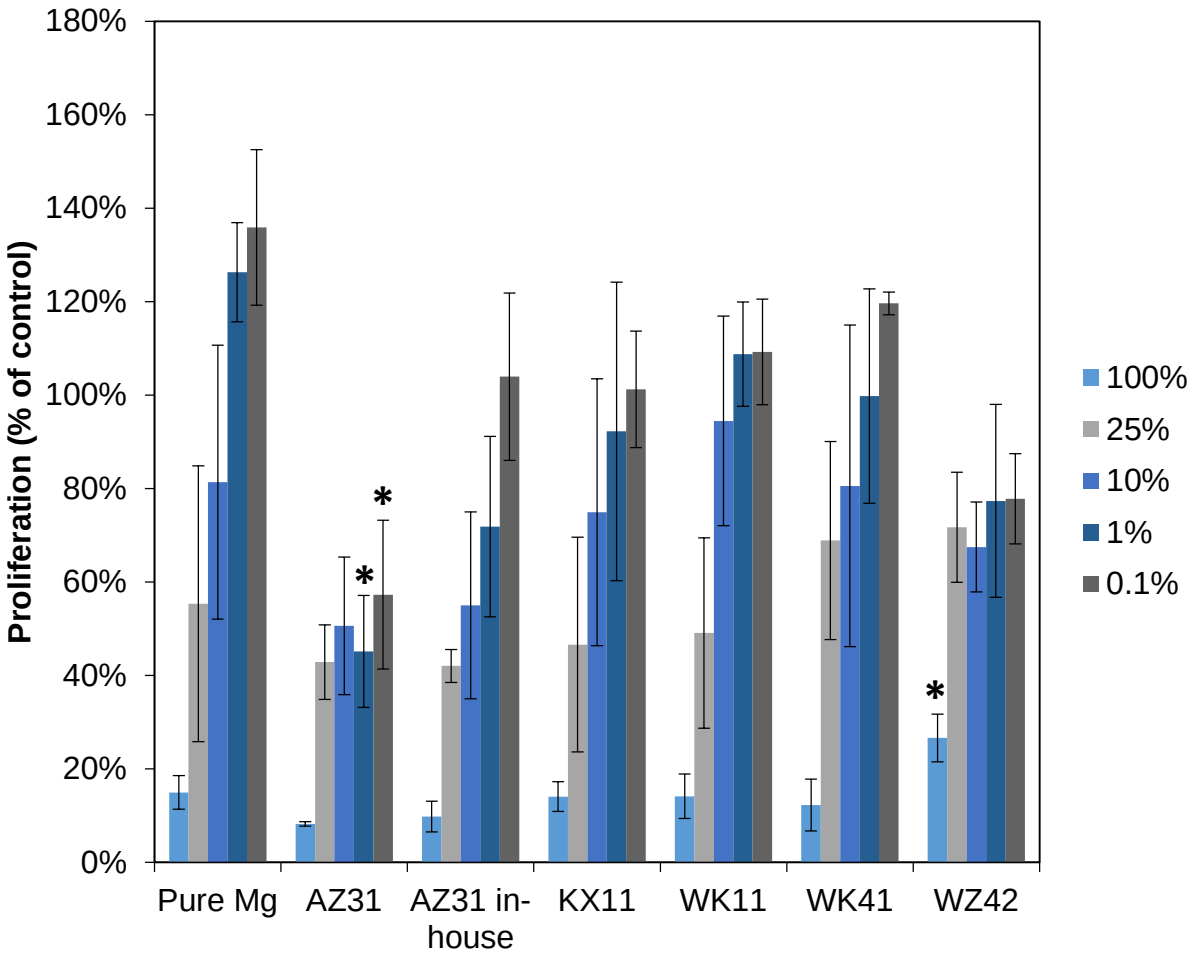

Figure 4.8. Proliferation of MC3T3 cells cultured for 3 days with extruded alloy extracts of AZ31, KX11, WK11, WK41, and WZ42 diluted to 25%, 10%, 1%, and 0.1%, compared to commercial pure Mg and AZ31 as a percentage of control cells cultured with regular extract media. Groups labeled * significantly different ($p < 0.05$) from other groups at same extract concentration. n = 4 per extract concentration per group per time point.

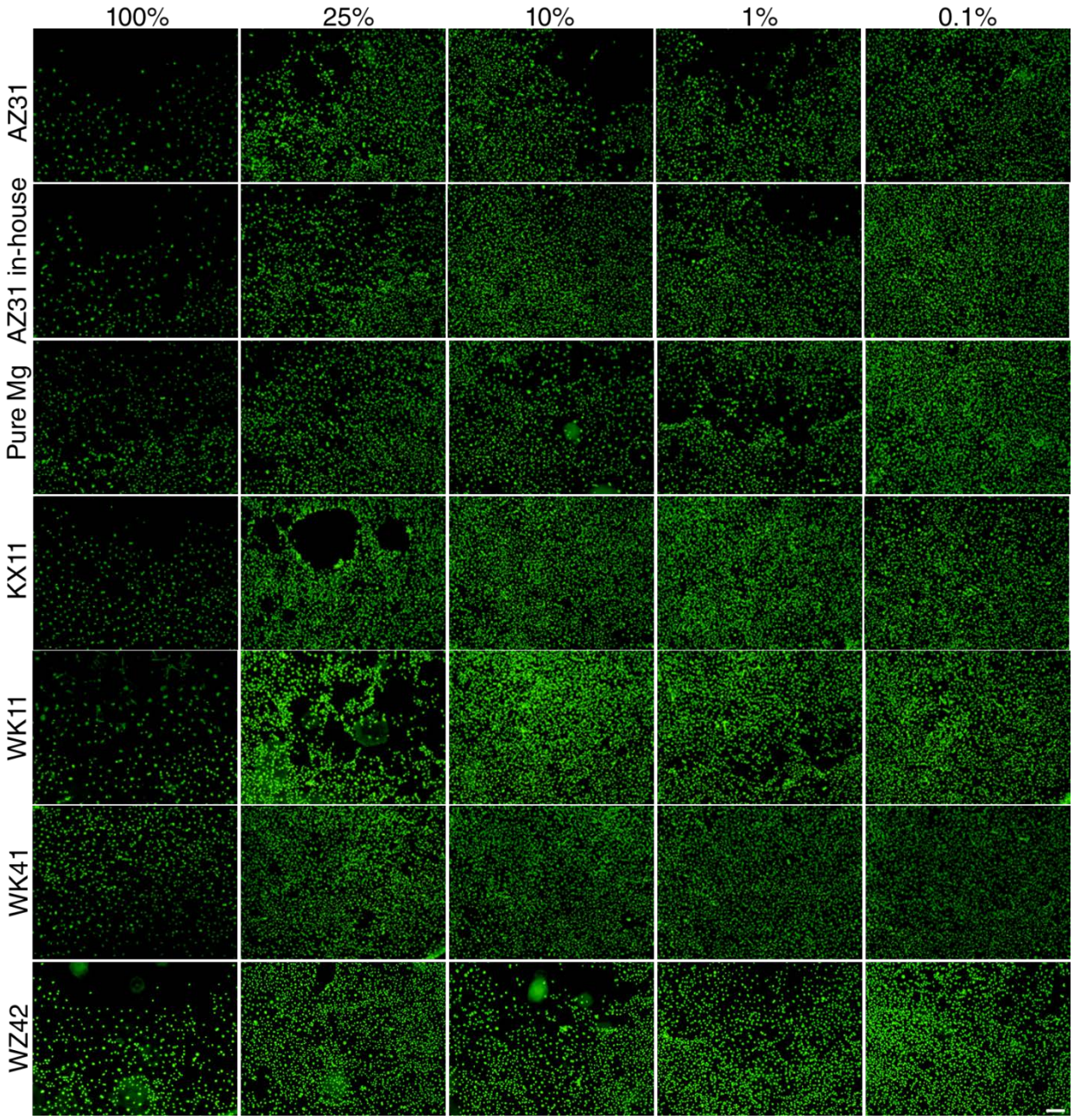

Figure 4.9. Florescence images of MC3T3 cells exposed to extruded alloy extracts diluted to 25%, 10%, 1%, and 0.1%, after 3 days culture with DNA bound to the CyQUANT dye. Scale bar (lower right, same for all images) = 200 µm.

Cell proliferation was also tested using hMSCs for 1, 3, and 5 days culture (Figure 4.10). For the alloys tested, near or above 100% proliferation compared to the growth media control without extract was observed for all the three time points. Cell number was also significantly higher compared to that of AZ31 after 1 day culture and at 100% extract concentration after 3 and 5 days culture. Fluorescent images showing cells incorporating the DNA-binding dye after 5 days culture are shown in Figure 4.11, confirming the attachment of proliferating of cells exposed to alloy extract.

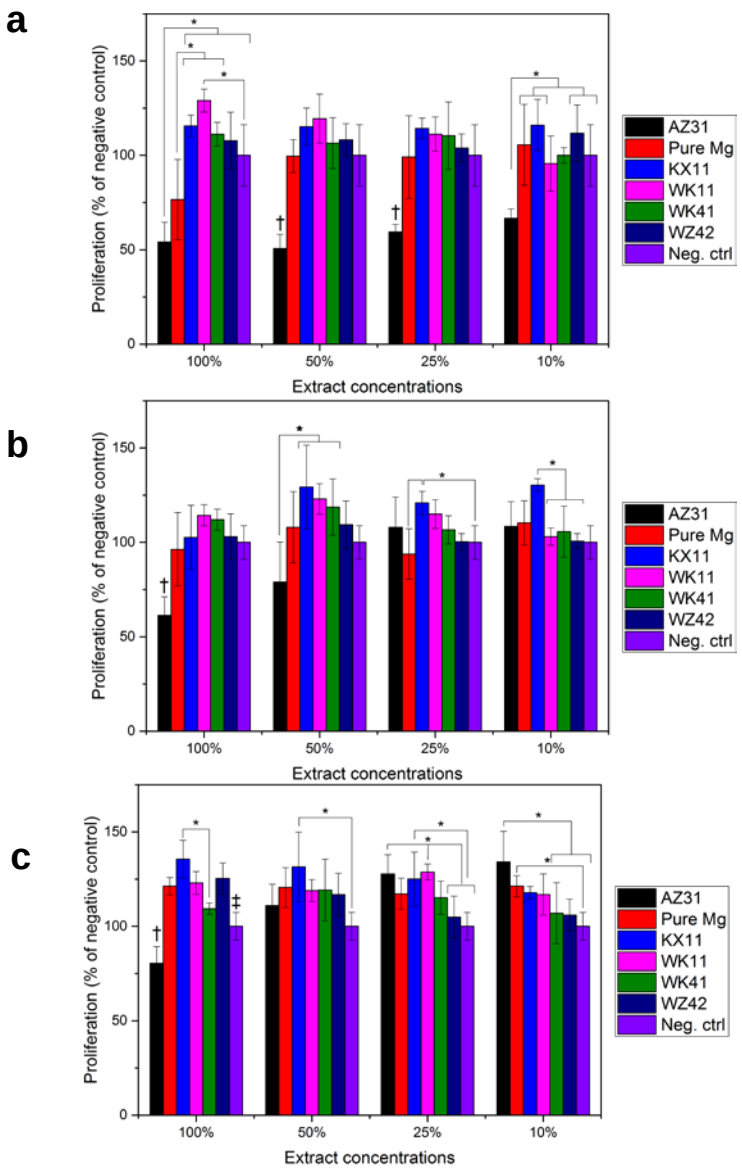

Figure 4.10. Proliferation of hMSCs cultured for a) 1 days, b) 3 days, and c) 5 days with extruded alloy extracts diluted to 50%, 25%, and 10% of AZ31, KX11, WK11, WK41, AND WZ42, compared to commercial pure Mg and AZ31 as a percentage of control cells cultured with regular extract media. Groups labeled * significantly different ($p < 0.05$) from one another. Groups labeled with † significantly different ($p < 0.05$) from all other groups at that time point. Groups labeled with ‡ significantly different from all other groups at that time point except WK41. n = 4 per extract concentration per group per time point.

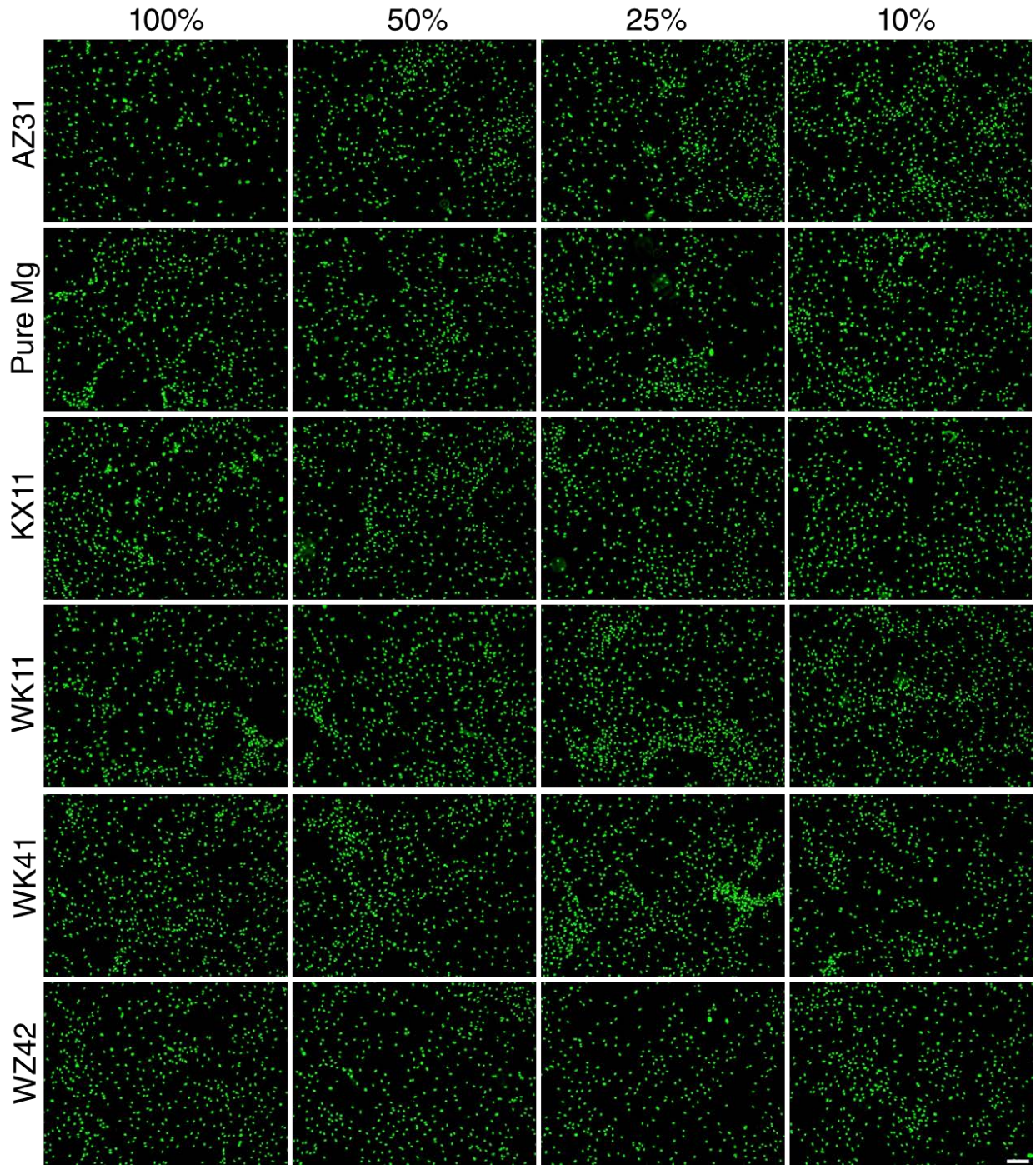

Figure 4.11. Florescence images of hMSCs exposed to extruded alloy extracts diluted to 50%, 25%, and 10% after 5 days culture with DNA bound to the CyQUANT dye. Scale bar (lower right, same for all images) = 200 μm.

4.3.4 Differentiation of human mesenchymal stem cells indirectly exposed to degradation products of Mg-Y-Ca-Zr based alloys

Human mesenchymal stem cells (hMSCs) were exposed to degradation products of the Mg alloys as collected in growth media and their ALP activity was accordingly compared to cells cultured in fresh growth media and differentiation media (Figure 4.12) after 3 days, 7 days and 14 days of culture with extracts. Higher ALP activity with lower concentration of extract was observed overall, with the highest ALP activity of the hMSCs occurring when exposed to 10% extract media. The ALP activity in cells exposed to Mg alloy extracts at lower concentrations of 10% and 25% remained similar to that of cells cultured with regular growth media after 3 days, while all groups demonstrated lower ALP activity than cells cultured in differentiation media, as expected. After 3 days, no difference in the ALP activity between the alloy extracts was observed. Higher ALP activity with the Mg alloy WZ42 was observed at 50%, 25%, and 10% extract concentration compared to commercial AZ31 and pure Mg at 7 days. After 14 days culture, no significant difference in ALP activity between the alloy extract groups and the growth media control were observed.

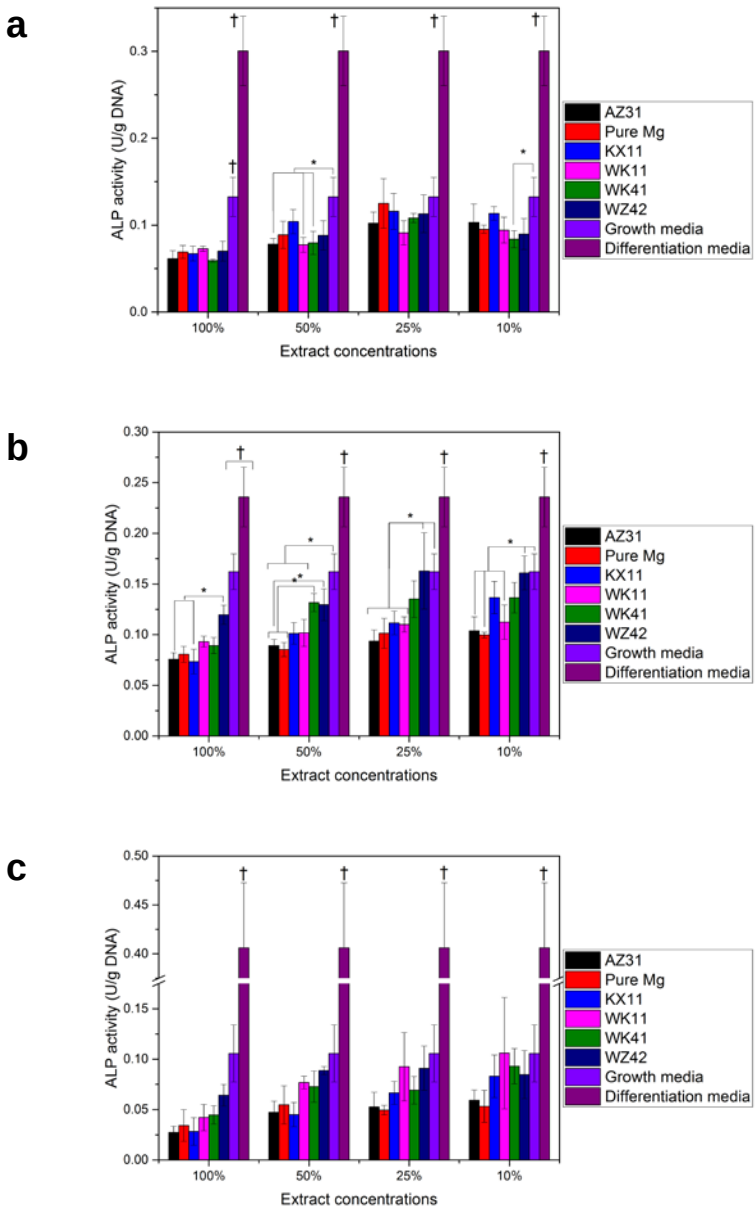

Figure 4.12. ALP quantification (normalized with DNA) using hMSCs in indirect method for extruded Mg alloys after a) 3 days, b) 7 days, and c) 14 days of culture with extracts diluted to 50%, 25%, and 10%. GM = growth media control; DM = differentiation media control. Groups labeled * significantly different ($p < 0.05$) from one another. Groups labeled with † significantly different ($p < 0.05$) from all other groups at that time point. n = 4 per extract concentration per group per time point.

Osteogenic differentiation markers based roughly on their stages of upregulation in differentiating mesenchymal stem cells - early (RUNX2), middle (ALP), and late stage (OCN), were measured to determine the effect of the degradation product of the Mg alloys on differentiation of hMSCs following 7 days, 14 days and 21 days exposure to 10% dilution extracts collected in hMSC differentiation media (Figure 4.13). WZ42 was the only alloy observed that appeared to result in upregulation of osteogenic markers, with higher fold increase compared to cells cultured in differentiation media without extracts of ALP after 7 days and 21 days culture, with higher osteocalcin expression observed after 14 days. Severe downregulation of osteocalcin, the late stage osteogenic differentiation marker at 14 and 21 days was observed in cells exposed to extract products of AZ31 and pure Mg. Relative to these controls materials – AZ31 and pure Mg, the novel alloys tested displayed upregulation of RUNX2 after 7 days, ALP after 14 days (except for WK11), and OCN after 21 days. However, this study was only completed with n = 1 and additional experiments with large sample sizes is necessary.

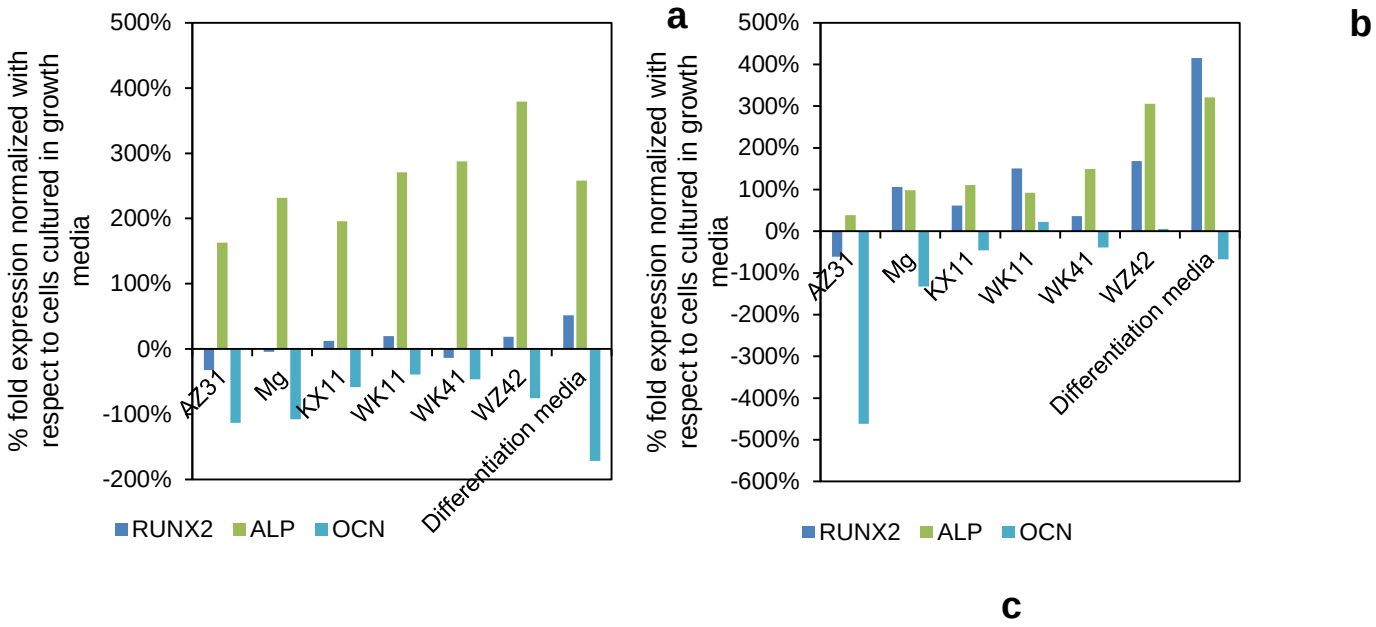

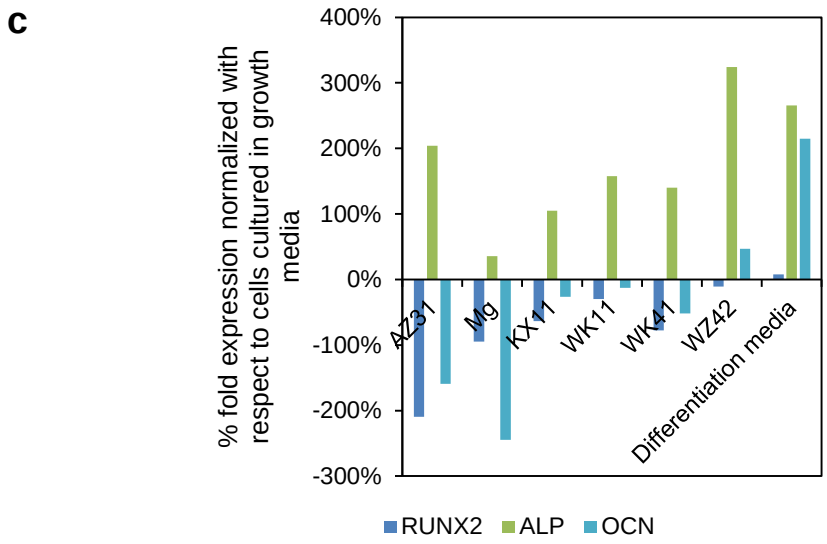

Figure 4.13. qRT-PCR gene expression data showing the expression of RUNX2, ALP, and OCN hMSCs cultured for a) 7 days, b) 14 days), and c) 21 days with 10% extracts diluted in differentiation media normalized with respect to cells cultured in growth media and compared to differentiation media group where media did not contain extracts. n = 1 for all groups.

4.3.5 Proliferation of human mesenchymal stem cells exposed to salts of Mg, Y, Ca, Zr, Zn, and Al

hMSCs cultured with chloride salts in growth media of Mg (in concentrations of 50 mM, 20 mM, 10 mM, and 1 mM) and Y, Ca, Zr, Zn, and Al (in concentrations of 1 mM, 0.1 mM, 0.01 mM, and 0.001 mM) were assessed for proliferation using the CyQUANT assay after culture for 1, 3, and 5 days and normalized with respect to regular growth media. After 1 day culture (Figure 4.14a), proliferation in the presence of Ca, Y, Zr, and Al was generally unaffected by the presence of the metal salts at all concentrations. For Mg and Zn, the upper concentrations tested (50 mM for Mg and 1 mM for Zn) both exhibited reduced proliferation of the hMSCs though this

was restored with further dilution. At 3 days of culture (Figure 4.14b), again high concentration of Mg and Zn reduced cell number, but an increase in cell number was observed at higher concentrations of Y, Zr, and Al. These trends were also retained after 5 days of culture. The dyed cells were imaged and shown in Figure 4.15, confirming the differences in cell numbers quantified in Figure 4.14.

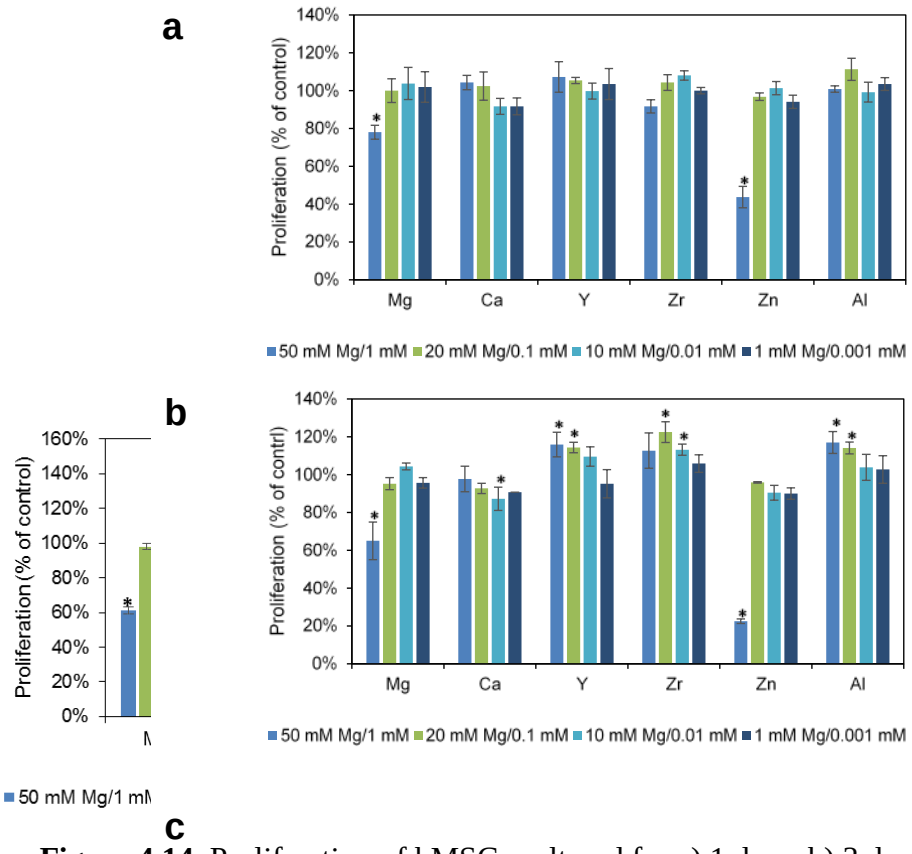

Figure 4.14. Proliferation of hMSCs cultured for a) 1 days, b) 3 days, and c) 5 days with chloride salts of Mg (in concentrations of 50 mM, 20 mM, 10 mM, and 1 mM) and Y, Ca, Zr, Zn, and Al (in concentrations of 1 mM, 0.1 mM, 0.01 mM, and 0.001 mM) dissolved in growth media, as a percentage of control cells cultured with growth media and differentiation media. Groups labeled * were significantly different ($p < 0.05$) from control cells cultured in fresh growth media. n = 3 per extract concentration per group per time point.

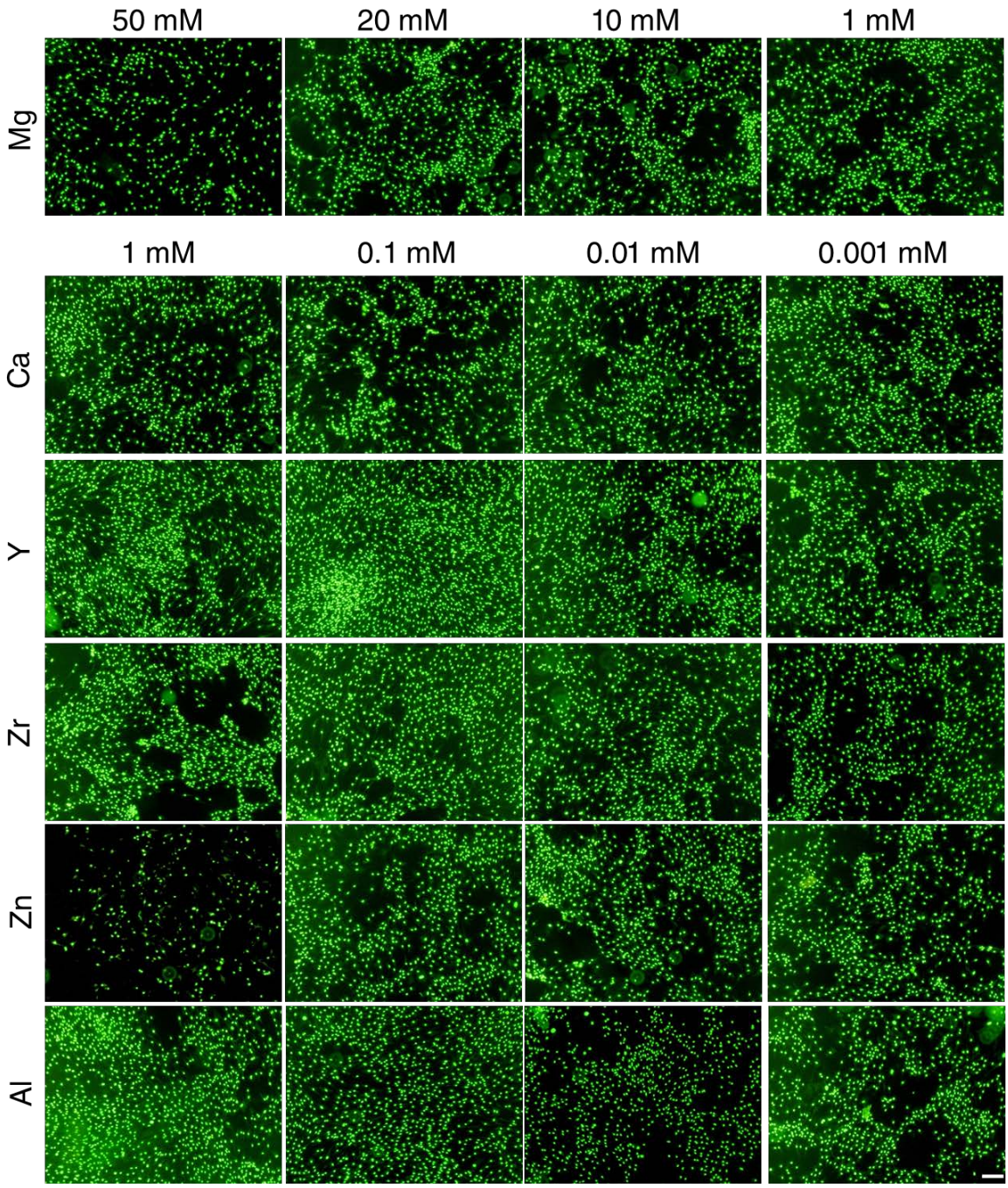

Figure 4.15. Florescence images of hMSCs exposed to alloying element chloride salts of Mg (in concentrations of 50 mM, 20 mM, 10 mM, and 1 mM) and Y, Ca, Zr, Zn, and Al (in concentrations of 1 mM, 0.1 mM, 0.01 mM, and 0.001 mM) dissolved in growth media after 5 days culture with DNA bound to the CyQUANT dye. Scale bar (lower right, same for all images) = 200 μm.

4.3.6 Differentiation of human mesenchymal stem cells exposed to salts of Mg, Y, Ca, Zr, Zn, and Al

ALP activity of hMSCs exposed to metal salts of elements present in the Mg alloys was compared to cells cultured in fresh growth media and differentiation media (Figure 4.16) after 14 days culture. Compared to growth media, the diluent in which the salts were dissolved into, Mg at 20 mM and 10 mM, Ca at 0.01 mM, and Zn at 1 mM resulted in cells with higher ALP activity than growth media and similar to that of hMSCs cultured in differentiation media. High concentration of Al (1 mM and 0.1 mM) reduced cellular expression of ALP.

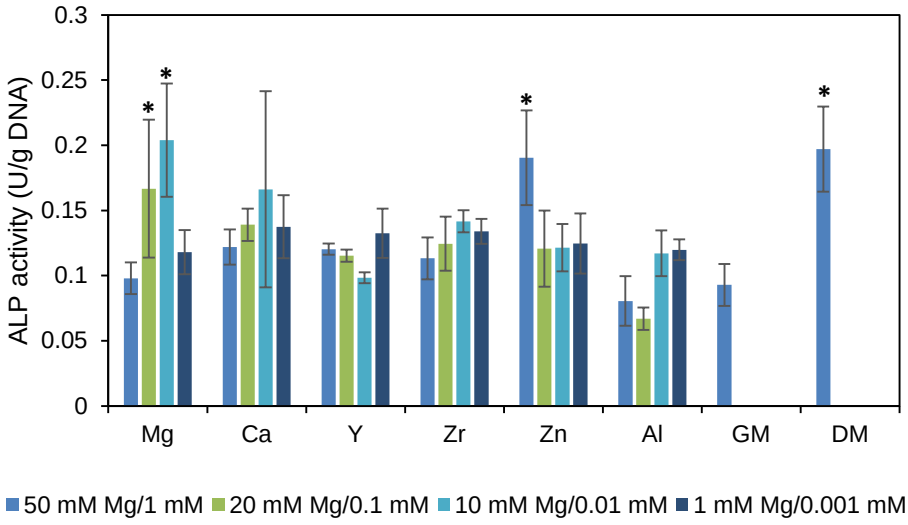

Figure 4.16. ALP quantification (normalized with DNA) using hMSCs in culture with chloride salts of Mg (in concentrations of 50 mM, 20 mM, 10 mM, and 1 mM) and Y, Ca, Zr, Zn, and Al (in concentrations of 1 mM, 0.1 mM, 0.01 mM, and 0.001 mM) dissolved in growth media for 14 days. Significant difference between groups labeled * and growth media control ALP activity. GM = growth media control; DM = differentiation media control. n = 3 per extract concentration per group per time point.

4.3.7 In vivo murine subcutaneous study

H&E staining of the local site of implantation of Mg-Y-Ca-Zr as-cast alloys, pure Mg, and AZ31 in the subcutis of nude mice is shown in Figure 4.17a-l. Minimal toxicity of the implanted alloys to the surrounding tissue was observed, while the region surrounding the implants appeared to be undergoing normal tissue repair. No significant accumulation of inflammatory cells was observed, whereas a layer of tissue composed of pink-stained collagen fibers and reactive

fibroblasts was seen after 7 days. At this time point, a relatively high density of fibroblasts in tissues adjacent to as-cast WX11 and WX41 alloy pellets suggests their presence did not inhibit the normal healing response in the implantation site. After 40 and 70 days implantation, dense collagenous connective tissue was seen surrounding the location of the Mg implants, without the presence of a high density of chronic inflammatory cells. Normal adipocytes could be faintly distinguished past the dermis.

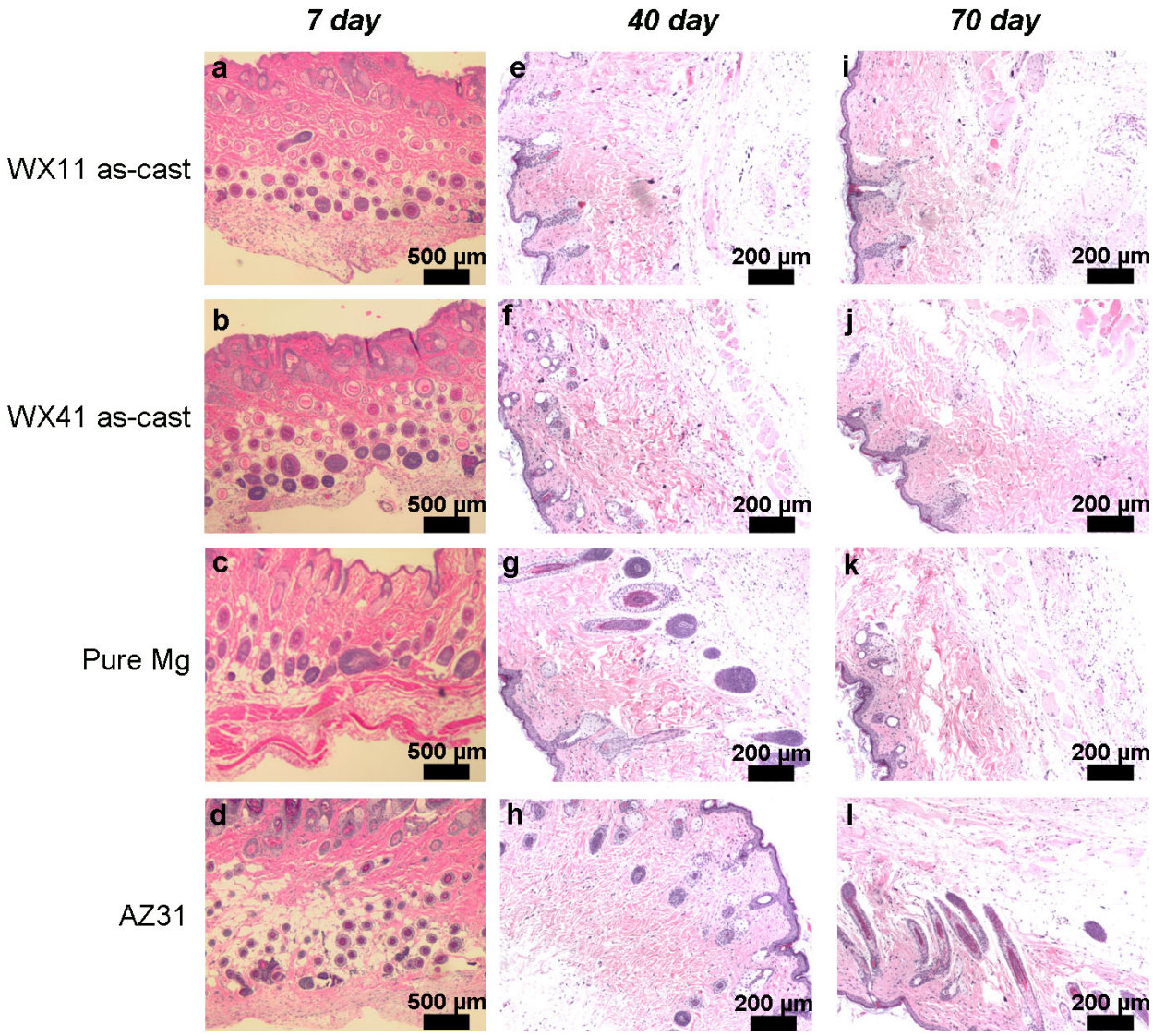

Figure 4.17. a-l) Histology images (H&E staining) of the skin above the implants of a, e, i) WX11 and b, f, j) WX41 as-cast alloys, c, g, k) pure Mg, and d, h, l) AZ31 after 7 days (a-d), 40 days (e-h), and 70 days (i-l) in the subcutis of nude mice.

In vivo corrosion as determined through mass loss (Figure 4.18) of as-cast WX41 was much lower than as-cast WX11 and similar to pure Mg and slightly higher compared to AZ31

after 70 days. This result is consistent with the *in vitro* corrosion behavior of the Mg-Y-Ca-Zr alloys, in which the higher Y-containing alloy, WX41, corroded more slowly than WX11.

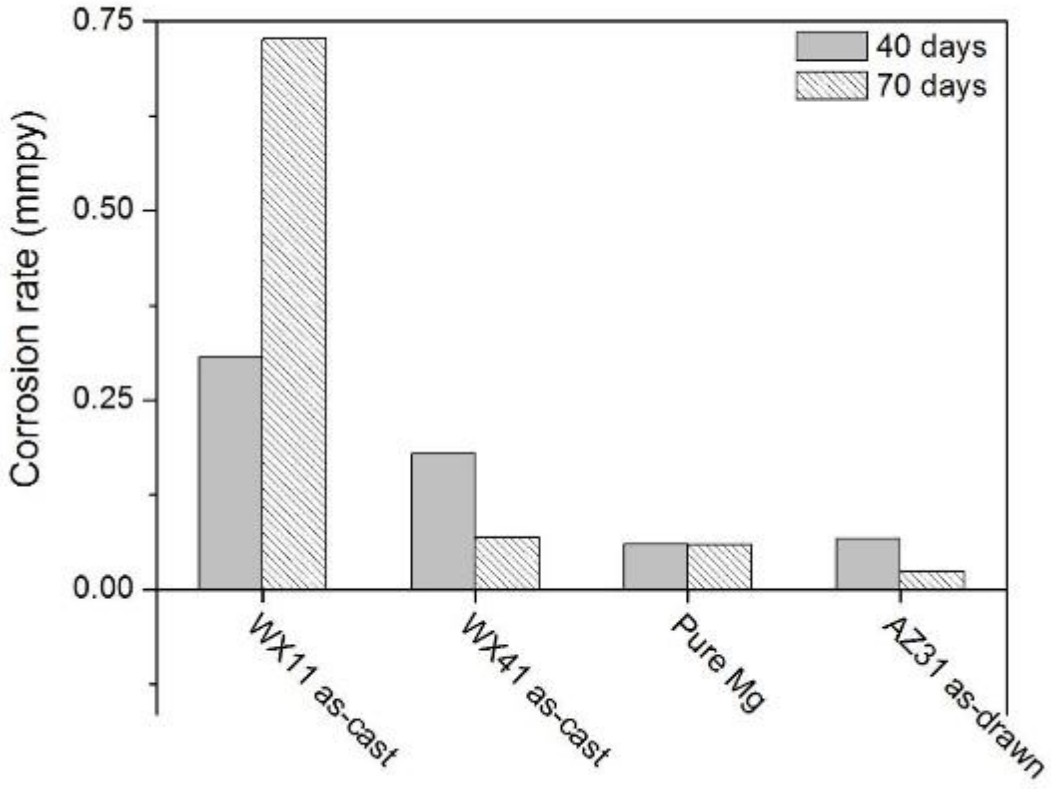

Figure 4.18. Corrosion rate as calculated by mass loss of pellet samples before and after murine subcutaneous implantation at time points of 40 and 70 days. n = 1 for each group.

The samples explanted after 70 day implantation were dried and imaged using SEM to assess the corrosion products formed (Figure 4.19) in comparison to those formed after static immersion (Figure 3.3). After *in vivo* corrosion, it can be seen from the elemental maps of the corrosion products, layers rich in C and O were observed to have formed on the alloy surface, similar to results from the immersion study. The cracked corrosion layer was seen to contain

higher Ca and P content compared to agglomerates of corrosion deposits. Removal of corrosion products revealed widespread corrosion resulting in irregular surface topography on all the explanted alloy materials as seen in Figure 4.20.

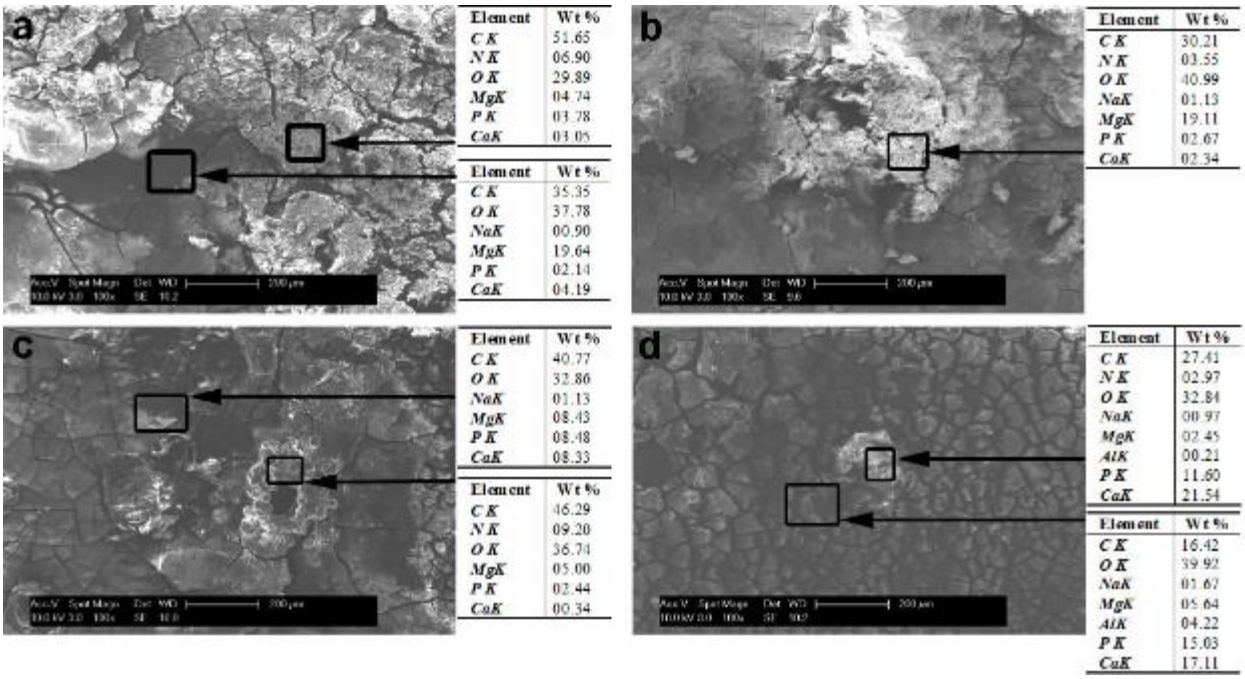

Figure 4.19. SEM images showing surface morphologies of a) WX11 as-cast; b) WX41 as-cast; c) pure Mg; d) AZ31 after 70 days implantation in murine subcutaneous tissue. EDX was performed at various spots as denoted by arrows.

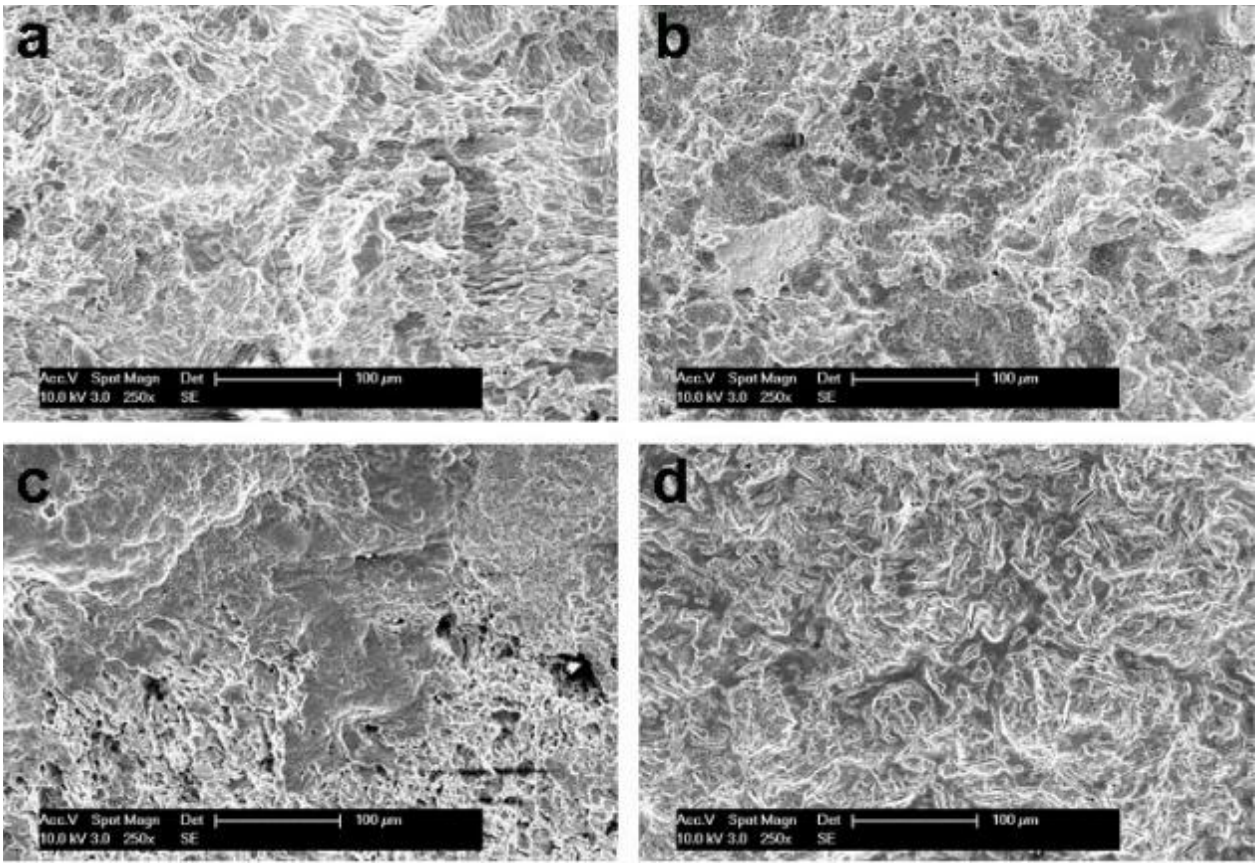

Figure 4.20. SEM images showing surface morphologies of a) WX11 as-cast; b) WX41 as-cast; c) pure Mg; d) AZ31 after 70 days implantation in murine subcutaneous tissue and cleaning with $CrO_3/AgNO_3$ solution.

4.4 DISCUSSION

The alloying elements used in this study have all shown to be biocompatible based on the literature as well as indicated in Table 4.1 showing the daily allowance and toxicity. Y has been shown to be non-toxic in longevity studies [181], non-hepatotoxic [187], and incorporated in alloys which were clinically well-tolerated as an absorbable metal stent [188] and fixation screw for chevron osteotomies in hallux valgus surgeries [95]. Y also has a high affinity for areas of

osteoblastic activity in bone through events leading to organic matrix formation [189] and may promote osteoblast proliferation and differentiation at concentrations of $1 \times 10^{-9} – 1 \times 10^{-4}$ M and 1×10^{-7} M, respectively [190], which may be related to altered vitronectin and collagen conformation and bioactivity [191]. Ca is well-known and an essential component in bone, while requiring Mg for incorporation into bone [192]. Zr ions have low cytotoxicity [176] and zirconium coatings have demonstrated improved osseointegration of metal implants *in vivo* [193]. Effects on *in vitro* cytocompatibility, proliferation, and differentiation from the Mg-Y-Ca-Zr alloys discussed above were determined by 1) exposing murine pre-osteoblast and human mesenchymal stem cells to media containing degradation products of the materials, 2) seeding cells directly onto the alloys and observing live and dead cell densities through the LIVE/DEAD assay, and 3) adding media containing various concentrations of the alloying element salts to the cells.

Figure 4.6 and Figure 4.7 present the results from the MTT assay, in which at high extract concentrations, (100% and 50%), cell viability was reduced in the as-cast and T4 treated alloys of Figure 4.6, as well as with the extruded WK11 alloy in day 1 and WK11 and WK41 alloys at day 3 at 100% extract concentration. This was likely due to reports of high extract concentrations causing cellular osmotic shock, suggesting a 10-fold extract dilution be used as an acceptable dilution for as-cast magnesium materials [182]. Indeed, at lower concentrations of extract (25% and 10% for as-cast and T4 treated WX11 and WX41 alloys and 50%, 25%, and 10% for all extruded alloys), high cell viability was observed for the alloys, indicating higher alloy degradation products resulted in lower cytotoxicity. Higher than 100% cell viability was observed from 25% and 10% extracts of WX11 and WX41 as-cast and T4 treated alloys after 1 day of culture, which may be facilitated by enhanced osteoblast activity in the presence of

corrosion product magnesium hydroxide [194]. Similarly, high density of live cells was observed attached to the surface of the Mg-Y-Ca-Zr alloys in Figure 4.1 and Figure 4.2. By directly culturing cells onto Mg-alloy substrates, this assay qualitatively shows the effect of hydrogen gas production, increased pH levels, and local concentration of corrosion products on cell attachment and viability. The differences observed in the corrosion rate however, did not appear to have bearing on the *in vitro* cytocompatibility results, with all as-cast and T4 treated Mg alloys harboring similar number of attached active cells, while appearing to have lower cell density compared to tissue culture plastic. This is consistent with these alloys' 3 day MTT results at 100% and 50% extract concentrations in which cell viability was lower than the control. The elongated, spread morphology of the adherent cells on the Mg-Y-Ca-Zr alloys after both 1 and 3 days of culture confirmed the cytocompatibility of the alloys, which did not corrode too rapidly to inhibit cell attachment. It appeared that higher densities were present on relatively slower corroding alloys (WK41 and WZ42 compared to KX11), which also were revealed to have higher percentages of Ca and P deposited on their surface where cells were attaching (Figure 4.5). This may indicate a correlation between corrosion stability with higher amounts of CaP deposits forming on the Mg alloy surface allowing for improved osteoblast adhesion and proliferation, as has been observed with CaP coatings on the surface of titanium [195].

In this study, cytocompatibility was conducted using MC3T3-E1 cells with samples immersed in αMEM + 10% FBS, and the presented results may vary with the use of different cell lines and respective cell culture media. Cells cultured in other media such as DMEM may exhibit different cytocompatibility results compared to αMEM, due to the presence of higher L-glutamine content in DMEM, which functions as a chelating agent for magnesium ions [196], potentially causing increased Mg ion release from alloys immersed in DMEM [197]. Thus, the

obtained cytocompatibility results presented here should be solely considered under cell culture conditions using αMEM as opposed to other media such as DMEM or HBSS, which would likely result in a higher corrosion rate of tested alloys, applying a different local environment to cultured cells.

Proliferation of the extruded alloys was also measured using the CyQUANT assay of DNA quantification. Proliferation was reduced with higher concentration of Mg alloy extract in Figure 4.8 similar to reduced viability seen in the MTT assay of Figure 4.6. hMSC proliferation on the other hand, was higher than MC3T3 cells in the presence of extract media, suggesting greater tolerance of hMSCs compared to MC3T3 cells. With hMSCs after 5 days of culture, proliferation was higher than cells cultured in regular growth media. Li et al [198] observed increase in hMSC proliferation with Mg-1Y (wt.%) alloy having a superior effect on proliferation compared to Mg-2Ca alloy. The increased proliferation was influenced via SMAD-dependent signaling pathway, with the largest increase in SMAD4 observed in the Y containing alloy. Y^{3+} ions also promoted the proliferation of mouse osteoblasts [190]. However, AZ31 resulted in reduced proliferation of both MC3T3 cells and hMSCs, with this negative effect on cell viability also being observed by other groups studying both AZ31 and AZ91 [199]. Little induction of differentiation due to the presence of Mg alloy extract media was observed as measured by ALP activity (Figure 4.12) and RUNX2, ALP, and OCN expression (Figure 4.13), with WZ42 alloy demonstrating a higher propensity compared to the other Mg alloy and pure Mg groups studied for promoting osteogenic differentiation. This may be due to this alloy containing a combination of Y – which promotes differentiation into osteoblast at low concentrations [190], while also including Zn excluded in the other alloys – which stimulates ALP activity and collagen concentration when tested with concentrations between 1 and 25 μM

[200]. Mg-Y also was found to increase levels of ALP in hMSCs by Li et al [198] compared to other Mg alloys and pure Mg. These encouraging findings regarding WZ42 corroborated the data from Specific Aim 2 to use this alloy for the animal model in the next aim.

In order to elucidate the effects of alloy addition to cells, it was also considered that each alloying element in the form of chloride salt be dissolved individually in media to use for cell culture and evaluation. It was found that in the range of concentrations tested (0.001 mM – 1 mM) of Ca, Y, Zr, and Al, cell proliferation was not affected, while at high concentrations of Mg (50 mM) and Zn (1 mM), proliferation was reduced, though upon further dilution the reduction in proliferation was restored. The 50 mM Mg concentration was above that of 10 mM Mg ions that Hallab et al [201] observed to result in in approximately 50% reduction in viability of MG-63 osteoblasts. The 1 mM Zn concentration also was above the IC50 of 0.09 mM for MC3T3 and L929 cells reported by Yamamoto et al [176]. Yamamoto also reported that the MC3T3 cell IC50 for Zr as 2.83 mM and for Al as 2.92 mM, above the maximum 1 mM used, resulting in no loss in proliferation. The IC50 for MC3T3 cells exposed to Y however, was 0.142 mM. In the present study, as seen in Figure 4.10, the 1 mM concentration Y salt did not cause a decrease in hMSC proliferation.

Promotion of osteoblastic differentiation of hMSCs due to alloying element salts was also investigated, which concluded that Mg at concentrations of 10 – 20 mM resulted in increased ALP activity from cells in the differentiation media. Yoshizawa et al [202] observed that 5 and 10 mM $MgSO_4$ concentration enhanced mineralization of ECM from human bone marrow stromal cells (hBMSCs) with maximum promotion of osteogenic factors at 10 mM Mg via HIF-2α and PGC-1α. The increase in activity for Zn at 1 mM concentration may not be indicative of a

positive effect on differentiation due to the reduction in cell number that resulted from Zn addition as seen in Figure 4.14, since ALP activity is normalized to DNA quantity.

Variations in the various *in vitro* cell tests conducted in this specific aim may be due to a number of factors. First, cell number may have varied from well to well, while variations in alloy sample dimensions and surface finishing may have deviated resulting in differences in the local environment of degradation products that cells were exposed to. Variations in pipetting volume of reagents and media may also have caused slight experimental error, as well as the method of measurements such as the microplate reader.

Past studies have shown acceptable host response and biocompatibility of RE-containing Mg alloys upon *in vivo* implantation [203]. Subcutaneous implantation of Mg–1.5%Nd–0.5%Y–0.5%Zr alloys with and without 0.4%Ca demonstrated adequate Mg metabolism, renal function, and host-tissue response as the Ti-6Al-4V control implant [204]. The murine subcutaneous study was conducted here in order to compare the *in vivo* corrosion and local tissue response of the selected materials: WX11 as-cast, WX41 as-cast, pure Mg, and AZ31. Histological slides stained using H&E (Figure 4.17) showed the Mg-Y-Ca-Zr alloys did not introduce toxicity or excessive inflammatory response to the surrounding tissue, presenting an acceptable host response with natural wound healing occurring as seen in the presence of a high density of fibroblasts which deposit collagen fibers in order to form new extracellular matrix during the tissue repair process [205]. This dense connective tissue was observed adjacent to the Mg alloy implants at all time points, indicating biocompatibility at varying magnitudes of alloy degradation. The *in vivo* mass loss corrosion rates (Figure 4.18) of the tested Mg alloys were lower than those measured from *in vitro* immersion. Witte et al. [206] concluded that i*n vitro* corrosion tests could not accurately predict *in vivo* corrosion rates after observing a four order of magnitude reduction of corrosion

rate *in vivo* compared to *in vitro*. Different environmental conditions, dynamic blood flow around the implant, and variations in pH as well as the local chemical environment of buffering ions could also be among reasons that could be provided to explain the discrepancy. The lower corrosion rates measured *in vivo* versus *in vitro* was in agreement with studies of Mg alloys implanted intramedullary in guinea pig femurs [206] and in a subcutaneous environment in Lewis rats [207]. Explanted samples displayed the formation of similar corrosion products and morphology to samples from immersion testing. After 70 days implantation, the extent of *in vivo* corrosion is clearly greater than after 3 weeks *in vitro*, as can be construed from the SEM images of the surfaces seen in Figure 4.19 and Figure 4.20. At the same time, corrosion products rich in C and O with the presence of Ca and P were still identified. The corrosion product morphology of a cracked corrosion layer with corrosion products deposited on top as seen both *in vitro* and *in vivo* is in agreement with results found in other studies [207, 208].

Nonetheless, *in vivo* corrosion rate following 40 and 70 days of implantation for as-cast WX41 was lower than as-cast WX11 and comparable to pure Mg and AZ31 after 70 days, which was consistent with the measured *in vitro* corrosion rates (Figure 3.1). This result is in agreement with established knowledge that while *in vitro* corrosion tests currently cannot accurately predict those seen *in vivo*, they may serve as a relatively inexpensive screening method to assess the relative corrosion resistance of Mg alloys. It can therefore serve to select alloys that could potentially yield a favorable response *in vivo* since a faster corroding alloy composition compared to a more stable system could likely also display faster corrosion under *in vivo* conditions. On an absolute scale, it may not be easy to derive the same conclusions due to the various factors of materials as well as the local chemical and biological environments that can affect the corrosion response of a given magnesium alloy.

5.0 SPECIFIC AIM 4: ASSESS THE IN VIVO CORROSION, BONE FORMATION, AND HOST RESPONSE OF MAGNESIUM-YTTRIUM-ZINC-CALCIUM-ZIRCONIUM ALLOY IN A RAT FEMUR OSTEOTOMY MODEL

5.1 INTRODUCTION

As discussed in earlier Chapters, magnesium based alloys have received the most attention in the medical products space for use in orthopedic applications ever since its reintroduction into biomedical research this millennium. Numerous studies in small animals (e.g. mice, rats, guinea pigs, and rabbits), large animals (e.g. sheep and goats), as well as humans have overall shown the good biocompatibility of magnesium alloys when implanted within in or surrounding bone. This combined with the high strength to weight ratio of Mg and its ability to degrade, thus reducing the need for secondary removal surgeries as conducted for permanent metallic hardware, have made Mg and Mg alloys an attractive option that is poised to be at the forefront to challenge the dominance of the current state of the art inert metallic and degradable polymeric orthopedic device landscape. Other important properties of magnesium that have been demonstrated include enhanced bone formation adjacent to or near the Mg alloy, high deposition of Ca-P minerals, and direct contact between the degradation product layer of Mg and new bone [154].

Of the various studies involving implantation of Mg alloys into bone, the vast majority comprised implanting rods, pins, or screws of Mg alloys into the femoral diaphysis (~8), with a

few in the femoral condyle and marrow cavity [154]. None of the 23 papers reviewed by Zheng et al [154] wherein Mg alloy was implanted into the bone, none represented a load bearing model, in every case a hole was predrilled into the bone with the implant then either press fit or screwed into place. The only cases in which a Mg implant was used to bear load to provide fixation for fractured bone was the plate and screw studies conducted by Chaya et al [127, 179]. In these studies, a full fracture was created in the ulna of New Zealand white rabbits with holes predrilled into the two sides of the fractured ulna to allow for placement of the plate and screw to stabilize the fracture. Despite these studies being the only assessments of a loaded fracture environment evaluating Mg orthopedic implants, all the rabbit radii were left intact during healing, which provided additional support to the fracture, supplementing that of the plate and screw.

In this study, it was decided to pursue a fully load bearing model where a full fracture of the rat femur was only fixed using implant pins of the Mg alloy Mg-Y-Zn-Zr-Ca (WZ42), whose materials and biological characteristics have been described in the preceding chapters, and compared to performance of the common medical titanium alloy, Ti6Al4V. This model selected has conceptual similarities mimicking orthopedic fixation devices such as Kirschner wires (K-wires) and Steinmann pins, thin rods that are drilled through bone fracture fragments to maintain the anatomical congruity and biomechanical stability required for optimal bone healing. Unfortunately, currently used K-wires need to be removed after the bone has healed, necessitating a secondary procedure. To allow for easy removal, the ends of the wires are usually left outside the skin, forming a “pin-tract” that acts as a conduit for causing infection and other complications. These shortcomings of these common orthopedic devices could be avoided though through the use of degradable Mg alloy K-wires.

In addition to the intramedullary fracture fixation pins, in separate animals, WZ42 wires were wrapped around the mid-diaphyseal region of unfractured femurs forming a cuff to compare degradation and tissue response to the Mg alloy implanted in different regions – intramedullary versus over the cortical bone. Furthermore, another goal of the study was to assess systemic toxicity through a complete blood profile as well as organ and tissue analysis comprising kidney and liver.

5.2 MATERIALS AND METHODS

5.2.1 Preparation of Mg-Y-Zn-Ca-Zr implants

The WZ42 alloy was melt and cast as described in section 2.2.1, with the nominal composition of Mg-4.0%Y-2.0%Zn-1.0%Zr-0.6%Ca (wt. %). After casting, a solution treatment of 400 °C was applied for 20 hours and the ingot was quenched in room temperature water to increase the alloys' ductility and homogenize the secondary phases. The ingot diameter was machined using a lathe down to 37.8 mm to allow it to be extruded with an extrusion ratio of 30 while being heated at 450 °C. The extruded WZ42 rod of diameter ~6.9 mm and control material of Ti6Al4V rod of diameter 5 mm (Goodfellow Corporation, Coraopolis, PA) were machined using a lathe into pins with dimensions of 15 mm length x 1.66 mm diameter and wires of 20 mm length and 0.68 mm diameter. Schematics and photographs of machined pins and wire cuffs are shown in Figure 5.1. The implants were sonicated in washes of pure acetone and isopropanol and dried before undergoing sterilization by gamma radiation (2x106 cGy, 23.5 Gy/min, cesium 137 source, Mark I 68, JL Shepherd and Associates, San Fernando, CA).

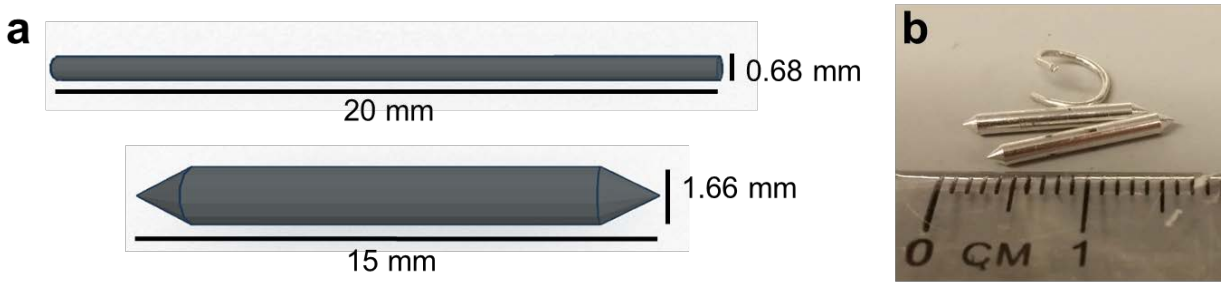

Figure 5.1. Schematic (a) and photograph (b) of pins (lower) inserted into the femoral intramedullary cavity and wire cuffs (upper) wrapped around the mid-diaphyseal region. In a) the wire was machined straight then bent around the femur during surgery.

5.2.2 Animal model

All animal experiments were approved by the University of Pittsburgh's Institutional Animal Case and Use Committee (IACUC). Before surgery, female Sprague-Dawley rats weighing 250-300 g were anesthetized by inhalation of isoflurane at a concentration of 2-5% for initiation of sedation, and 0.25-4% for maintenance. Each rat only received surgery in their right hind limb. Photographs of the surgical procedure are shown in Figure 5.2. First, the right hind limbs were shaved and disinfected, and an approximately 2 cm incision was made over the right femur, with location indicated in Figure 5.2a. The skin and mid-diaphyseal region of the right femurs were exposed through a lateral approach. A complete femoral osteotomy was created using a hand held drill (Figure 5.2b). The WZ42 or Ti6Al4V fixation pins were inserted first into the intramedullary space of the distal portion of the fractured femur (Figure 5.2c), then inserted into the intramedullary space of the proximal femur (Figure 5.2d), with the fracture approximated as seen in Figure 5.2e. In the case of the wire cuffs, the right femur was not cut, and the wires were wrapped around the midsection of the diaphysis and pressed against the bone to avoid translation

along the shaft of the femur or migration (Figure 5.2g). After the samples were implanted, the fascia and muscles were closed with VICRYL (J315) and the skin closed using non-absorbable monofilament polyamide sutures.

Post-operative pain and distress was observed daily for expressions of stress and behavioral abnormalities, changes in movement, food, and water intake. Furthermore, the right hind limbs were observed visually for signs of infection or presence of gas pockets.

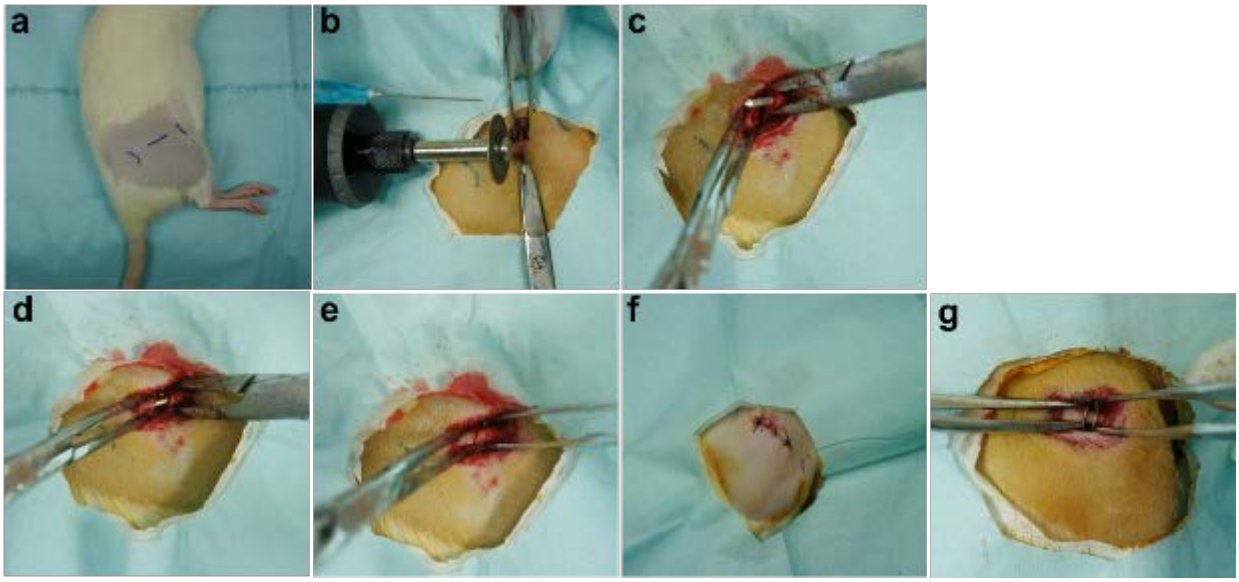

Figure 5.2. Surgical procedure used to implant metallic samples: a) Photograph of pins inserted into the femoral intramedullary cavity (bottom) and wire cuffs wrapped around the mid-diaphyseal region (top). Pin model - a) Lines indicating where incision was made to expose the femur; b) Fracture being created in rat femur using circular saw; c) Pin inserted into marrow space of one side of fractured femur; d) Pin inserted into other side of femur to bridge the fractured femur; e) Fracture closed with pin maintaining alignment and fixation; f) Surgical site fully closed and sutured. Cuff model - g) After incision to expose femur, the bone was left intact without osteotomy and a wire was wrapped around the midsection of the femur.

Groups of 5 animals for both WZ42 and Ti6Al4V pins were used for each time point of 2, 8, and 14 weeks for blood, liver, kidney, histology, and micro-CT analysis, and groups of 6 animals were implanted with wire cuffs with a single time point of 14 weeks, as displayed in Table 5.1. Rats were sacrificed using a gradual overdose of carbon dioxide followed by cervical dislocation. Immediately following sacrifice, the liver, kidney, and experimental group femurs were collected and stored for further analysis as described in the following sections. Three rats receiving no surgery were also sacrificed to serve as an operated control group.

Table 5.1. Summary of number of rats in each groups at time points used in study.

	2 weeks	**8 weeks**	**14 weeks**	**14 weeks**
	Intramedullary Pin			Cuff
Ti6Al4V	5	5	5	6
WZ42	5	5	5	6

5.2.3 X-ray imaging

X-ray imaging was performed on rats one week post-operatively to examine the position of the implants and stability of the fracture.

5.2.4 Blood-cell count and serum biochemical measurements

Blood samples were collected from animals before operation under anesthesia by tail snip and terminally (2, 8, and 14 weeks after implantation) by cardiac puncture and aspiration. For

determination of blood cell count, blood was collected in K2-EDTA tubes and analysis was performed by Marshfield Labs (Cleveland, OH) using a Sysmex XT2000i Automated Hematology Analyzer (Sysmex Corporation, Kobe, Japan). Serum samples were obtained by centrifuging collected blood at 2,000 rpm for 10 minutes at 4 °C. Serum biochemical tests were conducted by Marshfield Labs using an Olympus AU chemistry analyzer (Olympus Corporation, Tokyo, Japan).

5.2.5 Micro-computed tomography imaging

Plastic embedded rat femurs as were used for high resolution micro-computed tomography (μCT) scanning. Samples were scanned with continuous rotation μCT at 10.5 μm voxel size before implantation and immediately after retrieval post-operatively at 2, 8, and 14 weeks. The reconstructed data sets were used to generate a 3D volume from which we distinguished the remaining metal rod from surrounding degradation products and bone by using a histogram of grey values based on densities. A density threshold for the metal pins was used to isolate the volume of remaining magnesium alloy from surrounding material and compared to volume of the pins before implantation to estimate *in vivo* corrosion rate using the following equation:

$$C = (K \times V)/(A \times T)$$

Where C is the corrosion rate (mm $year^{-1}$, mmpy), the constant K is 8.76×10^4, V is the volume loss (cm^3), A is the initial sample area exposed (cm^2), and T is the time of exposure (h).

5.2.6 Histological preparation and analysis

Specimens of liver and kidney were fixed in 10% neutral buffered formalin, dehydrated, and infiltrated and embedded in paraffin. They were then inspected with hematoxylin and eosin (H&E) staining to assess whether the degradation of the WZ42 alloy resulted in any pathological changes in these critical visceral organs.

Femurs were fixed in 70% ethanol, dehydrated, and infiltrated and embedded in Osteo-Bed Plus methyl methacrylate-based embedding kit (Polysciences, Inc., Warrington, PA). The plastic blocks were sectioned with a rotary microtome (Leica RM 2255, Leica Biosystems, Buffalo Grove, IL) and stained using Goldner's Trichrome and alkaline phosphatase stains.

5.2.7 Tissue digestion and elemental analysis

Liver and kidney tissues were digested to allow for measurement of elemental concentration using ICP-OES. First, tissues were dried at 70 °C for 24 hours, then homogenized and weighed. Samples were then digested by immersion in 20 ml nitric acid/g tissue for 6 hours at 70 °C, followed by adding 4 ml hydrogen peroxide/g tissue for 1 hour, and 4 ml sulfuric acid/g tissue for 1 hour. Samples were then diluted 50x in water purified by a Milli-Q system (18 MΩ cm deionized water, Milli-Q Academic, Millipore, Billerica, MA), filtered in 0.45 µm syringe filters, and analyzed for Mg concentration by ICP-OES (Thermo Fisher).

5.3 RESULTS

5.3.1 Fixation of femoral defect using Mg-Y-Zn-Ca-Zr alloy pin

In order to provide fixation of a full osteotomy to the midsection of a femur, pins with sharpened ends were fabricated from the WZ42 alloy and Ti6Al4V alloy and inserted into the intramedullary cavity of the two halves of the fragmented femur. In addition, WZ42 and Ti6Al4V wires were wrapped around the midsection of native femurs to compare tissue response of the biomaterials inserted in the bone versus at the outer surface of the bone. The pins were successfully inserted into all femurs during surgery with the fractures being approximated as seen in the 7 day X-ray images of Figure 5.3a and b despite slight mismatches between the pin diameter and the diameter of the intramedullary cavity observed in some cases (Figure 5.3c, red arrow) resulting in a small gap. Some wire cuffs snapped during implantation but all maintained fixation around the femur as shown in Figure 5.3d and e.

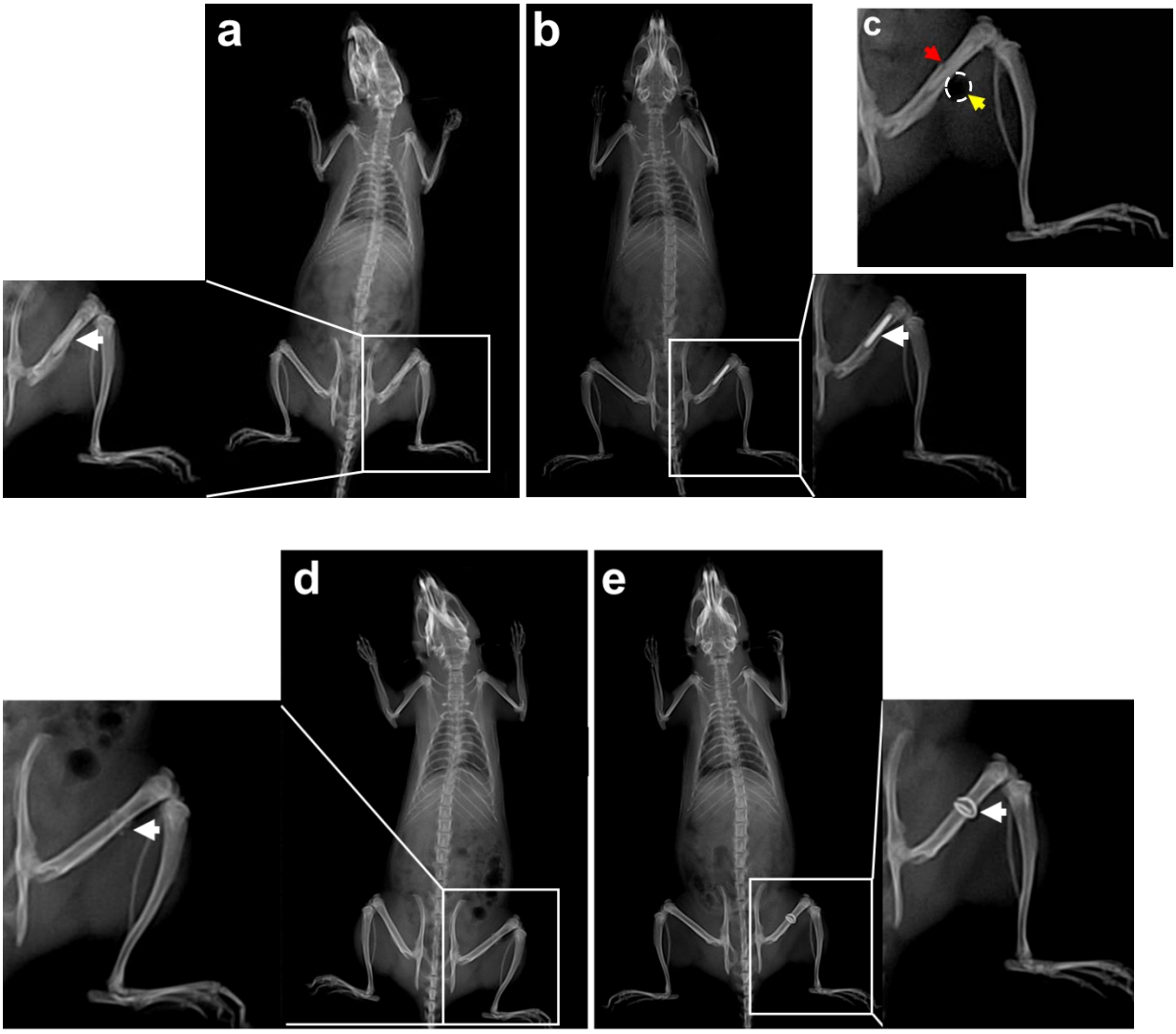

Figure 5.3. One week X-ray images of implanted WZ42 magnesium alloy (a) and Ti6Al4V (b) K-wires (designated by white arrow) in the right femur of rats; c) fracture misalignment (red arrow) and empty spaces near the WZ42 implants (yellow arrow, circled) were observed in some X-ray images. One week X-ray images of implanted WZ42 magnesium alloy (d) and Ti6Al4V (e) wire cuffs (designated by white arrow) in the right femur of rats.

Small pockets of empty space, as seen in Figure 5.3c, noted by the yellow arrow, were observed in the X-rays of 75% of rats with implanted WZ42 alloy pins or cuffs, likely caused by

hydrogen gas evolved from the degrading Mg implants. Despite their presence in the X-ray images, no bulges in the skin in the hind limb of rats were observed during frequent visual inspection of the rats. The rats regained mobility by 7 days post-operation.

5.3.2 Systemic toxicity to Mg-Y-Zn-Ca-Zr implants

Total blood cell count is listed in Table 5.2 below, which generally did not indicate any disturbances in the blood count, with parameters remaining within references ranges or near pre-operation levels. Small differences from the reference ranges or unoperated levels were observed from low platelet counts for WZ42 cuffs, and WZ42 and Ti6Al4V pins at 14 weeks, while elevated postoperative white blood cell count were seen at 2 weeks for both WZ42 and Ti6Al4V pins.

Table 5.2. Average blood cell count of unoperated animals and animals implanted with WZ42 and Ti6Al4V alloy pins at 2, 8, and 14 weeks after implantation.

Name	Implantation time	Red Blood Cell Count	Hemoglobin	Platelet Count	White Blood Cell Count
Units		10^6/uL	g/dL	10^3/uL	10^3/uL
Ref. ranges		(7.00-9.00)	(13.7-16.8)	(680-1280)	(1.1-7.5)
Unoperated		7.4 ± 0.3	14.1 ± 0.9	618.3 ± 200.6	6.8 ± 2.3
WZ42 pin	2 weeks	8.0	14.3	839.0	8.6
Ti6Al4V pin	2 weeks	7.8	14.9	656.0	9.0
WZ42 pin	8 weeks	7.4 ± 0.5	13.8 ± 1.2	N/A	6.8
Ti6Al4V pin	8 weeks	7.4 ± 0.3	14.2 ± 0.4	637.8 ± 168.6	5.9 ± 1.6
WZ42 pin	14 weeks	7.7 ± 0.4	14.2 ± 0.5	595.8 ± 179.8	5.9 ± 2.1
Ti6Al4V pin	14 weeks	7.5 ± 0.4	14.0 ± 0.7	563.0 ± 164.5	5.9 ± 2.7
WZ42 cuff	14 weeks	7.1 ± 0.2	13.9 ± 0.4	461.0 ± 56.6	2.2 ± 1.0
Ti6Al4V cuff	14 weeks	7.6 ± 0.4	13.8 ± 0.7	637.0 ± 96.5	5.8 ± 1.4

Similarly, serum biochemical parameters are shown in Table 5.3, with kidney function measured by creatinine and urea levels, and liver function measured by albumin, alkaline phosphatase, bilirubin, and glucose. All parameters remained within the reference ranges or near pre-operation levels, demonstrating little effect of the implanted alloy materials on the kidney and liver function and metabolism.

Table 5.3. Average values of serum metabolic parameters unoperated animals and animals implanted with WX42 and Ti6Al4V alloy pins at 2, 8, and 14 weeks after implantation.

Name	Implantation time	Glucose	ALT(GPT)	ALP	Total Bilirubin	Total Protein	Albumin	Urea N	Creatinine	Globulin	A/G Ratio
Units		mg/dL	U/L	U/L	mg/dL	g/dL	g/dL	mg/dL	mg/dL	g/Dl	
Ref. ranges		(70-308)	(59-166)	(232-632)	(0.0-0.1)	(5.8-7.1)	(3.2-3.7)	(13-19)	(0.3-0.5)	(2.6-3.5)	
Unoperated		181.2 ± 19.8	55.8 ± 9.2	175.2 ± 20.3	0.17 ± 0.10	5.7 ± 0.1	3.3 ± 0.1	20.7 ± 1.9	0.37 ± 0.08	2.4 ± 0.1	1.4 ± 0.1
WZ42 pin	2 weeks	155.8 ± 26.7	57.3 ± 7.9	148.3 ± 13.6	0.18 ± 0.05	6.3 ± 0.3	3.3 ± 0.2	20.3 ± 5.6	0.50 ± 0.00	3.0 ± 0.1	1.1 ± 0.1
Ti6Al4V pin	2 weeks	322.0 ± 94.4	66.3 ± 20.3	151.2 ± 21.8	0.14 ± 0.05	6.2 ± 0.1	3.3 ± 0.1	17.6 ± 2.1	0.42 ± 0.04	2.9 ± 0.2	1.1 ± 0.1
WZ42 pin	8 weeks	294.5 ± 205.0	80.4 ± 13.9	163.2 ± 30.4	0.24 ± 0.05	6.4 ± 0.3	3.5 ± 0.1	23.6 ± 2.1	0.52 ± 0.08	2.9 ± 0.3	1.2 ± 0.1
Ti6Al4V pin	8 weeks	204.8 ± 75.9	54.5 ± 17.9	201.5 ± 40.2	0.18 ± 0.05	6.4 ± 0.3	3.7 ± 0.2	21.8 ± 2.9	0.53 ± 0.05	2.7 ± 0.1	1.3 ± 0.1
WZ42 pin	14 weeks	177.8 ± 47.1	65.6 ± 8.7	183.8 ± 33.3	0.20 ± 0.00	6.4 ± 0.1	3.6 ± 0.1	22.2 ± 1.6	0.56 ± 0.05	2.7 ± 0.1	1.3 ± 0.1
Ti6Al4V pin	14 weeks	229.5 ± 198.5	56.8 ± 15.8	187.0 ± 33.5	0.18 ± 0.04	6.3 ± 0.3	3.7 ± 0.2	21.8 ± 2.5	0.52 ± 0.04	2.6 ± 0.2	1.4 ± 0.1
WZ42 cuff	14 weeks	123.6 ± 36.3	64.0 ± 7.7	155.2 ± 21.7	0.20 ± 0.00	6.3 ± 0.3	3.7 ± 0.2	24.8 ± 2.2	0.58 ± 0.04	2.6 ± 0.2	1.4 ± 0.1
Ti6Al4V cuff	14 weeks	154.4 ± 53.6	50.2 ± 3.4	163.6 ± 30.3	0.18 ± 0.04	6.2 ± 0.3	3.6 ± 0.1	19.6 ± 1.9	0.52 ± 0.04	2.6 ± 0.2	1.4 ± 0.1

Electrolyte parameters calcium, sodium, chloride, phosphorous, and magnesium were measured from serum samples which are shown in Table 5.4. Importantly, magnesium levels remained in the low end of the reference ranges indicating no accumulation of degrading Mg from the implants in the collected blood. All other electrolytes similarly remained consistent with unoperated rats and the prescribed allowable reference ranges.

Table 5.4. Average values of electrolyte parameters of unoperated animals and animals implanted with WX42 and Ti6Al4V alloy pins at 2, 8, and 14 weeks after implantation.

Name	Implantation time	Calcium	Sodium	Chloride	Phosphorous	Magnesium
Units		mg/dL	mmol/L	mmol/L	mg/dL	mg/dL
Ref. ranges		(9.5-13.9)	(146-151)	(98-104)	(5.6-16.8)	(3.8-5.5)
Unoperated		9.8 ± 0.2	138.2 ± 1.9	100.5 ± 1.0	5.5 ± 0.2	2.0 ± 0.2
WZ42 pin	2 weeks	11.2 ± 0.1	144.8 ± 1.7	101.0 ± 1.4	8.5 ± 0.9	2.9 ± 0.3
Ti6Al4V pin	2 weeks	11.5 ± 0.5	143.8 ± 1.6	100.2 ± 2.2	9.7 ± 1.9	3.4 ± 0.4
WZ42 pin	8 weeks	11.6 ± 0.5	144.4 ± 1.9	100.6 ± 2.8	9.7 ± 1.4	3.5 ± 0.5
Ti6Al4V pin	8 weeks	11.8 ± 0.6	146.5 ± 1.0	100.0 ± 1.4	11.3 ± 0.8	3.9 ± 0.4
WZ42 pin	14 weeks	11.4 ± 0.3	147.8 ± 1.9	100.2 ± 2.0	9.8 ± 0.7	3.6 ± 0.2
Ti6Al4V pin	14 weeks	12.2 ± 1.1	145.2 ± 2.6	99.0 ± 2.0	9.6 ± 1.2	3.6 ± 0.6
WZ42 cuff	14 weeks	11.3 ± 0.2	147.0 ± 0.7	101.4 ± 0.9	9.1 ± 1.4	3.2 ± 0.2
Ti6Al4V cuff	14 weeks	11.6 ± 0.3	147.6 ± 1.1	99.6 ± 1.7	9.2 ± 0.7	3.3 ± 0.2

ICP-OES results of the acid-digested liver and kidney (Figure 5.4) demonstrated no accumulation of Mg exceeding the normal levels seen in unoperated control rats was observed in the collected liver and kidney tissue in the WZ42 or Ti6Al4V groups. Ca and Zn concentration in the liver and kidney also did not deviate from the normal levels. The concentration of other alloying elements (Y and Zr) measured from the digested liver and kidney were also perceived to be too low to be differentiated from normal levels, with Y being present in <0.7 μg/g dry mass in both liver and kidney, and Zr present in <2.2 μg dry mass in both liver and kidney.

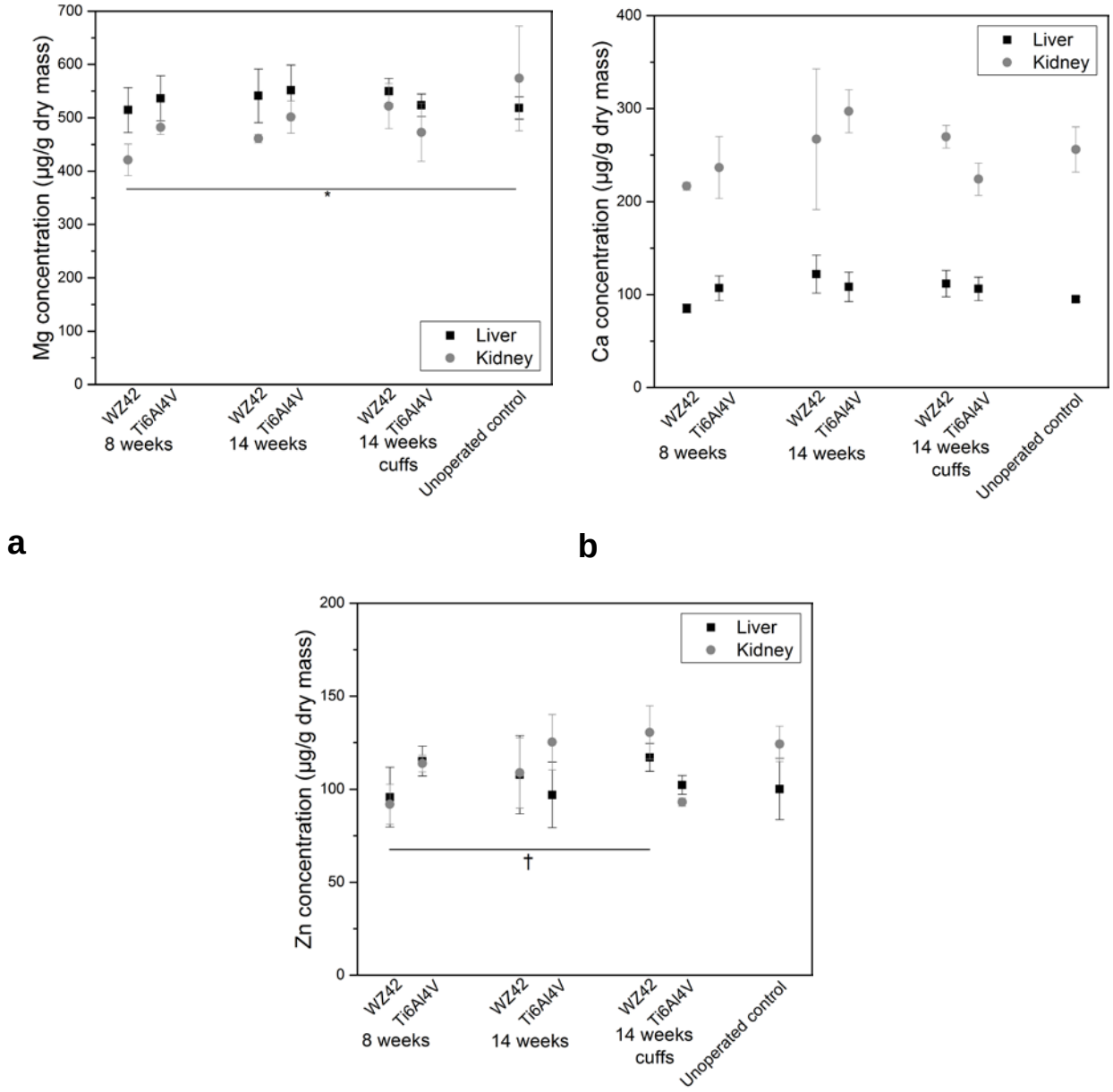

Figure 5.4. Average Mg (a), Ca (b), and Zn (c) concentration in digested liver and kidney samples of rats implanted with femoral pins and cuffs of WZ42 and Ti6Al4V for 8 and 14 weeks compared to unoperated control rats. Significant difference * ($p < 0.05$) between Mg concentration in kidneys of rats implanted with WZ42 pins for 8 weeks and unoperated control rats and between † ($p<0.05$) between Zn concentrations in kidneys of rats implanted with WZ42 pins for 8 weeks and cuffs. $n \leq 3$ per extract concentration per group per time point.

5.3.3 Histological examination of liver and kidneys

Liver and kidneys explanted from the Sprague-Dawley rats sacrificed at 8 and 14 weeks were processed into pathological sections and stained with hematoxylin and eosin (H&E). Optical microscopy images (Figure 5.5 for kidney and Figure 5.6 for liver) revealed that the cellular structure of the liver and kidney did not undergo morphological changes or infiltration by inflammatory cells. No signs of obvious abnormalities were observed in any of the organs sections.

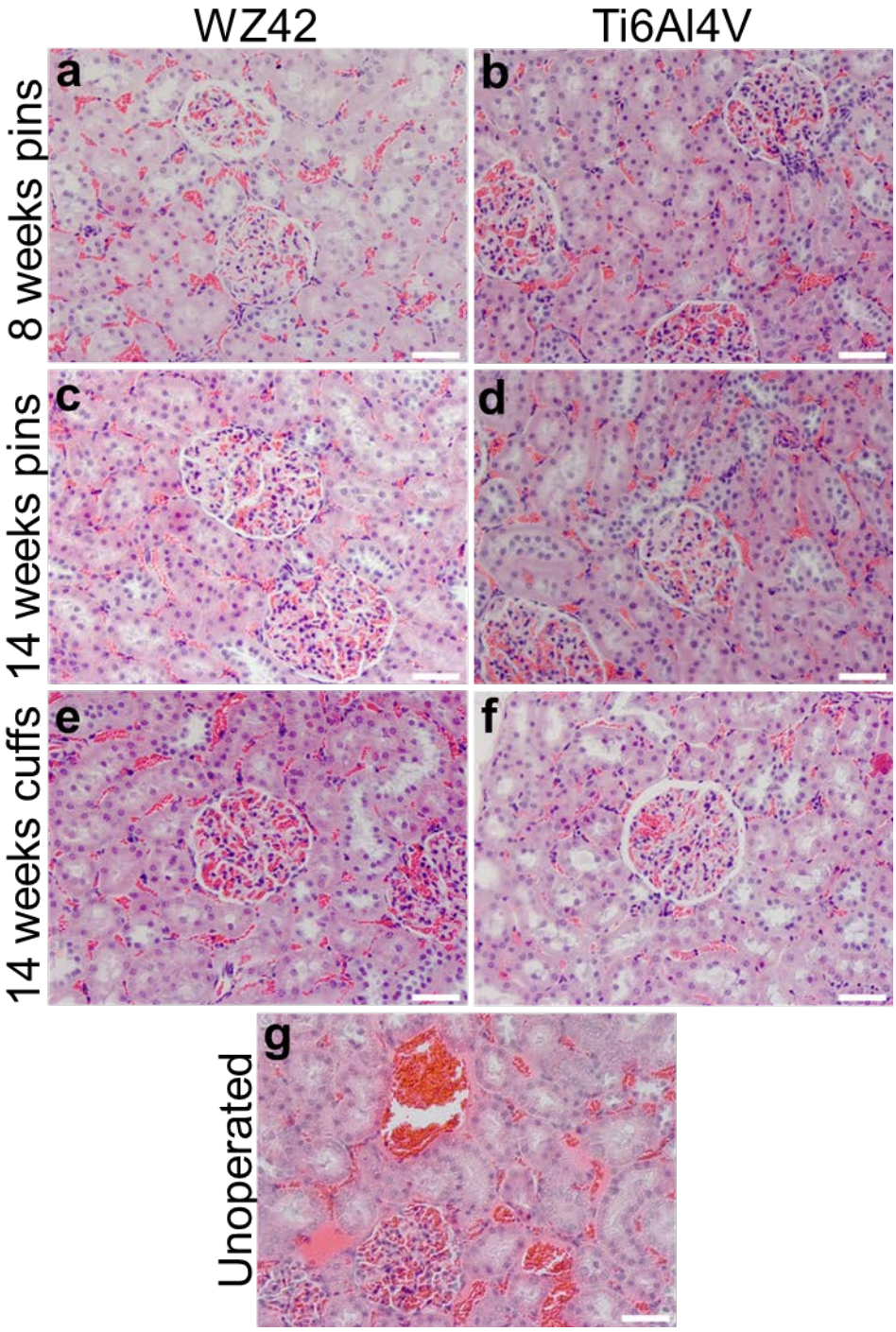

Figure 5.5. Photomicrographs of H&E stained kidneys of rats with femurs fixed by pins of WZ42 (a, c) and Ti6Al4V (b, d) after 8 weeks (a, b) and 16 weeks (c, d). Stained images of kidneys from rats with implanted wire cuffs of WZ42 (e) and Ti6Al4V (f) wrapped around bone for 14 weeks. Photomicrograph g) from rat that was left unoperated. Scale bar = 50 µm.

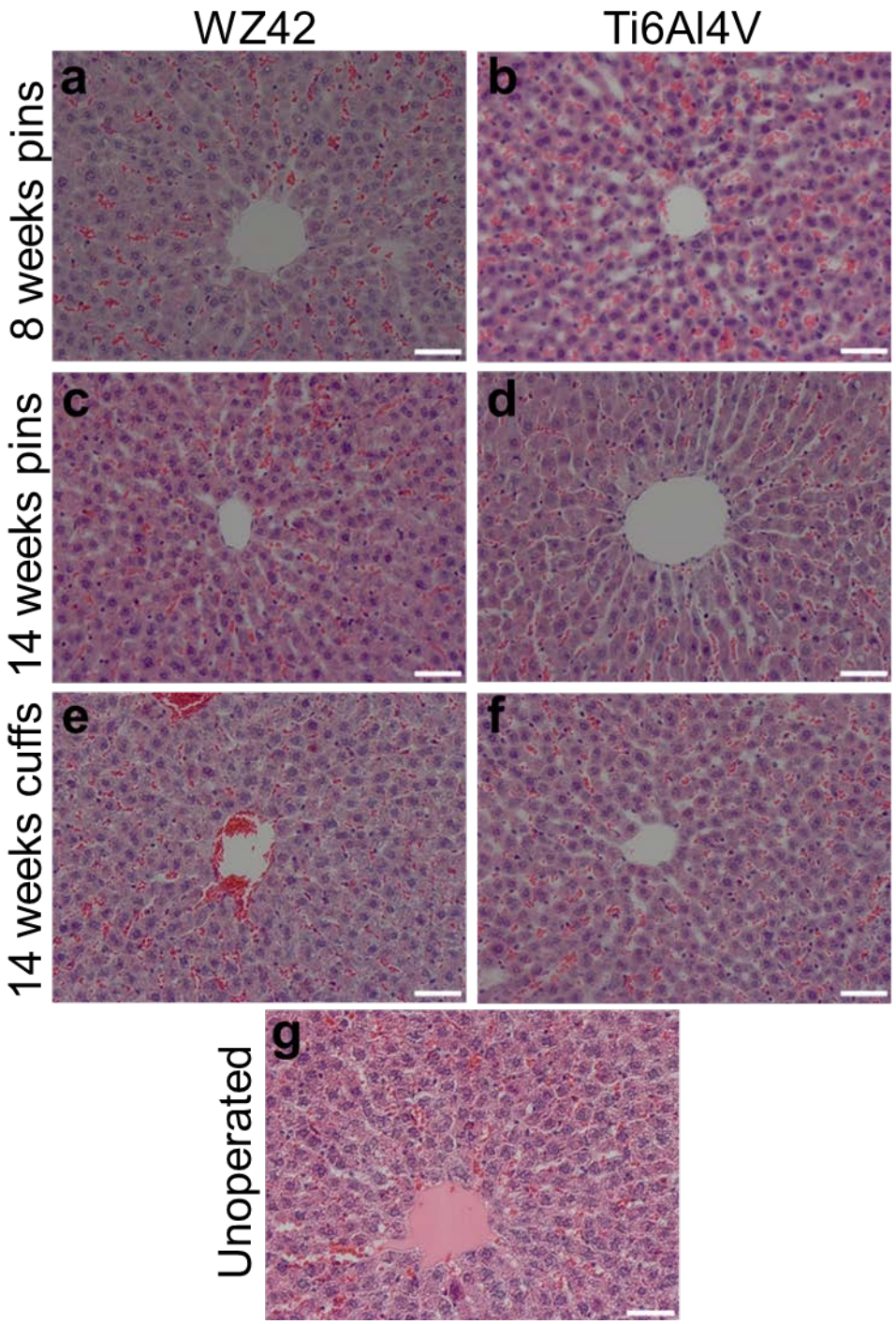

Figure 5.6. Photomicrographs of H&E stained livers of rats with femurs fixed by pins of WZ42 (a, c) and Ti6Al4V (b, d) after 8 weeks (a, b) and 16 weeks (c, d). Stained images of livers from rats implanted with wire cuffs of WZ42 (e) and Ti6Al4V (f) wrapped around bone for 14 weeks. Photomicrograph g) from rat that was left unoperated. Scale bar = 50 µm.

5.3.4 *In vivo* corrosion of Mg-Y-Zn-Ca-Zr alloy pins and morphology of surrounding bone

Example micro-CT slices obtained from the femur-implant complex are shown in Figure 5.7.

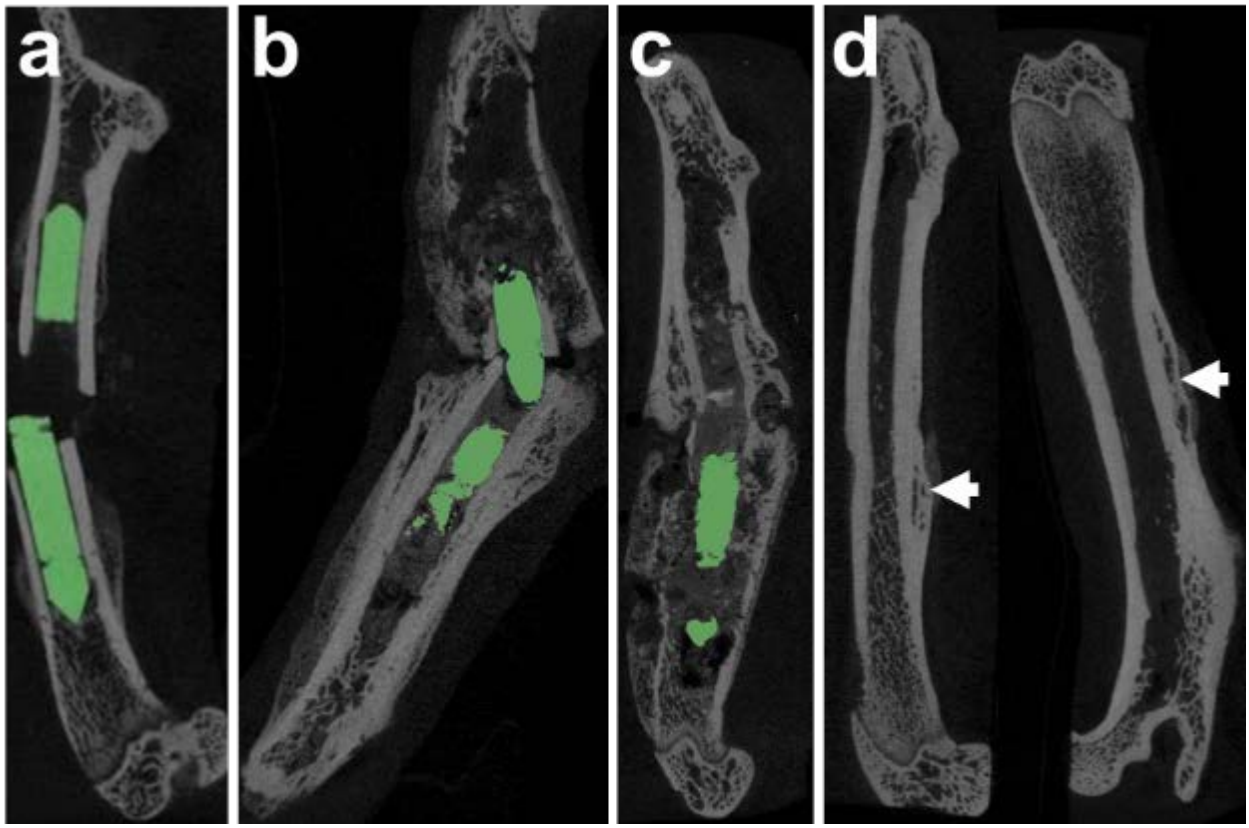

Figure 5.7. To determine volume of the degrading WZ42 alloy, pins were distinguished from surrounding bone in micro-CT scans based on density thresholding with representative examples highlighted in green after implantation times of a) 2 weeks, b) 8 weeks, c) 14 weeks. Cuffs were fully degraded after 14 weeks (d) but new bone formation was seen in the region the wires occupied (arrows).

After two weeks, the pins had broken as seen in Figure 5.7a. These pin failures occurred at the site of the femoral fracture, resulting in malunion. In addition, sites of corrosion appeared at junctions where the pins were clamped in collets during machining. Both these two regions where the corrosion/failure occurred corresponded with regions of higher stress. Progressive degradation throughout the pins was observed at 8 and 14 weeks (Figure 5.7b and c). Regions of the pin surrounded by the cortical bone appeared to degrade more slowly. Micro-CT scans of intact femurs with WZ42 wire cuffs wrapped around the midsection of the diaphysis (Figure 5.7d) revealed what appeared to be new bone formation in the region surrounding the degrading cuffs, despite the cuffs having completely degraded after 14 weeks indicating the favorable response of the implanted Mg alloys.

Following segmentation of the remaining WZ42 pins from the surrounding degraded product and bone, a 3D reconstruction of the pins was created from which the volume was calculated. This remaining volume was used to calculate the corrosion rate at the end of 2, 8, and 14 weeks as shown in Figure 5.8.

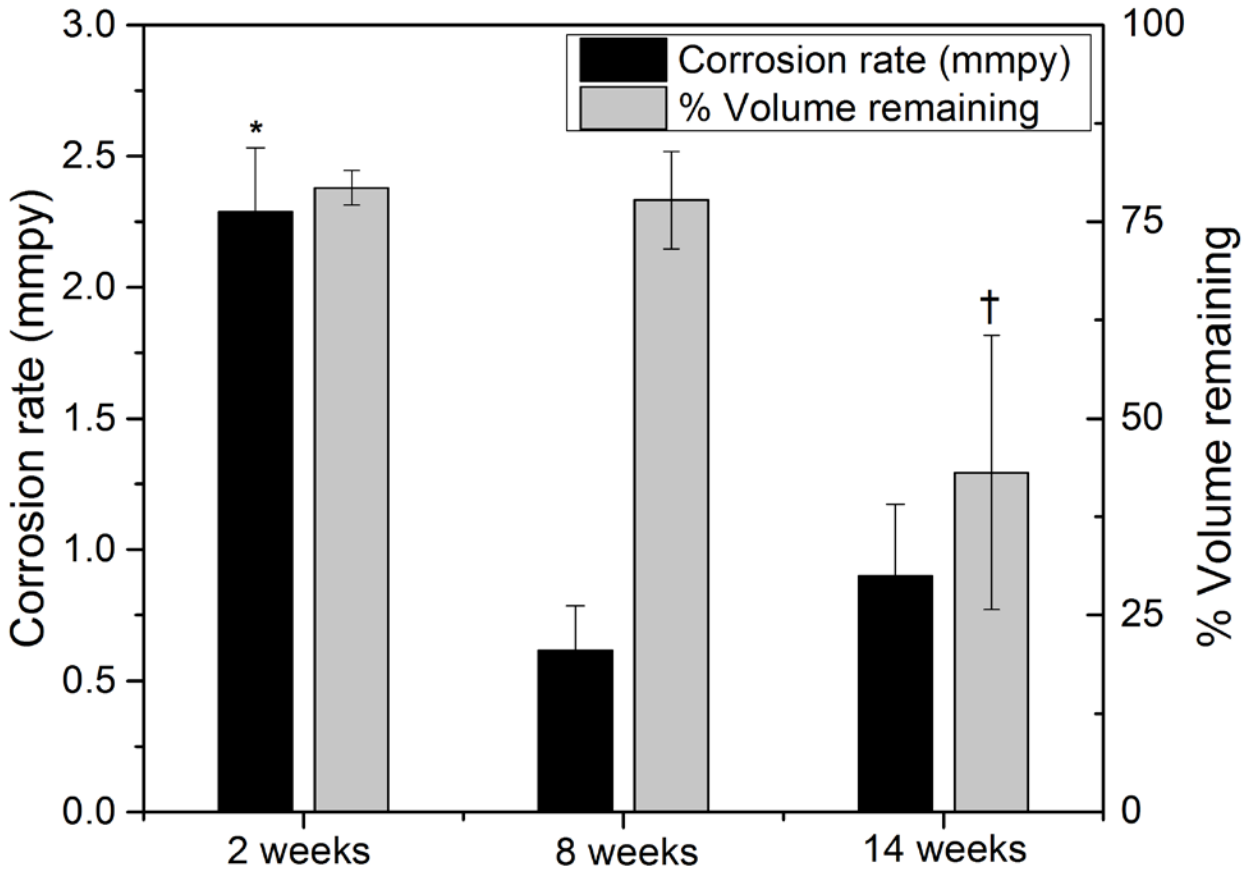

Figure 5.8. Corrosion rate and % volume remaining of WZ42 pins implanted in rat femurs for 2, 8, and 14 weeks. $n \geq 2$ for each group at each time point. * and † represent significant difference ($p < 0.05$) compared to measurements made at other time points.

Degradation was found to occur more rapid initially at 2 weeks, after which the corrosion appeared to have reduced and stabilized as seen by the lower corrosion rates perceived at 8 and 14 weeks. This may be related to passivation of the WZ42 alloy and callus formation limiting fluid exposure to the degrading alloy after early stages of bone healing.

5.3.5 Local tissue response to Mg-Y-Zn-Ca-Zr alloy pin

Femur explants were collected after 2, 8, and 14 weeks to assess the local tissue response to the WZ42 pins and cuffs and observe any fracture healing. Sections of the bone from femurs containing the pins were stained using Goldner's Trichrome and are shown in Figure 5.9.

After 2 weeks in rats implanted with the WZ42 alloy, empty pockets were observed over the fracture site in the fibrous tissue over the bone. This was likely due to accumulation of hydrogen gas forming gas pockets (GP) from the degrading magnesium alloy, as this is not observed in the Ti6Al4V pins. The presence of osteoids (Od) was observed surrounding the bone with fibrous tissue (Ft) surrounding the fracture site indicated by the dashed line demarcating the implant-bone interface. After 8 weeks, the gas pocket over the fracture site was not perceived to be as prominent, potentially due to a slowing of the corrosion rate, dissipation of gas, and ingrowth of fibrous tissue. A greater presence of osteoids as well as new bone formation (Nb) in the periosteal region was observed progressively after 8 and 14 weeks. After 14 weeks, the fracture was not yet completely healed when fixed with either WZ42 or Ti6Al4V pins.

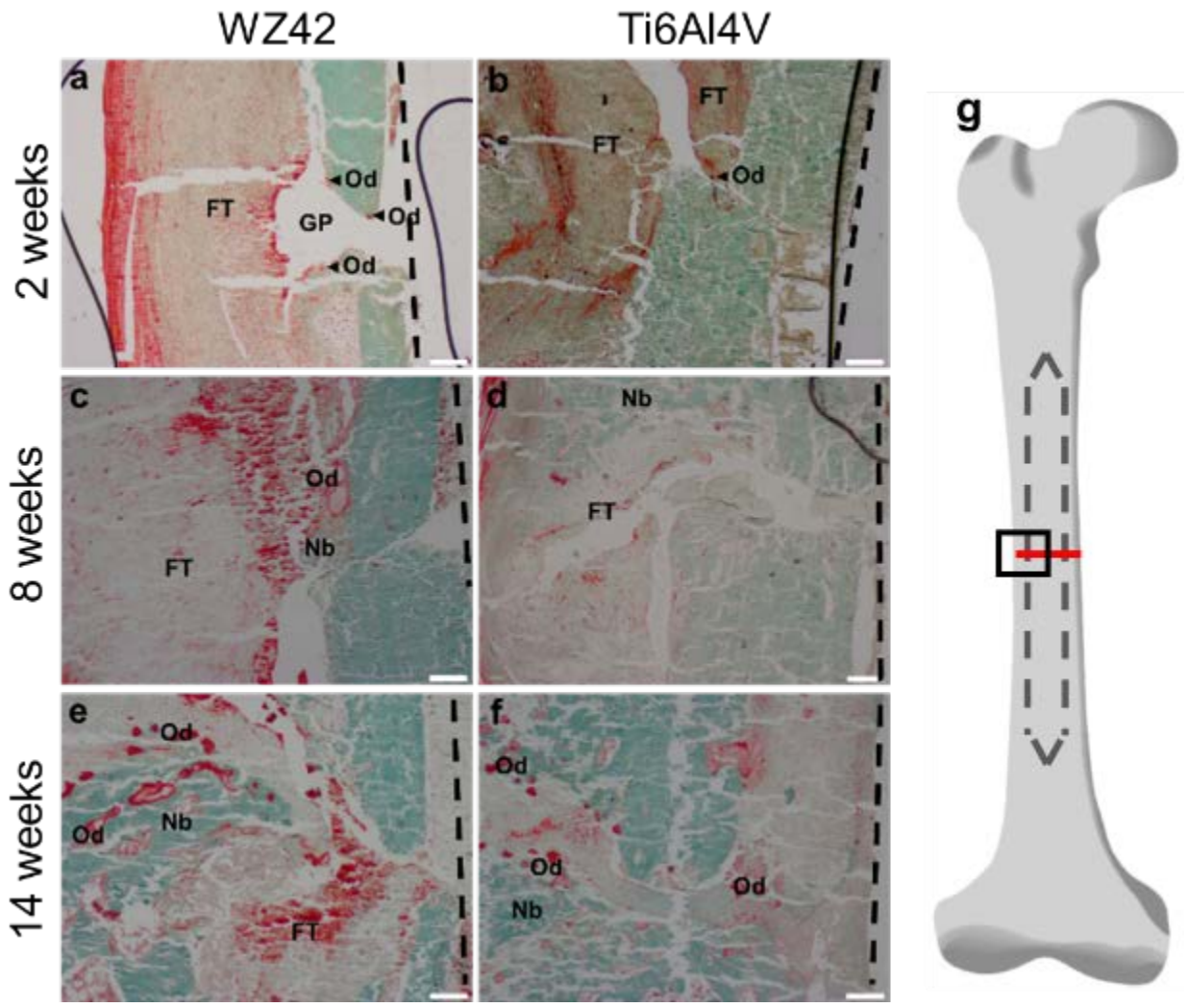

Figure 5.9. Photomicrographs of Goldner's Trichrome stained sections (40x) of soft and hard tissue at the defect site fixed by pins of WZ42 magnesium alloy (a, c, e) and Ti6Al4V (b, d, f) after 2 weeks (a, b), 8 weeks (c, d), and 14 weeks (e, f) of implantation; g) representation of region of interest imaged along longitudinal plane at defect site. Cytoplasm, fibrin, muscle, and osteoids are represented in red; collagen and bone are represented in green. The dashed line approximates the implant pin-bone interface.

Scale bar = 200 µm. Abbreviations: GP, gas pocket; Od, osteoids; FT, fibrous tissue; Nb, new bone.

Alkaline phosphatase staining was conducted to indicate osteoblast activity and the process of new bone formation in the region surrounding the defect. Osteoblast activity was more prolific surrounding the fracture in the femurs containing WZ42 (Figure 5.10a, c, e) compared to the femurs containing Ti6Al4V (Figure 5.10b, d, f). Presence of osteoblasts appeared to peak at 8 weeks for the WZ42 group.

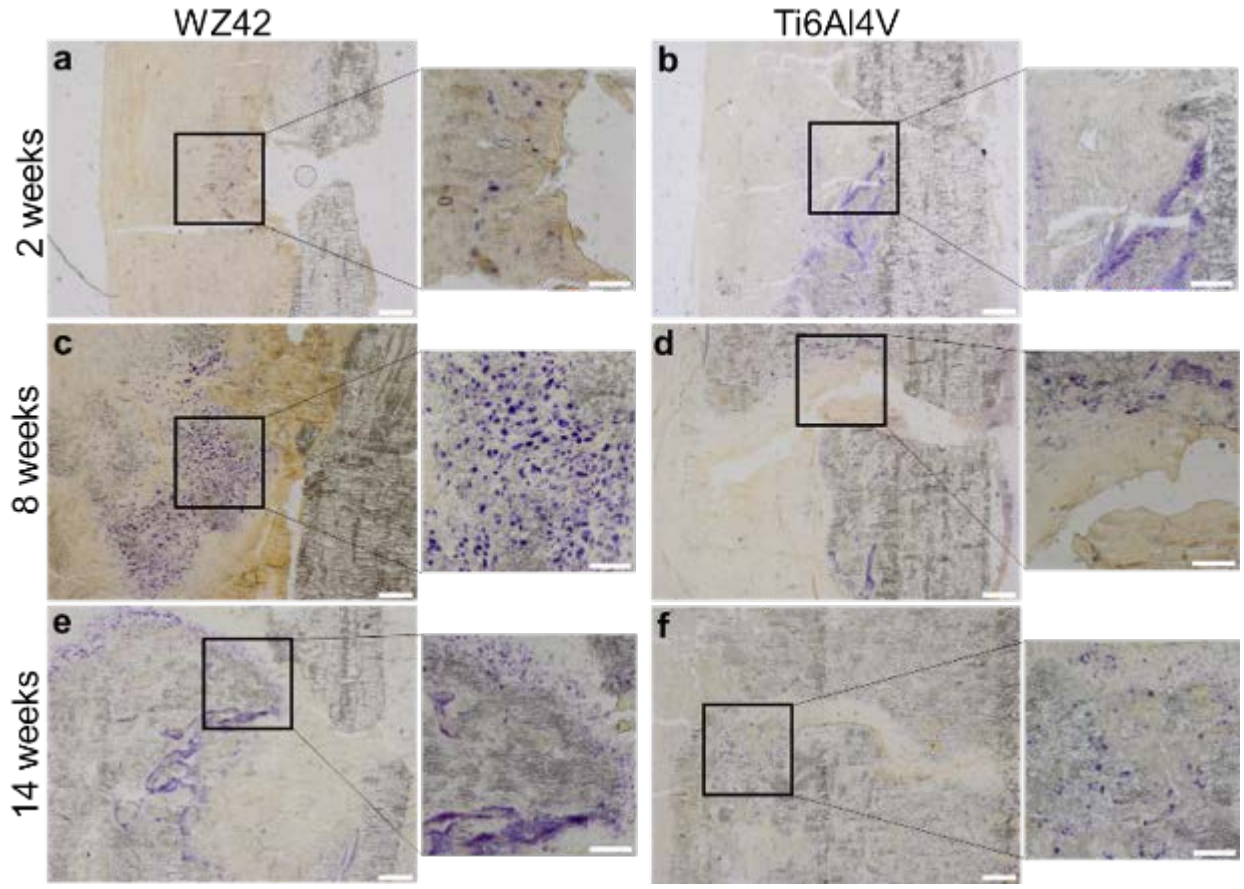

Figure 5.10. Photomicrographs of the localization of ALP at 40x and 100x (inset) of tissue at the defect site fixed by pins of WZ42 magnesium alloy (a, c, e) and Ti6Al4V (b, d, f) after 2 weeks (a, b), 8 weeks (c, d), and 14 weeks (e, f) of implantation. Scale bar = 200 μm in 40x images, 100 μm in 100x. Pin located on left side of image in all.

In Goldner's Trichrome stained sections of tissue near the site of wire cuff implantation (Figure 5.11), new bone as seen in light blue-green as well as fibrous tissue was found in the region surrounding the Mg alloy cuff implant (Figure 5.11a). On the other hand, new bone formation was not seen around the inert Ti6Al4V cuff (Figure 5.11b).

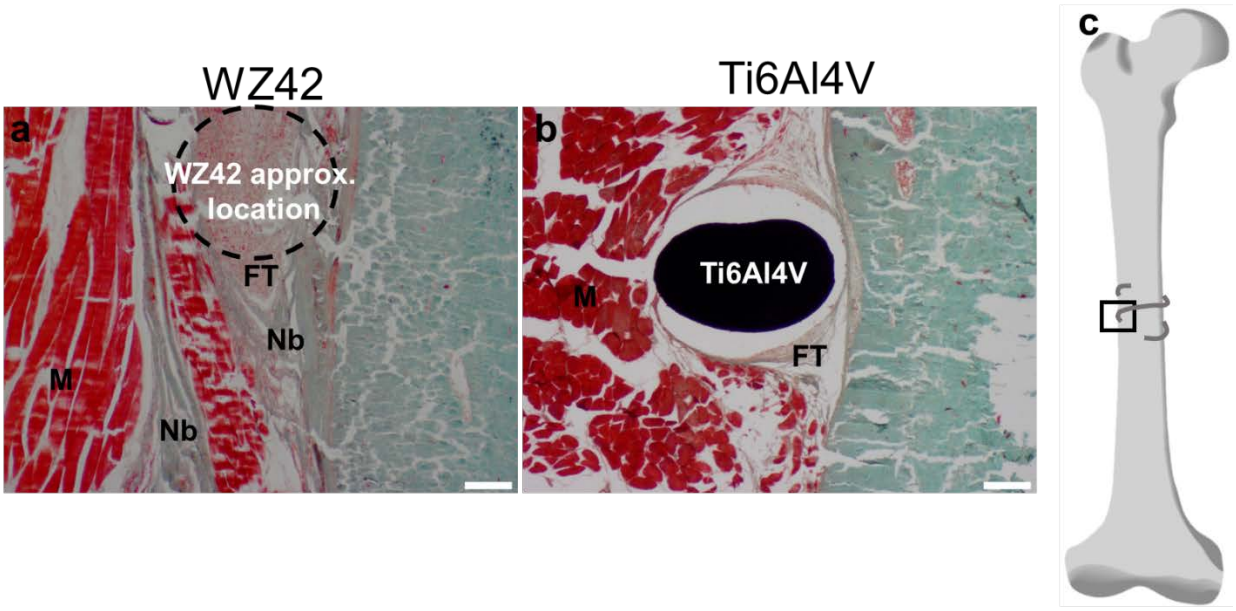

Figure 5.11. Photomicrographs of Goldner's Trichrome stained sections (40x) of soft and hard tissue at the implant-bone interface where wire cuffs of WZ42 magnesium alloy (a) and Ti6Al4V (b) were wrapped around bone for 14 weeks of implantation. c) Representation of region of interest imaged along longitudinal plane at defect site. Cytoplasm, fibrin, muscle, and osteoids are represented in red; collagen and bone are represented in green. The dashed line approximates the location of the WZ42 wire.

Scale bar = 200 µm. Abbreviations: FT, fibrous tissue; Nb, new bone; M, muscle; Ti, Ti6Al4V wire.

5.4 DISCUSSION

In this specific aim, the effects of the WZ42 magnesium alloy in terms of biocompatibility and systemic toxicity, degradation behavior, and local tissue response and healing was investigated. This animal model, a closed femoral fracture stabilized by an intramedullary pin, has been characterized by various groups studying the expression of genes for bone and cartilage matrix constituents [209] and growth factors [210], the production of cytokines [211], cell proliferation and apoptosis [212, 213], and to compare metals for bone healing and mineralization by permanent metals [214]. Despite these instances of stainless steel and Ni-Ti alloys being used to fix full osteotomies in rats, such an aggressive model representing a manifestation of large dynamic stress that favors corrosion had not been tested with magnesium alloys. In fact, no models of full load-bearing had been applied to a fracture fixation device manufactured from magnesium to date. It was also the intent to confirm the safety of Mg in this aggressive model and analyze the degradation behavior as a result of the high stress being placed on the Mg pins.

To assess the safety of the WZ42 implants, biochemical analysis of the blood and serum was also conducted. The lower than expected platelet levels for the WZ42 and Ti6Al4V pin groups at 14 weeks and WZ42 wire cuff group also at 14 weeks was likely due to platelet clumping in samples, which was reported in many samples analyzed. The elevated levels of white blood cells 2 weeks after surgeries for both WZ42 as well as Ti alloys represents a common indication of normal inflammation seen after surgical procedures are performed [215]. Blood cell counts measured at later time points saw the white blood cell count return to normal levels, suggesting that signs of any immediate infection or a long-term inflammatory response was not present. The consistent electrolyte levels as measured in blood and the stable Mg concentration measured in the digested kidney and liver signifies that the degradation of WZ42

did not cause disturbances in the balance of electrolytes necessary for the body's normal function. Other studies have similarly found that blood biochemistry and liver and kidney function were not affected by magnesium alloy degradation when implanted in bone, indicating the general safety of degradation Mg alloys [216-218]. Variability observed in the blood testing was expected from animal to animal, with additional error stemming from differences in blood sample quality such as hemolysis, clotting, and lipemia.

Along with the unaltered serum biochemical parameters suggesting that liver and kidney functions were not affected by the WZ42 alloy degradation, concentrations of Mg, Ca, and Zn (elements contained in the WZ42 alloy) in the liver and kidney did not rise above levels measured in unoperated rats (Figure 5.4) with Y and Zr too low to be differentiated from baseline levels. Concentrations were also consistent with rats implanted with Ti6Al4V samples compared at the same time points. Expected differences between animals, potentially incomplete dissolution of tissue in acid, and deviations in ICP-OES measurements may have resulted in variations in ion concentrations within groups.

To further demonstrate systemic biocompatibility, H&E staining of the liver and kidney did not reveal any signs of organ damage. No dark deposits of focal mineralizations, acute inflammatory cells, or necrosis were observed in the kidney tissue. In the liver, no aggregates of inflammatory cells or features of hepatocellular necrosis such as irregular patchy areas of coagulation necrosis were observed. These results clearly suggest that the degradation products of the WZ42 alloy have good systemic biocompatibility. Hartwig stated that intake of high concentration of Mg ions would not cause adverse reactions due to the high aptitude for the excretory system of the kidney and storage buffering capacity from bones to allow the body to maintain a balance of serum magnesium [219].

Progressive degradation was observed in the intramedullary WZ42 pins as seen in the reducing cross sectional area of the implants seen in Figure 5.7(a-c), and calculated corrosion rate and volume loss shown in Figure 5.8. Degradation appeared to occur preferentially at the fracture site, perpendicular to the fracture, where the stresses acting on the implanted pin would be perceived to be the highest. This synergy of mechanical loading combined with the corrosive environment of surrounding fluids in the body has been shown to cause sudden fracture of implants via the well-known stress corrosion cracking (SCC) mechanism [220]. This embrittlement phenomenon can occur even when applied stress does not exceed the yield strength of the material, reducing the time to fracture and causing premature brittle failure. Magnesium, suffering from pitting corrosion, a source from which SCC can develop, has shown susceptibility to SCC in chloride solutions and simulated body fluids [220, 221]. Other localized regions of corrosion, such as near the end of the pin in Figure 5.7a, occurred due to pre-existing flaws imparted during machining, which increased the susceptibility to SCC [222]. Degradation at the site of fracture was also promoted by the higher exposure to the surrounding fluid electrolyte, acting to produce fluid shear stress and remove local OH^- ions to reduce the protection from the passivation layer [223, 224]. The reduction in corrosion rate after the initial 2 week time point occurred as the surface of the Mg implant as expected became passivated and enclosed in fibrous tissue and newly formed bone, as observed in other studies of Mg implanted into bone [206]. The percentage volume remaining did not significantly change between 2 and 8 weeks because measurements were taken from different samples at each time point. For the implants used to calculate the 8 week measurements, the corrosion rate was lower so that over time, the volume remaining ended up the being not significantly different from the samples measured after 2 weeks which degraded at a much faster rate. In another sense, the corrosion rate

for 8 week samples was approximately one quarter of the 2 week corrosion rate, however, since the volume remaining was compounded over four times the length of time, the volume remaining ended up being similar. The variation between samples that caused the difference in degradation for 2 versus 8 week samples may be due to variability in when the pins failed, or pins not being fully surrounded by cortical bone thus being exposed to more surrounding fluid leading to more rapid corrosion.

The effect of the degrading Mg alloy on the surrounding tissue was investigated via Goldner's Trichrome and ALP staining after 2, 8, and 14 weeks implantation of the WZ42 and Ti6Al4V intramedullary pins and extra-cortical cuffs. After 2 weeks in rats implanted with the WZ42 alloy (Figure 5.3a, Figure 5.9a), gas pockets (GP) were observed over the fracture site forming empty cavities in the surrounding in fibrous tissue. This was likely due to accumulation of hydrogen gas from the degrading magnesium alloy, as this is not observed in the Ti6Al4V pins. The presence of osteoids (Od) was observed near bone with fibrous tissue (Ft), or callus surrounding the fracture site, part of the normal bone healing process. After 8 weeks (Fig. 5.7c), the gas pocket over the fracture site was not as prominent, potentially due to slowing of corrosion rate, dissipation of gas, and ingrowth of fibrous tissue. A greater presence of osteoids as well as new bone formation (Nb) in the periosteal region was observed progressively after 8 and 14 weeks. After 14 weeks (Figure 5.9e), the fracture was not yet completely healed when fixed with either WZ42 or Ti6Al4V pins. The elevated new bone formation seen in the WZ42 group at 8 and 14 weeks that was further confirmed by ALP staining. Osteoblast activity as indicated by ALP staining demonstrated promotion of new bone formation in the region surrounding the defect, at the leading edge to heal the fracture. Presence of osteoblasts peaked at 8 weeks for the WZ42 group with higher activity compared to the Ti6Al4V group. In the case of

the wire cuff placed over the cortical bone (Figure 5.11a), new bone formation as seen in blue was found in the region surrounding the Mg alloy cuff implant compared to the inert Ti6Al4V. Despite the fracture not having healed fully due to the instability of the intramedullary fixation, the healing process did not appear to be encumbered. In fact, the prevalence of new bone formation as seen in the mineralized new bone and osteoblast activity in regions adjacent to both types of Mg alloy implants confirms results of numerous studies reporting enhanced new bone formation around Mg-based implants [125, 127, 179] related to the cellular activity of Mg as discussed in Specific Aim 3 in Chapter 4 and due to osteoconductivity of the phosphate layer forming on the surface of magnesium-based implants [218]. Additionally, the consistent observations of a normal healing response of a fibrous capsule enclosing the operation site with no abnormal presence of inflammatory cells at the implant site as seen in other reports of Mg scaffolds showing good biocompatibility [225] indicated the local biosafety of the Mg alloy.

Overall, the positive biocompatibility and signs of healing with new bone formation indicate that the WZ42 alloy is a suitable candidate for orthopedic applications. Care must be taken however with limiting the mechanical stresses placed on the implant and that a consistent finish on the alloy is machined so as to reduce the onset of rapid corrosion and potential failure brought on by stress corrosion cracking. The model tested here represented an unusually high dynamic stress initiator on the implant site thus loading the femur completely transferring the load onto the Mg intramedullary pin leading to a highly aggressive load and corrosion condition causing the pins to ultimately fail. This aggressive load model nevertheless showed that despite having such an aggressive condition that could be perceived as an extreme event, the local and systemic safety of the alloy was still maintained under such high stresses leading to the alloy undergoing accelerated corrosion. Despite this release of degradation products, hydrogen gas

formation was not externally noticeable and the surrounding tissue response, kidney and liver, and blood parameters all remained normal. Thus, with temporary unloading as is required in the treatment of orthopedic injuries, the risk of failure of the WZ42 alloy would likely be diminished, still rendering the alloy as a promising orthopedic implant material, with possibilities in other medical device applications to be explored. In summary, considering the aggressive nature of the model providing high stress and accelerated corrosion conditions initially as is demonstrated by the results discussed, the fact that bone healing was observed as well as more importantly, all the serum and blood pathology profiles being normal combined with the histological analyses of the vital organs (liver and kidney) indicates the promise of the particular alloy, WZ42 for orthopedic fixation applications. The high strength and the favorable *in vitro* results discussed in aims 2 and 3 further complements the *in vivo* results discussed herein showing the promise of the system for possible exploration of its efficacy in other medical device applications. It is of the opinion of the author that semi or non-load bearing environments be placed on orthopedic Mg implants to fully demonstrate their safety and efficacy in these settings before targeting more demanding applications. Normally, orthopedic injuries are immobilized during early treatment, which should help reduce risk of Mg device failure as seen in the model here. Already, this pathway of lesser resistance has been observed in the Syntellix and K-Met screws used for minimally demanding bone fixation. To take our alloys further, first targeting a similar, low demand application would be prudent.

6.0 OVERALL CONCLUSIONS AND FUTURE WORK

This dissertation has presented a stream of research beginning with the alloy materials design and synthesis of Mg-Y-Ca-Zr-based alloys and testing of these alloys to validate the materials properties, evaluate their mechanical and corrosion behavior, investigation of their cytocompatibility and effects of the degrading Mg alloys on cells *in vitro*, and finally assess the *in vivo* biocompatibility, degradation, and bone healing response to implants manufactured from the Mg-Y-Zn-Zr-Ca alloy showing optimal properties in the previous results. A variety of alloy design parameters were modified to achieve the enhanced properties, including the addition of varying amounts of yttrium from 0 to 4.0 wt.%, adding Zn, applying the solution heat treatment, and hot working of the alloys using hot extrusion at various extrusion ratios. The work presented here represents novel alloy materials development for medical devices encompassing the selection of the alloy material components and analyzing the desired properties for various testing based on FDA, ISO, and ASTM standards adopted for degradable metals, for the ultimate goal of vetting the materials for orthopedic implant application, which was tested in the animal study. This thorough process described and discussed here can be applied to other degradable materials, serving as a basis for materials testing for resorbable orthopedic devices.

In the first aim, a variety of Mg-based alloys were processed, with the intention to control the corrosion rate, improve the mechanical properties, and maintain low toxicity in *in vitro* and *in vivo* studies. The initial study investigated as-cast and solution heat treated Mg-Y-Ca-Zr alloys

containing 1 wt.% and 4 wt.% Y [226] found that higher Y content present in WX41 contributed to an increase in grain size, while T4 solution treatment also resulted in grain coarsening. Upon applying extrusion to the cast alloys and heat treated alloys, grain size was dramatically reduced through the hot working and dynamic recrystallization processes. Despite X-ray diffraction showing the presence of single phase magnesium in all the alloys except the LPSO phases observed in the as-cast WZ42, secondary phase precipitates containing the alloying elements of Y, Ca, Zr, and Zn were present in all alloys at both the grain boundaries and within the grains. These precipitates became more dispersed after heat treatment and broken down during extrusion. The WZ42 alloy containing Y and Zn also contained the secondary phase $Mg_{12}YZn$ intermetallic which yielded enhanced properties as determined in later aims.

In specific aim 2, the corrosion and mechanical properties of the Mg-based alloys was investigated following synthesis in aim 1. Changes in the grain size through extrusion or heat treatment appeared to result in more uniform corrosion with the secondary phases being dissolved or disrupted to disperse the sites for microgalvanic corrosion as seen in section 3.3.1. By increasing the Y content in the Mg-based alloys, a more passive layer was formed as reported in first-principle studies on the stability of Y in Mg alloys conducted in the group earlier [139]. Strength of the alloys likewise improved with greater Y content in as-cast form, however in extruded alloys, addition of Y did not result in significant increase in strength due to the higher temperature required for extrusion leading to dynamic recrystallization and grain growth, partially negating the grain refining effect of extrusion and precipitation strengthening of the secondary phase. With extrusion and the significant grain refinement imparted, drastic improvements in strength and elongation however occurred as explained through the Hall-Petch relationship [105]. Above all other alloys and the commercial pure Mg and AZ31 materials

tested, the WZ42 (Mg-Y-Zn-Zr-Ca) alloy demonstrated significantly higher strength, placing it at the upper end of Mg alloys reported in literature, while maintaining a relatively low corrosion rate among those tested.

The results in specific aim 3 elucidated the effects on pre-osteoblasts and human mesenchymal stem cells cultured *in vitro* when directly in contact with the alloys and indirectly when in the presence of media containing the degradation products and alloying element chloride salts of the alloys discussed previously. High viability of the alloys, especially in extruded state was confirmed by MTT and Live/dead assays. The inspiration for the indirect studies drew from FDA recommendation of the use of ISO 10993:12 [227] where extract is collected from implant materials to expose to cells, as well as reports that diluting the collected extract at least 10x is required to [182] to obtain reliable *in vitro* cytotoxicity results of degradable materials. When testing both alloy extracts and the alloying element salts themselves, Mg-Y alloy degradation products and Y salts resulted in improved proliferation and higher ALP activity suggesting promotion of osteogenic differentiation. The WZ42 alloy in particular allowed for maximum proliferation and osteogenic differentiation, which along with the results from specific aim 2 warranted its selection to be implanted in the animal study of specific aim 4.

To culminate the transition from materials development to *in vivo* safety evaluation, the WZ42 pins were implanted into the intramedullary cavity of fractured rat femurs and as wires wrapped around the midsection of un-altered femurs, comparing the alloy to Ti6Al4V. Rats were sacrificed at 2, 8, and 14 weeks with material performance assessed based on 1) systemic toxicity analyzed by bloodwork, liver, and kidney histology, degradation product accumulation), 2) degradation measured by micro-CT reconstructions of the remaining WZ42 implants, and 3) local tissue response evaluated by histopathology of the local bone and surrounding soft tissue.

After successful implantation and maintained fracture stability after 1 week as confirmed by X-ray, it was found that degradation occurred leading to intramedullary pin failure due to perceived high stress related corrosion. Micro-CT analysis from 2 weeks onward revealed alloy pin degradation and fracture validating the stress corrosion cracking hypothesis initiated at the osteotomy site of high mechanical loading. However, the WZ42 alloy was still found to be with no recognizable accumulation of Mg or alloying elements in the blood, liver, or kidney, with no adverse effects in the blood count, metabolism, or kidney and liver function. Finally, histology of the local area at the implant site showed normal fracture healing and new bone formation. No abnormal inflammatory response was observed surrounding the implants.

Overall, the encouraging mechanical, bio-corrosion, and biological properties of the Mg-Y-Ca-Zn-Zr alloys, especially the WZ42 alloy, are indicative of their potential as viable orthopedic and craniofacial implant biomaterials. Future studies can be directed to further improve the quality and efficacy of the alloy processing to optimize the phase, composition and the microstructure keeping in mind the *in vitro* assessment showcasing the effects of the various alloying elements. This will in turn lead to optimized alloys with likely better mechanical and corrosion properties. The new and improved alloys can then be further investigated to explore the efficacy of the various alloys in the Mg-Y-Ca-Zn-Zr system in more relevant animal models that more accurately reflect the use of these novel class of alloys in various germane and critical orthopedic medical devices under low, semi-load as well as load bearing conditions optimally targeted to balance the corrosion and mechanical response with the desired biological outcome. Research in these directions will certainly help further the current research described herein and will promote the ultimate aim of this research study primarily, to optimize Mg alloys for orthopedic and craniofacial medical implant applications.

APPENDIX A

NOVEL PROCESSING OF IRON-MANGANESE ALLOY BASED BIOMATERIALS BY INKJET 3D PRINTING INKJET 3D PRINTING

The present work provides an assessment of 3D printed iron-manganese biodegradable scaffolds as a bone replacement materials. Iron-based alloys have been investigated due to their high strength and ability to slowly corrode. Current fabrications of Fe-based materials generate forms which must be machined into their desired form. By using 3D printing, mechanically milled Fe-30Mn (wt%) powder was directly processed into scaffolds, a technique which generates complex, customizable parts from powders. The 3D printed parts maintained an open porosity of 36.3% and formed a mixed phase alloy of martensitic ε and austenitic γ phases. Electrochemical corrosion tests showed that the 3D printed Fe-Mn to corrode significantly more rapidly than pure iron. The scaffolds exhibited similar tensile mechanical properties to natural bone which may reduce the risk of stress shielding, a harmful outcome of currently used permanent metallic biomaterials. Cell viability testing of MC3T3-E1 pre-osteoblast cells seeded directly onto the Fe-Mn scaffolds using the live/dead assay and with cells cultured in the presence of the degradation products of the scaffolds indeed demonstrated good in vitro cytocompatibility compared to tissue culture plastic. Cell infiltration into the open pores of the 3D printed scaffolds was also observed.

Based on this preliminary study, it was concluded that 3D printed Fe-Mn is a promising material for craniofacial biomaterial applications, and represents an opportunity for other biodegradable metals to be fabricated using this unique method.

A.1 INTRODUCTION

Critical size defects (CSDs) in bone arise when bone loss occurring through trauma, infection, or tumor resection exceeds a critical size whereby the injured bone cannot heal itself though mechanical fixation [228]. These bone defects result in nonunion fractures, and occur in 5-10% cases of traumatic fractures in the U.S. [229]. Treatment of critical size defects has typically been accomplished using bone grafting, either autologous or allogenic. Autologous bone grafting remains the preferred treatment because it fulfills goals of being osteogenic, osteoinductive, and osteoconductive. Due to complications arising from harvesting autologous bone such as donor site morbidity and pain, cadaveric bone or allograft bone may be used, though these treatments bare the risk for disease transmission that can prove to be fatal. Increasing interest has therefore been placed on developing synthetic bone grafts or bone graft substitutes which are relatively more abundant than bone grafts and carry reduced risk of disease transmission.

In order to fabricate synthetic bone scaffolds, three dimensional (3D) porous structures have been pursued to allow for bony ingrowth, infiltration of cells and fluids, and to mimic the natural cellular structure of bone [230]. Pore distribution, size, and orientation largely influences cell bone regeneration and scaffold degradation kinetics [231]. Furthermore, to treat these complexly shaped critical size defects in bone, alternative fabrication methods must be used and explored that go beyond the realms of conventional manufacturing classes of casting,

deformation, machining, and joining. Direct manufacture of porous scaffolds into desired geometries address needs of patients whose bone defect is outside the size range of pre-manufactured implants and allow for improved surgical outcome by providing a custom-fit to the anatomical site [5]. Thus, solid free-form fabrication (SFF) approaches have been gaining much attention of late, for developing bone scaffolds using powder arranged and consolidated layer-by-layer to generate 3D structures based on CAD models, which may be obtained from a variety of patient imaging modalities such as computed tomography (CT) or magnetic resonance imaging (MRI) [232]. SFF techniques such as electron beam melting (EBM) and selective laser melting (SLM) have been used to directly fabricate biomedical implants with specific microstructures and mechanical properties superior to wrought or cast parts of the same material [233]. The benefits of SFF approaches to recycle powder and control properties and design contribute to significant cost savings over conventional CNC machining [233]. Among SFF methods, the inkjet 3D printing (3DP) provides advantages such as its potential to selectively form parts from powder of any material given agglomeration through an appropriate binder formulation, as well as its high scalability, and cost efficiency. Developed in the early 1990s at MIT [234], this additive manufacturing technique begins with a thin layer of powder being spread across build platform using a roller. A printhead moves across the build platform, printing a layer of liquid binder selectively onto the layer of powder as defined by the CAD model. The roller spreads a new layer of powder on top of printed layer, and the process is repeated until each slice of the part has been completed. 3DP has been used to fabricate bone scaffolds from a wide range of materials among polymers, ceramics, and composites [235]. Metals, such as stainless steel [236], and titanium [237] and have also been fabricated and hold promise especially for load bearing applications. The use of a biodegradable metallic powder in 3DP

would allow for custom geometry parts to be fabricated with higher strength than attainable by polymers, higher ductility than attainable by ceramics, while degrading over time to allow for the scaffold to be replaced by new bone. Furthermore, 3DP could allow for control of the porous architecture of the printed scaffolds.

Interest in biodegradable metals has been increasing rapidly in recent years for clinical applications in orthopedic implants and cardiovascular stents. In order to provide treatment for bone defects, the biodegradable material must provide full mechanical stability upon implantation. While new bone formation occurs, the implant material degrades gradually, transferring the load to the regenerated bone. Among biodegradable metals, Fe-based alloys degrade more slowly and possess better mechanical properties than Mg-based alloys [63], holding potential for bone scaffold applications. Iron has been investigated as a biodegradable stent, without producing a pronounced inflammatory response or systemic toxicity during an 18 month period [74]. Fe stents also showed no significant obstruction of the stented vessel, however was believed to be infeasible as a biodegradable metal due to its slow corrosion rate [60].

Several studies have been performed to increase the degradation rate of Fe-based materials without compromising their mechanical properties. Alloying Fe [13, 58, 62-64, 66-68] and microstructural modification of pure iron have been pursued to accelerate corrosion [70, 71]. Among these approaches, powder metallurgy was used to process Fe-Mn alloys [13, 62, 63, 67] to generate bulk forms. Although reports have been made on biodegradable metals fabricated with a controlled structural topology by casting into a 3D printed template [238], no studies have shown biodegradable metals being inkjet 3D printed. In the present study, Fe-30Mn (wt%) powder was directly processed into scaffolds using 3DP. Fe-30Mn was one of the recommended

alloys by Hermawan et. al. [13] due to its magnetic, mechanical, and corrosion properties with the objective of use as scaffolds for reconstruction of bone defects. For this application, the scaffold must fulfill the criteria of filling the complicated 3D defects, providing temporary load bearing while the tissue heals, fully degrading after the bone has fully regenerated, and more importantly, allowing for perfusion of biofactors [239]. Scaffolds must also find a suitable porosity to be dense enough to withstand the necessary loads during tissue regeneration by possessing mechanical properties at least equivalent to the native tissue, while be porous enough to allow for delivery of biofactors. In addition, the scaffold must allow for uninhibited osteoblast cell adhesion throughout the scaffold surface and pores for bone remodeling to occur. The 3D printed Fe-Mn biomaterials described in this work were evaluated in terms of these bone scaffold criteria by testing *in vitro* cytocompatibility using direct and indirect pre-osteoblast cell viability tests, determining electrochemical corrosion behavior, and measuring tensile mechanical properties.

A.2 MATERIALS AND METHODS

A.2.1 Materials preparation and characterization

Elemental powders Fe (Alfa Aesar, Ward Hill, MA, 98%, -325 mesh) and Mn (Alfa Aesar, 99.3%, -325 mesh) corresponding to Fe-30Mn (wt%) were milled in a P5 planetary mill (Fritsche, Idar-Oberstein, Germany) for 30 min. Morphology of the precursor Fe and Mn powder and the mixed Fe-30Mn powder was imaged using scanning electron microscopy (SEM, JSM-6610, JEOL, Tokyo, Japan). The powder nominal compositions, determined by inductively

coupled plasma optical emission spectroscopy (ICP-OES, iCAP duo 6500 Thermo Fisher, Waltham, MA), are listed in Table A.1 and confirm to the originally measured nominal composition. The milled Fe-30Mn powder was 3D printed into parts for testing using an Ex-Lab (The ExOne Company LLC, North Huntingdon, PA) machine with a water-based organic binder. Parts were printed with a layer thickness of 100 μm. The parts were cured at 230°C for 3 h to remove binder and increase green strength to allow unbound powder to be removed using compressed air, after which the parts were sintered at 1200°C for 3 h in ultra-high purity N_2. Parts of dimensions 5 mm x 8 mm x 3 mm (n = 11) were measured before and after sintering to determine part shrinkage, with averages and standard deviations reported. Phase analysis of the mixed and sintered Fe-30Mn was conducted using X-ray diffraction (XRD) employing an X'pert Pro system (Philips, Amsterdam, the Netherlands) equipped with CuKα radiation (λ = 1.5418 Å) with a Si-detector (X'celerator) operated at 45 kV and 40 mA. Absolute density of the mixed powder and sintered 3DP parts were measured using an AccuPyc II 1340 helium pycnometer (Micromeritics, Norcross, GA). Envelope density of sintered 3DP parts was measured using a GeoPyc 1360 (Micromeritics). Using these density values, percent open porosity was calculated using the following equation:

$$\textit{Open porosity (\%)} = \textit{(absolute density – envelope density)/absolute density} \qquad \text{Eq. 1}$$

To determine the extent of oxide formation and debinding during the curing and sintering process, the oxygen and carbon content of polished sintered samples were measured using LECO TC600 and LECO CS600 systems (LECO, St. Joseph, MI) which operate by the inert gas fusion thermal conductivity method.

A.2.2 Microstructure characterization

3DP Fe-30Mn samples were mounted in epoxy (EpoxiCure, Buehler), mechanically polished (Tegramin-20, Struers, Ballerup, Denmark), and chemically etched in a nital solution (2% HNO3 in ethanol). The microstructure was observed under an optical microscope (Axiovert 40 MAT, Carl Zeiss, Jena, Germany) and SEM (JEOL JSM-6610 and Philips XL-30FEG, Amsterdam, the Netherlands) with energy dispersive X-ray (EDX) analyzer attached to the SEM to conduct elemental analysis.

Table A.1 Chemical composition with standard deviation of the mixed Fe-30Mn (wt.%) powder used for 3D printing.

Material	Chemical composition (wt.%)				
	Fe	Mn	Ni	Si	C
Fe-30Mn	71.221 ± 0.609	28.718 ± 0.611	0.015 ± 0.001	0.046 ± 0.001	>.001

A.2.3 Mechanical properties

Bar samples were printed, cured, and sintered, followed by machining into standard dogbone specimens (gage length 13.5 mm, width 3 mm, thickness 3 mm) along the direction of the inkjet printed lines in accordance with ASTM-E8-04 [240]. The uniaxial tensile tests were conducted at room temperature at a cross-head speed of 1.3 mm/min using an MTS11 – 50kN electro-mechanical load frame (MTS, Eden Prairie, MN) equipped with laser extensometer. A tensile stress-strain curve was generated from each sample, from which yield strength (YS), ultimate

tensile strength (UTS), Young's modulus (E), and percent elongation (%) were determined. The tensile yield strength was determined from the linear portion of the stress-strain curve. An average and standard deviation of measurements from 3 samples was reported.

A.2.4 Electrochemical corrosion test

Potentiodynamic polarization was used to test corrosion of the 3DP Fe-30Mn alloy (n = 4) compared to bulk pieces of pure Iron (Alfa Aesar, 99.97+%). Samples with an exposed surface of ~0.5 cm^2 were connected to a copper wire lead and mounted in epoxy resin. The mounted samples were mechanically polished down to 1 µm, leaving one surface exposed to the electrolyte, and were tested immediately and cleaned with isopropyl alcohol before use. Tests were carried out on an electrochemical workstation (CH-604A, CH Instruments, Inc., Austin, TX) and consisted of stabilization for one hour to reach open circuit potential followed by potentiodynamic polarization at a scanning rate of 1 mV/s and potential window of 500 mV above and 200 mV below the open circuit potential (OCP). A three electrode cell was employed with platinum as the counter electrode, Ag/AgCl as the reference electrode, and the sample as the working electrode. To simulate physiological conditions, tests were conducted in pH 7.4 Hanks' Balanced Salts solution (HBSS H1387, Sigma Aldrich, Canada) supplemented with 0.35 g/l sodium bicarbonate and held at 37.4 °C. The cathodic and anodic portions of the generated Tafel plots were fit linearly to allow determination of the total corrosion current, I_{corr}, at the intersection point with the corrosion potential, E_{corr}. In curves where the intersection did not occur at the corrosion potential, E_{corr}, the current where the anodic extrapolation intersected the corrosion potential was used to determine I_{corr} since this would be more indicative of the alloy corrosion.

Corrosion current density, i_{corr}, was calculated by dividing I_{corr} by the exposed surface area of the specimen. Two values of exposed surface area were used to estimate i_{corr} values. Nominal surface area was measured assuming the surface of the polished sample was flat without porosity, while true surface area was estimated with inclusion of surface area from open porosity. True surface area was approximated first by determining distribution of pore sizes using ImageJ (Version 1.46r, National Institutes of Health, Bethesda, MD). 200x magnification micrographs of random locations (n = 5) on samples polished to 1 μm were converted to binary to distinguish between the pores and matrix. The area of each pore was measured using the particle analysis function. Average pore depth was estimated by using the measuring tool of ImageJ drawn from the bulk surface to root of the pore in SEM images of random locations taken where the sample edge meets the surface (n = 8). Pores were approximated as cylinders and surface area of pores was extrapolated from the 500 μm × 375 μm window of the 200x micrograph to the entire nominal surface area.

From the i_{corr} value, corrosion rate (CR) utilizing nominal and true surface area was estimated according to calculations from ASTM G102-89 [241]:

$$CR = K \frac{i_{corr}}{\rho} EW \qquad \text{Eq. 2}$$

where CR has units of mm per year (mmpy), K = constant, (3.27×10^{-3} mm g/μA cm yr), i_{corr} = corrosion current density, ρ = density (g/cm^3), and EW = equivalent weight (g/eq). Equivalent weight was calculated based on the oxidation reaction of Fe and Mn to form Fe^{2+} and Mn^{2+}. For pure Fe, EW = 27.92 g/eq, for Fe-30Mn, EW = 27.78 g/eq. As measured absolute density values were used. Samples were rinsed with ethanol and air dried, and subsequently characterized using optical microscopy, SEM, and EDX to assess the formation and composition

of the corrosion products. Corrosion products were removed by brief immersion in a solution of 1000 ml HCl, 20 g Sb_2O_3, 50 g $SnCl_2$, and surface morphology was again captured using SEM.

A.2.5 Indirect cytotoxicity test

3DP Fe-30Mn samples (n=5) were barrel finished in a mass finishing unit (Denta2000, Howard Lake, MN), ultrasonically cleaned in isopropyl alcohol, air dried, and sterilized by ultraviolet radiation for 1 h. The specimens were incubated in modified Eagle's medium alpha (αMEM) supplemented with 10% fetal bovine serum (FBS), 100 U/ml penicillin, and 100 μg/ml streptomycin at a sample weight to extraction medium ratio was 0.2 g/ml in accordance with the EN ISO standard 10933:12, and incubated at 37 °C in a humidified atmosphere with 5% CO_2 for 72 h. The extract was collected, with less concentrated extracts prepared by diluting the 100% extract into 50%, 25%, and 10% extract solutions. Extracts were sterile filtered using 0.2 μm syringe filter before being added to cells. Fe and Mn concentration contained in the extract solutions was measured using ICP-OES. The samples immersed in αMEM were rinsed with ethanol, dried, and subsequently characterized using SEM and EDX to assess the formation of corrosion products.

The murine osteoblastic cell line (MC3T3-E1, American Type Culture Collection, Rockville, MD) used in *in vitro* cell cytotoxicity experiments was cultured in modified Eagle's medium alpha (αMEM), 10% fetal bovine serum, 100 U/ml penicillin and 100 μg/ml streptomycin at 37°C in a humidified atmosphere with 5% CO_2. The cells were seeded in 96-well cell culture plates at 6 x 10^3 cells/200 μl culture medium and incubated for 24 h to attach before adding the extraction medium. Fresh culture medium without extract served as the negative control while 10% DMSO in culture medium served as the positive control. The medium was

then replaced with 200 µl of extraction medium at 100%, 50%, 25%, and 10% extract concentrations and incubated under cell culture conditions for 1 and 3 days, after which the extracts were removed and replaced with fresh media. The MTT assay was performed to assess the cytotoxicity of the corrosion extracts according to the Vybrant MTT Cell Proliferation Kit (Invitrogen Corporation, Karlsruhe, Germany) by first adding 10 µl of 12mM 3-(4,5-Dimethylthiazol-2-yl)-2,5-diphenyltetrazolium bromide (MTT) dissolved in phosphate buffer solution (PBS, pH = 7.4) to each well. After 4 h of incubation at 37°C, 100 µl formazan solubilization solution (SDS-HCl solution) was added to each well and incubated for 12 h. The absorbance of the samples was measured using the Synergy 2 Multi-Mode Microplate Reader (BioTek Instruments, Winooski, VT) at 570 nm wavelength. The difference of sample absorbance and mean positive control absorbance was divided by the absorbance of the mean positive control subtracted from the mean negative control to determine percent viability of cells, with the negative control standardized as 100% viability.

A.2.6 Direct cell viability and adhesion test

To evaluate direct cell viability, MC3T3-E1 cells were cultured directly on 3DP Fe-30Mn samples. Cell culture conditions and media composition were the same as in the indirect cytotoxicity test. Samples were printed in dimensions of 10 mm x 10 mm x 1 mm, barrel finished, ultrasonically cleaned in isopropyl alcohol, air dried, and sterilized by ultraviolet radiation for 1 h. 3DP samples were incubated in culture media for 10 min after which cells were seeded on the samples at a density of 4×10^4 cells/ml. Viability of the seeded cells was evaluated after 1 and 3 days using the LIVE/DEAD Viability/Cytotoxicity Kit (Invitrogen Corporation, Karlsruhe, Germany) following the manufacturer‘s protocol. The assay determines the

viability/cytotoxicity of cells by differentiating between live and dead cells using fluorescence microscopy of two different dyes. Briefly, the 3DP samples with attached MC3T3-E1 cells were washed with PBS and stained for 30 min at room temperature in the dark with 2 μmol/L ethidium homodimer-1 and 4 μmol/L calcein AM dissolved in PBS. Live and dead cells images were then captured using fluorescence microscopy. To fix cells attached to the 3DP samples, they were rinsed in PBS, fixed in 2.5% glutaraldehyde solution for 15 minutes at room temperature, rinsed 3 times with the PBS, followed by dehydration in a gradient ethanol/PBS mixture (30%, 50%, 70%, 90%, 95%, 100%) for about 10 minutes each and dried. Sample surfaces with attached cells were then observed by SEM.

A.2.7 Statistical analysis

SPSS Statistics 17.0 (SPSS Inc., Chicago, IL) was used to conduct statistical analysis. A t-test was used to analyze the difference between the means of Fe-30Mn and Fe corrosion rates, whereas the Mann-Whitney U test was used to access difference in corrosion potential due to inequality of variance. Statistical significance was defined as $P < 0.05$.

A.3 RESULTS

A.3.1 Phase and microstructure characterization of Fe-Mn powder and 3D printed parts

Powder morphology of the Fe and Mn precursor powders used in this study as well as the Fe-30Mn powder after milling for 30 min are shown in Figure A.1. Both Fe and Mn powders were -

325 mesh, with particle size confirmed as smaller than 44 μm. However, a large variation in powder size was observed, with the presence of much finer particles (<10 μm). Particle shape also varied significantly with both angular and more spherical particles among the precursor powders, while the final mixed Fe-30Mn powder (Figure A.1c) was generally angular in morphology. XRD (Figure A.2) show the as-milled powder to consist of α-Fe and α-Mn phases. After curing and sintering, the 3D printed parts derived from this milled Fe-30Mn powder showed formation of martensitic ε and austenitic γ phases. Sintered parts contained 0.18 wt.% carbon and 1.79 wt.% oxygen as measured using inert gas fusion infrared and thermal conductivity detection. The low carbon content indicated adequate burnout of the polymeric binder.

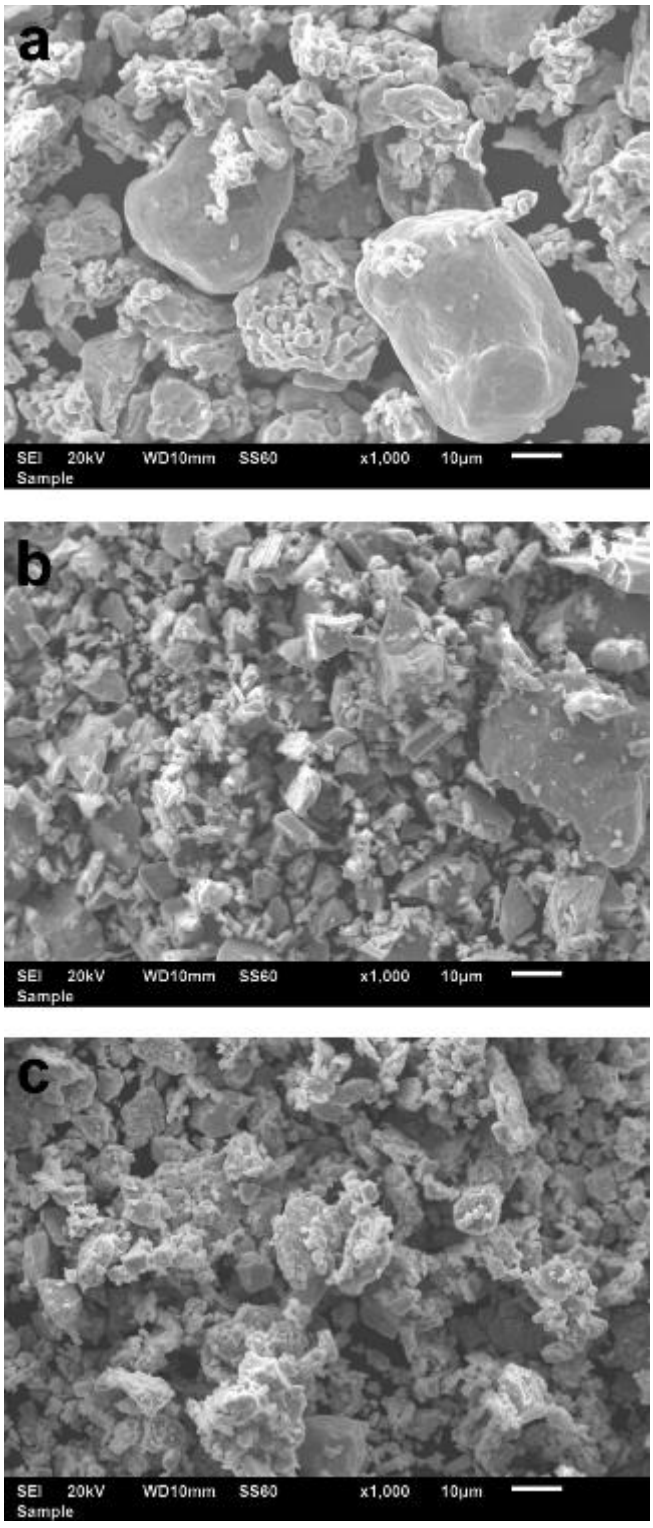

Figure A.1. SEM of powder precursors used to fabricate Fe-30Mn 3DP parts: a) Fe -325 mesh powder; b) Mn -325 mesh powder; c) 70 wt.% Fe – 30 wt.% Mn mixed powder.

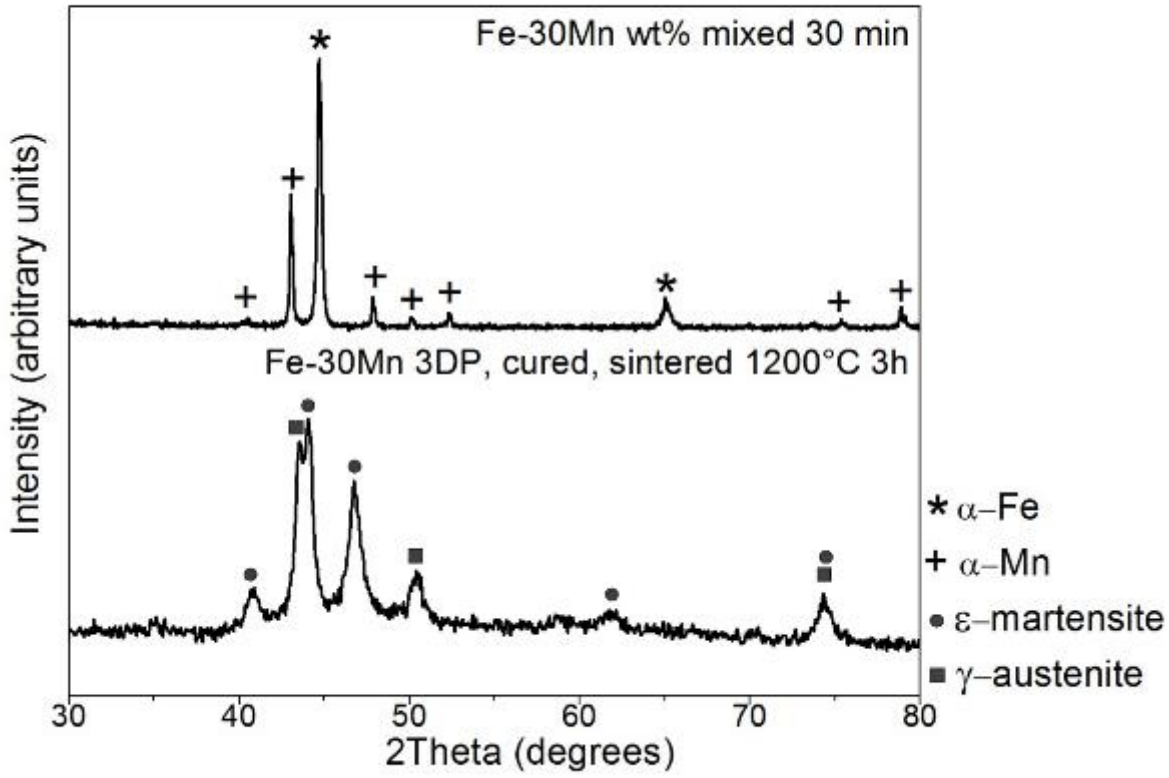

Figure A.2. XRD patterns of Fe-30Mn mixed powder and Fe-30Mn after 3DP, curing, and sintering.

Figure A.3 shows examples of the parts printed using the 3D printer using Fe-30Mn milled powder. Pores of diameter 1 mm (Figure A.3a) and 500 μm (Figure A.3b) were fabricated, demonstrating the potential of the technology to fabricate parts with user-controlled pore geometry. However, after curing the parts to remove the binder and improve the green strength, it was difficult to remove unbound powder from deep inside the pores without damaging the green construct. Figure A.3c and Figure A.3d display the ability of 3D printing to produce complex custom shaped designs as exemplified in the printing of the 3 cm long

miniaturized human femur. After sintering (Figure A.3c), however, the 3DP part surface is non-uniform and rough. In order to create a polished, uniform finish and to remove the oxide layers formed on the surface, the printed parts were barrel finished after sintering, with the result seen in Fig. A.3d. After sintering, the parts encountered shrinkage as expected, due to reduction in porosity by repacking, characteristic necking, and inter-atomic diffusion and other sintering related phenomena causing reduction in grain boundary area. Rectangular parts encountered fairly uniform shrinkage in all three axes: 19.5% ± 0.8% (axis along direction of printed lines), 18.0% ± 3.7% (axis perpendicular to direction of printed lines), and 21.2% ± 2.5% (axis normal to build platform). Density of the 3DP parts after sintering was also measured, with an absolute density of the Fe-30Mn 3DP parts as 7.62 g/cm^3, while the envelope density was 4.85 g/cm^3. Since absolute density measures the density of a specimen excluding open porosity while envelope density includes open porosity in its measurement, dividing the difference of absolute and envelope density by the absolute density gives an estimate of the percentage open porosity. Using Eq. 1, the percentage open porosity of the 3DP Fe-30Mn parts was found to be 36.3%, a value that can be considered conducive for facilitating cellular infiltration as well as inducing corrosion, a facet that is much needed in the Fe-based system as discussed earlier.

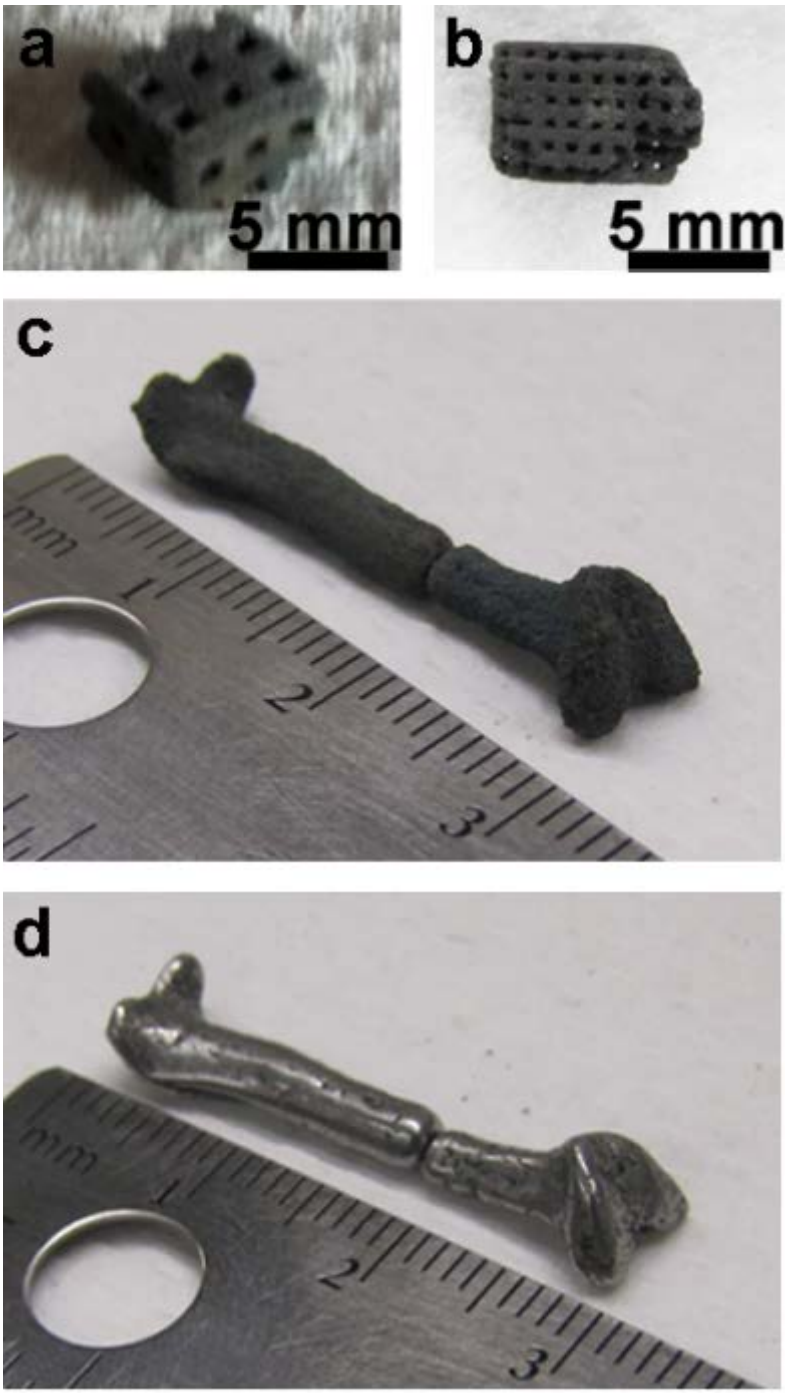

Figure A.3. Photographs of example parts 3D printed from Fe-30Mn powder after sintering: part with square pore sizes of lengths a) 1 mm and b) 500 μm; miniature human femur c) before tumble finishing and d) after tumble finishing.

Microstructure images are displayed in Figure A. 4, confirming the 3DP parts were not fully dense after sintering at 1200 °C for 3 h. The formation of classical necked regions between particles separated by grain boundaries was observed, with grain sizes ranging from 5 – 15 μm.. SEM and EDX analysis (Figure A. 4c) revealed grain boundaries containing higher Mn content compared to the bulk grain, indicating segregation of Mn-rich phases at the grain boundaries. The presence of Si in the EDX analysis may be attributed to polishing using SiC papers leaving residual SiC particles on the alloy surface.

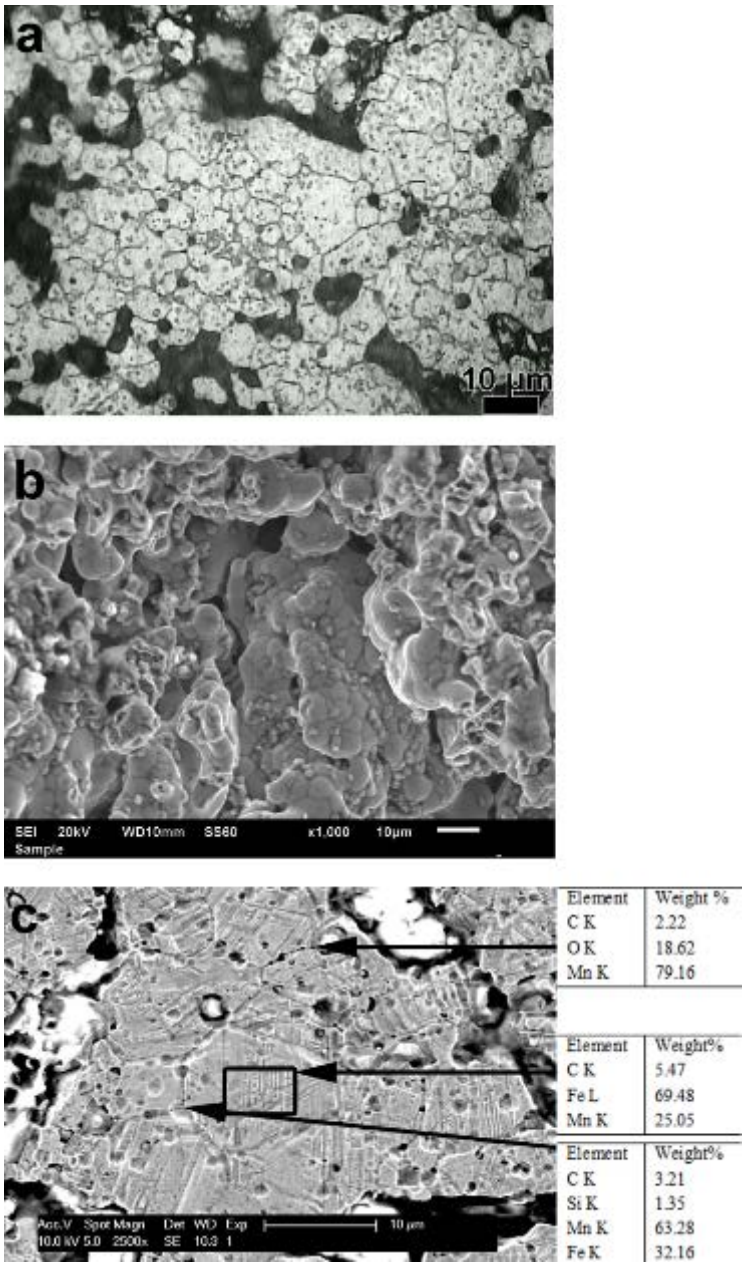

Figure A. 4. Microstructure of Fe-30Mn 3DP parts after sintering imaged using a) optical microscopy after polishing; b) SEM without polishing; c) SEM after polishing with EDX performed at regions indicated by arrows.

A.3.2 Tensile mechanical properties of 3DP Fe-30Mn

Tensile properties of the 3D printed Fe-30Mn alloy are presented in Table A.2 in comparison with sintered and rolled Fe-30Mn, pure iron, and natural bone. Due to the presence of pores, the tensile properties of the printed Fe-30Mn alloy were greatly reduced compared to the as-rolled Fe-30Mn and iron in terms of the reported values for yield strength, ultimate strength, and maximum elongation. However, the measured tensile properties for 3DP Fe-30Mn were very similar to those of natural bone: within the reported ranges of bone for yield and ultimate tensile strength, slightly less in terms of elongation, but double the value of Young's modulus, still very much lower than that of iron thus keeping the option for the 3-D printed material to exhibit reduced stress shielding when implanted as a metallic implant for orthopedic device applications.

Table A.2. Mechanical properties of 3D printed Fe-30Mn compared to Fe-30Mn produced by sintering and rolling, pure Fe, and natural bone.

Material	Tensile properties			
	Yield strength (MPa)	Ultimate strength (MPa)	Elongation (%)	Young's modulus (GPa)
Fe-30Mn 3DP	106.07 ± 8.13	115.53 ± 1.05	0.73 ± 0.15	32.47 ± 5.05
Fe-30Mn sintered and rolled [13]	239 ± 13	518 ± 14	19.0 ± 1.4	
Iron [13]	150	210	40	211
Natural bone [11]	104-121	86.5-151	1-3	14.1-17.3

A.3.3 Corrosion behavior of 3DP Fe-30Mn

Potentiodynamic polarization curves (Tafel plot) of polished 3DP Fe-30Mn and pure iron recorded at a scan rate of 1 mV/s in HBSS are shown in Figure A.5 as a representative plot of the multiple samples tested. As shown in the plot, corrosion current density, i_{corr}, corrosion potential, and corrosion rate were estimated using the Tafel plots and are listed as averages in Table A.3, with corrosion current density and corrosion rate reported after calculating using both nominal surface area and estimated true surface area, the averages of which are also listed in the table. With the estimated true surface area being higher than the nominal surface area as indicated in Table A.3, both, the corrosion current and corrosion rates were decreased, accounting for the higher surface area exposed to the electrolyte with greater access to microsites of different potentials [62]. Even after factoring in open porosity, the corrosion current density and corrosion rates were significantly higher for the 3DP Fe-30Mn than pure Fe, while corrosion potentials were lower, indicating lower stability in HBSS.

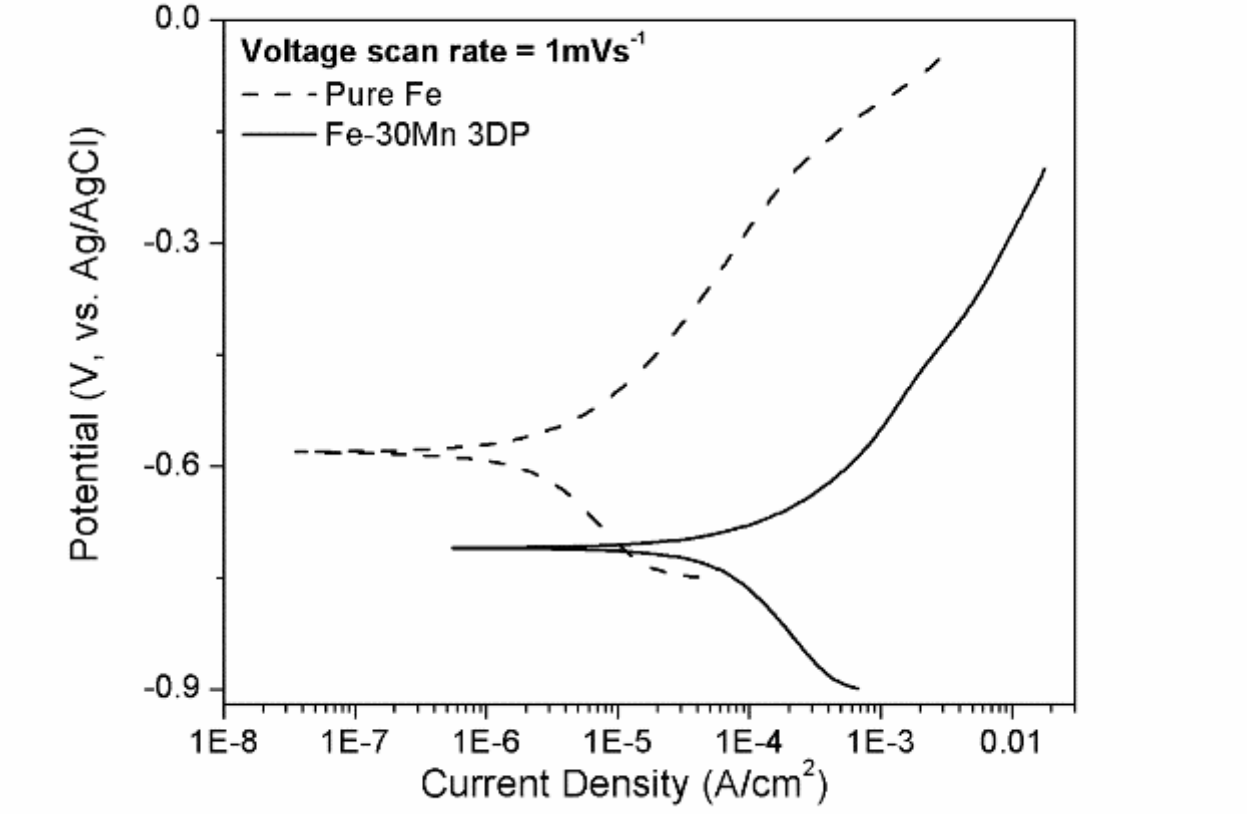

Figure A.5. Representative potentiodynamic polarization curves of 3D printed Fe-30Mn compared to pure Iron conducted in Hanks‘ Balanced Salts solution at 37 °C.

Figure A.6 clearly shows the difference between the corroded surface of the 3DP Fe-30Mn compared to the relatively uncorroded surface of iron. Optical microscopy showed 3DP Fe-30Mn (Figure A.6a) displayed red-brownish corrosion products on the surface, whereas the iron surface (Figure A.6b) and SEM image of iron (Figure A.6f) remained smooth, with scratches from polishing still apparent. EDX performed on various points on the corroded surface (Figure A.6d, inset of Figure A.6c) showed distinctive surface morphologies. Granular corrosion deposits rich in O and C, and also containing Na, as well as Cl, needle-like corrosion

products also rich in O and C as well as P and Cl were observed on the surface. Finally, most of the surface appeared to be blanketed by a cracked layer again rich in C and O with Na, Si, P, Cl, and Ca, on top of which the other corrosion products were observed. After removing the corrosion products as seen in the SEM micrograph of Figure A.6e, some areas of the surface appeared to have undergone corrosion while other areas appeared relatively un-corroded, confirming visual observations of localized corrosion occurring.

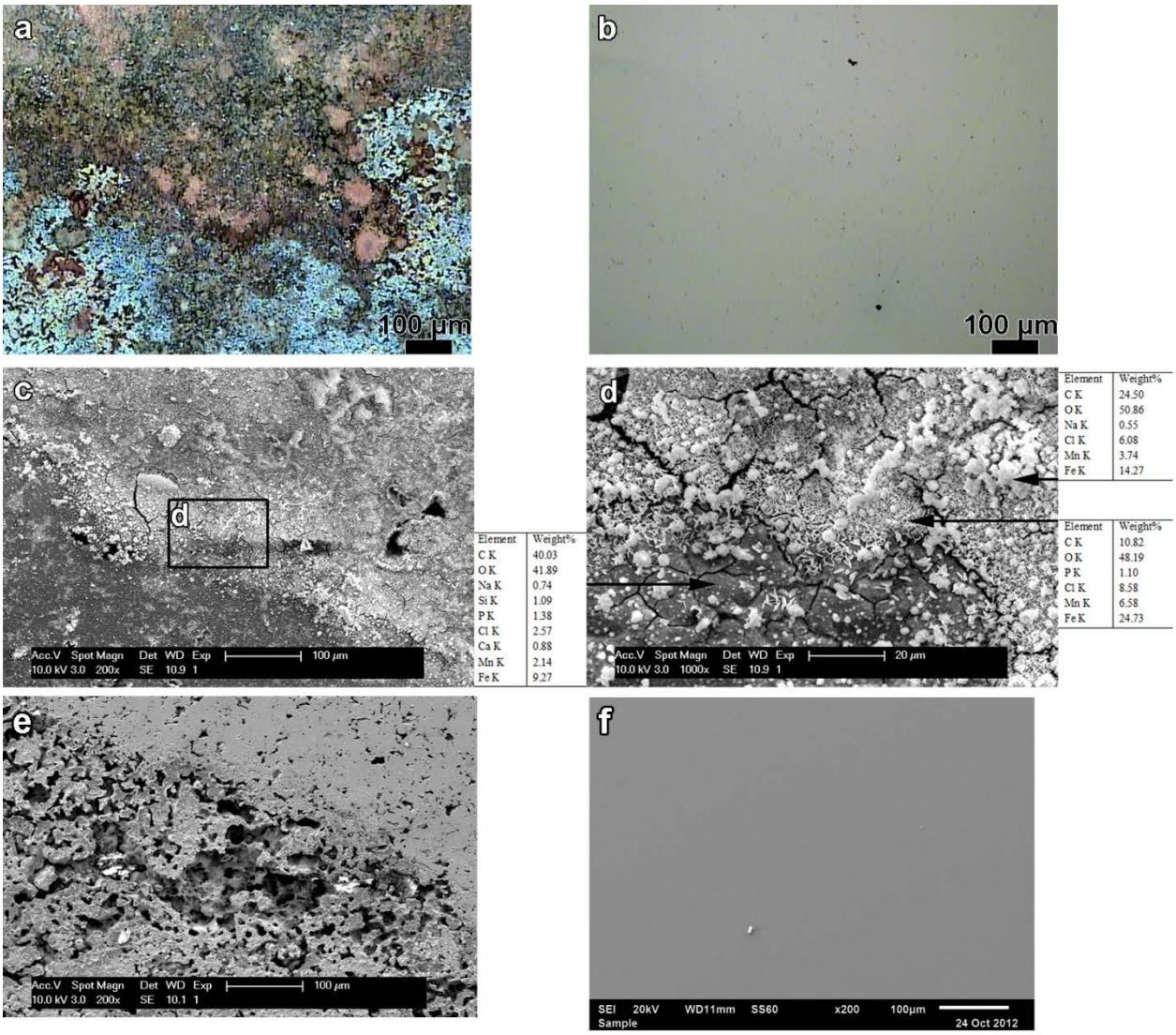

Figure A.6. Optical microscopy (a & b) and SEM images (c-f) showing surface morphologies of a, c, d) 3D printed Fe-30Mn with EDX analysis after potentiodynamic polarization tests and e) after cleaning in solution of HCl/Sb2O3/SnCl2; b & f) pure Iron after potentiodynamic polarization tests.

Table A.3. Electrochemical corrosion measurements conducted in Hanks' Balanced Salts solution at 37 °C of 3D printed Fe-30Mn and pure Fe: corrosion potential, corrosion current density, and corrosion current. * $p < 0.05$ between groups.

Material	Nominal surface area (cm^2)	Estimated true surface area (cm^2)	Corrosion potential, E_{corr} (V)	Corrosion current density using nominal surface area, i_{corr} ($\mu A\ cm^{-2}$)	Corrosion rate using nominal surface area, mm/year (mmpy)	Corrosion current density using estimated true surface area, i_{corr} ($\mu A\ cm^{-2}$)	Corrosion rate using estimated true surface area, mm/year (mmpy)
Fe-30Mn 3DP	0.42 ± 0.017	1.46 ± 0.074	-0.69 ± 0.045*	224.99 ± 70.35*	2.81 ± 0.88*	58.44 ± 17.27*	0.73 ± 0.22*
Iron	0.47 ± 0.13	0.47 ± 0.13	-0.58 ± 0.030	5.61 ± 2.54	0.065 ± 0.030	5.61 ± 2.54	0.065 ± 0.030

A.3.4 In vitro cytotoxicity of 3DP Fe-30Mn

Figure A.7 plots the indirect cytotoxicity results of 3DP Fe-30Mn corrosion extracts on MC3T3 cells cultured for 1 and 3 days using the MTT assay. After 1 day exposure to the corrosion extract, cells exhibited increasing viability with lower concentration of corrosion extract, indicating some cytotoxicity of the degradation products on the MC3T3 cells. After 3 days exposure to the corrosion extract, the MC3T3 cells displayed increased cell viability (>80% compared to the control of cell culture media without corrosion extract). Similar to results of 1 day culture, cells after 3 days culture showed higher viability with lower extract concentration. The collected extract solutions contained an average concentration of 13.43 ± 2.33 ppm Mn and 1.47 ± 0.30 ppm Fe after the 3 day incubation sample incubation period. After this immersion time in media, the samples were imaged using SEM (Figure A.8) to display again the effects of

corrosion on the alloy surface. Once again, corrosion products had formed, containing high amounts of C and O, with varying amounts of N, Na, and Cl. Pit formation was also observed with additional cracked corrosion deposits on the surrounding surface. Nonetheless, the surface of the samples appeared to have undergone relatively little corrosion and negligible weight loss after 3 days of immersion compared to the 3D printed alloy subjected to electrochemical corrosion.

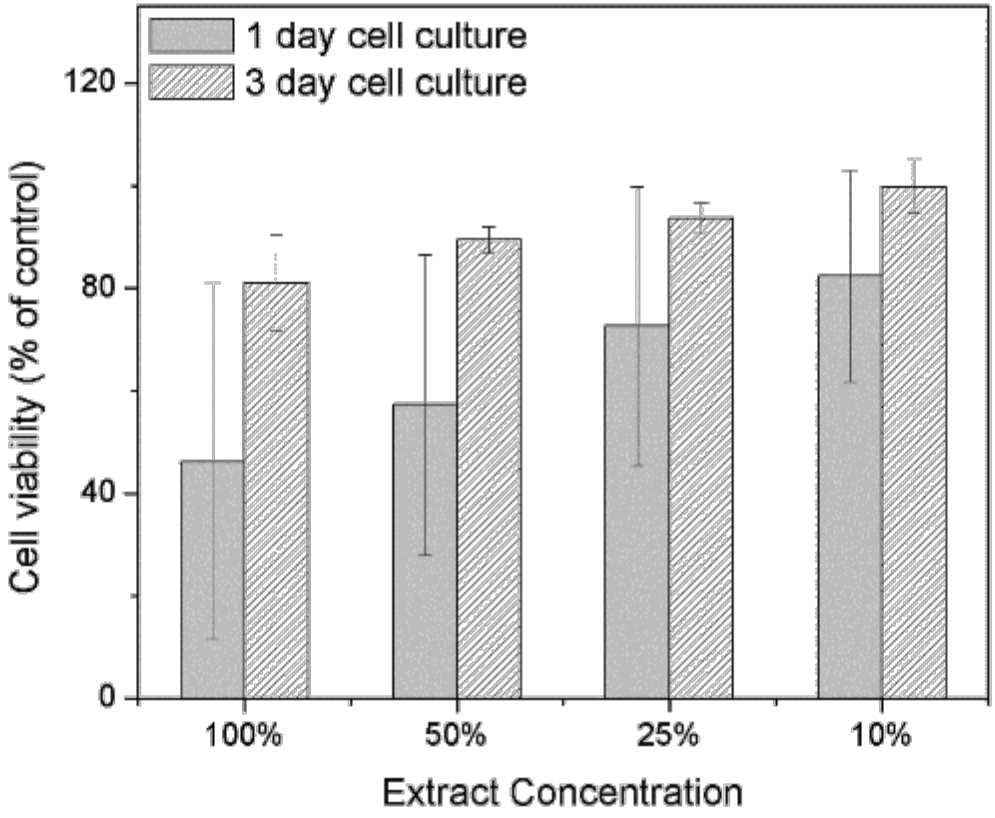

Figure A.7. Cytotoxicity of MC3T3 cells cultured for 1 and 3 days in extract media from 3D printed Fe-30Mn immersed in αMEM cell culture media supplemented with 10% FBS and 100 U/ml penicillin, and 100 μg/ml streptomycin.

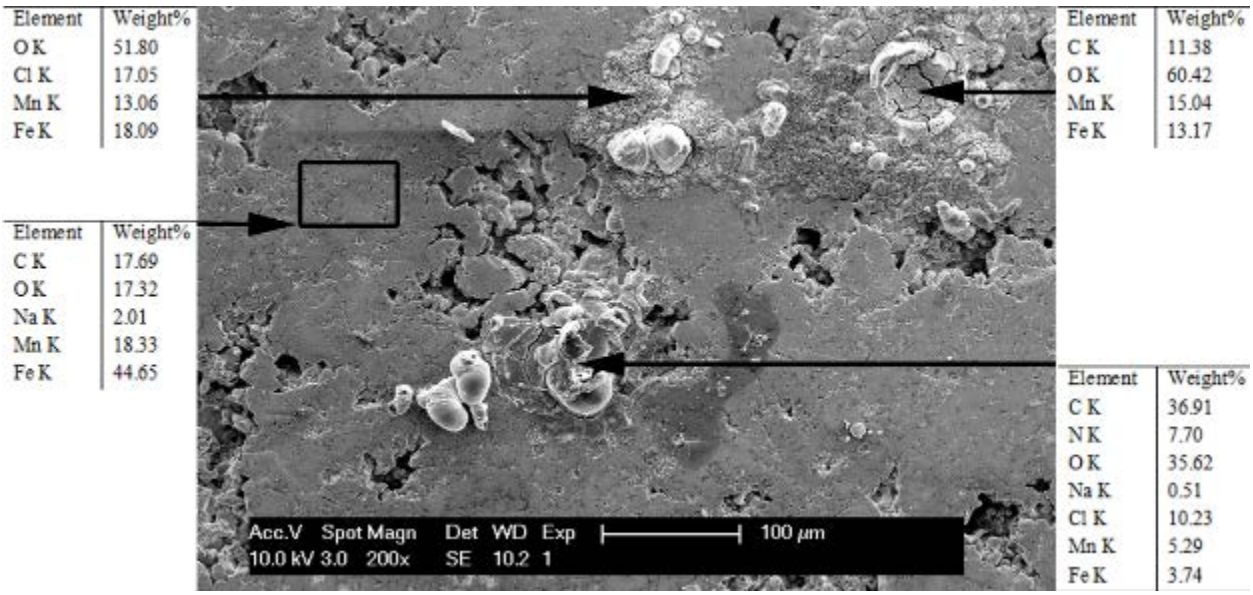

Figure A.8. SEM image and EDX analysis of 3D printed Fe-30Mn sample after 3 days immersion in αMEM cell culture media supplemented with 10% FBS and 100 U/ml penicillin, and 100 µg/ml streptomycin.

Fluorescence microscopy from the live/dead assay (Figure A.9) shows similar live MC3T3 cell (green) attachment, with very few dead (red) cells, on the surface of sintered 3DP Fe-30Mn (Figure A.9a) after one day compared to the tissue culture plastic control (Figure A.9b). After 3 days culture, 3DP Fe-30Mn again displayed high live cell attachment comparable to tissue culture plastic, with a higher cell density than day 1. SEM images of MC3T3 cells attached on the surface of the 3DP Fe-30Mn scaffold (Figure A.10) confirmed the live/dead assay results with high attached cell density not only on the surface, but also infiltrating within pores of the 3D printed parts. Again, SEM images of cells attached after 3 days culture (Figure A.10c & Figure A.10d) showed higher cell density compared to images of day 1 culture (Figure A.10a & Figure A.10b). The MC3T3 cells appeared to have formed cell–cell junctions (white

arrow in Figure A.10b) and developed cytoplasmic extensions on the substrate as well as bridging pore walls (black arrows in Figure A.10b & Figure A.10d). The high live cell coverage suggests good in vitro cytocompatibility of the sintered 3DP Fe-30Mn.

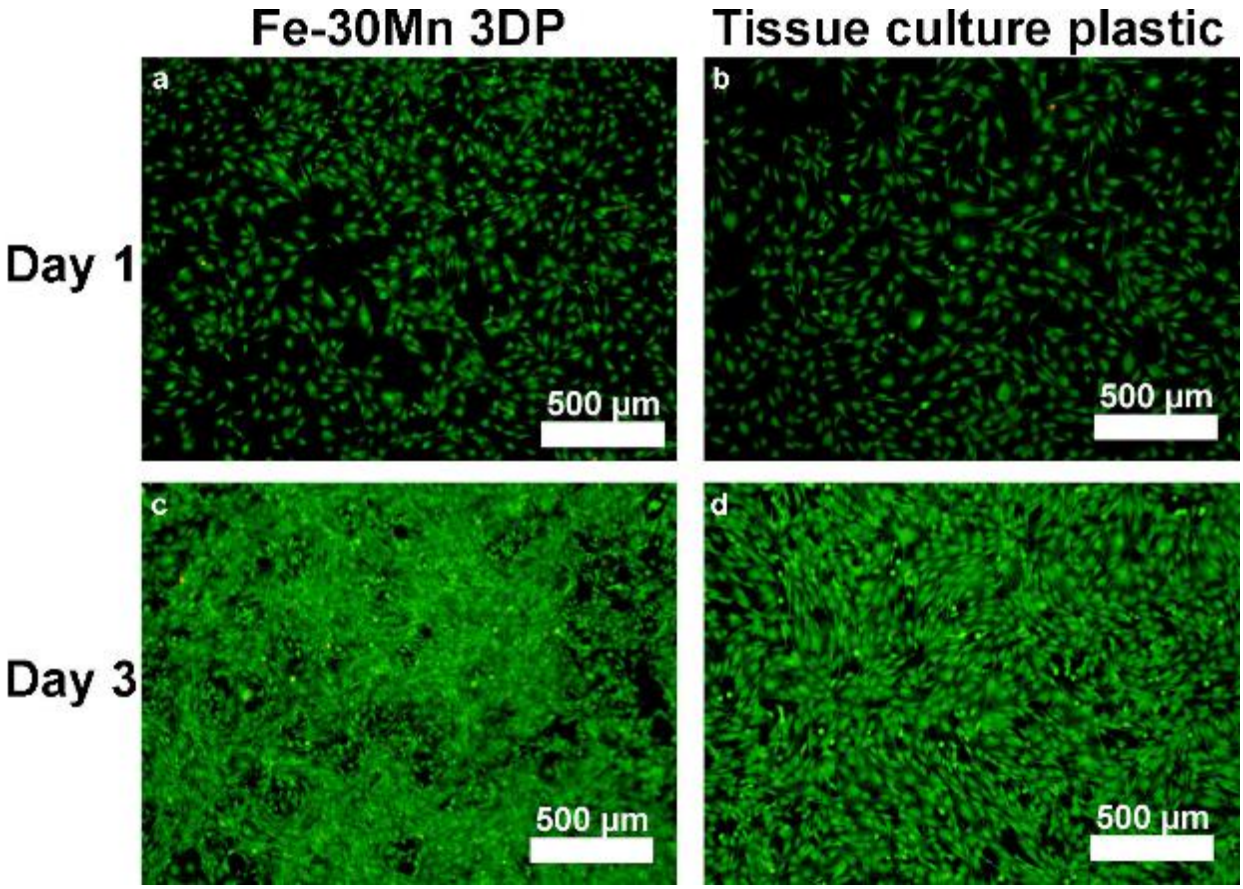

Figure A.9. Fluorescent images from the live/dead assay of live (green) and dead (red) MC3T3 cells attached after 1 and 3 days culture on a & c) 3D printed Fe-30Mn; b & d) tissue culture plastic.

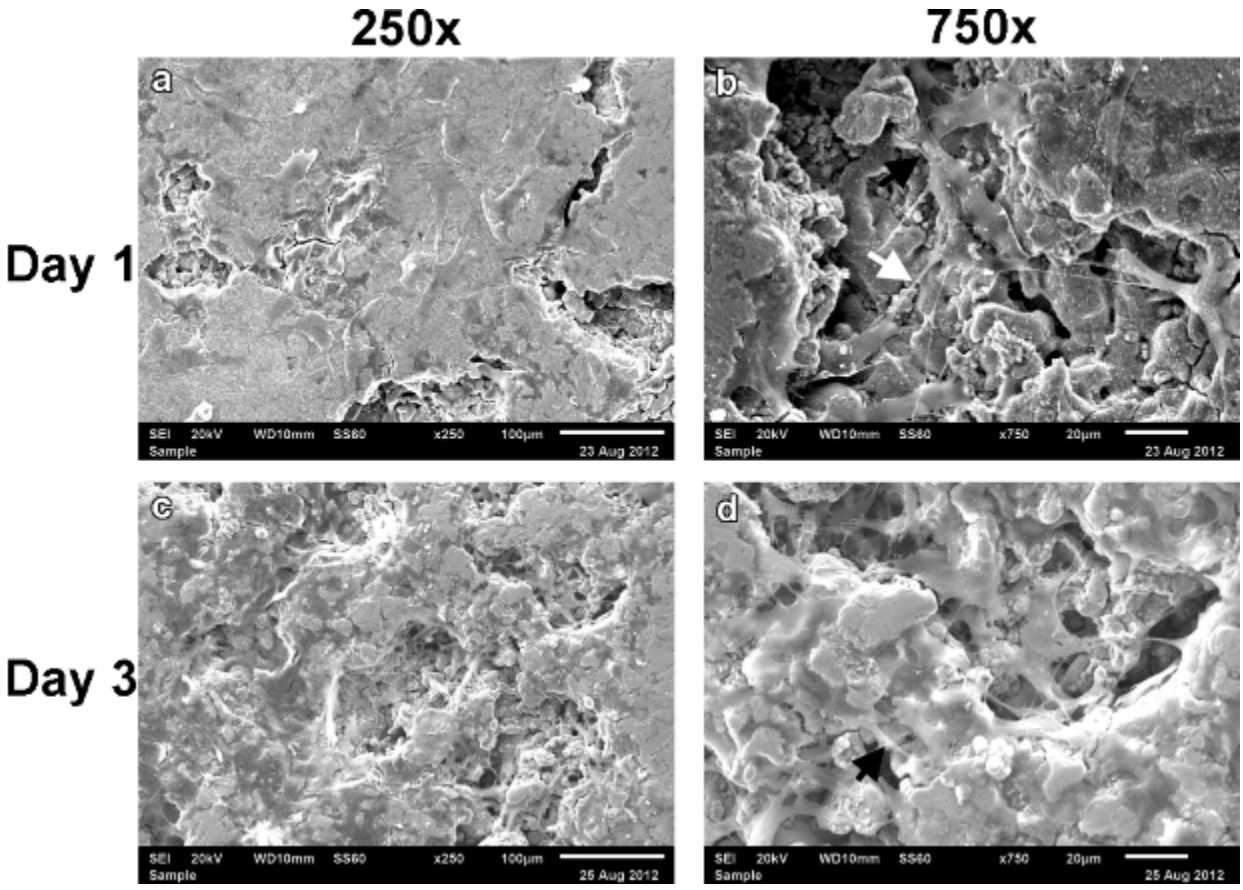

Figure A.10. SEM images of MC3T3 cells on the surface of 3DP Fe-30Mn after 1 and 3 days of culturing at a & c) 250x and b & d) 750x magnification. White arrow denotes cell-cell junction; black arrows denote cellular extensions to pore walls.

A.4 DISCUSSION

This preliminary study was aimed to investigate the feasibility of three dimensional inkjet printing biodegradable metallic Fe-30 wt.% Mn powders for the application of bone scaffolds. They were assessed in terms of biocorrosion, tensile mechanical properties, and *in vitro* cytocompatibility. Conclusions drawn from this study will provide the basis for future work to be

conducted in this growing field of additive manufacturing that will be focused primarily on further improving upon the first generation biodegradable scaffold.

3D printed parts were generated from mixed Fe and Mn powder and subsequently cured and sintered to facilitate particle bonding and part densification. The martensitic ε and austenitic γ phases present in the sintered parts are advantageous for medical applications because they have antiferromagnetic properties [72, 73] when present in Fe-Mn, thus allowing compatibility with magnetic resonance imaging (MRI). In Fe-Mn alloys with more than 23 wt.% Mn, the amount of ε decreases with increasing Mn, with more γ phase being present, as has been seen in as-cast and powder metallurgy of Fe-Mn alloys containing >28 wt.% Mn [13, 242, 243]. Whereas Fe-30Mn alloys produced by sintering and quenching formed a single γ phase [13], the 3DP alloy formed a mixed phase of γ and ε due to the lack of quenching employed, favoring the γ → ε transformation to occur during cooling. The high porosity observed in the 3DP Fe-30Mn after sintering may also have acted as free surfaces for stress relaxation which could lower the driving force of the γ → ε transformation as suggested for Fe-Mn alloys [13, 244].

Despite sintering at 1200 °C for 3 h with the formation of classical necked regions seen in Figure A. 4 and encountering ~20% part shrinkage in all directions, the parts still exhibited open porosity of 36.3%. Poor packing of powder during the spreading step due to the inhomogeneous powder morphology and size may have led to the formation of pores in the 3DP parts. The use of spherical powder of more uniform size distribution may improve the flowability [245] and allow for improved packing of powder which reduces formation of defects in the final product, thus reducing shrinkage by allowing for a more dense green structure [246]. Difficulty was encountered in removing the unbound powder after printing, especially from within the 500 μm pores of the part pictured in Figure A.3b, despite the maximum cavity diameter being over

five-fold larger than the average powder size, the limit to powder removal from pores [247]. Improvement of powder flowability also makes it easier to remove the loose powder, and thus may improve the maximum resolution of the printed parts [11].

Structurally, the bone scaffold should possess mechanical properties at least on par with natural bone to provide adequate initial strength and stiffness, while degrading to allow bone regeneration to restore the defect site's ability to bear load [248-250]. While the mechanical properties of the 3DP Fe-30Mn were significantly lower than reported values for as-rolled Fe-Mn and pure iron, they were very similar - within one order of magnitude, to natural bone. The reduced mechanical properties suggest the studied material may be more appropriate for non-load bearing applications, such as for craniofacial scaffolds, as opposed to use in high load bearing areas such as the long bone. Nonetheless, the measured Young's modulus of 32.47 GPa was only about twice that of natural bone, therefore 3DP Fe-30Mn should possess reduced risk for stress shielding compared to other metallic biomaterials of higher stiffness. The relatively low tensile properties may be attributed to several factors, the most prevalent being the open porosity. Furthermore, Mn segregation at the grain boundary has been argued to cause embrittlement in Fe-8wt.%Mn alloy in the absence of N and P [251], which may have occurred in this study due to higher Mn content observed in grain boundaries (Figure A. 4c) of the 3DP Fe-30Mn alloys. During the high temperature sintering process, oxidation may take place at grain boundaries of polycrystalline materials, acting as preferential sites for crack initiation and crack propagation [252]. With oxygen levels of 1.79 % remaining in the sintered parts as well as high oxygen content observed at the grain boundaries (Figure A. 4c), this oxidation-induced embrittlement may have led to low stress failure of the printed Fe-30Mn resulting in lower mechanical properties. Future work will attempt to improve mechanical properties by addressing

this issue using a reducing atmosphere to limit oxide content in sintered parts and by using powder with higher flowability to reduce void space between particles.

Corrosion parameters (Table A.3) of 3DP Fe-30Mn show a significant increase in corrosion current density and corrosion rate compared to pure iron after computation using both nominal and estimated true surface area to exclude and include surface porosity in the calculation. It should be noted that these are only estimates and not a measure of the actual values but nevertheless, still indicate the beneficial accelerated corrosion obtained from the 3DP Fe-30Mn alloy compared to pure Fe. These rough estimates of surface pore area in this work may be improved upon to provide more accurate assessments of corrosion by a more rigorous analysis which will be part of future work. The 3DP Fe-30Mn alloy contained a bi-phasic composition of γ and ε phases, accelerating the corrosion through micro-galvanic sites compared to single phase iron or single phase Fe-Mn alloys [13]. Segregation of Mn at grain boundaries as seen in Figure A. 4c may have also contributed to micro-galvanic corrosion with Mn corroding preferentially, leading to higher Mn content (13.43 ppm Mn vs. 1.47 ppm Fe) leaching into solution after 3 days immersion in cell culture media. The corrosion potential of Fe-30Mn was lower than pure iron due to the formation in high-manganese alloys of unstable manganese oxide which has a low passivity coefficient, thus reducing its corrosion resistance [253].

The corroded surface of the 3DP Fe-30Mn alloy shown in Figure A.6 confirms its higher tendency for corrosion over pure iron. Formation of red-brownish and black corrosion layers observed in Figure A.6a was believed to be due to released metal ions Fe^{2+} and Mn^{2+} from the anodic reaction reacting with hydroxyl ions from oxygen depolarization to form insoluble hydroxides such as FeO, Fe_3O_4, and Fe_2O_3 [64], which coincides with high O measured by EDX on the corroded surface seen in Figure A.6d and Figure A.8. Hydrogen depolarization may also

occur, reducing hydrogen ions to gaseous hydrogen and causing formation of corrosion pits at locations of potential differences where hydrogen ions are absorbed [254]. Hydrogen desorption results in cracks in the hydroxide layers observed in Figure A.6d and Figure A.6, also to a slight extent in Figure A.10, preventing homogenous coverage of the surface, allowing Cl^- ions in solution to attack and form metal chlorides with the Fe^{2+} and Mn^{2+} ions below the hydroxide layer, furthering pit formation [64, 254]. Although these metal chlorides are hydrolyzed by water expanding crater size in an autocatalytic reaction [64], corrosion products rich in Cl were still detected above the cracked hydroxide layers in Figure A.6d and Figure A.8. Deposition of Ca and P on corrosion products seen in Fig. A.6d was also observed in the work reported by Hermawan et al. [64], and may lead to formation of hydroxyapatite, the mineral component of natural bone.

Past studies have demonstrated positive biocompatibility and cytocompatibility of Fe and Fe-Mn, with iron degradation products shown to be cleared by macrophages without inducing local toxic effects [60], and Fe-Mn alloys demonstrating low fibroblast metabolic inhibition [64]. The current study also demonstrates the cytocompatibility of Fe-Mn produced using 3D printing with *in vitro* cell viability tests on MC3T3 pre-osteoblast cells. When cells were exposed to the degradation products of 3DP Fe-30Mn, high cell viability was demonstrated after 3 days cell culture and with <25% extract concentration after 1 day culture (Figure A.7). Higher viability after longer cell culture time indicated cell metabolic activity was uninhibited by the corrosion products. The reduction in cell viability after 1 day culture at higher extract concentrations was likely due to the higher Mn concentration (2.44×10^{-4} M) found in the corrosion extract compared to Fe (2.63×10^{-5} M). The half-maximal inhibitory concentration (IC_{50}) of Mn for MC3T3 cells was found to be 3.81×10^{-5} M while for Fe the IC_{50} was 3.28×10^{-4} M [176]. As

the corrosion extract concentration for Mn was found to be above its IC_{50}, cell viability when exposed to undiluted, 50% extract, and 25% extract concentrations were reduced compared to the negative control. Because the measured corrosion extract concentration of Fe was an order of magnitude below the IC_{50} value, Fe was not responsible for the decrease in cell viability. Similarly, Mn has been shown to reduce viability of MG63 human osteoblast cells by 50% at a concentration of $\sim 1 \times 10^{-4}$ M [255], also below the measured extract concentration. However, it is possible that under *in vivo* conditions the local concentration would conceivably be lower than the IC_{50} levels or what was measured *in vitro* due to the dynamic and highly perfused solution environment. Direct culture of MC3T3 cells with 3DP Fe-30Mn substrates however did not demonstrate reduced cell viability, with high live cell attachment observed using fluorescence microscopy after 1 and 3 day culture compared to tissue culture plastic (Figure A.9). The higher cell density observed after 3 days culture on 3DP Fe-30Mn implied cell proliferation was not inhibited by the Fe-30Mn substrate, local change in pH, or its corrosion products, as observed from the indirect MTT experiment after 3 days culture. Porosity is beneficial for bone scaffolds to allow for cell proliferation and differentiation throughout the bulk of the material to facilitate widespread tissue formation [248], a process which appeared to have begun seen through cell proliferation across and into pores observed in the SEM images of glutaraldehyde fixed cells (Fig. A.10). The positive cytocompatibility of the printed Fe-Mn was further reinforced by observations of healthy elongated and spread morphologies of the adhered cells, suggesting the promising nature of these 3D printed custom designed Fe-Mn parts. Further studies are however necessary to elucidate *in vivo* corrosion and the corresponding inflammatory response and toxicology of Fe-Mn alloys, as despite past indications of limited local inflammation from pure iron implants, migration and accumulation of iron has been observed distant from the location of

the implant [256]. *In vivo* assessments also must determine the effect of porosity on corrosion to achieve clinically appropriate degradation and optimal cell infiltration and bone formation through the scaffold without compromising temporary mechanical function which occurs with increasing porosity [257]. These aspects are planned to be elucidated following animal implantation experiments that will be conducted in the near future.

A.5 CONCLUSIONS

3D printed Fe-30Mn was sintered to form and γ and ε phases with inter-particle necking indicating diffusion induced densification. Despite the presence of high open porosity, the printed scaffolds demonstrated mechanical property values very similar to those of natural bone and appropriate for low-load bearing applications such as craniofacial scaffolds. Considering the slow corrosion rate being the main detriment to pure iron as a candidate biodegradable metal for medical implants, the 3DP Fe-30Mn alloy presented an estimated corrosion rate higher than that of pure iron, while depositing corrosion products containing bone mineral components Ca and P indicating its promise for bone replacement applications. *In vitro* pre-osteoblast cell viability studies also suggested excellent cytocompatibility with pore infiltration of cells in Fe-30Mn 3DP parts. The overall results of this preliminary study suggest that 3D printed Fe-Mn may be useful for craniofacial biomaterial applications. Further optimization of the materials and methods will be attempted to increase the bulk densification and reduce oxidation of the printed scaffolds varying the sintering environments while comparing various pore orientations. *In vivo* corrosion rates for biodegradable metals are not easily predicted by *in vitro* corrosion tests [206], hence animal implantation of the printed scaffolds is necessary in order to assess corrosion, bone

formation, and local and systemic toxicity. Nevertheless, this being the first reported study on fabricating scaffolds of biodegradable metals using 3D inkjet printing based on an extensive review and compilation of the literature to date, it is anticipated that 3D inkjet printing will emerge as a promising method for fabricating other biodegradable alloy systems for various medical device applications.

APPENDIX B

OPTIMIZATION OF T4 SOLUTION TREATMENT CONDITIONS

Figure B.1 shows the WX41 alloy after T4 solution treatment at 400 °C for 10 h up to 70 h to investigate the effects of longer heat treatment at lower temperature. While T4 heat treatment had initially been conducted on the WX41 alloy at 525 °C for 6 h, due to grain growth, we investigated the effects of heat treatment at a lower temperature while extending the time to still promote diffusion of secondary phases. We found that precipitates (white areas) in Figure B.1 became more dispersed with longer time. We also compared the degradation rate of each T4 heat treatment time to determine which was most effective at minimizing corrosion rate, which is shown in Figure B.2. Because after 20 h of T4 heat treatment at 400 °C the WX41 alloy resulted in the lowest relative corrosion rate while providing some dissolution of secondary phases and not increasing grain size, this condition was used for T4 heat treatment for KX11, WK11, WK41, and WZ42 alloys prior to extrusion.

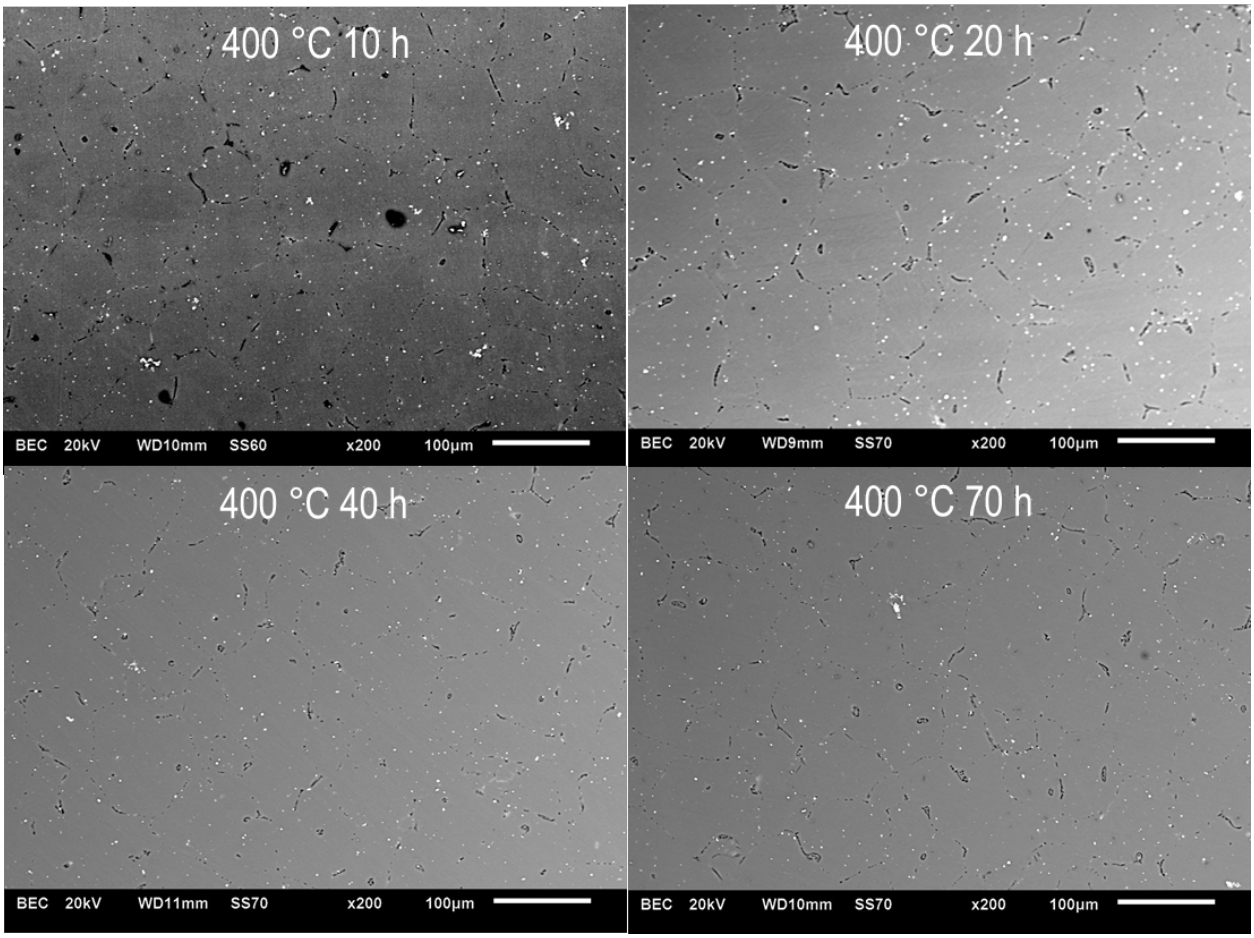

Figure B.1. Backscattered electron microscopty of WK41 alloy with T4 solution treatment applied after casting at 400 °C for 10, 20, 40, and 70 h followed by water quenching.

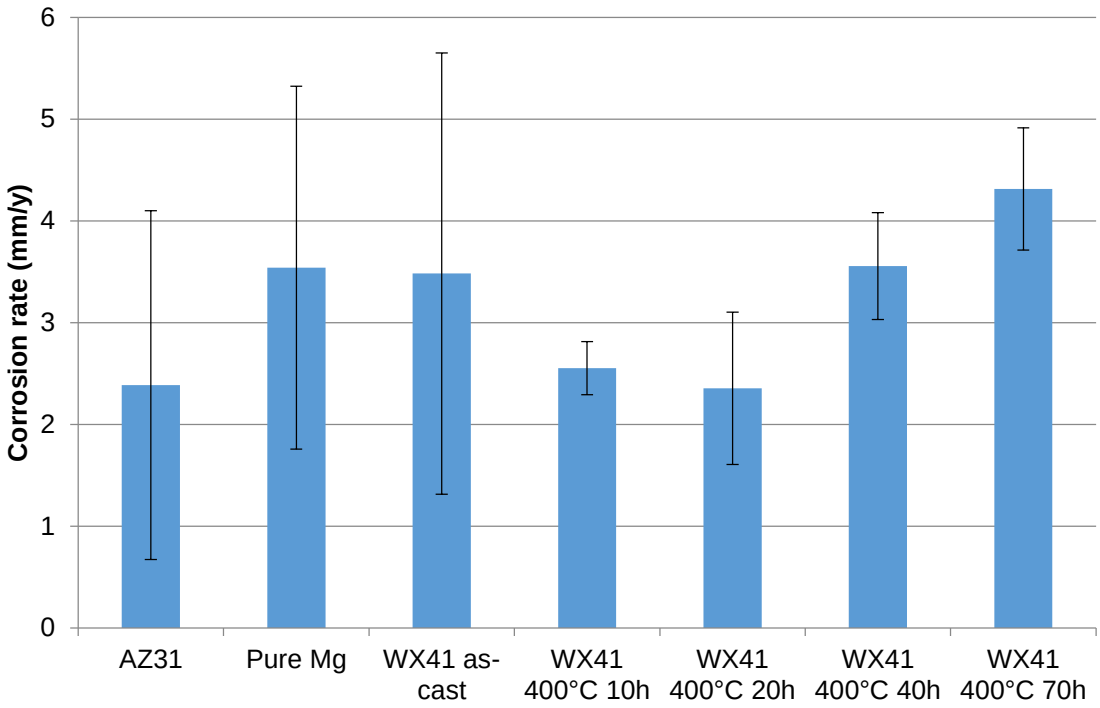

Figure B.2. Corrosion rate of WX41 alloy as-cast and T4 heat treated at 400 °C for various times and compared to commercial AZ31 and pure Mg after 10 days immersion in HBSS.

APPENDIX C

PERMISSIONS

The thesis has text, figures and tables reprinted/reproduced with permission from publishing companies and societies listed below. All the journal papers listed here have been published in print and electronic form, wherein I (Da-Tren Chou) am a co-author.

The journal paper listed below has been used in **Section 2**, **Section 3**, and **Section 4:**

Chou D, Hong D, Saha P, Ferrero J, Lee B, Tan Z, Dong Z, Kumta PN. In vitro and in vivo corrosion, cytocompatibility and mechanical properties of biodegradable Mg-Y-Ca-Zr alloys as implant materials. *Acta Biomaterialia*. 9 (10) 8518-8533, Copyright © 2013. Reprinted with permission from Elsevier.

The journal paper listed below has been used in **Appendix A:**

Chou D, Wells D, Hong D, Lee B, Kuhn H, Kumta PN. Novel processing of iron-manganese alloy-based biomaterials by inkjet 3-D printing. *Acta Biomaterialia.* 9 (10) 8593-8603, Copyright © 2013. Reprinted with permission from Elsevier.

BIBLIOGRAPHY

[1] Crubzy E, Murail P, Girard L, Bernadou J-P. False teeth of the Roman world. Nature 1998;391:29-.

[2] Scott M. 32,000 years of sutures. NATNews 1983;20:15-7.

[3] Fick A. Eine Contactbrille. Arch Augenheilkd 1888;18:279-89.

[4] Williams DF, European Society for B. Definitions in biomaterials : proceedings of a consensus conference of the European Society for Biomaterials, Chester, England, March 3-5, 1986. Amsterdam; New York: Elsevier.

[5] Navarro M, Michiardi A, Castaño O, Planell JA. Biomaterials in orthopaedics2008.

[6] Orthopedic Industry Overview. Harris Williams & Co.; 2014.

[7] Brandes EA, Brook GB, Paufler P. Smithells Metals Reference Book. Butterworth-Heinemann Ltd., Oxford, 1992. 1746 Seiten, Preis 150 £, ISBN 0-7506-1020-4. Crystal Research and Technology 1993;28:530-.

[8] Brånemark PI, Breine U, Johansson B, Roylance PJ, Röckert H, Yoffey JM. REGENERATION OF BONE MARROW. Cells Tissues Organs 1964;59:1-46.

[9] Long M, Rack HJ. Titanium alloys in total joint replacement--a materials science perspective. Biomaterials 1998;19:1621-39.

[10] Dai K, Chu Y. Studies and applications of NiTi shape memory alloys in the medical field in China. Bio-medical materials and engineering 1996;6:233-40.

[11] Reilly DT, Burstein AH. The Mechanical Properties of Cortical Bone. The Journal of Bone & Joint Surgery 1974;56:1001-22.

[12] Hermawan H, Ramdan D, Djuansjah JRP. Metals for Biomedical Applications2011.

[13] Hermawan H, Dubé D, Mantovani D. Degradable metallic biomaterials: Design and development of Fe–Mn alloys for stents. Journal of Biomedical Materials Research Part A 2010;93A:1-11.

[14] Huiskes R, Weinans H, Van Rietbergen B. The relationship between stress shielding and bone resorption around total hip stems and the effects of flexible materials. Clinical orthopaedics and related research 1992:124-34.

[15] Jacobs JJ, Gilbert JL, Urban RM. Corrosion of metal orthopaedic implants. Journal of Bone and Joint Surgery - Series A 1998;80:268-82.

[16] Jacobs JJ, Hallab NJ, Skipor AK, Urban RM. Metal Degradation Products: A Cause for Concern in Metal-Metal Bearings? Clinical orthopaedics and related research 2003:139-47.

[17] Jacobs JJ, Skipor AK, Patterson LM, Hallab NJ, Paprosky WG, Black J, et al. Metal release in patients who have had a primary total hip arthroplasty: A prospective, controlled, longitudinal study. Journal of Bone and Joint Surgery - Series A 1998;80:1447-58.

[18] Lhotka C, Szekeres T, Steffan I, Zhuber K, Zweymüller K. Four-year study of cobalt and chromium blood levels in patients managed with two different metal-on-metal total hip replacements. Journal of Orthopaedic Research 2003;21:189-95.

[19] Orringer JS, Barcelona V, Buchman SR. Reasons for Removal of Rigid Internal Fixation Devices in Craniofacial Surgery. Journal of Craniofacial Surgery 1998;9:40-4.

[20] Yaremchuk MJ, Fiala TGS, Barker F, Ragland R. The Effects of Rigid Fixation on Craniofacial Growth of Rhesus Monkeys. Plastic and Reconstructive Surgery 1994;93:1-10.

[21] Sullivan PK, Smith JF, Rozzelle AA. Cranio-Orbital Reconstruction: Safety and Image Quality of Metallic Implants on CT and MRI Scanning. Plastic and Reconstructive Surgery 1994;94:589-96.

[22] Gilardino MS, Chen E, Bartlett S. Choice of internal rigid fixation materials in the treatment of facial fractures. Craniomaxillofacial Trauma & Reconstruction 2009;2:49-60.

[23] Charnley J. Anchorage of the femoral head prosthesis to the shaft of the femur. The Journal of bone and joint surgery British volume 1960;42-b:28-30.

[24] Swanson AB. Silicone rubber implants for replacement of arthritic or destroyed joints. The Hand 1969;1:38-9.

[25] Goodman SB, Chin RC, Chiou SS, Schurman DJ, Woolson ST, Masada MP. A clinical-pathologic-biochemical study of the membrane surrounding loosened and nonloosened total hip arthroplasties. Clinical orthopaedics and related research 1989:182-7.

[26] Niebauer JJ, Landry RM. Dacron--silicone prosthesis for the metacarpophalangeal and interphalangeal joints. Hand 1971;3:55-61.

[27] Maguire JK, Jr., Coscia MF, Lynch MH. Foreign body reaction to polymeric debris following total hip arthroplasty. Clinical orthopaedics and related research 1987:213-23.

[28] Vert M, Li SM, Spenlehauer G, Guerin P. Bioresorbability and biocompatibility of aliphatic polyesters. J Mater Sci: Mater Med 1992;3:432-46.

[29] Li S, McCarthy S. Further investigations on the hydrolytic degradation of poly (DL-lactide). Biomaterials 1999;20:35-44.

[30] Gilding DK, Reed AM. Biodegradable polymers for use in surgery—polyglycolic/poly(actic acid) homo- and copolymers: 1. Polymer 1979;20:1459-64.

[31] Middleton JC, Tipton AJ. Synthetic biodegradable polymers as orthopedic devices. Biomaterials 2000;21:2335-46.

[32] Cordewener FW, Schmitz JP. The future of biodegradable osteosyntheses. Tissue engineering 2000;6:413-24.

[33] Hirvensalo E. Fracture fixation with biodegradable rods Forty-one cases of severe ankle fractures. Acta Orthopaedica 1989;60:601-6.

[34] Bostman O, Hirvensalo E, Makinen J, Rokkanen P. Foreign-body reactions to fracture fixation implants of biodegradable synthetic polymers. The Journal of bone and joint surgery British volume 1990;72:592-6.

[35] Bergsma EJ, Rozema FR, Bos RRM, Bruijn WCD. Foreign body reactions to resorbable poly(l-lactide) bone plates and screws used for the fixation of unstable zygomatic fractures. Journal of Oral and Maxillofacial Surgery 1993;51:666-70.

[36] Hirvensalo E, Bostman O, Tormala P, Vainionpaa S, Rokkanen P. Chevron osteotomy fixed with absorbable polyglycolide pins. Foot & ankle 1991;11:212-8.

[37] Santavirta S, Konttinen YT, Saito T, Gronblad M, Partio E, Kemppinen P, et al. Immune response to polyglycolic acid implants. The Journal of bone and joint surgery British volume 1990;72:597-600.

[38] Bostman OM. Osteoarthritis of the ankle after foreign-body reaction to absorbable pins and screws: a three- to nine-year follow-up study. The Journal of bone and joint surgery British volume 1998;80:333-8.

[39] Moore JW, Brekke JH. Foreign body giant cell reaction related to placement of tetracycline-treated polylactic acid: Report of 18 cases. Journal of Oral and Maxillofacial Surgery 1990;48:808-12.

[40] Bergsma JE, Rozema FR, Bos RRM, Boering G, de Bruijn WC, Pennings AJ. In vivo degradation and biocompatibility study of in vitro pre-degraded as-polymerized polylactide particles. Biomaterials 1995;16:267-74.

[41] Joziasse CAP, Grijpma DW, Bergsma JE, Cordewener FW, Bos RRM, Pennings AJ. The influence of morphology on the (hydrolytic degradation of as-polymerized and hot-drawn poly(L-lactide)). Colloid Polym Sci 1998;276:968-75.

[42] Nakamura T, Shimizu Y, Okumura N, Matsui T, Hyon S-H, Shimamoto T. Tumorigenicity of poly-L-lactide (PLLA) plates compared with medical-grade polyethylene. Journal of biomedical materials research 1994;28:17-25.

[43] Ignatius AA, Claes LE. In vitro biocompatibility of bioresorbable polymers: poly(L, DL-lactide) and poly(L-lactide-co-glycolide). Biomaterials 1996;17:831-9.

[44] Suganuma J, Alexander H. Biological response of intramedullary bone to poly-L-lactic acid. Journal of Applied Biomaterials 1993;4:13-27.

[45] Taylor MS, Daniels AU, Andriano KP, Heller J. Six bioabsorbable polymers: In vitro acute toxicity of accumulated degradation products. Journal of Applied Biomaterials 1994;5:151-7.

[46] van Sliedregt A, Radder AM, de Groot K, van Blitterswijk CA. In vitro biocompatibility testing of polylactides Part I Proliferation of different cell types. J Mater Sci: Mater Med 1992;3:365-70.

[47] Boutin P. [Total arthroplasty of the hip by fritted aluminum prosthesis. Experimental study and 1st clinical applications]. Revue de chirurgie orthopedique et reparatrice de l'appareil moteur 1972;58:229-46.

[48] Saikko VO, Paavolainen PO, Slätis P. Wear of the polyethylene acetabular cup: metallic and ceramic heads compared in a hip simulator. Acta Orthopaedica 1993;64:391-402.

[49] Spaans CJ, Belgraver VW, Rienstra O, de Groot JH, Veth RPH, Pennings AJ. Solvent-free fabrication of micro-porous polyurethane amide and polyurethane-urea scaffolds for repair and replacement of the knee-joint meniscus. Biomaterials 2000;21:2453-60.

[50] Dutta SR, Passi D, Singh P, Bhuibhar A. Ceramic and non-ceramic hydroxyapatite as a bone graft material: a brief review. Irish journal of medical science 2015;184:101-6.

[51] Takahashi Y, Yamamoto M, Tabata Y. Osteogenic differentiation of mesenchymal stem cells in biodegradable sponges composed of gelatin and β-tricalcium phosphate. Biomaterials 2005;26:3587-96.

[52] Ginebra MP, Traykova T, Planell JA. Calcium phosphate cements as bone drug delivery systems: a review. Journal of controlled release : official journal of the Controlled Release Society 2006;113:102-10.

[53] Ignatius AA, Augat P, Ohnmacht M, Pokinskyj P, Kock HJ, Claes LE. A new bioresorbable polymer for screw augmentation in the osteosynthesis of osteoporotic cancellous bone: a biomechanical evaluation. Journal of biomedical materials research 2001;58:254-60.

[54] Bohner M. Calcium orthophosphates in medicine: from ceramics to calcium phosphate cements. Injury 2000;31, Supplement 4:D37-D47.

[55] Boccaccini AR, Roelher JA, Hench LL, Maquet V, Jérŏme R. A Composites Approach to Tissue Engineering. 26th Annual Conference on Composites, Advanced Ceramics, Materials,

and Structures: B: Ceramic Engineering and Science Proceedings: John Wiley & Sons, Inc.; 2008. p. 805-16.

[56] Claes LE. Mechanical characterization of biodegradable implants. Clinical Materials 1992;10:41-6.

[57] Haynes WM. CRC Handbook of Chemistry and Physics, 93rd Edition: Taylor & Francis; 2012.

[58] Schinhammer M, Hänzi AC, Löffler JF, Uggowitzer PJ. Design strategy for biodegradable Fe-based alloys for medical applications. Acta Biomaterialia 2010;6:1705-13.

[59] Peuster M, Wohlsein P, Brügmann M, Ehlerding M, Seidler K, Fink C, et al. A novel approach to temporary stenting: Degradable cardiovascular stents produced from corrodible metal - Results 6-18 months after implantation into New Zealand white rabbits. Heart 2001;86:563-9.

[60] Peuster M, Hesse C, Schloo T, Fink C, Beerbaum P, von Schnakenburg C. Long-term biocompatibility of a corrodible peripheral iron stent in the porcine descending aorta. Biomaterials 2006;27:4955-62.

[61] Kraus T, Moszner F, Fischerauer S, Fiedler M, Martinelli E, Eichler J, et al. Biodegradable Fe-based alloys for use in osteosynthesis: outcome of an in vivo study after 52 weeks. Acta Biomater 2014;10:3346-53.

[62] Hermawan H, Alamdari H, Mantovani D, Dubé D. Iron–manganese: new class of metallic degradable biomaterials prepared by powder metallurgy. Powder Metallurgy 2008;51:38-45.

[63] Hermawan H, Dubé D, Mantovani D. Development of Degradable Fe-35Mn Alloy for Biomedical Application. Advanced Materials Research 2006;15-17:107-12.

[64] Hermawan H, Purnama A, Dube D, Couet J, Mantovani D. Fe–Mn alloys for metallic biodegradable stents: Degradation and cell viability studies. Acta Biomaterialia 2010;6:1852-60.

[65] Liu B, Zheng YF. Effects of alloying elements (Mn, Co, Al, W, Sn, B, C and S) on biodegradability and in vitro biocompatibility of pure iron. Acta Biomaterialia 2011;7:1407-20.

[66] Liu B, Zheng YF, Ruan L. In vitro investigation of Fe30Mn6Si shape memory alloy as potential biodegradable metallic material. Materials Letters 2011;65:540-3.

[67] Moravej M, Amira S, Prima F, Rahem A, Fiset M, Mantovani D. Effect of electrodeposition current density on the microstructure and the degradation of electroformed iron for degradable stents. Materials Science and Engineering: B 2011;176:1812-22.

[68] Wegener B, Sievers B, Utzschneider S, Müller P, Jansson V, Rößler S, et al. Microstructure, cytotoxicity and corrosion of powder-metallurgical iron alloys for biodegradable bone replacement materials. Materials Science and Engineering: B 2011;176:1789-96.

[69] Chou DT, Wells D, Hong D, Lee B, Kuhn H, Kumta PN. Novel processing of iron-manganese alloy-based biomaterials by inkjet 3-D printing. Acta Biomater 2013;9:8593-603.

[70] Moravej M, Prima F, Fiset M, Mantovani D. Electroformed iron as new biomaterial for degradable stents: Development process and structure-properties relationship. Acta Biomaterialia 2010;6:1726-35.

[71] Moravej M, Purnama A, Fiset M, Couet J, Mantovani D. Electroformed pure iron as a new biomaterial for degradable stents: In vitro degradation and preliminary cell viability studies. Acta Biomaterialia 2010;6:1843-51.

[72] Ishikawa Y, Endoh Y. Antiferromagnetism of gamma-FeMn Alloys. Journal of Applied Physics 1968;39:1318-9.

[73] Rabinkin A. On magnetic contributions to γ→ε phase transformations in Fe-Mn alloys. Calphad 1979;3:77-84.

[74] Peuster M, Wohlsein P, Brügmann M, Ehlerding M, Seidler K, Fink C, et al. A novel approach to temporary stenting: degradable cardiovascular stents produced from corrodible metal—results 6–18 months after implantation into New Zealand white rabbits. Heart 2001;86:563-9.

[75] Vojtech D, Kubasek J, Serak J, Novak P. Mechanical and corrosion properties of newly developed biodegradable Zn-based alloys for bone fixation. Acta Biomaterialia 2011;7:3515-22.

[76] X. Wang HML, X.L. Li, L. Li, Y.F. Zheng. Effect of cooling rate and composition on microstructures and properties of Zn-Mg alloys. Transactions of Nonferrous Metals Society of China 2007;17:s122-s5.

[77] Bowen PK, Drelich J, Goldman J. Zinc exhibits ideal physiological corrosion behavior for bioabsorbable stents. Advanced materials (Deerfield Beach, Fla) 2013;25:2577-82.

[78] Jiao W, Li HF, Zhao K, Bai HY, Wang YB, Zheng YF, et al. Development of CaZn based glassy alloys as potential biodegradable bone graft substitute. Journal of Non-Crystalline Solids 2011;357:3830-40.

[79] Friedrich HE, Mordike BL. Magnesium Technology: Metallurgy, Design Data, Automotive Applications: Springer; 2006.

[80] Huse EC. A New Ligature: W. B. Keen, Cooke; 1878.

[81] Payr E. Beiträge zur Technik der Blutgefäss- und Nervennaht nebst Mittheilungen über die Verwendung eines resorbirbaren Metalles in der Chirurgie. Arch Klin Chir 1900;62:67-93.

[82] Payr E. Blutgefäß- und Nervennaht (nebst Mittheilung über die Verwendung eines resorbirbaren Metalles in der Chirurgie). Centralblatt für Chirurgie 1901;28:31-7.

[83] Payr E. Zur Verwendung des Magnesiums für resorbirbare Darmknöpfe und andere chirurgisch-technische Zwecke. Centralblatt Chir 1901;28:513-5.

[84] E. Payr AM. Experimentelle und klinische Beiträge zur Lebernaht und leberresection (Magnesiumplattennaht). Arch Klin Chir 1905;77:962–98.

[85] Payr E. Ueber Verwendung von Magnesium zur Behandlung von Blutgefässerkrankungen. Deut Z Chir 1902;63:503-11.

[86] Payr E. Zur Technik der Behandlung kavernöser Tumoren. Zentralblatt Chir 1903;30:233-4.

[87] Payr E. Weitere Erfahrungen über die Behandlung von Blutgefäßgeschwülsten mit Magnesiumpfeilen. Zentralblatt Chir 1905;49:1335-8.

[88] Lambotte A. L'utilisation du magnesium comme materiel perdu dans l'osteosynthè se. Bull Mém Soc Nat Cir 1932;28:1325–34.

[89] Verbrugge J. La tolérance du tissu osseux vis-à-vis du magnésium métallique. Presse Med 1933;55:1112–4.

[90] Verbrugge J. Le matériel métallique résorbable en chirurgie osseuse. Presse Med 1934;23:460-5.

[91] Verbrugge J. L’utilisation du magnésium dans le traitement chirurgical des fractures. Bull Mém Soc Nat Cir 1937;59:813–23.

[92] McBride EDMDFACS. MAGNESIUM SCREW AND NAIL TRANSFIXION IN FRACTURES. Southern Medical Journal 1938;31:508-14.

[93] McBride EDMDFACS. Absorbable metal in bone surgery: A further report on the use of magnesium alloys. Journal of the American Medical Association 1938;111:2464-7.

[94] Troitskii VV, Tsitrin, D.N. The resorbing metallic alloy 'Osteosinthezit' as material for fastening broken bone. Khirurgiia 1948;8:41-4.

[95] Windhagen H, Radtke K, Weizbauer A, Diekmann J, Noll Y, Kreimeyer U, et al. Biodegradable magnesium-based screw clinically equivalent to titanium screw in hallux valgus surgery: short term results of the first prospective, randomized, controlled clinical pilot study. Biomedical engineering online 2013;12:62.

[96] Staiger MP, Pietak AM, Huadmai J, Dias G. Magnesium and its alloys as orthopedic biomaterials: A review. Biomaterials 2006;27:1728-34.

[97] Baker H, Committee ASMIH. ASM Specialty Handbook: Magnesium and Magnesium Alloys: ASM International; 1999.

[98] Taylor GI. Plastic Strain in Metals. Journal of the Institute of Metals 1938;62.

[99] Yoshinaga H, Horiuchi R. Deformation Mechanisms in Magnesium Single Crystals Compressed in the Direction Parallel to Hexagonal Axis. Transactions of the Japan Institute of Metals 1963;4:1-8.

[100] Emley EF. Principles of magnesium technology. Oxford; New York: Pergamon Press; 1966.

[101] Chapman JA, Wilson DV. The room-temperature ductility of fine-grain magnesium. J Inst Met 1962;91:39-40.

[102] Koike J. Enhanced deformation mechanisms by anisotropic plasticity in polycrystalline Mg alloys at room temperature. Metall and Mat Trans A 2005;36:1689-96.

[103] Koike J, Kobayashi T, Mukai T, Watanabe H, Suzuki M, Maruyama K, et al. The activity of non-basal slip systems and dynamic recovery at room temperature in fine-grained AZ31B magnesium alloys. Acta Materialia 2003;51:2055-65.

[104] Hall EO. The Deformation and Ageing of Mild Steel: III Discussion of Results. Proceedings of the Physical Society Section B 1951;64:747.

[105] Petch NJ. The cleavage strength of polycrystals. The Journal of the Iron and Steel Institute 1953;174.

[106] Pourbaix M. Atlas of electrochemical equilibria in aqueous solutions: National Association of Corrosion Engineers; 1974.

[107] Shaw BA. Corrosion resistance of magnesium alloys. ASM Handbook - Corrosion: Fundamentals, Testing, and Protection. Materials Park: ASM International; 2003. p. 692-6.

[108] Kokubo T. Formation of biologically active bone-like apatite on metals and polymers by a biomimetic process. Thermochimica Acta 1996;280-281:479-90.

[109] Li Z, Gu X, Lou S, Zheng Y. The development of binary Mg–Ca alloys for use as biodegradable materials within bone. Biomaterials 2008;29:1329-44.

[110] Witte F, Hort N, Vogt C, Cohen S, Kainer KU, Willumeit R, et al. Degradable biomaterials based on magnesium corrosion. Current Opinion in Solid State & Materials Science 2008;12:63-72.

[111] Gu XN, Li N, Zheng YF, Kang F, Wang JT, Ruan L. In vitro study on equal channel angular pressing AZ31 magnesium alloy with and without back pressure. Materials Science and Engineering: B 2011;176:1802-6.

[112] Aung NN, Zhou W. Effect of grain size and twins on corrosion behaviour of AZ31B magnesium alloy. Corrosion Science 2010;52:589-94.

[113] op't Hoog C, Birbilis N, Estrin Y. Corrosion of Pure Mg as a Function of Grain Size and Processing Route. Advanced Engineering Materials 2008;10:579-82.

[114] Andrei M, Eliezer A, Bonora PL, Gutman EM. DC and AC polarisation study on magnesium alloys Influence of the mechanical deformation. Materials and Corrosion 2002;53:455-61.

[115] Kutniy KV, Papirov II, Tikhonovsky MA, Pikalov AI, Sivtzov SV, Pirozhenko LA, et al. Influence of grain size on mechanical and corrosion properties of magnesium alloy for medical implants

Einfluss der Korngröße auf die mechanischen und korrosionstechnischen Eigenschaften von Magnesiumlegierungen für medizinische Implantate. Materialwissenschaft und Werkstofftechnik 2009;40:242-6.

[116] Bobby Kannan M, Dietzel W, Blawert C, Atrens A, Lyon P. Stress corrosion cracking of rare-earth containing magnesium alloys ZE41, QE22 and Elektron 21 (EV31A) compared with AZ80. Materials Science and Engineering: A 2008;480:529-39.

[117] Sivakumar M, Rajeswari S. Investigation of failures in stainless steel orthopaedic implant devices: pit-induced stress corrosion cracking. J Mater Sci Lett 1992;11:1039-42.

[118] Bombara G, Cavallini M. Stress corrosion cracking of bone implants. Corrosion Science 1977;17:77-85.

[119] Miller WK. Stress-corrosion cracking of Magnesium Alloys. Stress-Corrosion Cracking: Material Performance and Evaluation. Metals Park, OH: ASM International; 1992. p. 251-63.

[120] Chakrapani DG, Pugh EN. Hydrogen embrittlement in a Mg-Al alloy. MTA 1976;7:173-8.

[121] Xin Y, Hu T, Chu PK. Influence of test solutions on in vitro studies of biomedical magnesium alloys. Journal of the Electrochemical Society 2010;157:C238-C43.

[122] Saris NE, Mervaala E, Karppanen H, Khawaja JA, Lewenstam A. Magnesium. An update on physiological, clinical and analytical aspects. Clin Chim Acta 2000;294:1-26.

[123] Seiler H, Sigel A, Sigel H. Handbook on Metals in Clinical and Analytical Chemistry: Taylor & Francis; 1994.

[124] Groves EWH. An experimental study of the operative treatment of fractures. British Journal of Surgery 1913;1:438-501.

[125] Witte F, Kaese V, Haferkamp H, Switzer E, Meyer-Lindenberg A, Wirth CJ, et al. In vivo corrosion of four magnesium alloys and the associated bone response. Biomaterials 2005;26:3557-63.

[126] Zreiqat H, Howlett CR, Zannettino A, Evans P, Schulze-Tanzil G, Knabe C, et al. Mechanisms of magnesium-stimulated adhesion of osteoblastic cells to commonly used orthopaedic implants. Journal of biomedical materials research 2002;62:175-84.

[127] Chaya A, Yoshizawa S, Verdelis K, Noorani S, Costello BJ, Sfeir C. Fracture Healing Using Degradable Magnesium Fixation Plates and Screws. Journal of Oral and Maxillofacial Surgery 2015;73:295-305.

[128] Song GL, Atrens A. Corrosion Mechanisms of Magnesium Alloys. Advanced Engineering Materials 1999;1:11-33.

[129] Wu A-r, Xia C-q. Study of the microstructure and mechanical properties of Mg-rare earth alloys. Materials & Design 2007;28:1963-7.

[130] Liu M, Schmutz P, Uggowitzer PJ, Song G, Atrens A. The influence of yttrium (Y) on the corrosion of Mg–Y binary alloys. Corrosion Science 2010;52:3687-701.

[131] Drynda A, Hassel T, Hoehn R, Perz A, Bach F-W, Peuster M. Development and biocompatibility of a novel corrodible fluoride-coated magnesium-calcium alloy with improved degradation kinetics and adequate mechanical properties for cardiovascular applications. Journal of Biomedical Materials Research Part A 2010;93A:763-75.

[132] Saha P, Lolies K, Viswanathan S, Gokhale A, Batson R. A Systematic Study of the Grain Refinement of Magnesium by Zirconium: Minerals, Metals and Materials Society/AIME, 420 Commonwealth Dr., P. O. Box 430 Warrendale PA 15086 USA; 2010.

[133] Song G, StJohn D. The effect of zirconium grain refinement on the corrosion behaviour of magnesium-rare earth alloy MEZ. Journal of Light Metals 2002;2:1-16.

[134] Witte F. The history of biodegradable magnesium implants: A review. Acta Biomaterialia 2010;6:1680-92.

[135] Gu XN, Zhou WR, Zheng YF, Cheng Y, Wei SC, Zhong SP, et al. Corrosion fatigue behaviors of two biomedical Mg alloys-AZ91D and WE43-In simulated body fluid. Acta Biomaterialia 2010;6:4605-13.

[136] Chang S-Y, Tezuka H, Kamio A. Mechanical Properties and Structure of Ignition-Proof Mg-Ca-Zr Alloys Produced by Squeeze Casting. Materials Transactions, JIM 1997;38:526-35.

[137] Fan J, Chen Z, Yang W, Fang S, Xu B. Effect of yttrium, calcium and zirconium on ignition-proof principle and mechanical properties of magnesium alloys. Journal of Rare Earths 2012;30:74-8.

[138] Gao J-c, Wu S, Qiao L-y, Wang Y. Corrosion behavior of Mg and Mg-Zn alloys in simulated body fluid. Transactions of Nonferrous Metals Society of China 2008;18:588-92.

[139] Velikokhatnyi OI, Kumta PN. First-principles studies on alloying and simplified thermodynamic aqueous chemical stability of calcium-, zinc-, aluminum-, yttrium- and iron-doped magnesium alloys. Acta Biomaterialia 2010;6:1698-704.

[140] Ilich JZ, Kerstetter JE. Nutrition in bone health revisited: a story beyond calcium. J Am Coll Nutr 2000;19:715-37.

[141] Saha P, Viswanathan S. An Analysis of the Grain Refinement of Magnesium By Zirconium. Magnesium Technology 2011: John Wiley & Sons, Inc.; 2011. p. 175-80.

[142] Saha P, Viswanathan S. Engineering an efficient zirconium-based grain refiner for magnesium alloys. International Journal of Metalcasting 2010;4:70-1.

[143] Saha P, Viswanathan S. Grain refinement of magnesium by zirconium: characterization and analysis (11-066). AFS Transactions-American Foundry Society 2011;119:469-80.

[144] Haude M, Erbel R, Erne P, Verheye S, Degen H, Bose D, et al. Safety and performance of the drug-eluting absorbable metal scaffold (DREAMS) in patients with de-novo coronary lesions: 12 month results of the prospective, multicentre, first-in-man BIOSOLVE-I trial. Lancet 2013;381:836-44.

[145] Uematsu Y, Tokaji K, Kamakura M, Uchida K, Shibata H, Bekku N. Effect of extrusion conditions on grain refinement and fatigue behaviour in magnesium alloys. Materials Science and Engineering: A 2006;434:131-40.

[146] ASTM B275-05 Standard Practice for Codification of Certain Nonferrous Metals and Alloys, Cast and Wrought. Annual book of ASTM standards. Philadelphia, PA: ASTM; 2005.

[147] Qian M, StJohn DH, Frost MT. Zirconium alloying and grain refinement of magnesium alloys. Magnesium Technology 2003 2003;2003:209-14.

[148] ASTM E112 Standard Test Methods for Determining Average Grain Size. Annual book of ASTM standards. Philadelphia, PA: ASTM; 2010.

[149] Qian M, Zheng L, Graham D, Frost MT, StJohn DH. Settling of undissolved zirconium particles in pure magnesium melts. Journal of Light Metals 2001;1:157-65.

[150] Pan F-s, Chen M-b, Wang J-f, Peng J, Tang A-t. Effects of yttrium addition on microstructure and mechanical properties of as-extruded AZ31 magnesium alloys. Transactions of Nonferrous Metals Society of China 2008;18, Supplement 1:s1-s6.

[151] Zhang BP, Geng L, Huang LJ, Zhang XX, Dong CC. Enhanced mechanical properties in fine-grained Mg–1.0Zn–0.5Ca alloys prepared by extrusion at different temperatures. Scripta Materialia 2010;63:1024-7.

[152] Chen Y, Wang Q, Peng J, Zhai C, Ding W. Effects of extrusion ratio on the microstructure and mechanical properties of AZ31 Mg alloy. Journal of Materials Processing Technology 2007;182:281-5.

[153] Hirano M, Yamasaki M, Hagihara K, Higashida K, Kawamura Y. Effect of Extrusion Parameters on Mechanical Properties of Mg97Zn1Y2 Alloys at Room and Elevated Temperatures. Materials Transactions 2010;51:1640-7.

[154] Zheng YF, Gu XN, Witte F. Biodegradable metals. Materials Science and Engineering: R: Reports 2014;77:1-34.

[155] Butler DL, Goldstein SA, Guilak F. Functional Tissue Engineering: The Role of Biomechanics. Journal of Biomechanical Engineering 2000;122:570-5.

[156] Ahsan T, Sah RL. Biomechanics of integrative cartilage repair. Osteoarthritis and Cartilage 1999;7:29-40.

[157] Song G, Atrens A. Understanding Magnesium Corrosion—A Framework for Improved Alloy Performance. Advanced Engineering Materials 2003;5:837-58.

[158] ASTM G31-72 Standard Practice for Laboratory Immersion Corrosion Testing of Metals. Annual book of ASTM standards. Philadelphia, PA: ASTM; 2004.

[159] ASTM E8-04 Standard Test Methods for Tension Testing of Metallic Materials. Annual book of ASTM standards. Philadelphia, PA: ASTM; 2004.

[160] ASTM E9-09 Standard Test Methods of Compression Testing of Metallic Materials at Room Temperature. Annual book of ASTM standards. Philadelphia, PA: ASTM; 2009.

[161] Krause A, von der Höh N, Bormann D, Krause C, Bach F-W, Windhagen H, et al. Degradation behaviour and mechanical properties of magnesium implants in rabbit tibiae. Journal of Materials Science 2010;45:624-32.

[162] Luffy SA, Chou DT, Waterman J, Wearden PD, Kumta PN, Gilbert TW. Evaluation of magnesium-yttrium alloy as an extraluminal tracheal stent. Journal of biomedical materials research Part A 2014;102:611-20.

[163] Xu L, Yu G, Zhang E, Pan F, Yang K. In vivo corrosion behavior of Mg-Mn-Zn alloy for bone implant application. Journal of Biomedical Materials Research Part A 2007;83A:703-11.

[164] Argade GR, Panigrahi SK, Mishra RS. Effects of grain size on the corrosion resistance of wrought magnesium alloys containing neodymium. Corrosion Science 2012;58:145-51.

[165] Alvarez-Lopez M, Pereda MD, del Valle JA, Fernandez-Lorenzo M, Garcia-Alonso MC, Ruano OA, et al. Corrosion behaviour of AZ31 magnesium alloy with different grain sizes in simulated biological fluids. Acta Biomaterialia 2010;6:1763-71.

[166] Zhang F, Ma A, Jiang J, Xu H, Song D, Lu F, et al. Enhanced biodegradation behavior of ultrafine-grained ZE41A magnesium alloy in Hank's solution. Progress in Natural Science: Materials International 2013;23:420-4.

[167] Neil WC, Forsyth M, Howlett PC, Hutchinson CR, Hinton BRW. Corrosion of heat treated magnesium alloy ZE41. Corrosion Science 2011;53:3299-308.

[168] Wang Q, Liu Y, Fang S, Song Y, Zhang D, Zhang L, et al. Evaluating the improvement of corrosion residual strength by adding 1.0 wt.% yttrium into an AZ91D magnesium alloy. Materials Characterization 2010;61:674-82.

[169] Liu M, Schmutz P, Uggowitzer PJ, Song G, Atrens A. The influence of yttrium (Y) on the corrosion of Mg-Y binary alloys. Corrosion Science 2010;52:3687-701.

[170] Shi Z, Atrens A. An innovative specimen configuration for the study of Mg corrosion. Corrosion Science 2011;53:226-46.

[171] Song GL. Corrosion of Magnesium Alloys: Elsevier Science; 2011.

[172] Xin Y, Huo K, Tao H, Tang G, Chu PK. Influence of aggressive ions on the degradation behavior of biomedical magnesium alloy in physiological environment. Acta Biomaterialia 2008;4:2008-15.

[173] Yamamoto A, Hiromoto S. Effect of inorganic salts, amino acids and proteins on the degradation of pure magnesium in vitro. Materials Science & Engineering C-Biomimetic and Supramolecular Systems 2009;29:1559-68.

[174] Hu H, Nie X, Ma Y. Corrosion and Surface Treatment of Magnesium Alloys2014.

[175] Hagihara K, Kinoshita A, Sugino Y, Yamasaki M, Kawamura Y, Yasuda HY, et al. Effect of long-period stacking ordered phase on mechanical properties of Mg97Zn1Y2 extruded alloy. Acta Materialia 2010;58:6282-93.

[176] Yamamoto A, Honma R, Sumita M. Cytotoxicity evaluation of 43 metal salts using murine fibroblasts and osteoblastic cells. Journal of biomedical materials research 1998;39:331-40.

[177] Ratner BD, Hoffman AS, Schoen FJ, Lemons JE. Biomaterials Science - An Introduction to Materials in Medicine (2nd Edition). Elsevier.

[178] Duncan RL, Turner CH. Mechanotransduction and the functional response of bone to mechanical strain. Calcified Tissue International 1995;57:344-58.

[179] Chaya A, Yoshizawa S, Verdelis K, Myers N, Costello BJ, Chou DT, et al. In vivo study of magnesium plate and screw degradation and bone fracture healing. Acta Biomater 2015;18:262-9.

[180] Stanek III EJ, Calabrese E, Barnes RM, Keegan E, Lasztity A, Wang X, et al. Ingestion of trace elements from food among preschool children: Al, Ba, Mn, Si, Ti, V, Y, and Zr. J of Trace Elem Exp Med 1988;1:179-90.

[181] Schroeder HA, Mitchener M. Scandium, Chromium(VI), Gallium, Yttrium, Rhodium, Palladium, Indium in Mice: Effects on Growth and Life Span. The Journal of Nutrition 1971;101:1431-7.

[182] Fischer J, Pröfrock D, Hort N, Willumeit R, Feyerabend F. Improved cytotoxicity testing of magnesium materials. Materials Science and Engineering: B 2011;176:830-4.

[183] Golub EE, Boesze-Battaglia K. The role of alkaline phosphatase in mineralization. Current Opinion in Orthopaedics 2007;18:444-8 10.1097/BCO.0b013e3282630851.

[184] Komori T. Regulation of osteoblast differentiation by Runx2. Advances in experimental medicine and biology 2010;658:43-9.

[185] Pittenger MF, Mackay AM, Beck SC, Jaiswal RK, Douglas R, Mosca JD, et al. Multilineage Potential of Adult Human Mesenchymal Stem Cells. Science 1999;284:143-7.

[186] Nakamura A, Dohi Y, Akahane M, Ohgushi H, Nakajima H, Funaoka H, et al. Osteocalcin Secretion as an Early Marker of In Vitro Osteogenic Differentiation of Rat Mesenchymal Stem Cells. Tissue Engineering Part C: Methods 2009;15:169-80.

[187] Nakamura Y, Tsumura Y, Tonogai Y, Shibata T, Ito Y. Differences in Behavior among the Chlorides of Seven Rare Earth Elements Administered Intravenously to Rats. Toxicological Sciences 1997;37:106-16.

[188] Zartner P, Cesnjevar R, Singer H, Weyand M. First successful implantation of a biodegradable metal stent into the left pulmonary artery of a preterm baby. Catheterization and Cardiovascular Interventions 2005;66:590-4.

[189] Horovitz CT. Biochemistry of Scandium and Yttrium, Part 2: Biochemistry and Applications: Springer US; 2012.

[190] Zhang J, Liu C, Li Y, Sun J, Wang P, Di K, et al. Effect of yttrium ion on the proliferation, differentiation and mineralization function of primary mouse osteoblasts in vitro. Journal of Rare Earths 2010;28:466-70.

[191] Webster TJ, Ergun C, Doremus RH, Bizios R. Hydroxylapatite with substituted magnesium, zinc, cadmium, and yttrium. II. Mechanisms of osteoblast adhesion. Journal of biomedical materials research 2002;59:312-7.

[192] Serre CM, Papillard M, Chavassieux P, Voegel JC, Boivin G. Influence of magnesium substitution on a collagen–apatite biomaterial on the production of a calcifying matrix by human osteoblasts. Journal of biomedical materials research 1998;42:626-33.

[193] Plecko M, Sievert C, Andermatt D, Frigg R, Kronen P, Klein K, et al. Osseointegration and biocompatibility of different metal implants - a comparative experimental investigation in sheep. BMC Musculoskeletal Disorders 2012;13:32.

[194] Janning C, Willbold E, Vogt C, Nellesen J, Meyer-Lindenberg A, Windhagen H, et al. Magnesium hydroxide temporarily enhancing osteoblast activity and decreasing the osteoclast number in peri-implant bone remodelling. Acta Biomaterialia 2010;6:1861-8.

[195] Subramani K, Ahmed W. Emerging Nanotechnologies in Dentistry: Processes, Materials and Applications: Elsevier Science; 2011.

[196] Schmidbaur H, Bach I, Wilkinson DL, Müller G. Metal ion binding by amino acids. Preparation and crystal structures of magnesium, strontium, and barium L-glutamate hydrates. Chemische Berichte 1989;122:1433-8.

[197] Bobe K, Willbold E, Morgenthal I, Andersen O, Studnitzky T, Nellesen J, et al. In vitro and in vivo evaluation of biodegradable, open-porous scaffolds made of sintered magnesium W4 short fibres. Acta Biomater 2013.

[198] Li RW, Kirkland NT, Truong J, Wang J, Smith PN, Birbilis N, et al. The influence of biodegradable magnesium alloys on the osteogenic differentiation of human mesenchymal stem cells. Journal of biomedical materials research Part A 2014;102:4346-57.

[199] Ur Rahman Z, Pompa L, Haider W. Electrochemical characterization and in-vitro bio-assessment of AZ31B and AZ91E alloys as biodegradable implant materials. Journal of materials science Materials in medicine 2015;26:217.

[200] Seo H-J, Cho Y-E, Kim T, Shin H-I, Kwun I-S. Zinc may increase bone formation through stimulating cell proliferation, alkaline phosphatase activity and collagen synthesis in osteoblastic MC3T3-E1 cells. Nutrition Research and Practice 2010;4:356-61.

[201] Hallab NJ, Vermes C, Messina C, Roebuck KA, Glant TT, Jacobs JJ. Concentration- and composition-dependent effects of metal ions on human MG-63 osteoblasts. Journal of biomedical materials research 2002;60:420-33.

[202] Yoshizawa S, Brown A, Barchowsky A, Sfeir C. Magnesium ion stimulation of bone marrow stromal cells enhances osteogenic activity simulating the effect of magnesium alloy degradation. Acta Biomaterialia.

[203] Witte F, Fischer J, Nellesen J, Vogt C, Vogt J, Donath T, et al. In vivo corrosion and corrosion protection of magnesium alloy LAE442. Acta Biomaterialia 2010;6:1792-9.

[204] Aghion E, Levy G, Ovadia S. In vivo behavior of biodegradable Mg–Nd–Y–Zr–Ca alloy. J Mater Sci: Mater Med 2012;23:805-12.

[205] Midwood KS, Williams LV, Schwarzbauer JE. Tissue repair and the dynamics of the extracellular matrix. The International Journal of Biochemistry & Cell Biology 2004;36:1031-7.

[206] Witte F, Fischer J, Nellesen J, Crostack H-A, Kaese V, Pisch A, et al. In vitro and in vivo corrosion measurements of magnesium alloys. Biomaterials 2006;27:1013-8.

[207] Walker J, Shadanbaz S, Kirkland NT, Stace E, Woodfield T, Staiger MP, et al. Magnesium alloys: Predicting in vivo corrosion with in vitro immersion testing. Journal of Biomedical Materials Research Part B: Applied Biomaterials 2012;100B:1134-41.

[208] Ullmann B, Reifenrath J, Dziuba D, Seitz J-M, Bormann D, Meyer-Lindenberg A. In Vivo Degradation Behavior of the Magnesium Alloy LANd442 in Rabbit Tibiae. Materials 2011;4:2197-218.

[209] Yamazaki M, Majeska RJ, Yoshioka H, Moriya H, Einhorn TA. Spatial and temporal expression of fibril-forming minor collagen genes (types V and XI) during fracture healing. Journal of Orthopaedic Research 1997;15:757-64.

[210] Bostrom MPG, Lane JM, Berberian WS, Missri AAE, Tomin E, Weiland A, et al. Immunolocalization and expression of bone morphogenetic proteins 2 and 4 in fracture healing. Journal of Orthopaedic Research 1995;13:357-67.

[211] Einhorn TA, Majeska RJ, Rush EB, Levine PM, Horowitz MC. The expression of cytokine activity by fracture callus. Journal of Bone and Mineral Research 1995;10:1272-81.

[212] Iwaki A, Jingushi S, Oda Y, Izumi T, Shida JI, Tsuneyoshi M, et al. Localization and quantification of proliferating cells during rat fracture repair: Detection of proliferating cell nuclear antigen by immunohistochemistry. Journal of Bone and Mineral Research 1997;12:96-102.

[213] Hausman MR, Schaffler MB, Majeska RJ. Prevention of fracture healing in rats by an inhibitor of angiogenesis. Bone 2001;29:560-4.

[214] Ryhänen J, Kallioinen M, Serlo W, Sandvik P, Niemelä E, Tuukkanen J. Bone Healing and Mineralization of Femoral Osteotomy Fixed with Intramedullary NiTi Rod. SMST-2000 : Proceedings of the International Conference on Shape Memory and Superelastic Technologies. Materials Park, OH, USA: ASM International; 2001. p. 339 - 45.

[215] Lamm G, Auer J, Weber T, Berent R, Ng C, Eber B. Postoperative white blood cell count predicts atrial fibrillation after cardiac surgery. J Cardiothorac Vasc Anesth 2006;20:51-6.

[216] Mushahary D, Sravanthi R, Li Y, Kumar MJ, Harishankar N, Hodgson PD, et al. Zirconium, calcium, and strontium contents in magnesium based biodegradable alloys modulate the efficiency of implant-induced osseointegration. International journal of nanomedicine 2013;8:2887-902.

[217] Hou L, Li Z, Pan Y, Du L, Li X, Zheng Y, et al. In vitro and in vivo studies on biodegradable magnesium alloy. Progress in Natural Science: Materials International 2014;24:466-71.

[218] Zhang E, Xu L, Yu G, Pan F, Yang K. In vivo evaluation of biodegradable magnesium alloy bone implant in the first 6 months implantation. Journal of biomedical materials research Part A 2009;90:882-93.

[219] Hartwig A. Role of magnesium in genomic stability. Mutation Research/Fundamental and Molecular Mechanisms of Mutagenesis 2001;475:113-21.

[220] Choudhary L, Singh Raman RK. Magnesium alloys as body implants: Fracture mechanism under dynamic and static loadings in a physiological environment. Acta Biomaterialia 2012;8:916-23.

[221] Kannan MB, Raman RKS. In vitro degradation and mechanical integrity of calcium-containing magnesium alloys in modified-simulated body fluid. Biomaterials 2008;29:2306-14.

[222] Choudhary L, Singh Raman RK, Hofstetter J, Uggowitzer PJ. In-vitro characterization of stress corrosion cracking of aluminium-free magnesium alloys for temporary bio-implant applications. Materials Science and Engineering: C 2014;42:629-36.

[223] Levesque J, Hermawan H, Dube D, Mantovani D. Design of a pseudo-physiological test bench specific to the development of biodegradable metallic biomaterials. Acta Biomaterialia 2008;4:284-95.

[224] Chen Y, Zhang S, Li J, Song Y, Zhao C, Zhang X. Dynamic degradation behavior of MgZn alloy in circulating m-SBF. Materials Letters 2010;64:1996-9.

[225] Witte F, Ulrich H, Rudert M, Willbold E. Biodegradable magnesium scaffolds: Part I: Appropriate inflammatory response. Journal of Biomedical Materials Research - Part A 2007;81:748-56.

[226] Chou DT, Hong D, Saha P, Ferrero J, Lee B, Tan Z, et al. In vitro and in vivo corrosion, cytocompatibility and mechanical properties of biodegradable Mg-Y-Ca-Zr alloys as implant materials. Acta Biomater 2013;9:8518-33.

[227] International Organization for Standardization. Biological evaluation of medical devices -- Part 12: Sample preparation and reference materials. ISO 10993-12:2007.

[228] Schmitz JP, Hollinger JO. The critical size defect as an experimental model for craniomandibulofacial nonunions. Clinical Orthopaedics and Related Research 1987;205:299-308.

[229] Allan Praemer SF, Dorothy P. Rice. Musculoskeletal Injuries. Park Ridge, IL: American Academy of Orthopedic Surgeons; 1992.

[230] Olivier V, Faucheux N, Hardouin P. Biomaterial challenges and approaches to stem cell use in bone reconstructive surgery. Drug Discovery Today 2004;9:803-11.

[231] Hollister SJ. Porous scaffold design for tissue engineering. Nat Mater 2005;4:518-24.

[232] Sun W, Starly B, Nam J, Darling A. Bio-CAD modeling and its applications in computer-aided tissue engineering. Comput Aided Des 2005;37:1097-114.

[233] Murr LE, Quinones SA, Gaytan SM, Lopez MI, Rodela A, Martinez EY, et al. Microstructure and mechanical behavior of Ti–6Al–4V produced by rapid-layer manufacturing, for biomedical applications. Journal of the Mechanical Behavior of Biomedical Materials 2009;2:20-32.

[234] Sachs E, Cima M, Cornie J. Three-Dimensional Printing: Rapid Tooling and Prototypes Directly from a CAD Model. CIRP Annals - Manufacturing Technology 1990;39:201-4.

[235] Butscher A, Bohner M, Hofmann S, Gauckler L, Müller R. Structural and material approaches to bone tissue engineering in powder-based three-dimensional printing. Acta Biomaterialia 2011;7:907-20.

[236] Sachs E, Wylonis E, Allen S, Cima M, Guo H. Production of injection molding tooling with conformal cooling channels using the three dimensional printing process. Polymer Engineering & Science 2000;40:1232-47.

[237] Wiria FE, Shyan JYM, Lim PN, Wen FGC, Yeo JF, Cao T. Printing of Titanium implant prototype. Materials & Design 2010;31, Supplement 1:S101-S5.

[238] Staiger MP, Kolbeinsson I, Kirkland NT, Nguyen T, Dias G, Woodfield TBF. Synthesis of topologically-ordered open-cell porous magnesium. Materials Letters 2010;64:2572-4.

[239] Hollister SJ, Lin CY, Saito E, Lin CY, Schek RD, Taboas JM, et al. Engineering craniofacial scaffolds. Orthodontics & Craniofacial Research 2005;8:162-73.

[240] ASTM E8-04 Standard Test Methods for Tension Testing of Metallic Materials. Annual book of ASTM standards. Philadelphia, PA: ASTM; 2004.

[241] International A. G102 - 89 Standard Practice for Calculation of Corrosion Rates and Related Information from Electrochemical Measurements. 2010.

[242] Martínez J, Cotes SM, Cabrera AF, Desimoni J, Fernández Guillermet A. On the relative fraction of ε martensite in γ-Fe–Mn alloys. Materials Science and Engineering: A 2005;408:26-32.

[243] Volynova TF, Medov IB, Sidorova IB. Mechanical properties and the fine structure of powdered iron-manganese alloys. Powder Metallurgy and Metal Ceramics 1986;25:999-1006.

[244] Gartstein E, Rabinkin A. On the f.c.c. → h.c.p. phase transformation in high manganese-iron alloys. Acta Metallurgica 1979;27:1053-64.

[245] Irsen SH, Leukers B, Höckling C, Tille C, Seitz H. Bioceramic Granulates for use in 3D Printing: Process Engineering Aspects. Materialwissenschaft und Werkstofftechnik 2006;37:533-7.

[246] Yoo J, Cima M, Khanuja S, Sachs E. Structural Ceramic Components by 3D Printing. Proceedings of the Solid Freeform Fabrication Symposium 1993:40-50.

[247] Curodeau A, Sachs E, Caldarise S. Design and fabrication of cast orthopedic implants with freeform surface textures from 3-D printed ceramic shell. Journal of Biomedical Materials Research 2000;53:525-35.

[248] Risbud MV, Sittinger M. Tissue engineering: advances in in vitro cartilage generation. Trends in biotechnology 2002;20:351-6.

[249] Cheung H-Y, Lau K-T, Lu T-P, Hui D. A critical review on polymer-based bio-engineered materials for scaffold development. Composites Part B: Engineering 2007;38:291-300.

[250] Bonadio J, Smiley E, Patil P, Goldstein S. Localized, direct plasmid gene delivery in vivo: prolonged therapy results in reproducible tissue regeneration. Nat Med 1999;5:753-9.

[251] Nasim M, Edwards BC, Wilson EA. A study of grain boundary embrittlement in an Fe–8%Mn alloy. Materials Science and Engineering: A 2000;281:56-67.

[252] Yamaura SI, Tsurekawa S, Watanabe T. The control of oxidation-induced intergranular embrittlement by grain boundary engineering in rapidly solidified Ni-Fe alloy ribbons. Materials Transactions 2003;44:1494-502.

[253] Kannan MB, Raman RKS, Khoddam S. Comparative studies on the corrosion properties of a Fe–Mn–Al–Si steel and an interstitial-free steel. Corrosion Science 2008;50:2879-84.

[254] Grajcar A, Kołodziej S, Krukiewicz W. Corrosion resistance of high-manganese austenitic steels. Archives of Materials Science and Engineering 2010;41:77-84.

[255] Hallab NJ, Vermes C, Messina C, Roebuck KA, Glant TT, Jacobs JJ. Concentration- and composition-dependent effects of metal ions on human MG-63 osteoblasts. Journal of Biomedical Materials Research 2002;60:420-33.

[256] Mueller PP, Arnold S, Badar M, Bormann D, Bach F-W, Drynda A, et al. Histological and molecular evaluation of iron as degradable medical implant material in a murine animal model. Journal of Biomedical Materials Research Part A 2012;100A:2881-9.

[257] Ramay HRR, Zhang M. Biphasic calcium phosphate nanocomposite porous scaffolds for load-bearing bone tissue engineering. Biomaterials 2004;25:5171-80.